A Detailed Study of Galaxy Clusters
with
Weak Gravitational Lensing
and
X-rays

Dissertation

zur
Erlangung des Doktorgrades (Dr. rer. nat.)
der
Mathematisch–Naturwissenschaftlichen Fakultät
der
Rheinischen Friedrich–Wilhelms–Universität Bonn

vorgelegt von

Jennifer Miriam Piel
aus
Bonn

Bonn, März 2012

Angefertigt mit Genehmigung der
Mathematisch–Naturwissenschaftlichen Fakultät der
Rheinischen Friedrich–Wilhelms–Universität Bonn

1. Gutachter: Prof. Dr. Peter Schneider

2. Gutachter: Prof. Dr. Thomas H. Reiprich

Tag der Promotion: 18. Juni 2012

Erscheinungsjahr: 2012

Abstract

During the past decade observations of the Cosmic Microwave Background (CMB), the growth rate of linear density perturbations or the mass function of galaxy clusters among others have independently suggested that our Universe is composed of $\sim$ 4% baryons, $\sim$ 23% dark matter and $\sim$ 73% dark energy. By combining those methods, the values of cosmological parameters can be constrained and the dynamics and geometrics of the Universe can be determined. In particular, the cluster mass function is sensitive to the matter density $\Omega_{\rm m}$ which comprises both dark and baryonic matter, the amplitude of mass fluctuations on cluster scales σ_8, and the dark energy density $\Omega_{\rm de}$ and equation-of-state parameter w.

As non-linear tracers of the Cosmic Web, galaxy clusters represent the top of hierarchical structure formation with the largest dark matter halos. Therefore, cosmological studies based on galaxy clusters allow important consistency checks to e.g CMB results. Since the most extensive studies of galaxy clusters so far have been carried out in X-rays and in the optical, it is of particular interest to cross-calibrate cluster masses with both methods. Furthermore, the combination of both approaches allows to calibrate scaling relations between X-ray observables and mass. To perform cluster cosmology we require large, well defined cluster samples and precise cluster masses. This thesis focuses on the latter – the precise calibration of cluster masses on a sample of five galaxy clusters at high and intermediate redshifts ($0.3 < z < 0.55$) spanning a wide range in mass and morphology. For all clusters high-quality space-based data from ACS@HST are available for accurate weak lensing shape measurements. Independent and complementary mass estimates arise from high-quality X-ray data from *XMM-Newton* and *Chandra*. The combination of weak gravitational lensing and X-rays allows us to investigate cluster properties, such as mass, concentration and velocity dispersion and to discuss our results with respect to dynamical state, morphology and projected 2d-morphology. Using weak lensing masses, we can further cross-calibrate the scaling relations between X-ray masses and observables which may evolve with redshift (e.g. Voit 2005). For the redshifts of our sample we might observe such an evolution compared to samples at lower redshifts.

The weak lensing analysis of this project was carried out as follows: With the aperture mass statistics ($M_{\rm ap}$–statistics, e.g. Schneider 1996) the weak lensing signal of the clusters was measured and position and amplitude of its peak were confirmed using simulations. Using magnitude-redshift relations (Schrabback et al. 2007, 2010), the mean distance ratios and effective mean source redshifts of the lensed background galaxies were estimated to optimise the lensing signal. We showed that the peak of the lensing signal can be used as alternative definition for the cluster centre and used its position to calculate the tangential shear profiles to which we fitted commonly used mass models to obtain the cluster masses. We found that our cluster masses are widely consistent with previous studies, such as X-rays, the Sunyaev-Zeldovich Effect or dynamical estimates, which we used as cross-check because no uniformly obtained cluster masses for our sample were available. As an example study, we used archival multi-colour data from the ground-based facilities MegaPrime@CFHT and Suprime-Cam@SUBARU to estimate the photometric redshifts of the lensed background galaxies and calibrated them against spectroscopic redshifts

from DEIMOS@Keck-II (Moran et al. 2007). With the inclusion of such photometric redshifts, we can improve our weak lensing analysis in two regards: Firstly, the strength of a lensing system depends on the distance between lens and background sources among others. Secondly, we can remove unlensed foreground galaxies using photometric redshifts. Since only 5% of our sources of MS0451.6−0305 have photometric redshifts, this effect is only marginal.

In the second step of this project, the X-ray analysis was performed for three clusters which were observed with *XMM-Newton* and one cluster which was observed with *Chandra*. Using the flux-weighted X-ray centroid as cluster centre, temperature and gas density profiles were obtained which we used to determine the X-ray hydrostatic masses at an overdensity of $\Delta = 500$ compared to the mean density of the Universe at the redshift of the cluster. Using the corresponding radius r_{500}, the global observables temperature, luminosity and metallicity were obtained. Especially, for our disturbed clusters, we found offsets between the flux-weighted X-ray centroid and the weak lensing peak which can also be observed for e.g. the Bullet Cluster 1E0657-56 (e.g. Clowe et al. 2007). Furthermore, the X-ray hydrostatic masses are $\sim 20\%$ lower than the weak lensing masses because most of our clusters are not in hydrostatic equilibrium which is the main assumption in X-rays. A comparison with previous X-ray studies shows that our cluster masses are $\sim 20 - 35\%$ lower which is due to the fact that our masses were obtained from temperature profiles instead of using isothermality (e.g. Zhang et al. 2005) and the old *Chandra*-calibration (e.g. Snowden et al. 2008).

The scaling relations were calibrated with slopes from self-similar predictions and well-established samples (Zhang et al. 2006, 2008, 2010), and the normalisations were determined. We found that our normalisations are widely consistent with previous studies as far as cosmology, method and slope are comparable to ours. We could not prove whether there is an evolution with redshift for our scaling relations because either there is no evolution or the uncertainty is too high. To investigate whether there is an evolution with redshift, a larger sample would be required. Furthermore, we would need lensing data covering larger field-of-views which would reduce the errors on lensing mass as well as deep photometric redshifts for all clusters.

Even if there is only one possible unified theory, it is just a set of rules and equations. What is it that breathes fire into the equations and makes a universe for them to describe? The usual approach of science of constructing a mathematical model cannot answer the questions of why there should be a universe for the model to describe. Why does the universe go to all the bother of existing?

Stephen W. Hawking

Contents

Chapter 0

Introduction

Galaxy clusters are of special interest for modern cosmology because they represent the most gravitationally bound structures of the cosmic matter distribution embedded into the largest dark matter halos. In hierarchical structure formation theories, galaxy clusters emerged via gravitational collapse from fluctuations in the primordial density field. Probing the large-scale-structure (LSS), they provide constraints on cosmological parameters via the cluster mass function which comprises the number density and the redshift evolution of galaxy clusters as well as their large-scale distribution. Thus, the cluster mass function is very sensitive to e.g. the matter density $\Omega_{\rm m}$, the amplitude of mass fluctuations on cluster scales σ_8, and to the dark energy density $\Omega_{\rm de}$ and equation-of-state parameter w (e.g. Eke et al. 1996; Bahcall & Fan 1998; Borgani et al. 1999; Reiprich & Böhringer 2002; Schuecker et al. 2003a,b; Mantz et al. 2008; Vikhlinin et al. 2009a,b). As cosmological probes, galaxy clusters provide an independent and complementary tool compared to other approaches such as the distance-redshift test using standard candles (e.g. SNIa, Perlmutter et al. 1999; Riess et al. 2004; Kowalski et al. 2008), Baryonic-Acoustic-Oscillations (e.g. Eisenstein et al. 2005; Percival et al. 2007), the growth rate of linear density perturbations (e.g. Huterer & Turner 2001) or measurements of the temperature fluctuations of the Cosmic Microwave Background (CMB, e.g. Dunkley et al. 2009; Larson et al. 2011).

The theoretical expectation for the cluster abundance can be obtained either from analytical models (Press & Schechter 1974; Sheth & Tormen 1999) or from N-body simulations (e.g. Jenkins et al. 2001; Warren et al. 2006; Tinker et al. 2008) which precisely predict the abundance of dark matter halos as a function of mass and redshift. Since the cluster mass is not directly measurable, it has to be inferred from observations in various wavelength ranges of the electromagnetic spectrum. For instance, the cluster masses can be derived in the optical from measuring the velocity dispersion of the cluster galaxies (e.g. Girardi & Mezzetti 2001) or gravitational lensing (e.g. Schneider 1996; Dahle et al. 2003; Clowe et al. 2006b; Gavazzi & Soucail 2007; Schirmer et al. 2007; Holhjem et al. 2009; Israel et al. 2011). In X-rays, cluster masses can be inferred from the temperature and density distributions of the hot intra-cluster medium (ICM, e.g. Zhang et al. 2005, 2006, 2008). At sub-millimetre wavelenghts, we can obtain cluster masses via the energy CMB-photons gain when they encounter the ICM (Sunyaev-Zeldovich Effect, e.g. Kravtsov et al. 2006). Since galaxy clusters are richly labelled objects, many of their properties correlate well with mass. To understand the relation between direct observables, such as X-ray luminosity $L_{\rm X}$ or temperature $T_{\rm X}$, and the total cluster mass, is crucial for precision cluster cosmology. Compared to N-body simulations, theoretical predictions about directly observational quantities can become difficult because baryonic physics may be more complicated as can be modelled with simulations. In addition, mass uncertainties are often quoted as the main source of uncertainty in cluster-based cosmology (e.g. Vikhlinin et al. 2009b; Mantz et al. 2010b). Independent cluster mass estimates

are essential to understand the systematic uncertainties of cluster masses. For these reasons, mass proxies based on scaling relations between observables and cluster mass must be carefully tested and cross-checked with observations (e.g. Zhang et al. 2008, 2010).

The most extensive studies of galaxy clusters so far have been carried out in X-rays (e.g. Böhringer et al. 2000, 2004; Reiprich & Böhringer 2002; Allen et al. 2003; Mantz et al. 2008; Vikhlinin et al. 2009a,b) and in the optical (e.g. Gladders & Yee 2000; Goto et al. 2002; Bahcall et al. 2003; Gladders et al. 2007; Koester et al. 2007), wherefore it is of particular interest to correlate and cross-check samples observed in both wavelength ranges and to investigate the strengths and weaknesses of both methods. The combination of lensing and X-ray allows us to calibrate scaling relations between X-ray observables and mass (e.g. Okabe & Umetsu 2008; Kawaharada et al. 2010; Okabe et al. 2010; Zhang et al. 2010).

In X-ray studies, cluster masses can be inferred from the temperature and density distributions of the hot intra-cluster medium which emits X-ray because it is compressed and shock-heated by the gravitational potential of the cluster. The accuracy with which cluster masses are obtained depends on the validity of hydrostatic equilibrium between the ICM and the gravitational potential which can be disturbed due to merging. But the accuracy is also a function of the photon statistics, the spatial resolution of the telescope and the radius up to which the X-ray emission can be measured. With the current instruments, good photon statistics for reliable hydrostatic mass estimates are available only out to r_{500}. A detailed temperature profile can only be obtained for the brightest and nearby clusters. For distant clusters, often only a global temperature or luminosity can be determined wherefore we have to rely on scaling relations between temperature and X-ray luminosity with mass.

In the optical, the masses of galaxy clusters can be inferred from gravitational lensing (e.g. Mellier 1999; Bartelmann & Schneider 2001). In this theory, one considers the distortion and magnification of light from background galaxies which is deflected by a foreground cluster. To first order, the gravitational field of a foreground mass provides a coherent, tangential alignment of background sources around the centre of the mass concentration. For very massive lens systems and appropriate geometrical alignment between observer, lens and source, *strong gravitational lensing* manifests in strongly elongated sources (*giant arcs*) and in some cases multiple images of a source can be observed. This allows one to directly model the mass distribution in the central cluster region. In the cluster outskirts, the image distortions are so weak that their distortions have to determined by statistical means. By assuming that the galaxies are intrinsically randomly oriented, *weak gravitational lensing* leads in the presence of a mass to a significant, non-zero mean ellipticity of galaxy images which allows us to infer the total projected cluster mass and to reconstruct the two-dimensional mass distribution of galaxy clusters. Since the background sources are completely independent of the cluster, we do not have to rely on relations between light and matter to infer the cluster properties. However, gravitational lensing has the drawback that it is prone to projection effects such as halo triaxiality and matter distributed along the line-of-sight. For this reason, it is important to cross-check weak lensing cluster masses with hydrostatic mass estimates from X-ray studies which are free of such projection effects.

The accuracy of lensing masses is further limited by the available data quality. Deep observations and high-resolution imaging are required to achieve high number densities of the background source population and to obtain accurate shape measurements. In addition, multi-colour data allow us to determine the photometric redshifts of the sources and to separate foreground and background galaxies but it also improves the estimates on the spatial geometry between observer, lens and sources. Especially for high-redshift clusters, such as studied in this work, these criteria are important because they are more sensitive to contaminations of the background sample than low-redshift clusters. To trace the gravitational lens effect beyond the cluster outskirts, wide-field images from ground-based facilities or mosaic observations from space are crucial to constrain the

cluster mass and to reduce its errors. Anyhow, space-based data provides the best quality of shape measurements since shorter exposure times are required to achieve the desired depth and it is free of the blurring due to atmospheric turbulences.

Recent studies suggest that X-ray scaling relations are self-similar and show no strong evolution for massive galaxy clusters up to $z \sim 0.3$ compared to samples at higher redshifts (e.g. Maughan et al. 2006, 2008) which are primarily homogeneous and consist mostly of relaxed clusters (Zhang et al. 2007). Cluster masses based on X-ray and weak lensing analyses are in good agreement for clusters in this redshift range (e.g. Zhang et al. 2008 and references therein). For clusters at higher redshifts, where evolution effects become more pronounced than in the local Universe, extensive studies on large statistical samples still need to be performed. To make progress in this area, this thesis is devoted to the detailed weak gravitational lensing and X-ray analysis of five galaxy clusters at high and intermediate redshifts ($0.3 \lesssim z \lesssim 0.55$) spanning a wide range in mass and morphology. The analysis presented in this work is performed with deep space-based data from the Hubble Space Telescope (HST) which allow accurate shape measurements and provide a coverage up to the cluster outskirts by the mosaic-pattern of the observations. In addition, multi-colour ground-based data from MegaPrime@CFHT and Suprime-Cam@SUBARU are available to estimate photometric redshifts for the cluster MS0451.6−0305. These optical data are complemented by high-resolution X-ray data from *XMM-Newton* and *Chandra*.

This work will be organised as follows: In Chapter 1, the cosmological background knowledge for the scope of this thesis will be provided. Chapter 2 and Chapter 3 introduce gravitational lensing theory and X-ray physics, respectively. The cluster sample and the data used for this analysis will be described in Chapter 4. Since photometric redshifts are available for one cluster, their accuracy and their effect on a weak lensing analysis will be estimated and discussed in Chapter 5. The results from the weak lensing analysis will be presented in Chapter 6 followed by the results from the X-ray analysis in Chapter 7. Scaling relations including X-ray observables as well as X-ray hydrostatic and weak lensing masses will be discussed in Chapter 8. A concluding summary will be provided in Chapter 9. Throughout this work we assume a flat ΛCDM-cosmology with $\Omega_\mathrm{m} = 0.27$, $\Omega_\Lambda = 0.73$ and $h = 0.72$.

Chapter 1

Cosmology

Cosmology is a scientific discipline that deals not only with the origin and the evolution of the Universe as a whole but also with its fundamental structure. Thereby this science connects particle physics, observational astronomy and philosophy. Sprouting from a mythical and religious world picture, such as e.g. in the ancient China or Babylonia, cosmology has grown to a fundamental research which has the goal to explain the past, present and future of our Universe using the four known fundamental interactions gravity, electromagnetism and strong and weak interactions. The latter two act only on atomic scales and it is believed that electromagnetism does not play a role in cosmology as well, because the Universe is supposed to be charge neutral. For this reason, gravity is the only fundamental force that acts on large distances and thus it dominates the cosmic evolution. In this chapter, we will learn that not only gravity drives cosmic evolution. There is another, mysterious force which is responsible for the expansion of space via the negative pressure of the vacuum, not only very recently, but also in the beginning. This force is called *dark energy* and its nature is still unknown.

Since we can only observe our own Universe and do not have knowledge about other universes, we have to distinguish carefully between serendipitous incidents and actual laws of Nature. Provided that the nature of space-time is mathematically describable, we can only observe events on our backward light cone which limits the observable part of the Universe. Yet, this allows us to study our Universe at earlier times back to when it was only 380,000 years old and the CMB was formed. In addition, we can infer the evolution of objects in our cosmic neighbourhood, such as objects in the Milky Way or galaxies of the Local Group from observations of their distant past progenitors.

In this chapter, I will describe the theory upon which the cosmological standard model ΛCDM is based and how galaxy clusters – the subjects of this dissertation – are embedded in this model. I will describe how these massive objects consisting of hundreds of galaxies have evolved from quantum fluctuations to the most significant peaks in the matter distribution of the Universe. In Sect. 1.1, I will briefly outline the cosmic history from very beginning of time and space, the Big Bang to the time at which the CMB was created. Some of the processes which happened during that period are supposed to be responsible for the large-scale structures we observe today. In Sect. 1.2, I will introduce kinematics and energy components of the Universe. Section 1.3 describes the formation of primordial small-scale overdensities which develop to the locally highly inhomogeneous structures we observe today in forms of galaxy clusters, filaments and voids. Section 1.4 will be dedicated to galaxy clusters and their importance for modern cosmology. Detailed reviews on the physics discussed in this chapter are given by e.g. Peacock 1999, Dodelson 2003 and Schneider 2006a.

1.1 Big Bang and nucleosynthesis

From our present knowledge drawn from various observations, the genesis of time, space and matter was an infinitesimal small and infinite hot, dense singularity from which space and time decoupled due to expansion. This event is known as the Big Bang.

Proposed by Lemaître (1927), the Big Bang theory has become popular because it gives the most complete and accurate explanation for various astronomical observations. Evidence that such an event had happened was found in: (1) The recession velocities of distant galaxies (Hubble 1929), (2) the radiation of the Cosmic Microwave Background (e.g. Penzias & Wilson 1965), (3) the abundances of primordial elements (Steigman 2006), (4) the large-scale distribution of galaxies (e.g. Bertschinger 1998; Tegmark et al. 2006) and (5) primordial gas clouds (Fumagalli et al. 2011).

There is no information on the $t \ll 1$ seconds of our Universe since the physics of the corresponding energy scales of interest are not well understood. Yet, physicists prefer among others the idea of inflation in which the Universe expanded rapidly due to the negative-pressure of the vacuum energy density which dominated the expansion. During inflation, any gravitationally-caused space curvature was smoothed to an almost flat space and the seeds for matter inhomogeneities that appear homogeneous on large scales today were sowed. The picture of inflation was first postulated by Guth (1981) and Sato (1981) to explain the vast homogeneity and flatness of the Universe. Although its complete particle physics mechanism is still unknown, it became the most popular theory to describe the birth of our Universe because it explains why the CMB fluctuates only by $\sim 10^{-5}$ over the whole sky when the angular separation of causally-connected regions at its creation subtends only $\sim 1^\circ$ (*Horizon problem*) and why our Universe is so flat (*Flatness problem*).

After inflation, the Universe was reheated to the temperature it had before the onset of inflation due to the phase transition of vacuum energy back into Standard Model particles after. Thus, 1 s after the Big Bang, the temperature was still high enough for nucleosynthesis of the first stable primordial nuclei. Big Bang nucleosynthesis was first postulated by Alpher et al. (1948) who predicted the correct abundances of primordial elements. A detailed review is on this subject is given by Pospelov & Pradler (2010). The nucleosynthesis lasted ~ 3 min because due to expansion, the temperature and the number densities of the particles dropped. As a consequence, the conditions for thermal equilibrium between the particles changed permanently until thermal equilibrium could not be maintained anymore. Thus, neutrinos decoupled from electrons ($\nu\bar{\nu} \leftrightarrow e^+e^-$) at ~ 1.5 MeV. At $T \lesssim 0.5$ MeV the photon energy dropped below the rest mass of elections wherefore pair creation ($\gamma\gamma \rightarrow e^+e^-$) was not longer possible. Hence, the annihilation of electron/positron pairs was initiated until a small fraction of electrons remained. When the temperature dropped below ~ 0.3 MeV, ^{4}He could theoretically form from protons and neutrons, but the deuterium and ^{3}He abundances required for fusion were still too low because these nuclei were destroyed immediately by high-energetic photons after their formation. Only at a temperature of ~ 0.1 MeV which is $\sim 10^9$ K, the Universe had cooled enough to form ^{4}He efficiently. Small fractions of heavier elements were also created before the conditions for nuclear fusion became too poor. Afterwards, the Universe was composed of 75% ^{1}H, 25% ^{4}He and fractions of ^{2}D, ^{3}He, ^{7}Li and ^{7}Be. The more massive elements we know from the periodic table were generated lateron in stars by nuclear burning and during the violent death of massive stars - the supernovae.

The abundances of H and He are supported by observations of e.g. low-metallicity HII regions (e.g. Izotov et al. 2007) or blue compact dwarf galaxies (e.g. Thuan 2008), where only little nuclear synthesis by stars has taken place. The baryon-photon ratio on which the time scale of the primordial nucleosynthesis depends is confirmed by CMB-observations. Besides, the Big

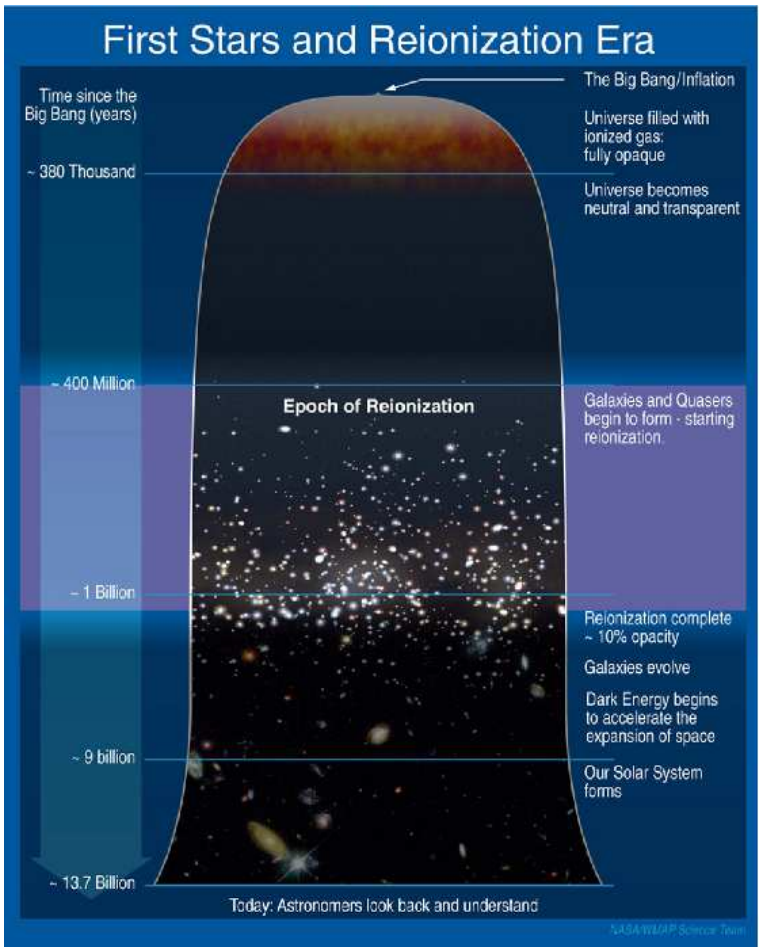

Figure 1.1: This figure illustrates how the Universe has evolved from a singularity to the large-scale distribution of galaxies we observe today. During inflation the Universe expanded rapidly because dark energy dominated the expansion. Compared to this enormous expansion, it has expanded slower since then, although dark energy recently has taken over the expansion again. 380,000 years after the Big Bang, the Universe had cooled down sufficiently to form neutral hydrogen. At that time, the photons which were released in the Big Bang interacted with matter for the last time and we now observe them as the Cosmic Microwave Background (CMB). After a dark period the Universe was illuminated again by the first stars and in the time since, more stars formed as well as all other structures we observe today. From http://imagine.gsfc.nasa.gov/docs/ .

Bang nucleosynthesis predicts the same number of neutrino families $N_\nu = 3$ as it was empirically determined by the decay of the Z-boson.

Before nuclei could combine with free electrons to atoms, the Universe had to cool down to $\sim 0.3\,\mathrm{eV}$. This process known as *recombination* happened at a redshift of $z \approx 1100$, i. e. 380,000 years after the Big Bang and lasted over a longer period ($\Delta z \approx 80$). In fact, neutral hydrogen could have been created at 13.6 eV, but since there are $\sim 10^{-8}$ baryons than photons which exhibit a Planck distribution, there were still enough high energetic photons which could easily reionise the newly formed atoms. In addition, the photons that were emitted when protons and electrons combined to neutral H could reionise other hydrogen atoms. Thus, recombination could only efficiently take place via the quantum-mechanically forbidden two-photon decay of the first excited state of H (^1S-state) with a lifetime of 0.1 s because those photons were too low-energetic to excite other hydrogen atoms.

After recombination, the energy of the existing photons was too low to excite any atoms again. Their Planck distribution was conserved and redshifted to a microwave radiation, the CMB.

The current temperature of the CMB was measured with observations of the *COBE*-satellite to $T = 2.735 \pm 0.060\,\mathrm{K}$ (Boggess et al. 1992) or more recently $T = 2.725 \pm 0.002\,\mathrm{K}$ with seven-year data of the *WMAP*-satellite (Noterdaeme et al. 2011), which surveys the CMB (Fig. 1.2). Since the CMB-photons had too low energies to excite atoms, the Universe went dark until the first stars illuminated the Universe again. This *reionisation* took place between $20 \gtrsim z \gtrsim 6$. How single atoms could form massive structures in forms of stars, galaxies and galaxy clusters will be discussed in Sect. 1.3. An illustrative overview of the history of our Universe is shown in Fig. 1.1.

1.2 The expanding Universe

Since the Big Bang, our Universe has been expanding. To understand the formation of structure in more detail, I will introduce the formalism that describes the expansion behaviour in the framework of General Relativity which is related to the dynamics of the Universe. Although the Universe appears highly inhomogeneous by observing our cosmic neighbourhood, it is homogeneous and isotropic on large scales, wherefore homogeneous and isotropic world models can be considered to describe its large-scale expansion history.

1.2.1 Hubble's constant and definition of redshift

In 1929, Edwin Hubble empirically confirmed a law which was firstly derived two years earlier by Lemaître (1927). This law states that the Doppler-shift which is observed in the spectra of galaxies corresponds to a relative velocity between those galaxies and to Earth and that this recession velocity v increases proportional with distance D

$$v = H_0 D\,. \tag{1.1}$$

Here, the constant of proportionality, H_0, is Hubble's constant which is parametrised as $H_0 = 100\,h\,\mathrm{km\,s^{-1}\,Mpc^{-1}}$ (Hubble 1929). The current value for h is conveniently fixed to 0.72 ± 0.08 (Freedman et al. 2001), based on HST-observations of Cepheid variable stars. More recent results were published by e.g. Suyu et al. (2010) who determined $h = 0.726 \pm 0.031$ via gravitational lensing observations with the HST. One year later, Larson et al. (2011), obtained $h = 0.71 \pm 0.025$ from seven-year *WMAP*-data.

Hubble's observation was the first empirical evidence that our Universe is expanding. Nowadays, we know that the relation between redshift $z = \Delta\lambda/\lambda$, which is the shift of the spectrum an astronomical object emits, and recession velocity is not due to the Doppler effect, but to the expansion of space. In the 1920's, however, it was an acceptable explanation in the context of special relativity. Since then, this approach was replaced by a cosmological model, that relates v with the cosmic expansion.

An expanding universe implies that the physical distances D between galaxies were smaller in the past. For convenience, a *comoving* coordinate system is used, in which the distance χ between two objects remains fixed,

$$\boldsymbol{D}\,(t) = a\,(t)\,\boldsymbol{\chi}\,. \tag{1.2}$$

Here, the *scale factor* $a(t)$ relates physical to comoving coordinates. For an expanding universe $a(t)$ is a monotonically increasing function of time, but it describes any expansion or contraction the Universe could encounter. For the current epoch we set $a(t_0) = 1$. The *redshift* can be expressed via the scale factor as follows: Light that is emitted from a galaxy at time t_e and arrives the observer at t_0, is redshifted due do the cosmic expansion by a factor of $z = \frac{a(t_0)}{a(t_\mathrm{e})} - 1$. With $a(t_0) = 1$ it follows that $a(t) = \frac{1}{1+z}$.

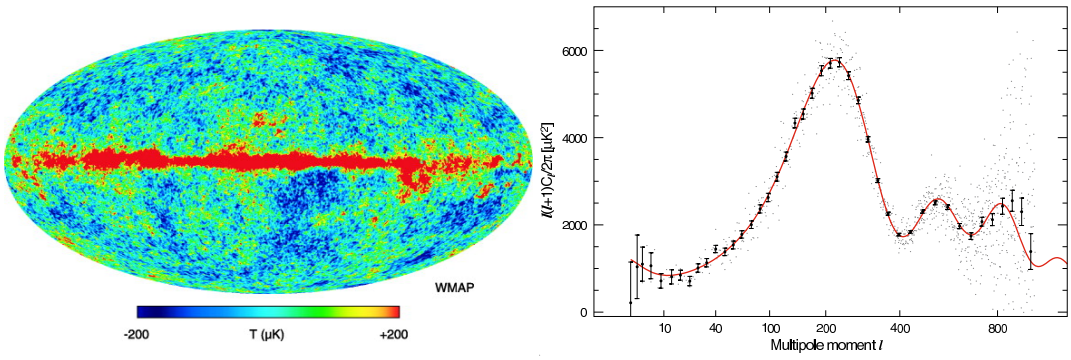

Figure 1.2: *Left:* The CMB-temperature map from the first-year *WMAP*-results in the W-band. The red string that divides the upper and lower part of the map is microwave emission from the galactic plane. Temperature fluctuations are distributed istropically over the CMB. From Bennett et al. (2003). *Right:* The angular power spectrum of the CMB-fluctuations for the best fit ΛCDM-model. The grey dots denote the unbinned data and the black dots are the binned data with 1σ errors composed of noise and cosmic variance. From from Dunkley et al. (2009).

1.2.2 Einstein's field equations and Friedmann expansion

About ten years before Hubble detected evidence of a cosmic expansion, a consistent theory that relates space and time was established by Albert Einstein using the field equations of General Relativity which he formulated in 1915. Since the predominant world picture at that time supported a static universe, the dynamic solution provided by this theory disagreed with the notion of most scientists.

Einstein's field equations,

$$G_{\mu\nu} + \Lambda g_{\mu\nu} = -\frac{8\pi G}{c^2} T_{\mu\nu}\,, \tag{1.3}$$

relate the geometry of space-time described by the Einstein tensor $G_{\mu\nu}$ to the energy-momentum tensor $T_{\mu\nu}$, which grasps the energy and matter content of the Universe as a source of gravity. G is the gravitational constant, c is the speed of light and $g_{\mu\nu}$ is the metric tensor which is symmetric. The *cosmological constant* Λ, which was believed to be zero after the discovery that the Universe is expanding, is today interpreted as energy density of the vacuum.

By applying the *cosmological principle*, which states that our Universe is homogeneous and isotropic on large scales for any comoving observer, to $g_{\mu\nu}$ we can solve Eq. (1.3) and consider homogeneous and isotropic world models in the framework of General Relativity that describe the complete expansion history of the Universe. The geometry which satisfies the cosmological principle is given by the Friedmann-Lemaître-Robertson-Walker metric (FLRW-metric) which was independently defined by Friedmann (1922, 1924), Lemaître (1933), Robertson (1935) and Walker (1937)

$$\mathrm{d}s^2 = \sum_{\mu,\nu=0}^{3} g_{\mu\nu}\mathrm{d}x^\mu \mathrm{d}x^\nu = c^2\mathrm{d}t^2 - a^2(t)\left[\mathrm{d}^2\boldsymbol{\chi}^2 + f_K(\chi)\left(\mathrm{d}\theta^2 + \sin^2(\theta)\,\mathrm{d}\varphi^2\right)\right], \tag{1.4}$$

where the comoving vector $\boldsymbol{\chi} = (\chi, \theta, \varphi)$ is expressed in spherical coordinates. The spatial part $\mathrm{d}\boldsymbol{\chi}^2$ refers to a three-dimensional space with constant curvature K, whereby $f_K(\chi)$ is a function of the curvature parameter K

$$f_K(\chi) = \begin{cases} \frac{1}{\sqrt{K}}\sin\left(\sqrt{K}\chi\right) & K > 0 \quad \text{closed \& spherical} \\ \chi & K = 0 \quad \text{flat} \\ \frac{1}{\sqrt{-K}}\sinh\left(\sqrt{-K}\chi\right) & K < 0 \quad \text{open \& hyperbolic}\,. \end{cases} \tag{1.5}$$

Solving Einstein's field equations by inserting the FLRW-metric (Eq. 1.4) provides us with two equations that describe the evolution of the scale factor and thus the expansion history, i.e. the *Friedmann equations* (Friedmann 1922)[1]

$$\left(\frac{\dot{a}(t)}{a(t)}\right)^2 = \frac{8\pi G}{3}\sum_i \rho_i(a(t)) - \frac{Kc^2}{a^2(t)} + \frac{\Lambda}{3}c^2 \tag{1.6}$$

$$\frac{\ddot{a}(t)}{a(t)} = -\frac{4\pi G}{3}\sum_i \left[\rho_i(a(t)) + \frac{3p_i(a(t))}{c^2}\right] + \frac{\Lambda}{3}c^2 . \tag{1.7}$$

Equation (1.6) is the expansion equation with the Hubble parameter $H(a) = \dot{a}(t)/a(t)$, with which the Hubble law (Eq. 1.1) can be derived alternatively by calculating the time derivative of Eq. (1.2), i. e. $v = \mathrm{d}D(t)/\mathrm{d}t = D(t)\dot{a}(t)/a(t) = H(a)D(t)$. Equation (1.7) states that pressure acts like a source of gravity. The sum accounts for different fluids with different densities.

To obtain a more concrete picture of the cosmic expansion, we have to consider individual energy components and how they evolve with time. As matter – or rather energy because the two are related via $E = mc^2$ – can be treated as a perfect fluid, we apply the *first law of thermodynamics* to obtain the *adiabatic equation*

$$\frac{\mathrm{d}\left[a^3(t)\,\rho(a(t))\,c^2\right]}{\mathrm{d}a(t)} = -p(a(t))\,\frac{\mathrm{d}a^3(t)}{\mathrm{d}a}, \tag{1.8}$$

which can easily be solved for a time-independent equation-of-state parameter $w = p_i/\rho_i c^2$ with

$$\rho_i(t) = \rho_{i,0}\,a(t)^{-3(1+w_i)} . \tag{1.9}$$

We will now evaluate the different components of the energy density $\rho_i(t)$ by inserting Eq. (1.9) into Eq. (1.8) for different w_i.

If the kinetic energy of particles is much smaller than their rest mass ($v \ll c$), we refer to them as non-relativistic matter because their pressure can be neglected. In this case, the matter density evolves with

$$\rho_\mathrm{m}(t) = \rho_{\mathrm{m},0}\,a(t)^{-3} , \tag{1.10}$$

because $p_\mathrm{m} \ll \rho_\mathrm{m}c^2$ and $w_\mathrm{m} \ll 1$. Hence, the number of particles in a comoving volume is constant and decreases with a^{-3} in a proper volume due to the three-dimensional expansion of space. The definition "matter" comprises both baryonic and dark matter. Since the former is $\sim 1/6$ of all non-relativistic matter, "matter" is often equalised with dark matter. More about the nature of dark matter is provided in Sect. 1.4.

Relativistic particles have random velocities of $v \approx c$, wherefore we cannot neglect their pressure. They exert radiation pressure $p_\mathrm{r} = \rho_\mathrm{r}c^2/3$, and hence $w_\mathrm{r} = 1/3$. Inserting this in Eq. (1.9) yields

$$\rho_\mathrm{r}(t) = \rho_{\mathrm{r},0}\,a(t)^{-4} . \tag{1.11}$$

Compared to the matter density (Eq. 1.10), the radiation density drops with an additional factor a^{-1} because the photons lose energy as they become redshifted due to cosmic expansion. Thus, this energy component does not play a role in the current Universe.

[1] Actually, Alexander Friedmann derived Eqs. (1.6) and (1.7) in 1922 from Einstein's field equations to show that the Universe might expand at a rate which can be calculated with these equations. Georges Lemaître independently found a similar solution in 1927 (Lemaître 1927). Their idea of an expanding spacetime would eventually lead to the Big Bang and Steady State theories of cosmology.

Provided the energy density of the vacuum is finite, it can be considered as the cosmological constant. From Eq. (1.6) this yields

$$\rho_\Lambda = \frac{\Lambda c^2}{8\pi G} \tag{1.12}$$

and thus the vacuum energy density is independent of time. Inserting the time derivative in Eq. (1.8) further gives $w_\Lambda = p_\Lambda/\rho_\Lambda c^2 = -1$ which suggests that the negative pressure of the vacuum drives the expansion of space.

For reasons of completeness we also give the time-dependent dark energy density, with $w_{\rm de} < 0$ but not necessarily $= -1$,

$$\rho_{\rm de}\,(t) = \rho_{\rm de,0}\,\exp\left(-3\int_0^{a(t)}\frac{{\rm d}a'}{a'}\left[1+w(a')\right]\right). \tag{1.13}$$

For constant $w = 1/3, 0, -1$, this equation also yields Eqs. (1.10)-(1.12). Here, $w_{\rm de} \leq -1$ due to $p < 0$.

It is convenient to define a *critical density*, $\rho_{\rm cr}(t) = 3H^2(t)/8\pi G$ which is $\rho_{\rm cr} = 1.88 \times 10^{-29}\,h^2\,{\rm g/cm^3}$ for t_0, and to normalise the energy densities with that scale

$$\Omega_{\rm r}\,(t) = \frac{\rho_{\rm r,0}}{\rho_{\rm cr}\,(t)}\,, \quad \Omega_{\rm m}\,(t) = \frac{\rho_{\rm m,0}}{\rho_{\rm cr}\,(t)}\,, \quad \Omega_\Lambda\,(t) = \frac{\Lambda c^2}{3H^2\,(t)} \quad \text{or} \quad \Omega_{\rm de}\,(t) = \frac{\rho_{\rm de,0}}{\rho_{\rm cr}\,(t)}\,. \tag{1.14}$$

The total density parameter is the sum over these three energy components, i.e. $\Omega_{\rm tot} = \Omega_{\rm r} + \Omega_{\rm m} + \Omega_\Lambda$, and accordingly $\Omega_{\rm tot} = \Omega_{\rm r} + \Omega_{\rm m} + \Omega_{\rm de}$ for a time-dependent component of dark energy. Current values for the density parameters arise from amplitude and position of the peaks in the CMB power spectrum (Fig. 1.2 *right*) inferred from seven-year *WMAP*-data because these peaks are sensitive to the cosmological parameters. From these data, Larson et al. (2011) determined the density parameters of dark matter, baryons and dark energy to $\Omega_{\rm dm} = 0.2269 \pm 0.0262$, $\Omega_{\rm b} = 0.0449 \pm 0.0028$ and $\Omega_\Lambda = 0.734 \pm 0.029$, whereby the total matter density is $\Omega_{\rm m} = \Omega_{\rm dm} + \Omega_{\rm b}$. These values indicate that our Universe is flat and dominated by dark energy, while dark matter and baryons contribute smaller fractions to the total energy density of the Universe. A universe with such a constellation of the different energy species is usually referred to as ΛCDM-Universe where "CDM" stands for cold dark matter. This means that dark matter is non-relativistic and thus able to build the structures we observe today.

Independent measurements of the cosmological parameters with SNIa (e.g. Riess et al. 2004; Kowalski et al. 2008) or Baryonic Acoustic Oscillations (BAO, e.g. Eisenstein et al. 2005; Percival et al. 2007) can help to constrain $\Omega_{\rm m}$ and Ω_Λ (Fig. 1.3). A combination of these measurements yields $\Omega_{\rm m} = 0.274^{+0.016+0.013}_{-0.016-0.012}$ and $\Omega_\Lambda = 0.713^{+0.024+0.036}_{-0.029-0.039}$ (Kowalski et al. 2008) whereby the first errors denote the statistical and the second the systematic errors on both parameters.

With the density parameters defined in Eq. (1.14) and $a(t) = (1+z)^{-1}$ we can rewrite the first Friedmann equation (Eq. 1.6) to

$$\begin{aligned} H^2\,(z) &= H_0^2 E^2\,(z) \\ &= H_0^2\left[\Omega_{\rm r}\,(1+z)^4 + \Omega_{\rm m}\,(1+z)^3 + \Omega_\Lambda + (\Omega_{\rm tot}-1)\,(1+z)^2\right], \end{aligned} \tag{1.15}$$

for constant vacuum energy density. $E^2\,(z)$ is the so-called redshift evolution factor which accounts for the fact that the density parameters depend on the critical density and thus on redshift. Neglecting radiation and curvature, this function is defined as

$$E^2\,(z) = \Omega_{\rm m}\,(1+z)^3 + \Omega_\Lambda\,. \tag{1.16}$$

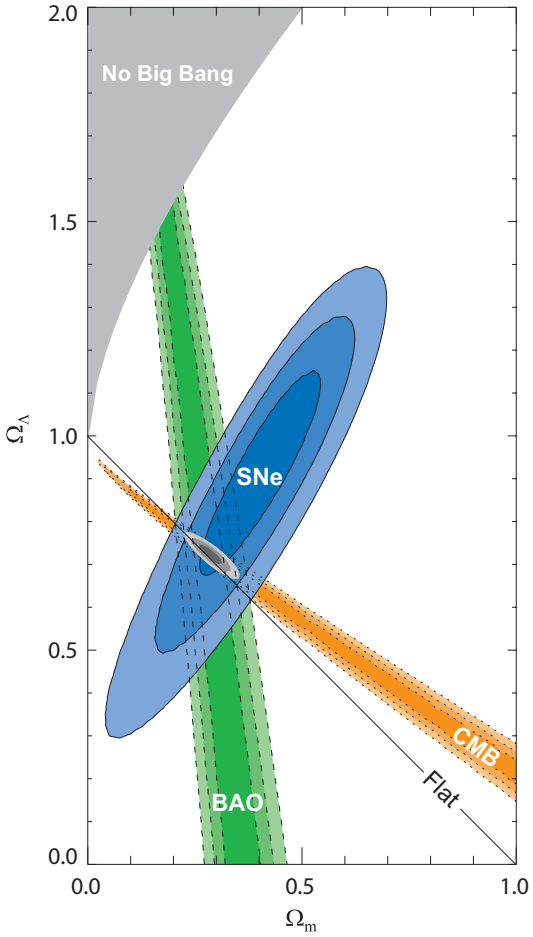

Figure 1.3: Parameter space of Ω_m and Ω_Λ. Cosmologies without Big Bang and with $\Omega_m + \Omega_\Lambda < 1$ are ruled out by observations. The contours show the 68.3%, 95.4% and 99.7% confidence levels on Ω_Λ and Ω_m as obtained from CMB, BAO and SNIa as well as their combination assuming $w = -1$. Their intersection (grey ellipse) strongly supports a ΛCDM-universe, giving the confidence limits for Ω_m and Ω_Λ. From Kowalski et al. (2008).

We will use Eq. (1.16) in Chapter 8 to scale our cluster masses such that they are independent of the critical density at their redshift. From the definition of $E^2(z)$ in Eq. (1.15) we can derive how the expansion behaviour of the Universe changes with respect to the density parameters. In very early times, the expansion was dominated by radiation, at $z_{eq} = \Omega_m/\Omega_r - 1 = 3196^{+134}_{-133}$ (Larson et al. 2011) matter took over and in the current era the expansion is governed by Ω_Λ.

Applying $H = \frac{1}{a}\frac{da}{dt}$, the age of the Universe (*Hubble time*) can be calculated from Eq. (1.15)

$$\begin{aligned} t_H(z) &= \int_0^{a'(z)} \frac{da'(z)}{a'(z)H(a'(z))} \\ &= \frac{1}{H_0}\int_z^\infty dz' \frac{(1+z')}{\sqrt{\Omega_r(1+z')^4 + \Omega_m(1+z')^3 + (1-\Omega_{tot})(1+z')^2 + \Omega_\Lambda}}. \end{aligned} \quad (1.17)$$

The most recent value for the age of the Universe is $t_H(z=0) = 13.75 \pm 0.13\,\mathrm{Gyr}$ obtained from seven-year *WMAP*-data (Larson et al. 2011).

1.2.3 Cosmological distance measures

Since the geometry of space-time is non-Euclidean, there is no unique definition of the distance between objects at cosmological scales, wherefore the notion of distance depends on the method of measurement. Furthermore, distance measurements are inevitably inertwined with time because they are measured along our backward light cone and because the speed of light is finite.

The most prevalently used measures are the *angular diameter distance* D_A and the *luminosity distance* D_L. The former is obtained by the angular diameter $\mathrm{d}\theta$ an object subtends at the sky, provided its physical diameter d is known, such that $D_\mathrm{A}(z) = d/\theta = f_K(\chi)/(1+z)$. The angular diameter distance is non-additive because of its prefactor $a = 1/(1+z)$. Thus, the angular diameter distance between two objects at redshifts z_1 and z_2 is

$$D_\mathrm{A}(z_1, z_2) = \frac{1}{1+z_2} f_K(\chi(z_2) - \chi(z_1)) \neq D_\mathrm{A}(z_2) - D_\mathrm{A}(z_1) \,. \tag{1.18}$$

Here, $\chi(z)$ is the *comoving distance*

$$\begin{aligned} \chi(z) &= \int_0^z \frac{\mathrm{d}z'}{H(z')} \\ &= \frac{1}{H_0} \int_0^z \mathrm{d}z' \left[\Omega_\mathrm{r}(1+z')^4 + \Omega_\mathrm{m}(1+z')^3 + \Omega_\Lambda + (\Omega_\mathrm{tot} - 1)(1+z')^2\right]^{-1/2} \,. \end{aligned} \tag{1.19}$$

To obtain the luminosity distance, the measured flux $f(z)$ is related to the intrinsic luminosity L of a source, $D_\mathrm{L} = \sqrt{L/4\pi f(z)} = (1+z) f_K(\chi)$.

Both angular diameter distance and luminosity distance are linked via the scale parameter because the light a source emits is redshifted while it propagates to the observer

$$D_\mathrm{L}(z) = (1+z)^2 D_\mathrm{A}(z) = (1+z)\, f_K(\chi) \tag{1.20}$$

as shown by Etherington (1933).

1.3 From quantum fluctuations to galaxy clusters

The Universe consists of small matter inhomogeneities in form of quantum-mechanically fluctuations since the very beginning (Sect. 1.1). During inflation, these tiny fluctuations were amplified to macroscopic scales and we can observe them in the temperature fluctuations of the CMB (Fig. 1.2).

After the Universe had cooled down sufficiently for so that structures could form, these primordial fluctuations grew due to gravitational instability and accumulated larger and larger overdensities. While their evolution is linear in first place and easy to treat mathematically, they have to be investigated by numerical simulations when they become non-linear.

Nowadays, the largest inhomogeneities formed by thousands of galaxies such as the "Great Walls" that show up in the Sloan Digital Sky Survey (SDSS, Fig. 1.4) extend over $200h^{-1}$ Mpc. Only on much larger scales the Universe can still be considered as homogeneous and isotropic with its web of voids enclosed by filaments, at whose intersections galaxy clusters reside.

In the following, I will describe structure formation in more detail by including also the underlying physics, because this is the basis to understand how galaxy clusters have formed. A detailed description is given by e.g. Schneider (2006a).

1.3.1 Linear structure formation

To describe structure formation using a simple mathematical treatment, we have to consider perturbations that are well inside the linear regime and neglect the pressure of photons, because after recombination, the remaining photons do not interact with matter anymore. Furthermore, by neglecting General Relativity we can assume a flat space-time. This allows us to study overdensities

whose extent is smaller than the horizon, which is defined as the distance up to which light could propagate since the Big Bang.

With these assumptions, structure growth can be treated using linear perturbation theory and matter can be considered as a fluid. For the beginning of structure growth, we can use linear perturbation theory because the small temperature fluctuations of the CMB measured by the *COBE*-satellite to $\Delta T/T \approx 10^{-5}$ indicate small matter perturbations over large spatial scales and for a long temporal interval.

We can now describe matter with a set of differential equations assuming a fluid with random density field $\rho(\mathbf{x}, t)$ and negligible pressure

$$0 = \frac{\partial \delta(\mathbf{x},t)}{\partial t} + \frac{1}{a(t)} \boldsymbol{\nabla}_x \cdot [(\delta(\mathbf{x},t)+1)\,\mathbf{v}(\mathbf{x},t)] \qquad \text{Continuity equation (1.21)}$$

$$-\frac{1}{a(t)} \boldsymbol{\nabla}_x \Phi = \frac{\partial \mathbf{v}(\mathbf{x},t)}{\partial t} + \frac{\dot{a}(t)}{a(t)} \mathbf{v}(\mathbf{x},t) + \frac{1}{a(t)} [\mathbf{v}(\mathbf{x},t) \cdot \boldsymbol{\nabla}_x]\,\mathbf{v}(\mathbf{x},t) \qquad \text{Euler equation (1.22)}$$

$$\nabla_x^2 \Phi = \frac{3H_0^2 \Omega_\mathrm{m}}{2a(t)} \delta(\mathbf{x},t) \qquad \text{Poisson equation (1.23)}$$

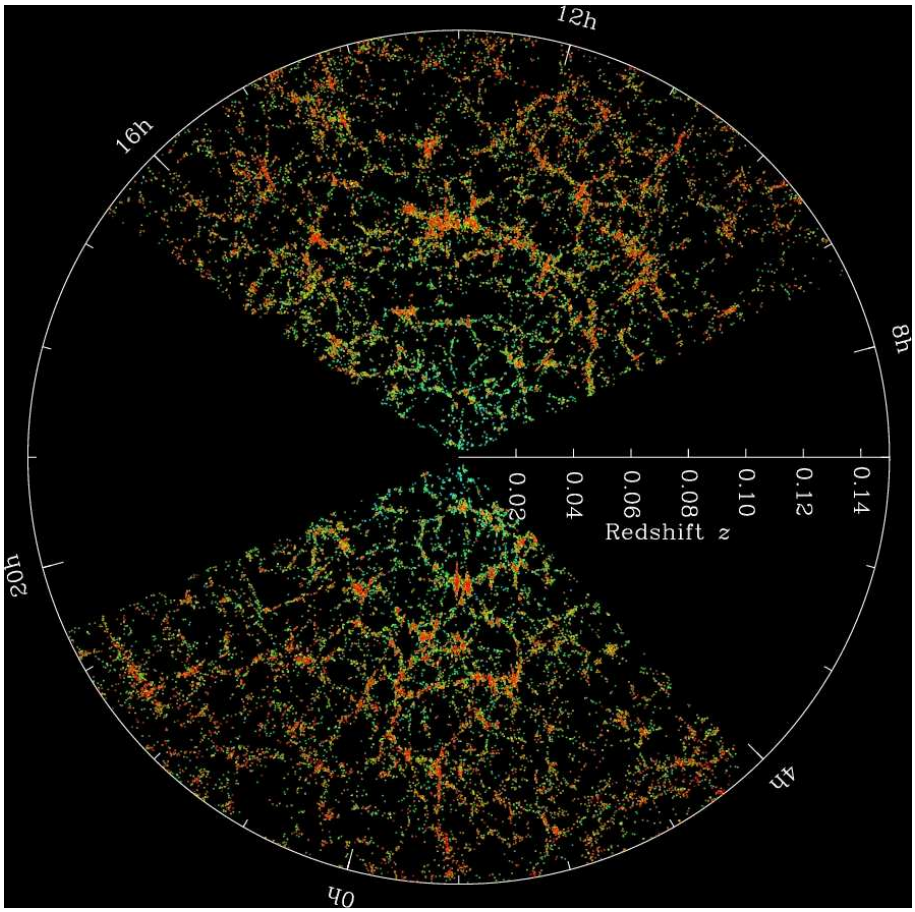

Figure 1.4: The large-scale distribution of local galaxies observed by the Sloan Digital Sky Survey which surveyed more than 25% of the sky over eight years and observed more than 930,000 galaxies. This image shows a slice plane of the total survey and the black wedges are regions where no observations could be performed due to dust in the Milky Way. The survey shows that galaxies build filamentary structures and galaxy clusters are located at the intersections of those filaments. The empty regions between the filaments are so-called “voids”. From http://www.sdss.org/ .

Here, $\delta(\mathbf{x},t)$ is the relative overdensity of $\rho(\mathbf{x},t)$ with respect to the mean density $\bar{\rho}(t)$ of the Universe, $\mathbf{v}(\mathbf{x},t)$ is the peculiar velocity and Φ is the gravitational potential.

For small $\delta(\mathbf{x},t)$ and $\mathbf{v}(\mathbf{x},t)$, Eqs. (1.21) and (1.22) can be linearised such that their time derivatives combined with Eq. (1.23) provides a differential equation for matter growth which only depends on the scale factor and two cosmological parameters, H_0 and Ω_m,

$$\frac{\partial^2\delta}{\partial t^2} + \frac{2\dot{a}}{a}\frac{\partial\delta}{\partial t} - \frac{3H_0^2\Omega_\mathrm{m}}{2a^3}\delta = 0\,. \tag{1.24}$$

This equation is independent of the gravitational potential and the peculiar velocity. Since Eq. (1.24) does not explicitly depend on $\mathbf{x}$, it can be solved via the separation approach $\delta = D_+(t)\,\Delta_+(\mathbf{x}) + D_-(t)\,\Delta_-(\mathbf{x})$, which is a factorised solution with a temporal and spatial component. While $D_-(t)$ decays with time, only the growing solution $D_+(t)$ of the two linearly independent solutions remains

$$\begin{aligned} D_+(t) &\propto H(t)\,H_0^2 \int_0^t \frac{\mathrm{d}t'}{a^2(t')\,H^2(t')} \\ &= \frac{H(a)}{H_0}\int_0^a \frac{\mathrm{d}a'}{\left[\Omega_\mathrm{m}/a' + \Omega_\Lambda a'^2 - (\Omega_\mathrm{m}+\Omega_\Lambda-1)\right]^{3/2}}\,, \end{aligned} \tag{1.25}$$

which is normalised to $D_+(t_0) = 1$. Here, we have already neglected the radiation density parameter Ω_r. Depending on whether the expansion is dominated by Ω_r, Ω_m or Ω_Λ and in which of these epochs a perturbation enters the horizon, $D_+(t)$ has a different growth behaviour.

Apart from this simplified picture, structure formation happens in each cosmic epoch and at all scales. The growth of these perturbations, however, depends on their length scale compared to the horizon. For perturbations which extend over scales that are larger the horizon, relativistic effects have to be considered. Such perturbations *enter* the horizon when the horizon exceeds the length of the perturbation scale at a_enter via cosmic expansion.

The growth behaviour of radiation, baryons and dark matter can be derived similarly to the derivation above, but one has to consider additional effects, such as relativity or effects of pressure. Equation (1.24) has then to be adapted to the additional physics. If we consider the primordial density fluctuations as a homogeneous, isotropic Gaussian density field $\delta(\mathbf{x},t)$, we can account for the different growth behaviour of these energy species as follows. This Gaussian density field is completely defined by its power spectrum $P(k) = \langle|\tilde{\delta}(t,\mathbf{k})|^2\rangle$, where $\tilde{\delta}(t,\mathbf{k})$ is the Fourier transform of the density contrast and $\mathbf{k}$ is the comoving wave vector of the perturbation. The power spectrum can be expressed in terms of the growth factor $P(k,a) = D_+^2(a)\,P_0(k)$ with $P_0(k) = P(a=1, k=|\mathbf{k}|)$. Usually, the power spectrum is assumed to be a power law $P(k) \propto k^{n_\mathrm{s}}$ with index n_s which describes the power spectrum of density fluctuations. There is evidence that n_s is slightly smaller than unity[2]. However, $n_\mathrm{s} = 1$ (*Harrison-Zeldovich spectrum*) implies that density fluctuations which enter the horizon always have the same amplitude, regardless at which epoch.

Now, we introduce the *transfer function* $T(k)$ which accounts for the growth of all different types of density fluctuations. This function considers how a perturbation deviates from any perturbation in the matter-dominated era on sub-horizon scales. Thereby, small perturbations are suppressed by a factor of $\left(a_\mathrm{enter}(\lambda)/a_\mathrm{eq}\right)^2$ compared to those that enter the horizon later. $T(k)$ evolves the density contrast from some initial time t_i to the present epoch $\delta_0(k) = \frac{\delta(k,t_\mathrm{i})}{D_+(t_\mathrm{i})}T_k$. Just after inflation all perturbations were larger than the horizon and entered the horizon in different

[2]Tegmark et al. (2004) have measured $n_\mathrm{s} = 0.995 \pm 0.049$ and recently, Larson et al. (2011) have measured $n_\mathrm{s} = 0.963 \pm 0.014$.

epochs depending on their size λ and their growth behaviour. At the present time t_0 we assume that all perturbations are inside the horizon.

The transfer function has to be calculated by numerical means, but in the limiting cases of very small and very large fluctuations it can be solved analytically for a ΛCDM-model

$$T_k \approx \begin{cases} 1 & \lambda \gg d_{\mathrm{H,com}}\left(a_{\mathrm{eq}}\right) \\ \left(\frac{\lambda}{d_{\mathrm{H,com}}\left(a_{\mathrm{eq}}\right)}\right)^2 & \lambda \ll d_{\mathrm{H,com}}\left(a_{\mathrm{eq}}\right) , \end{cases} \tag{1.26}$$

where $d_{\mathrm{H,com}}\left(a_{\mathrm{eq}}\right)$ is the comoving horizon at matter-radiation equality. The power spectrum then is

$$P\left(k, a\right) = \frac{D_+^2\left(a\right)}{D_+^2\left(a_{\mathrm{i}}\right)} T^2\left(k\right) A k^{n_{\mathrm{s}}} . \tag{1.27}$$

Applying Eq. (1.26) and $k = 2\pi/\lambda$, the power spectrum is linear in k for larger perturbations and non-linear with k^{-3} for small perturbations for $n_{\mathrm{s}} = 1$. Here, A is the normalisation of the power spectrum which is usually denoted as σ_8 because it describes the dispersion of density fluctuations on cluster scales inside a sphere of $8h^{-1}$ Mpc which is of the order of unity. Details on the relation of this cosmological parameter to galaxy clusters will be provided in Sect. 1.4.3.

1.3.2 Non-linear structure formation

When density fluctuations become non-linear ($\delta \not\ll 1$), linear perturbation theory is no longer valid and higher orders have to be considered. However, higher-order perturbation theory fails for $\delta \lesssim 1$. Numerical simulations, e.g. the *Millennium Simulation*, are a more convenient tool to describe perturbations of astronomical interest, such as galaxy clusters which are on the top of non-linear structure formation.

We will now briefly introduce the *Spherical collapse model* which is a simple model to describe the formation of dark matter halos. It considers the evolution of a spherical overdensity and as a special case of non-linear structure formation it can be solved analytically.

A sphere of homogeneously distributed matter with an overdensity that is slightly higher than the mean density of the Universe has linear density contrast ($\delta \ll 1$). Due the self-gravitatiion of its particles, the sphere would expand slower than the Hubble rate. Thus δ increases, which decelerates the expansion further. Eventually, the density contrast reaches a critical value δ_{cr} at which the expansion comes to a halt before the sphere re-collapses.

The recollapse takes as much time as the expansion, but the sphere does not recollapse back to a point, because the matter particles have peculiar velocities. Instead, the sphere reaches virial equilibrium radius $r_{\mathrm{vir}} = r_{\mathrm{max}}/2 = GM/2E_{\mathrm{kin}}$. This process is called *violent relaxation*. Here, E_{kin} is the kinetic energy of the sphere. The virial overdensity $\Delta_{\mathrm{vir}} = \rho_{\mathrm{vir}}/\rho_{\mathrm{crit}}$ can be approximated as e.g. by Bryan & Norman (1998) for a flat Universe

$$\Delta_{\mathrm{vir}} = 18\pi^2 + 82\left(\Omega_{\mathrm{m}} - 1\right) - 39\left(\Omega_{\mathrm{m}} - 1\right)^2 , \tag{1.28}$$

which gives $\rho_{\mathrm{vir}} \approx 97$ for $\Omega_{\mathrm{m}} = 0.27$. For an Einstein-de Sitter universe[3] the overdensity is $\Delta_{\mathrm{vir}} \approx 178$. The parametrisation from Navarro et al. (1997) gives $\rho_{\mathrm{vir}} \simeq 178\Omega_{\mathrm{m}}^{-0.6}\overline{\rho}\left(z\right) \approx 200\rho_{\mathrm{crit}}\left(z\right)$, where $\overline{\rho}\left(z\right)$ is the mean comoving density at the redshift of collapse. A galaxy cluster is often defined as a dark matter halo with an overdensity of $\Delta = 200$ although strictly speaking the virialised region of a cluster is not exactly the region inside which galaxy clusters have an overdensity of 200 times the critical density.

[3]This is a model with vanishing curvature, $\Omega_{\mathrm{m}} = 1$ and $\Omega_\Lambda = 0$ that is often used for mathematical simplifications.

Since $\Delta_{\rm vir}$ depends on $\rho_{\rm crit}$ and thus on the redshift, the halos that collapse earlier are denser than those that collapse later in cosmic time. Low-mass halos also collapse earlier and they are more abundant than massive halos due to the scenario of hierarchical structure formation in which small structures form first and build more massive structures by accretion and merging.

A useful application of the spherical collapse model is to study the number density n of collapsed dark matter halos as a function of mass and cosmic time. For this issue, one basically counts regions with $\delta_{\rm cr} > 1.69$ and from these number counts the abundance of collapsed halos is predicted by the *cluster* or *halo mass function* (Press & Schechter 1974). This function has been prevalently calculated and tested against numerical simulations and parametrisations with initial Gaussian conditions. Pillepich et al. (2010) provide a good overview. In their notation, the halo mass function reads

$$\frac{{\rm d}n}{{\rm d}M}(M,z) = f(\sigma)\frac{\bar{\rho}_{\rm m}}{M}\frac{{\rm d}\ln\left[\sigma^{-1}(M,z)\right]}{{\rm d}M}\,, \tag{1.29}$$

with the mean background matter density $\bar{\rho}_{\rm m}$ of the current epoch and the variance of the linear density field, which is defined as

$$\sigma^2(M,z) = \frac{1}{2\pi^2}\int_0^\infty {\rm d}k\, kP_{\rm lin}(k,z)\,W^2(k,M)\,. \tag{1.30}$$

Here, a filter function W enters, which is a top-hat function in real space that smooths out mass peaks which are smaller than the considered mass M and $P_{\rm lin}(k,z)$ is the linear power spectrum that corresponds to the density field of interest.

The function $f(\sigma)$ in Eq. (1.29) accounts for the different calculations. The first parametrisation is from Press & Schechter (1974)

$$f_{\rm PS}(\sigma) = \sqrt{\frac{2}{\pi}}\frac{\delta_{\rm c}}{\sigma}\exp\left(-\frac{\delta_{\rm c}^2}{2\sigma^2}\right), \tag{1.31}$$

with $\delta_{\rm c} = 1.686$. Other parametrisations arise from Sheth & Tormen (1999) or, more recently, from Warren et al. (2006)

$$f_{\rm W}(\sigma) = A\left(\sigma^{-a}+b\right)\exp\left(-\frac{c}{\sigma^2}\right), \tag{1.32}$$

with $A = 0.7234$, $a = 1.625$, $b = 0.2538$ and $c = 1.1982$.

Since the halo mass function has an uncertainty of 5-20% that depends on the redshift of the halo, the underlying cosmology and the exact definition of the halo mass, Tinker et al. (2008) defined a slightly different equation

$$f_{\rm T}(\sigma) = A\left[\left(\frac{\sigma}{b}\right)^{-a}+1\right]\exp\left(-\frac{c}{\sigma^2}\right), \tag{1.33}$$

where the parameters vary with halo overdensity. This expression allows redshift-dependent corrections which pushes the uncertainty down to 5% in simulations of the halo mass function.

1.4 Galaxy Clusters

1.4.1 Properties of galaxy clusters

Being the most massive collapsed structures in the Universe with the deepest potential wells, galaxy clusters represent the end stage of the hierarchical structure formation scenario. Formed by the merging of smaller structures like galaxies and galaxy groups along large-scale filaments

(e.g. Springel et al. 2001), most galaxies (except for a small number of field galaxies) in the Universe have gathered together to these impressing structures due to self-gravitation. With dynamical timescales of $\sim 10^9$ yrs, galaxy clusters are rather young structures that often reveal irregular morphologies, especially if they are in the process of merging. Schuecker et al. (2001) thus found that at least in the local Universe the geometry of $\sim 50\%$ of galaxy clusters deviates from spherical symmetry. Especially at high redshifts, only few clusters show spherical symmetry and are not relaxed because they are still in the process of forming and not virialised yet. A classification of galaxy clusters due to morphology is given by e.g. Rood & Sastry (1971) who classified galaxy clusters depending how many very luminous galaxies are located in the cluster centre, or how the cluster galaxies are distributed. Another classification using X-ray observations of ~ 200 clusters with the *Einstein*-satellite is given by Forman & Jones (1991) who defined cluster morphologies as e.g. "single", "double", "complex" or "off-center".

Although galaxy clusters show various morphologies, their matter content is approximately similar. They are composed of $\sim 3\%$ of luminous matter from galaxies and stars that are not bound to the galaxies, $\sim 15\%$ of hot X-ray emitting gas with low densities ($n \lesssim 0.1\,\text{particles}\,\text{cm}^{-3}$) and high temperatures ($10^7 - 10^8\,\text{K}$) and a small fraction of relativistic particles. But the dominating component is dark matter which contributes $\sim 82\%$ to the total gravitating cluster mass and thus is responsible for the deep gravitational potential well.

The assumption that galaxy clusters are composed of such a high fraction of dark matter dates back to the 1930's when Fritz Zwicky (1933) measured the velocity dispersion of galaxies in the Coma cluster which were much higher than the mass of the visible matter suggested ("missing mass" problem). The existence of such collisionless matter that interacts only via gravitation is supported by observations of galaxy clusters with weak gravitational lensing and X-rays (e.g. Clowe et al. 2007; Bradač et al. 2008a,b). But dark matter also explains why the rotation curves of spiral galaxies do not drop out to large radii from the centre (e.g. de Blok & McGaugh 1997; Bekenstein 2004). Observations of the CMB also indicate the existence of dark matter because its temperature power spectrum is sensitive to dark matter among others.

The masses of galaxy clusters range between $\sim 10^{14} - 10^{15} M_\odot$, galaxy groups rather occupy a lower mass range ($\sim 10^{13} M_\odot$) and are less bound. In addition, there are fossil groups which are surrounded by an extended X-ray halo. These galaxy groups have an elliptical galaxy in the centre which is at least two magnitudes brighter than the other group members which indicates that this central galaxy has accreted the smaller galaxies (e.g. Mendes de Oliveira & Carrasco 2007). Typically, galaxy clusters have several hundreds to thousand galaxies with a velocity dispersion of $\sigma_v \sim 1000\,\text{km}\,\text{s}^{-1}$ inside the virial radius $r_{\text{vir}} \gtrsim 1.5 h^{-1}\,\text{Mpc}$. In the centre of most massive clusters, the *cD-galaxy* which is a very massive and luminous[4] galaxy that accretes smaller cluster members is resided. The other cluster galaxies, however, are predominantly composed of early-type galaxies with low gas content such as ellipticals or S0-galaxies, while spiral galaxies are more abundant in the field. The cluster galaxies have lost most of their gas due to ram-pressure stripping (e.g. Schindler 2004) wherefore they are on average redder than galaxies in the field. Galaxy formation theories also predict that elliptical galaxies evolve from the merging of spiral galaxies which happens more frequently in galaxy clusters than in the field. The gas of the cluster galaxies, however, falls into the potential well of the cluster where it is heated and compressed and thus it is no longer available for star formation. For these reasons, galaxy clusters consist of the reddest galaxies at a given redshift, called the *cluster red sequence*, which can be used to identify clusters and give a rough estimation of their redshift (e.g. Bower et al. 1992, Gladders & Yee 2005). Apart from that, the hot cluster gas provides information about processes such as feedback

[4] according to its size, because the actual surface brightness is low

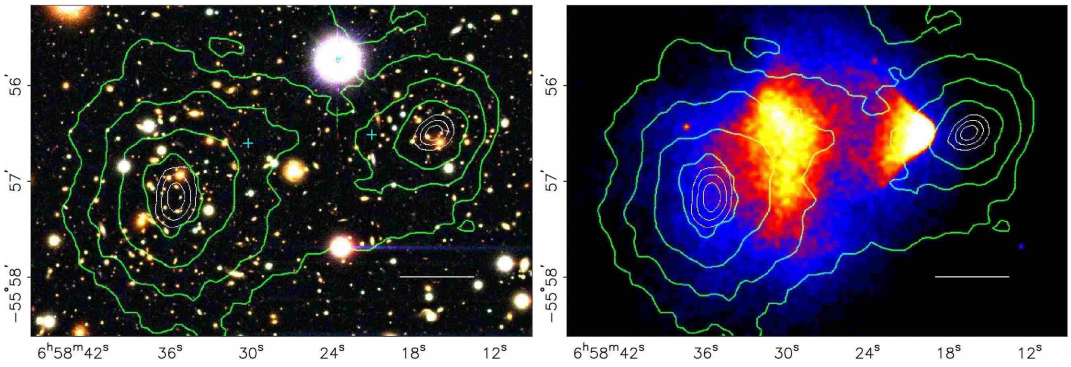

Figure 1.5: *Left:* Colour image of the Bullet cluster composed from observations with the Magellan telescope. The white bar corresponds to 200 kpc at the redshift of the cluster and the blue crosses denote the X-ray emission peaks of the ICM. *Right: Chandra*-image showing the same field-of-view for the ICM emission. The green contours in both images are from weak lensing mass reconstruction and the white contours show the 68.3%, 95.5%, and 99.7% confidence levels of the corresponding mass peak. Due to merging, the peaks of the ICM and the weak lensing mass reconstruction contours show an offset. From Clowe et al. (2006a).

heating, radiative cooling or the chemical enrichment history from supernovae and AGN in the cluster galaxies (for detailed reviews see e.g. Rosati et al. 2002, Arnaud et al. 2005 or Voit 2005).

Due to the scenario of hierarchical structure formation, galaxy clusters evolved from the merging of smaller systems with a rate that increases towards higher redshifts (e.g. Burkey et al. 1994; Lin et al. 2004; Fakhouri & Ma 2008). Merger events disturb the geometry and the ICM of galaxy clusters which has an impact on the cluster mass we can infer from observations. In lensing-based mass estimates, usually spherically-symmetric mass models are used which provide unreliable cluster masses for merging clusters. In X-rays, mass estimates are based on hydrostatic equilibrium between the ICM and the gravitational potential of the cluster. Merging can violate the assumption of hydrostatic equilibrium due to shock-heating of the ICM which boosts temperature and luminosity before a new equilibrium is achieved as shown in simulations of Ricker & Sarazin (2001). Thus, merging can provide artificially high X-ray masses. A demonstrative example for a merging cluster is the *Bullet Cluster* 1E0657-56 at $z = 0.296$ (e.g. Clowe et al. 2007) which is shown in Fig. 1.5. During collision, the hot ICM was decelerated but the collisionless dark matter did not interact during the process. The observation of the Bullet Cluster has confirmed that the ICM is not the most massive component in clusters, as it is proposed by alternative theories of gravity and that dark matter is required to explain the missing mass in galaxy clusters.

Galaxy clusters themselves tend to accumulate together in filamentary structures with extents of ~ 100 Mpc called *superclusters* (e.g. Tanaka et al. 2001). Those structures have masses of more than $10^{16}\,M_\odot$ and are not collapsed yet. They enclose large underdense regions known as *voids* which are observed e.g. with the Two Degree Redshift Survey (Peacock et al. 2001) or the SDSS (e.g. Tegmark et al. 2004; Gott et al. 2005). Our home galaxy, the Milky Way, however, is resided in galaxy group, the *Local Group* with ~ 30 galaxies. The brightest members of the Local Group are the Milky Way, the Andromeda Galaxy, M33 and the Small and Large Magellanic Clouds. The other galaxies are small and faint satellite galaxies that are gravitationally bound to the more massive group members. The most nearby clusters are the Virgo Cluster and the Coma Cluster at ~ 16 and ~ 90 Mpc distance, respectively.

To compare galaxy clusters, their masses are usually given within a radius r_Δ which is defined by the overdensity Δ with respect to the critical density (Sect. 1.3.2). In weak lensing, this is often r_{200} from the NFW-model (Sect. 6.2.1). In X-rays, usually $\Delta = 500$ is used because good photon statistics for reliable hydrostatic mass estimates are available only out to r_{500} with the current instruments.

In the next two chapters, I will introduce the two methods with which the galaxy clusters in this work are studied. These are weak gravitational lensing in the optical (Chapter 2) and X-rays (Chapter 3). Other methods to infer cluster masses, such as dynamical estimates or the Sunyaev-Zeldovich effect, will be briefly introduced here because the results in this thesis will also be compared to such studies.

1.4.2 Galaxy clusters in multiple wavelenghts

Galaxy clusters can be observed in multiple wavelengths ranging from radio- up to γ-rays. In this section, I will describe their properties in the different wavelength bands.

Galaxy clusters in radio

Radio emission from galaxy clusters is primarily caused by non-thermal relativistic electrons which gyrate long the magnetic field lines whereby they emit synchrotron radiation. The radio emission of galaxy clusters is diffuse and extends over $\gtrsim 1\,\mathrm{Mpc}$ as *radio halo* with a regular morphology which is similar to the X-ray morphology of the cluster. The Coma cluster is the first cluster for which a radio halo was found (Willson 1970). So far, the most luminous radio halo was detected for the Abell cluster A2163 at $z = 0.203$ (Feretti et al. 2001). At the centre of cool-core clusters (Sect. 3.1.3) also smaller halos with $\lesssim 500\,\mathrm{kpc}$ can be found surrounding a very radio-luminous galaxy. Apart from that, galaxy clusters can also show radio relics which are supposed to be caused by merger events because they cannot be associated with any of the galaxies (e.g. Giovannini et al. 1999).

Radio observations of galaxy clusters provide information on their magnetic fields and on interactions of active galactic nuclei (AGN) with the intracluster gas. For merging clusters, the radio emission is correlated with the X-ray emission (Feretti & Giovannini 2008) while X-ray luminous relaxed cool-core clusters do not show a radio halo. Furthermore, the radio emission of individual cluster galaxies can extend out to several 100 kpc beyond their optical confines which indicates interaction with the ICM. Where those radio lobes are observed, the X-ray emission shows cavities (e.g. Fabian et al. 2000). It is assumed that these radio lobes are caused by an AGN in the cluster centre which emits rather symmetric jets of relativistic plasma that pushes away the thermal X-ray emitting gas (Böhringer et al. 1993). A detailed review of the radio properties of galaxy clusters is provided by Feretti & Giovannini (2008).

Galaxy clusters at millimetre wavelenghts

At millimetre wavelenghts galaxy clusters can be studied via the Sunyaev-Zeldovich Effect (SZE, Sunyaev & Zeldovich 1970) which was first observed by Gull & Northover (1976), but it took more than a decade until it could be studied in more detail. Detailed reviews are given by e.g. Birkinshaw (1999) and Carlstrom et al. (2002). The SZE is caused by CMB-photons with initial frequency ν_0 which interact with the hot ICM-electrons via Compton-scattering. Thereby those photons gain energy corresponding to a frequency shift $\Delta\nu$ which disturbs the Planck spectrum of the CMB at the low-energy end ($\lambda \gtrsim 1\,\mathrm{mm}$).

The optical depth of the Sunyaev-Zeldovich Effect $\tau = \int n_\mathrm{e}(r)\sigma_\mathrm{T}\mathrm{d}l$ is low because the electron number density n_e is low. With the *cross-section*

$$\sigma_\mathrm{T} = \frac{8\pi}{3}\left(\frac{e^2}{m_\mathrm{e}^2 c^2}\right)^2 , \tag{1.34}$$

where e is the electron charge and m_e the electron mass, the *Compton y-parameter* is an integral along the line-of-sight dl

$$y = -\Delta\nu/2\nu_0 = \int \mathrm{d}l \, \frac{k_B T_{gas}}{m_e c^2} \sigma_T n_e \,, \tag{1.35}$$

with Boltzmann's constant k_B and the temperature of the cluster gas T_{gas}. Thus, the intensity of the SZE is proportional to the gas pressure $P = nk_B T_{gas}$ integrated along the line-of-sight. The y-parameter is of the order $10^{-4} - 10^{-5}$. To obtain the mass of galaxy clusters via SZE, hydrostatic equilibrium (Sect. 3.1.5) has to be assumed for which temperature and gas density have to be entangled. This can be either done by assuming isothermality, which is not very accurate, or by using X-rays to obtain T_{gas} and its gradient. Compared to X-ray techniques, the SZE is less prone to small-scale inhomogeneities in the ICM since the electron number density n_e contributes only linearly instead of quadratically as we will learn in Sect. 3.1.

Since the SZE-intensity is independent of redshift, it can be used to detect high-redshift clusters because those clusters often are too faint to be detected in the optical or X-rays. For instance, the Atacama Cosmology Telescope (ACT, e.g. Menanteau et al. 2010), the South Pole Telescope (SPT, e.g. Brodwin et al. 2010; Foley et al. 2011; Story et al. 2011) or the *Planck*-mission (e.g. Planck Collaboration et al. 2011) detected galaxy clusters which were previously unknown. The Bullet Cluster 1E0657-56 was also studied with the Sunyaev-Zeldovich effect using the APEX-SZ Telescope in Chile (Halverson et al. 2009).

Galaxy clusters in the optical

In the optical, galaxy clusters can be identified as local overdensities of bright galaxies. The probably most famous galaxy catalogue was established by George O. Abell in 1958 (*Abell catalogue*) which consists of $\sim$ 2700 low-redshift clusters ($z \lesssim 0.2$). Abell defined a galaxy cluster as a accumulation of at least 50 galaxies with magnitudes of $m > m_3 + 2$, whereby m_3 is the magnitude of the third-brightest galaxy in that accumulation, within the *Abell radius* $\theta_A = 1'.7/z$. The catalogue was later extended to more than 4000 galaxies (Abell et al. 1989). Only a few years later, the Zwicky-catalogue was established from 1961-1968 by Fritz Zwicky consisting of $\sim 10,000$ galaxy clusters. More recent catalogues are e.g. the Red-Sequence Cluster Survey with $\sim 1,000$ clusters at $0.35 < z < 0.94$ (Gladders & Yee 2005) or the The Two Micron All Sky Survey (2MASS, Skrutskie et al. 2006).

To ensure that overdensities of galaxies are not due to projection effects along the line-of-sight, the redshifts of those galaxies have to be compared which can be done with spectroscopy of photometry (e.g. Miller et al. 2005; Koester et al. 2007; Milkeraitis et al. 2010). Alternatively, information on the radial distribution of the galaxies within a cluster and the galaxy luminosity function (e.g. Postman et al. 1996) can be used.

The optical spectra of galaxies allow us to study galaxy evolution with respect to their environment. Thus, cluster galaxies are on average redder than field galaxies and their morphology and gas content differ from their counterparts in the field (e.g. Dressler 1980; Whitmore et al. 1993). Apart from that, the spectra of cluster galaxies can be used to study their dynamics, as e.g. in *dynamical estimates*, in which galaxy clusters are assumed to be in virial equilibrium. With the *virial theorem* $2E_{kin} + E_{pot} = 0$ and $E_{kin} = M\langle v^2\rangle/2$, $E_{pot} = -GM^2/R$ and $\langle v^2\rangle = 3\sigma_v^2$ for an isotropic velocity distribution, the virial mass can be estimated with

$$M_{vir} = \frac{3\sigma_v^2}{G} r_{vir} \,. \tag{1.36}$$

Here, σ_v is the velocity dispersion of the cluster galaxies which can be inferred from their spectra. For non-relaxed clusters, Eq. (1.36) may provide unreliable cluster mass estimates because the

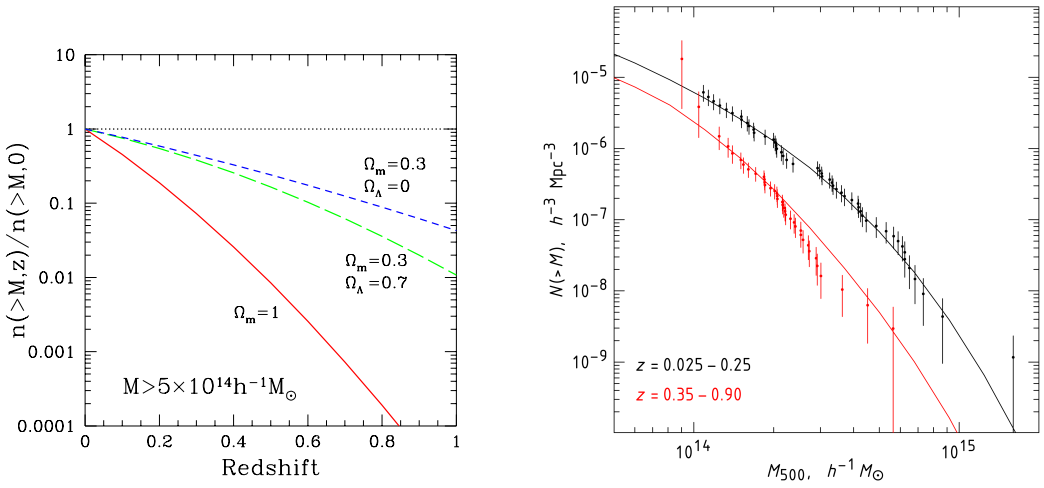

Figure 1.6: *Left:* The sensitivity of the cluster mass function on the underlying cosmology for clusters with $M > 5 \times 10^{14} h^{-1} M_{\odot}$ normalised to unity at the current epoch. The behaviour of $n(M, z)$ is shown for three different cosmologies: For an Einstein-de Sitter universe (red solid line) the evolution is strongest, because of the high matter density ($\Omega_{\rm m} = 1$). The evolution in a ΛCDM-universe (green long-dashed line) is slower but not as slow as in an open low-density universe without dark energy (blue, short-dashed line). For EdS, $\sigma_8 = 0.5$ was chosen due to its high matter density and $\sigma_8 = 0.8$ for the low-density models. From Rosati et al. (2002). *Right:* The cluster mass function for clusters at low redshifts (black) and for cluster at high redshifts (red) assuming $\Omega_{\rm m} = 0.25$, $\Omega_{\Lambda} = 0.75$ and $h = 0.72$. The solid line shows the fitted mass function, where σ_8 was left free. For the red sample, the evolution with z becomes visible. From Vikhlinin et al. (2009b).

assumption of virial equilibrium is violated and the velocity distribution of the cluster galaxies may deviate from isotropy.

Another important feature of galaxy clusters in the optical is gravitational lensing (Chapter 2).

Galaxy clusters in X-rays

A detailed treatment of this topic will be provided in Chapter 3.

Galaxy clusters in γ-rays

Gamma-ray emission from galaxy clusters has been predicted in hydrodynamical simulations of structure growth (e.g. Pinzke & Pfrommer 2010). The π^0-decay, $\pi^0 \rightarrow 2\gamma$, is supposed to dominate the emission spectrum of clusters at most γ-ray energies. Up to now, no gamma-ray emission from galaxy clusters has been detected yet. The *Fermi*-telescope which was launched in 2008 is expected to shed light on this topic.

1.4.3 Galaxy clusters as cosmological probes

Since galaxy clusters are the largest collapsed structures in our Universe, they provide an important contribution to constrain cosmological parameters and thus to confirm our ΛCDM-model (e.g. Zhang & Wu 2003; Balogh et al. 2006; Henry et al. 2009; Vikhlinin et al. 2009a,b). The cluster mass function (Eq. 1.29) is sensitive to the evolution of collapsed structures and to the cosmic expansion (e.g. Rosati et al. 2002; Schuecker et al. 2003a), wherefore cosmological parameters such as $\Omega_{\rm m}$, Ω_{Λ}, σ_8 and the dark energy equation-of-state parameter w can be inferred from the cluster mass functions of representative cluster samples. The dependence of the cluster mass function on redshift provides further information on dark energy, especially for high-redshift cluster samples.

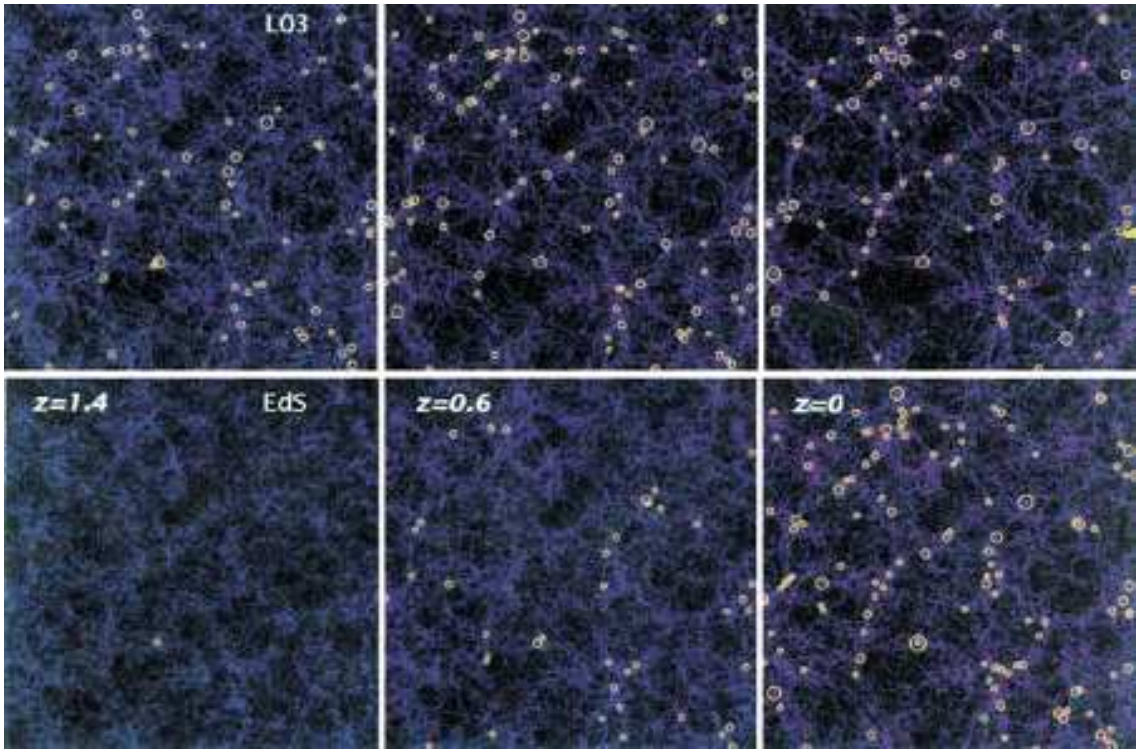

Figure 1.7: Simulated evolution of galaxy clusters for two cosmologies showing that structure formation strongly depends on the densities of dark matter and dark energy. . The three upper panels illustrate the structure formation for a ΛCDM-model ($\Omega_\mathrm{m} = 0.3$, $\Omega_\Lambda = 0.7$) compared to an Einstein-de Sitter universe ($\Omega_\mathrm{m} = 1$, $\Omega_\Lambda = 0$) in the three lower panels at three different redshifts ($z = 1.4$, $z = 0.6$ and $z = 0$ from left to right) for a region with $250h^{-1}$ Mpc edge length and a thickness of $75h^{-1}$ Mpc. For both simulations the amplitude of the power spectrum is consistent with the number density of nearby galaxy clusters and with the large-scale CMB anisotropies. The yellow circles denote positions where galaxy cluster would show up that can be observed in X-rays with $T > 3$ keV. From Borgani & Guzzo (2001).

The dark matter and dark energy densities, Ω_m and Ω_Λ, significantly influence structure formation and thus the cluster mass function (Figs. 1.7 and 1.6). Structures develop faster in a universe with high matter density, such as in an Einstein-de Sitter universe (EdS, $\Omega_\mathrm{m} = 1$, $\Omega_\Lambda = 0$), than in a low-matter universe than ours. Therefore, we would observe only few clusters at high redshifts in an EdS universe compared to a low-matter universe as simulations show (e.g. Borgani & Guzzo 2001). We can exclude high matter density models because we observe massive galaxy clusters at high redshifts (e.g. Rosati et al. 2009; Brodwin et al. 2010). Besides Ω_m, dark energy also drives the evolution of the mass function (Fig. 1.6) such that it counteracts structure formation with increasing Ω_Λ or more negative w because the influence of dark energy becomes more significant towards higher redshifts. For this reason, structures had to grow faster in the past to be observed as we do today.

Constraints on σ_8 arise from e.g. the amplitude of the cluster mass function which predicts the number density $n(M, z)$ of clusters as a function of mass and redshift (e.g. Vikhlinin et al. 2009b; Mantz et al. 2009). According to Reiprich & Böhringer (2002), the halo mass function predicts $\sigma_8 = 0.43\Omega_\mathrm{m}^{-0.36}$, while Vikhlinin et al. (2009b) obtained $\sigma_8 = 0.813 \pm 0.013$ from *Chandra* X-ray data. With a combination of CMB-measurements and cosmic shear, Schrabback et al. (2010) derived $\sigma_8 = 0.802^{+0.028}_{-0.027}$.

However, cosmology with galaxy clusters demands an accurate determination of total cluster masses. Since the definition of total mass is inertwined with the critical density and thus with the redshift at which the cluster has formed, all correlations between cluster mass and observables

such as temperature, gas mass or luminosity (*scaling relations*) may evolve with redshift (Voit 2005). We will learn more about these scaling relations in Sect. 3.2. Especially for low-mass systems like small galaxy clusters or groups, the definition of mass is a significant source of uncertainty (Pierpaoli et al. 2001).

Another important quantity for cluster cosmology is the gas-mass fraction $f_{\rm gas} = M_{\rm gas}/M_{\rm tot}$ which is an increasing function of cluster radius. Here, $M_{\rm gas}$ is the total gas mass which can be inferred by integrating the electron number density ($n_{\rm e}$) distribution of the ICM which can be obtained from the surface brightness ($S_{\rm X}$) distribution, because $S_{\rm X} \propto \int n_{\rm e}^2 {\rm d}l$. According to simulations it is a good mass proxy due to its small scatter (Fabjan et al. 2011). Typical values of the gas-mass fraction for clusters are $f_{\rm gas} \sim 0.1$, for galaxy groups $f_{\rm gas}$ is lower. The gas-mass fraction is supposed to reflect the baryon to dark matter mass ratio $\Omega_{\rm b}/\Omega_{\rm m}$, since most baryons in clusters reside in the ICM, while only $\sim 15\%$ of the total baryons in clusters are stars as indicated in simulations (e.g. Kravtsov et al. 2006). Indeed, $f_{\rm gas} < \Omega_{\rm b}/\Omega_{\rm m}$ ("missing baryon" problem). To constrain $\Omega_{\rm m}$ with the baryon fraction in clusters derived from the gas mass, one has to include the stellar mass from the stars in the cluster galaxies because besides the ICM, stars are assumed to provide the main contribution to the baryon content in clusters (Zhang et al. 2011b and references therein). The inclusion of stellar masses was supposed to solve the "missing baryon" problem but the baryon fraction in clusters is still significantly lower than the cosmic average $\Omega_{\rm b}/\Omega_{\rm m}$ probed by the CMB (LaRoque et al. 2006). Zhang et al. (2011b) concluded from their work and recent observations (e.g. Krick & Bernstein 2007; Gonzalez et al. 2007; Zibetti et al. 2005) that still some baryon mass is missing. Since $f_{\rm gas}$ may be a function of cluster mass it included in constraining cosmological parameters with the gas fraction (Vikhlinin et al. 2009a).

Using weak lensing masses, $M_{\rm wl}$, the gas-mass fraction, $f_{\rm gas} = M_{\rm gas}/M_{\rm wl}$, does not depend on the dynamical state as predicted in numerical simulations (Zhang et al. 2010). Yet, $f_{\rm gas}$ is below the cosmic baryon to dark matter ratio $\Omega_{\rm b}/\Omega_{\rm m}$ (e.g. Vikhlinin et al. 2009a; Fabjan et al. 2010; Zhang et al. 2011a). At $\Delta = 2500$, gas-mass fractions using weak lensing and X-ray masses are consistent, which strengthens the prospect to use $f_{\rm gas}$ at $\Delta = 2500$ to probe the dark energy equation-of-state parameter w (Zhang et al. 2006).

Chapter 2

Gravitational Lensing

One prediction of General Relativity states that light rays are deflected in the presence of masses, because they propagate along the null geodesics of space-time which are curved under the influence of gravitation. This effect is known as *Gravitational Lensing*. Owing to its independence of nature and state of the deflecting matter, gravitational lensing is one of the most interesting methods to investigate the mass distribution in the Universe. Hence, it is ideally suited to study the distribution of dark matter, of which we still know very little.

In general, the gravitational lens effect is subdivided into *strong gravitational lensing* and *weak gravitational lensing*. While the former is the more demonstrative effect by producing highly distorted and magnified (and sometimes even multiple) images of a background source, the latter considers the statistics of a large distribution of background sources with distortions at the edge of perception. Figure 2.1 demonstrates the effects of strong lensing for the galaxy cluster Abell 2218. Both strong and weak lensing are convenient tools to study galaxy clusters. In this thesis, I will use the weak gravitational lens effect because it probes the total mass distribution of a lens out to the outskirts, while strong lensing can only provide the total mass distribution inside the so-called *Einstein radius* (e.g. Richard et al. 2010; Donnarumma et al. 2011). Further applications of gravitational lensing are *galaxy-galaxy lensing* (e.g. Parker et al. 2007; van Uitert et al. 2011), where the distortion between single galaxies is investigated, the continuous deflection of light from large-scale structure (*cosmic shear*, e.g. Hilbert et al. 2009; Schrabback et al. 2010), or the search for MACHOS[1] in our host galaxy (e.g. Zhao 2000).

Gravitational lensing was first postulated about 200 years ago by Laplace, Cavendish and Soldner, but Albert Einstein gave the first precise description of gravitational light deflection in 1915 when he published his theory of General Relativity. Gravitational lensing by galaxies was first predicted by Fritz Zwicky in 1937, but its first discovery lasted until 1979 when identical quasar sources were observed by Walsh, Carswell & Weymann[2] with the Kitt Peak National Observatory 2 m telescope. These sources were identified as a multiple image pair lensed by a galaxy in 1980 by Stockton (1980) and Young et al. (1980). The development of CCD detectors in 1979 which replaced the previously used photographic plates and the improvement of computer technologies pushed optical astronomy forward. With the launch of the Hubble Space Telescope (HST) in 1990, high-resolution imaging enabled precision cosmology by deep observations of space.

Weak lensing of galaxy clusters was first detected by Tyson et al. (1990) in the galaxy clusters A1689 and CL1409+52 followed by many observations of other galaxy clusters. Soon methods not only for the scientific analysis but also for data handling had to be established, such as the aperture mass statistics (Schneider 1996) on which the weak lensing analysis in this work is based

[1] MAssive Compact Halo ObjectS

[2] For a detailed history of this discovery see Walsh (1989).

and which was successfully applied in various publications (e.g. Schirmer et al. 2007; Maturi et al. 2007 and references therein). One of the commonly used reduction packages for the optical data is the publicly available `GaBoDS/THELI` image processing pipeline (Erben et al. 2005) which was also used for some of the data in this work.

In this chapter, I will give an overview of the gravitational lens theory. In Sect. 2.1, I will introduce the principle and describe the general properties of the lens mapping. The theoretical background of weak lensing will be provided in Sect. 2.2. In Sect. 2.3, I will introduce the weak lensing aperture mass statistics as a tool to investigate the weak lensing properties of galaxy clusters and describe how these can be optimised by the choosing a suitable filter function and by including individual source redshifts. I will also briefly summarise the main aspects of mass reconstruction. A detailed description of gravitational lensing theory is given by e.g. Schneider et al. (1992), Bartelmann & Schneider (2001) and Schneider (2006a).

2.1 The principle

2.1.1 Refraction index and deflection angle

In all cases of astrophysical interest, the following assumptions in lens theory are valid: Firstly, the spatial extent of a lens is small compared to the distances between source and lens as well as between lens and observer (*thin lens approximation*). Thus, one can assume that the light deflection only happens in a plane perpendicular to the line-of-sight at the position of the lens (*lens plane*). Secondly, the angular extent of the source has to be small compared to the scale, where the gravitational potential Φ changes. This allows us to measure the lens properties such that the distortion can be easily determined. Thirdly, the gravitational field of the lens is weak, i.e. $|\Phi| \ll c^2$.

With these preliminary considerations, the light propagation close to a lens can be described in a locally Minkowskian space-time to first post-Newtonian order. Similar to an optical lens, the effect of a curved space-time can be expressed in terms of a refraction index $n = 1 + 2|\Phi|/c^2$, with which the deflection of light can be expressed as

$$\vec{\hat{\alpha}} = -\int \vec{\nabla}_\perp n \, \mathrm{d}l = \frac{2}{c^2} \int \vec{\nabla}_\perp \Phi \, \mathrm{d}l \,. \tag{2.1}$$

Here $\mathrm{d}l$ is the light path and $\vec{\nabla}_\perp n$ denotes the gradient of n perpendicular to $\mathrm{d}l$. This expression can be simplified, if one assumes that the light is not deflected along its path $\mathrm{d}l$, but only at the lens position. Then the *deflection angle* of a point mass M at a distance ξ is

$$\hat{\alpha} = \frac{2}{c^2} \int \vec{\nabla}_\perp \Phi \, \mathrm{d}z = \frac{4GM}{c^2 \xi} = \frac{2R_\mathrm{s}}{\xi} \,, \tag{2.2}$$

with the gravitational potential $\Phi(\xi, z) = -GM/\sqrt{\xi^2 + z^2}$, the Schwarzschild Radius $R_\mathrm{s} = 2GM/c^2$ and the distance along the unperturbed light ray from the point of closest approach z. Equation (2.2) was predicted by Einstein's General Relativity and observationally confirmed during a solar eclipse in 1919.

In a more realistic scenario, gravitational lenses, such as galaxy clusters, have extended mass distributions. Thus, the light deflection does not happen as simple as Eq. (2.2) suggests. Yet, the thin lens approximation is valid because the extent of a galaxy cluster is much smaller than the distances between observer, lens and source. This allows us to project the three-dimensional mass distribution $\rho(\vec{r})$ of the lens onto a *mass sheet* in the lens plane. The integration of $\rho(\vec{r})$ along the line-of-sight provides us with the *surface mass density*

$$\Sigma(\boldsymbol{\xi}) = \int \mathrm{d}z \, \rho(\boldsymbol{\xi}, z) \,, \tag{2.3}$$

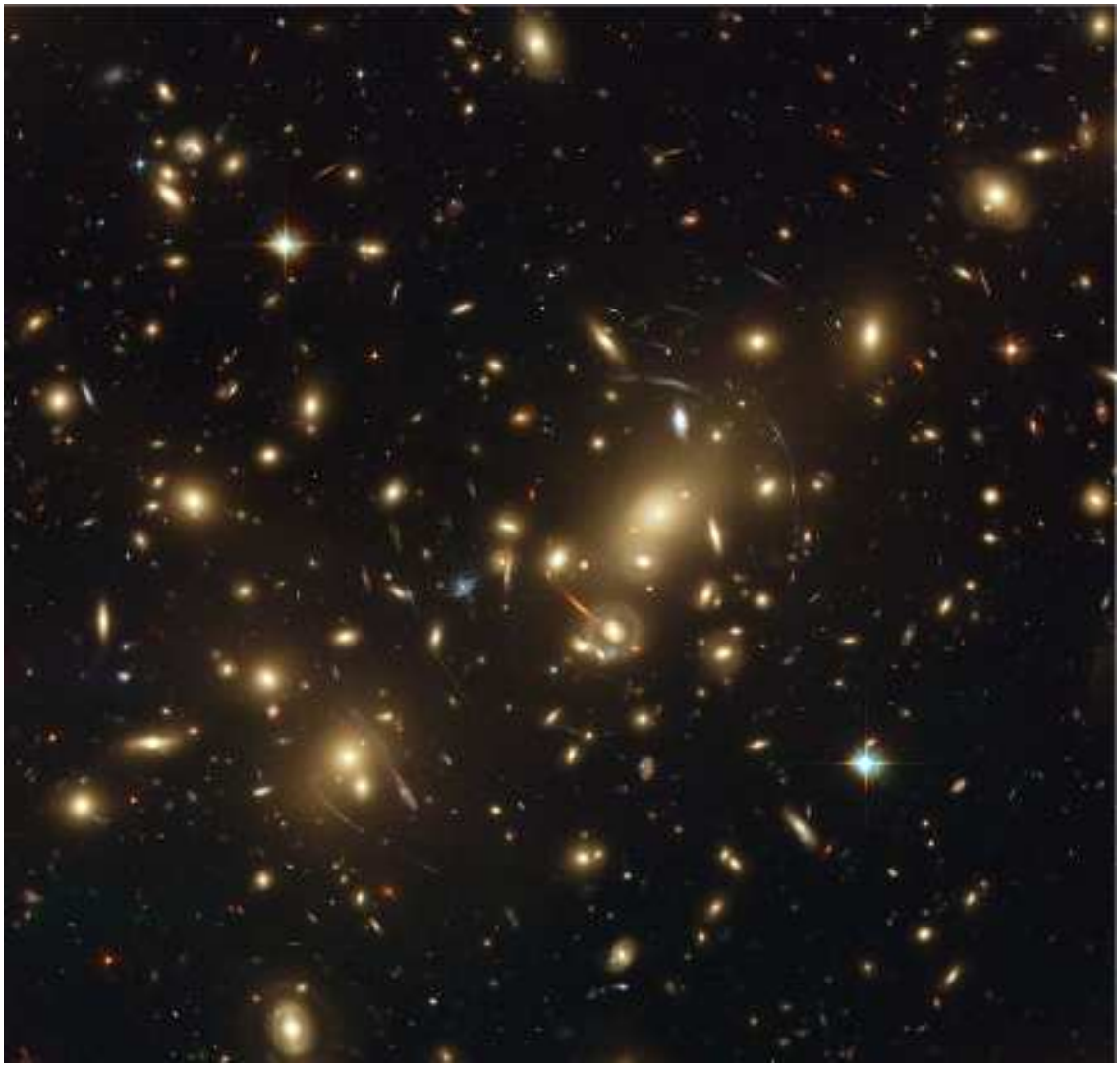

Figure 2.1: The very rich strong lensing cluster Abell 2218 at $z = 0.18$ is beautiful example for the distortion and magnification of background sources due gravitational lensing. The image is a composition of optical and near-infrared observations with ACS and an infrared observation with NICMOS, both mounted at the HST. The cluster galaxies are not distributed symmetric which suggests that the underlying dark matter distribution may not be spherically-symmetric as it is presumed at first order. The image shows several giant arcs from strong lensing, but also multiple images can be observed. The orange arc right below the bright cD-galaxy is a lensed elliptical galaxy at $z = 0.7$ and the blue arcs are lensed star-forming galaxies at $1 < z < 2.5$. Some arcs are so thin that they cannot be resolved even with the HST which indicates very high magnifications. The field-of-view is $\sim 7\farcm5 \times 7\farcm5$. From http://sci.esa.int/ , copyright by NASA, ESA, and Johan Richard (Caltech, USA), acknowledgement: Davide de Martin & James Long (ESA/Hubble) .

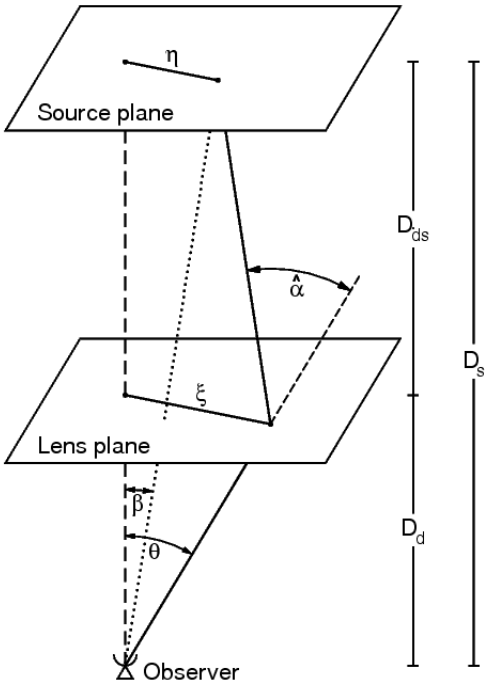

Figure 2.2: Schematic sketch of a typical gravitational lens system in the thin lens approximation consisting of source, lens and observer, which are connected by the optical axis. The lens plane is defined such that it is perpendicular to the optical axis and the intersection of optical axis and lens plane defines the origin of its coordinate system with the lens at position $\boldsymbol{\xi}$. The source plane is defined similar, with the source at $\boldsymbol{\eta}$. Due to lensing, the source is observed under an angle $\boldsymbol{\theta}$, while it would be observed under an angle of $\boldsymbol{\beta}$ without lensing. Note that we can only see the projected angular positions of $\boldsymbol{\eta}$ and $\boldsymbol{\xi}$. From Schneider (2006a).

whereby $\vec{r}$ is decomposed into the line-of-sight component z and two coordinates for the lens plane, $\boldsymbol{\xi} = (\xi_1, \xi_2)$. By subdividing the lens into mass elements $\mathrm{d}m_i = \mathrm{d}^2\,\xi\Sigma\,(\boldsymbol{\xi}')$ with spatial density $\rho\,(\boldsymbol{\xi}, z)$ and volume $\mathrm{d}V$, the deflection angle becomes the vectorial sum of deflection elements caused by each mass element

$$\hat{\boldsymbol{\alpha}}\,(\boldsymbol{\xi}) = \sum_i \hat{\boldsymbol{\alpha}}_i = \frac{4G}{c^2} \sum_i \mathrm{d}m_i\,\rho\left(\xi_1', \xi_2', z'\right) \frac{\boldsymbol{\xi} - \boldsymbol{\xi}'}{|\boldsymbol{\xi} - \boldsymbol{\xi}'|^2} = \frac{4G}{c^2} \int \mathrm{d}^2\xi'\,\Sigma\,(\boldsymbol{\xi}')\,\frac{\boldsymbol{\xi} - \boldsymbol{\xi}'}{|\boldsymbol{\xi} - \boldsymbol{\xi}'|^2}\,. \tag{2.4}$$

For galaxy clusters, the mass distribution is assumed to be spherically-symmetric at first order. If one assumes that the dark matter which dominates the gravitational potential of the cluster is spherically-symmetric, the galaxies should follow this distribution. As Fig. 2.1 shows, this is not always the case and then the total mass of a galaxy cluster may be over- or underpredicted by assuming spherical symmetry. However, if the mass distribution is spherically-symmetric, the surface mass density is only a function of $\boldsymbol{\xi}$, i.e. $\Sigma\,(|\boldsymbol{\xi}|) = \Sigma\,(\xi)$ and the deflection angle becomes a scalar due to axial symmetry similar to Eq. (2.2).

2.1.2 The lens equation

The gravitational potential causes a lensed source at $\boldsymbol{\beta} = \boldsymbol{\eta}/D_\mathrm{s}$ to be observed at $\boldsymbol{\theta} = \boldsymbol{\xi}/D_\mathrm{d}$ with the angular diameter distances D_s and D_d between lens and source and observer and source, respectively, whereby the subscript "d" means "deflector" (Fig. 2.2). The analogue writing of $\boldsymbol{\beta}$ and $\boldsymbol{\theta}$ suggests that $\boldsymbol{\eta}$ is a two-dimensional vector in the source plane as $\boldsymbol{\xi}$ is in the lens plane and that $\boldsymbol{\beta}$ and $\boldsymbol{\theta}$ are angular positions of source and image with respect to the line of sight. These true and projected positions are correlated via the *lens equation* which can be derived by geometrical considerations and the intercept theorems (Fig. 2.2),

$$\boldsymbol{\beta} = \boldsymbol{\theta} - \frac{D_\mathrm{ds}}{D_\mathrm{s}}\hat{\boldsymbol{\alpha}}\,(D_\mathrm{d}\boldsymbol{\theta}) = \boldsymbol{\theta} - \boldsymbol{\alpha}\,(\boldsymbol{\theta})\,. \tag{2.5}$$

Here, $\boldsymbol{\alpha}(\boldsymbol{\theta}) = \hat{\boldsymbol{\alpha}}(D_\mathrm{d}\boldsymbol{\theta})\, D_\mathrm{ds}/D_\mathrm{s}$ is the *scaled deflection angle* and D_s is the angular diameter distance between observer and source. Equation (2.5) is only valid for small deflection angles ($\hat{\alpha} \ll 1'$) because then $\sin(\alpha) \approx \alpha$ as it is the case for gravitational lenses[3].

The lens equation predicts the source position as a function of its image for any mass distribution $\Sigma(\boldsymbol{\xi})$. But the number of images $\boldsymbol{\theta}$ for a given source at position $\boldsymbol{\beta}$ is a priori unknown. For a fixed $\boldsymbol{\beta}$, Eq. (2.5) can have several solutions in forms of multiple images if $\Sigma(\boldsymbol{\theta}D_\mathrm{d})$ exceeds the *critical surface mass density*

$$\Sigma_\mathrm{cr} = \frac{c^2}{4\pi G}\frac{D_\mathrm{s}}{D_\mathrm{d}D_\mathrm{ds}}\,, \tag{2.6}$$

with the angular diameter distance D_d between observer and lens. Normalising the surface mass density by this value yields the *dimensionless surface mass density* or *convergence*

$$\kappa(\boldsymbol{\theta}) = \frac{\Sigma(\boldsymbol{\theta}D_\mathrm{d})}{\Sigma_\mathrm{cr}}\,, \tag{2.7}$$

which allows us to distinguish between strong lenses ($\kappa(\boldsymbol{\theta}) \gtrsim 1$) capable of producing multiple images and weak lenses for which Eq. (2.5) always has only one solution ($\kappa(\boldsymbol{\theta}) \ll 1$).

2.1.3 The Jacobian matrix and gravitational shear

Provided the angular extent of a source is smaller than the scale where the gravitational potential Φ, and hence $\hat{\alpha}$, changes significantly, the lens equation (Eq. 2.5) can be linearised by calculating it's first Taylor expansion

$$\boldsymbol{\beta} - \boldsymbol{\beta_0} = \mathcal{A}(\boldsymbol{\theta_0})\,(\boldsymbol{\theta} - \boldsymbol{\theta_0})\,, \tag{2.8}$$

with an arbitrary reference point $\boldsymbol{\beta_0}$ within the source and the corresponding position at which it is observed, $\boldsymbol{\theta_0}$. Here, we introduced the *Jacobian matrix* $\mathcal{A}$ which is defined as

$$\begin{aligned}\mathcal{A}(\boldsymbol{\theta}) &= \frac{\partial\boldsymbol{\beta}}{\partial\boldsymbol{\theta}} = \left(\delta_{ij} - \frac{\partial\alpha_i(\boldsymbol{\theta})}{\partial\theta_j}\right) \\ &= (1-\kappa)\,\mathbb{1}_2 - |\gamma|\begin{pmatrix}\cos(2\varphi) & \sin(2\varphi)\\ \sin(2\varphi) & -\cos(2\varphi)\end{pmatrix},\end{aligned} \tag{2.9}$$

with $\mathcal{A}_{ij} = \partial\beta_i/\partial\theta_j$ and eigenvalues $(1 - \kappa \pm |\gamma|)$. In the last step of Eq. (2.9), we decomposed $\mathcal{A}$ into the two essential properties of the lens mapping: The first term describes the focus and magnification of the image, whereby the magnification $|\mu| = \det(\mathcal{A})^{-1}$ can let the image appear fainter or brighter, depending on $\boldsymbol{\theta}$. This is because the surface brightness at frequency ν, I_ν, is conserved in lensing as Liouville's theorem states[4]. The traceless part of $\mathcal{A}$ is a measure for the image distortion with respect to its amplitude $|\gamma|$ and its orientation φ via the *shear*

$$\gamma = \gamma_1 + \mathrm{i}\gamma_2 = |\gamma|\mathrm{e}^{2\mathrm{i}\varphi}\,, \tag{2.10}$$

with components γ_1 and γ_2. Thus, intrinsically round sources are distorted into elliptical images with semi-axes $(1 - \kappa \pm |\gamma|)^{-1}$. Owing to its definition as the traceless part of the Jacobian matrix, the shear is a polar since an ellipse transforms into itself after a rotation of 180° and thus twice after a full rotation, which is also indicated by the factor 2 in the exponent of Eq. (2.10). By

[3] For galaxy clusters $\hat{\alpha}$ is $\approx 30''$ and for individual galaxies it is with $\hat{\alpha} \approx 1''$ even less.

[4] In Lensing, the surface brightness I_ν of an image is conserved at each frequency while the flux S_ν changes according to the solid angles of unlensed source and lensed image ν: $S_\nu^{(\mathrm{s})} = I_\nu \mathrm{d}\omega^{(\mathrm{s})} = I_\nu \mathrm{d}\omega = S_\nu$, whereby the index 's' denotes the source.

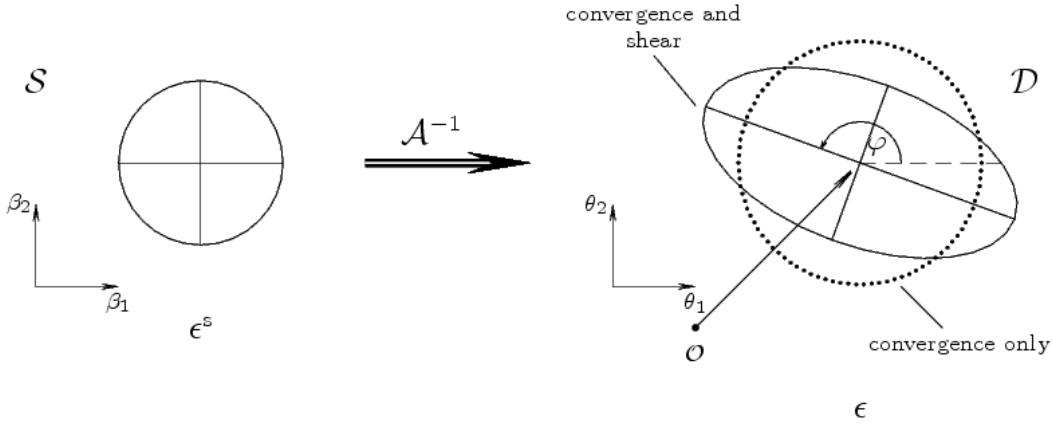

Figure 2.3: A circular source with angular coordinates β_1 and β_2 is transformed by the inverse of the Jacobian matrix $\mathcal{A}^{-1}$ from the source plane into the lens plane with θ_1 and θ_2. According to the definition of $\mathcal{A}$ in Eq. (2.9), the image remains a circle in the absence of shear, but with a different radius depending on κ, since only magnification effects occur. If the image suffers an additional distortion, its shape is transformed into an ellipse. From Schneider 2006b.

introducing the *reduced shear*

$$g(\boldsymbol{\theta}) = \frac{\gamma(\boldsymbol{\theta})}{1-\kappa(\boldsymbol{\theta})}, \qquad g = g_1 + \mathrm{i}g_2 = |g|\mathrm{e}^{2\mathrm{i}\varphi}, \tag{2.11}$$

we can rewrite Eq. (2.9) as

$$\mathcal{A}(\boldsymbol{\theta}) = [1-\kappa(\boldsymbol{\theta})]\begin{pmatrix} 1-g_1(\boldsymbol{\theta}) & -g_2(\boldsymbol{\theta}) \\ -g_2(\boldsymbol{\theta}) & 1+g_1(\boldsymbol{\theta}) \end{pmatrix}. \tag{2.12}$$

Figure 2.3 illustrates the mapping of a circular image with unit radius from the source to the lens plane by changing its size with κ and its shape with γ by the inverse of the Jacobian matrix $\mathcal{A}^{-1}$. After the transformation, the circle has become an ellipse with semi-axes $[(1-\kappa)(1\pm|g|)]^{-1}$ and angle φ between the θ_1-axis of the lens plane and the major axis of the ellipse.

We will show later that g is the only observable in weak lensing that depends on shape measurements (Sect. 2.2.2). Its components define how the source shapes change from their intrinsic to their observed shape under lensing. As the shear, g has polar properties.

2.2 Weak gravitational lensing

In weak gravitational lensing, the Jacobi matrix $\mathcal{A}$ is very close to the unit matrix because of $|\kappa| \ll 1$ and $|\gamma| \ll 1$, which implies weak distortions and small magnifications. Intrinsically, galaxies are not round but have typical mean ellipticities with $\langle\epsilon\rangle = 0.3$. Their shapes are affected only marginally by the shear in weak gravitational lensing, wherefore this effect is not measurable at individual galaxies. Instead, it has to be investigated by statistical means, such as the aperture mass statistics which will be introduced in Sect. 2.3.1. To obtain high accuracies in weak lensing studies, the number density of background sources has to be large which reduces the statistical errors. This can be achieved by observations with large field-of-views and long exposure times. Distant galaxies observed in the optical or near-infrared are perfectly suited for this issue because they reveal the densest population of distant objects in the sky. But projected onto the sky, these galaxy images are also faint and small, and hence their observed shapes are strongly affected by telescope optics and for ground-based observations also by atmospheric turbulences. These

effects can be accounted for via the Point Spread Function (PSF) which can be approximated with a Gaussian at first order. Its full width at half maximum (FWHM) is called *seeing* and it is given in arcseconds. The observed brightness profile of a source is thus a convolution of its intrinsic brightness profile and the PSF. Figure 2.4 compares the quality of ground- and space-based data to demonstrate how seeing affects the image ellipticities.

A detailed description of the first weak lensing results is given by Mellier (1999) and the theoretical basis for weak lensing is described by Kaiser & Squires (1993). Furthermore, Bartelmann & Schneider (2001) and Schneider (2006a) provide a comprehensive theory of weak gravitational lensing.

2.2.1 Distortion of faint galaxy images

Usually, a background source is neither circular nor does it have circular isophotes. Most galaxies reveal an intrinsic ellipticity because they are either spiral galaxies with an inclination towards the line-of-sight or intrinsically elliptic. Thus, the intrinsic shape of a source galaxy has to be disentangled from its shear, which we now quantify in more detail.

Light is distorted differentially when it propagates through a tidal gravitational field. But in weak lensing, the image extent is small compared to the scale, where differential distortion becomes notable. Thus, the surface brightness profile of a lensed image can be expressed in terms of the linearised lens equation (Eq. 2.8)

$$I(\boldsymbol{\theta}) = I^{(\mathrm{s})}\left[\boldsymbol{\beta}(\boldsymbol{\theta})\right] = I^{(\mathrm{s})}\left[\boldsymbol{\beta_0} + \mathcal{A}(\boldsymbol{\theta_0})(\boldsymbol{\theta} - \boldsymbol{\theta_0})\right] , \tag{2.13}$$

which is valid due to the conservation of surface brightness in lensing. From Eq. (2.13), lensed properties like the shear can be inferred by calculating the first and second moments of the surface brightness profile

$$I_1(\boldsymbol{\theta}) \;=\; \boldsymbol{\theta_0} = \frac{\int \mathrm{d}^2\theta\, q_I\left[I(\boldsymbol{\theta})\right]\boldsymbol{\theta}}{\int \mathrm{d}^2\theta\, q_I\left[I(\boldsymbol{\theta})\right]} \tag{2.14}$$

$$I_2(\boldsymbol{\theta}) \;=\; Q_{ij} = \frac{\int \mathrm{d}^2\theta\, I(\boldsymbol{\theta})\, q_I\left[I(\boldsymbol{\theta})\right](\theta_i - \theta_{i,\mathrm{c}})\left(\theta_j - \theta_{j,\mathrm{c}}\right)}{\int \mathrm{d}^2\theta\, I(\boldsymbol{\theta})\, q_I\left[I(\boldsymbol{\theta})\right]} . \tag{2.15}$$

The first moment defines the centre of each image and the second is a convenient expression to measure image ellipticities. Similar to the definition of $\mathcal{A}$, the trace of Q contains information about the image size and the traceless part of Q describes the image ellipticity. For an image with circular isophotes the components of Q are $Q_{11} = Q_{22}$ and $Q_{12} = Q_{21} = 0$. With the second moment of surface brightness (Eq. 2.15), the complex ellipticities $\epsilon = \epsilon_1 + \mathrm{i}\epsilon_2$ and $\chi = \chi_1 + \mathrm{i}\chi_2$ are defined as

$$\epsilon \;=\; \frac{Q_{11} - Q_{22} + 2\mathrm{i}Q_{12}}{\mathrm{tr}\,(Q) + 2\sqrt{\det(Q)}} = \begin{cases} \dfrac{\epsilon^{(\mathrm{s})} + g}{1 + g^*\epsilon^{(\mathrm{s})}} & |g| \leq 1 \\[2ex] \dfrac{1 + g\epsilon^{(\mathrm{s})*}}{\epsilon^{(\mathrm{s})*} + g^*} & |g| > 1 \end{cases} \tag{2.16}$$

$$\chi \;=\; \frac{Q_{11} - Q_{22} + 2\mathrm{i}Q_{12}}{\mathrm{tr}\,(Q)} = \frac{\chi^{(\mathrm{s})} + 2g + g^2\chi^{(\mathrm{s})*}}{1 + |g|^2 + 2\mathcal{R}\mathrm{e}\left(g\chi^{(\mathrm{s})*}\right)} , \tag{2.17}$$

where in each last step the transformation of second-order brightness moments $Q^{(\mathrm{s})} = \mathcal{A}Q\mathcal{A}$ was applied which provides a connecting prescription between source and image. The asterisk for ϵ

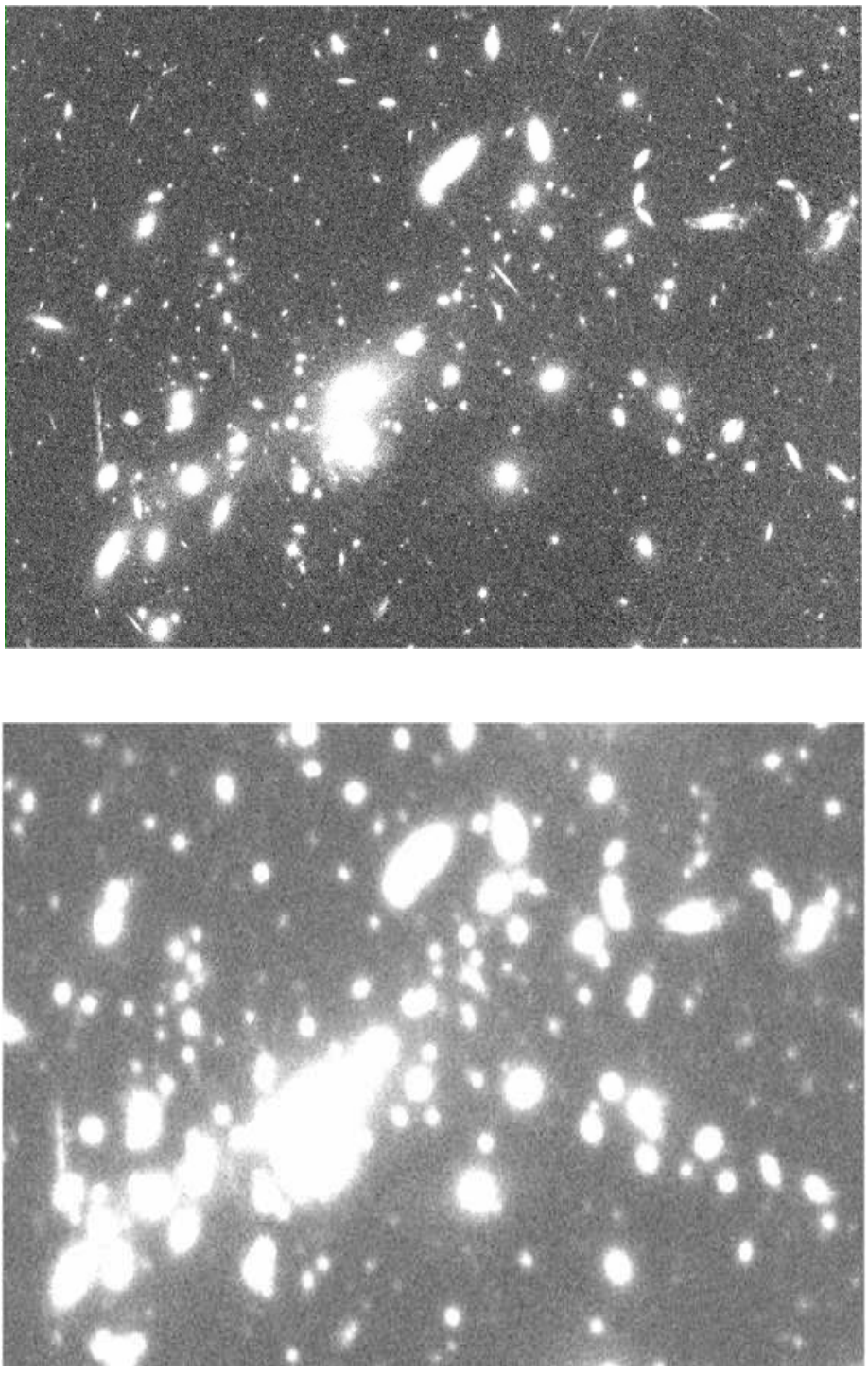

Figure 2.4: Comparison of ground- (*lower*) and space-based data (*upper panel*). The images show the centre of the galaxy cluster MS0451.6−0305 observed with ACS@HST in F606W (Table 4.1) and Suprime-Cam@SUBARU in the *I*-band (Table 4.2). In the space-based image, the galaxy shapes can be well distinguished. Also some strong lensing arcs can be identified. In the ground-based image, the shapes are blurred due to atmospheric turbulences. Elliptical galaxies appear more round and the strong lensing arcs cannot be identified anymore. Furthermore, neighbouring sources are merged together which also affects shape measurements. For these reasons, space-based data is the better choice for weak lensing studies. The field-of-view is $\sim 1\farcm5 \times 1\farcm0$.

and g denotes complex conjugation. For an image with elliptical isophotes of minor-to-major axis ratio $0 \leq r \leq 1$, the ellipticity definitions have these absolute values

$$|\epsilon| = \frac{1-r}{1+r} \qquad |\chi| = \frac{1-r^2}{1+r^2}\,, \tag{2.18}$$

which are independent of the image size.

From Eq. (2.16), we cannot distinguish between weak and strong lensing by considering only one single galaxy or a small solid angle of the sky. This effect is called *local degeneracy* and it can be broken by observing large fields around galaxy clusters so that strong lensing occupies only a very small area in the cluster centre. But $|g| > 1$ only occurs inside a small, central region compared to the total extent of the cluster and thus only for few sources. By applying $\kappa \ll 1$, $|\gamma| \ll 1$ and $|g| < 1$, Eqs. (2.16) and (2.17) can be reduced to $\epsilon \approx \epsilon^{(\mathrm{s})} + g$ and $\chi \approx \chi^{(\mathrm{s})} + 2g$.

2.2.2 Estimating the reduced shear

By decomposing the observed image ellipticity ϵ into an intrinsic component $\epsilon^{(\mathrm{s})}$ and the reduced shear, it is possible to reduce the noise caused by $\epsilon^{(\mathrm{s})}$ by averaging over many galaxy images. One main assumption in weak lensing is that the intrinsic galaxy shapes are oriented randomly because the distant galaxies used for weak lensing studies are distributed over a large spatial range enclosed by their broad redshift distribution. Thus, the expectation value for the complex ellipticities vanishes

$$\langle \chi^{(\mathrm{s})} \rangle = 0 = \langle \epsilon^{(\mathrm{s})} \rangle\,, \tag{2.19}$$

which implies that expectation value of Eq. (2.16) after rearranging for ϵ reads

$$\mathcal{E}(\epsilon) = \begin{cases} g & |g| \leq 1 \\ \dfrac{1}{g^*} & |g| > 1\,. \end{cases} \tag{2.20}$$

This equation shows that the reduced shear is the only quantity in weak lensing that can be measured from the image ellipticities, which is not possible for shear and convergence. Eq. (2.20) also implies that each image ellipticity yields an unbiased estimator of the local reduced shear which is very noisy. This noise can be expressed by the *intrinsic ellipticity dispersion*

$$\sigma_\epsilon = \sqrt{\frac{1}{2N}\sum_{i=1}^{N}\left(\epsilon_{1,i}^2 + \epsilon_{2,i}^2\right)}\,, \tag{2.21}$$

with ellipticity components ϵ_1 and ϵ_2. For individual sources, the shear signal is indeed very noisy, which is the reason why statistical methods for a large sample of galaxies with high number densities are required to measure precisely the shear. Another reason is that the two cases of Eq. (2.20) are locally indistinguishable, and hence wide source planes and high number densities are required to decide whether the measured ellipticity is due to strong or weak lensing.

2.2.3 Tangential and cross component of shear

A convenient measure to study the mass distribution of galaxy clusters and their effect on source galaxies is the *tangential shear* γ_t and its *cross component* $\gamma_\times$. These quantities describe the orientation of image shapes in a rotated reference frame, in which they are measured with respect to

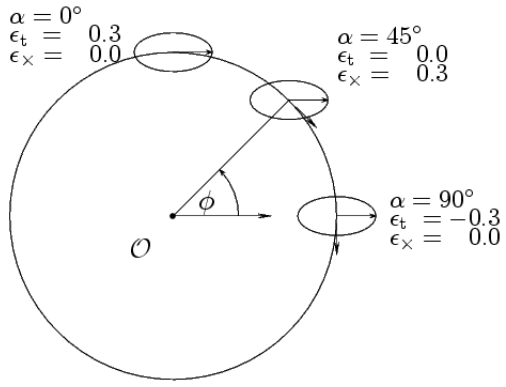

Figure 2.5: Tangential ellipticity ϵ_t and its cross-component $\epsilon_\times$ for different position angles with respect to a reference point. The absolute value of the ellipticity is always $|\epsilon| = 0.3$ because of $\epsilon^2 = \epsilon_t^2 + \epsilon_\times^2$. The orientation of the tangential vector for a source with angle ϕ w.r.t. the reference point is $\alpha = \pi - \phi$. From Schneider 2006b.

a specified direction ϕ, which is the cluster centre (Fig. 2.5). The tangential and cross component of γ are defined as

$$\gamma_t = -\mathcal{R}e\left[\gamma e^{-2i\phi}\right], \qquad \gamma_\times = -\mathcal{I}m\left[\gamma e^{-2i\phi}\right]. \tag{2.22}$$

The negative sign is chosen such that a negative tangential ellipticity corresponds to a radial oriented image. If the alignment of the image is truly tangential[5], γ_t will always be positive in this notation. At first order, the dark matter distribution of galaxy clusters is assumed to be spherically symmetric, wherefore the images are supposed to be tangentially aligned around the cluster centre. In this idealised case, the absolute value of the shear would directly yield the tangential shear, $|\gamma| = \gamma_t$. Furthermore, the cross component vanishes but in reality we would have $\gamma_\times \neq 0$ even for a spherically-symmetric mass distribution due to the noise from the intrinsic source ellipticities. Yet, we can cross-check systematics in the weak lensing analysis with $\gamma_\times$ because it is supposed to vanish on average.

2.3 Mass reconstruction

2.3.1 The Aperture Mass statistics ($\hat{M}_{\rm ap}$-statistics)

The *aperture mass* is a convenient tool to detect galaxy clusters and to quantify their weak lensing properties. It is defined as an integrated function of the surface mass density multiplied by a compensated filter $U(|\vec{\theta}|)$

$$M_{\rm ap}(\boldsymbol{\theta}_0) = \int_0^{\theta_{\rm ap}} \mathrm{d}^2\theta\, \kappa(\boldsymbol{\theta})\, U(|\boldsymbol{\theta} - \boldsymbol{\theta}_0|), \qquad \text{with} \quad \int_0^{\theta_{\rm ap}} \mathrm{d}\theta\, \theta\, U(\theta) = 0. \tag{2.23}$$

Here, $\theta_{\rm ap}$ is the radius of the aperture inside which κ is calculated. The centre of the aperture is denoted as $\boldsymbol{\theta}_0$ and $\boldsymbol{\theta}$ is the position of a point within the aperture. To make sure that $M_{\rm ap}$ is not affected by the *mass-sheet degeneracy* which comprises transformations of $(1 - \kappa) \rightarrow \lambda(1 - \kappa)$, a compensated filter is required. If $U(|\boldsymbol{\theta}|)$ has the shape of a Mexican hat, $M_{\rm ap}$ will have a maximum, provided it is placed on the centre of a mass concentration. Although $U(|\boldsymbol{\theta}|)$ compensates the mass-sheet degeneracy, it does not follow the mass profile of a cluster, because it gives negative weight to some regions of the aperture.

[5]Radial orientation occurs in the strong lensing regime, but has to be accounted for in the analysis, by e.g. cutting off the inner regions of a galaxy cluster.

The aperture mass can be directly written as a filtered integral in terms of the tangential shear γ_t (Schneider 1996),

$$M_\mathrm{ap}\left(\boldsymbol{\theta_0}\right) = \int \mathrm{d}^2\theta\, Q\left(|\boldsymbol{\theta}|\right) \gamma_\mathrm{t}\left(\boldsymbol{\theta}, \boldsymbol{\theta_0}\right) , \tag{2.24}$$

whereby $Q\left(|\boldsymbol{\theta}|\right)$ is a radially symmetric filter function that replaces the compensated filter, i.e.

$$Q(\theta) = \frac{2}{\theta^2} \int_0^\theta \mathrm{d}\theta'\, \theta' U(\theta') - U(\theta) . \tag{2.25}$$

Q resembles the tangential shear profile of a cluster which maximises the lensing signal when the aperture is centred on a mass concentration. In this work, the Q-filter from Schirmer et al. (2007) is used. It is defined as

$$Q_\mathrm{TANH}\left(x\right) = E\left(x\right) \frac{\tanh\left(x/x_\mathrm{c}\right)}{x/x_\mathrm{c}} , \tag{2.26}$$

with a box-shaped function $E\left(x\right)$ having exponentially smoothed edges:

$$E\left(x\right) = \left[1 + \exp\left(6 - 150x\right) + \exp\left(-47 + 50x\right)\right]^{-1} . \tag{2.27}$$

The distance to the aperture centre in units of the aperture radius θ_ap is $x = \theta/\theta_\mathrm{ap}$ and x_c is a dimensionless parameter changing the sharpness of the filter such that small x_c gives more weight at small radii (Fig. 2.6). The lensing signal is weighted over a large area inside the aperture. A too large x_c can assign too little weight to the objects at the outer parts of the aperture where the lensing signal is weak. Therefore, the measured galaxy shapes can be affected by noise if the aperture radius is too large. Empirically, $x_\mathrm{c} = 0.5$ is a good compromise.

- $Q_\mathrm{TANH}(x)$ approximates an NFW-profile (Navarro et al. 1996) and is thus suitable for cluster detections. For $x \gg x_\mathrm{c}$, it drops like x^{-1}.
- The hyperbolic function $\tanh(x)$ absorbs the singularity at $x = 0$ since it is $\propto x$ at small x. Thus objects at the inner radii of a cluster are excluded.
- $E(x)$ ensures $Q_\mathrm{TANH}(x)$ to decrease to zero in the inner and outer 10% of the aperture. It suppresses strong lensing effects and forfeits contributions from cosmic shear and large-scale structures.
- $E(x)$ also avoids fluctuations in the weak lensing signal-to-noise ratio when the aperture mass is calculated on grids because $E(x)$ gives less weight to galaxies near the aperture centre.

To apply the aperture mass to real data, Eq. (2.24) is discretised by replacing the integral with the sum of galaxies within the introduced grids. Furthermore, the tangential shear γ_t is replaced by the tangential ellipticity ϵ_t which is an unbiased estimate of the shear. With these changes, the estimator of M_ap is

$$\hat{M}_\mathrm{ap}\left(\boldsymbol{\theta_0}\right) = \frac{1}{n} \sum_{i=1}^{N} \epsilon_{\mathrm{t}i}\left(\boldsymbol{\theta_0}\right) Q\left(|\boldsymbol{\theta}_i - \boldsymbol{\theta_0}|\right) , \tag{2.28}$$

where $n = N/\theta_\mathrm{ap}^2\pi$ is the number density of objects within the aperture. The tangential ellipticity of the ith image at position $\boldsymbol{\theta}_i$ is defined as $\epsilon_{\mathrm{t}i} = -\mathcal{R}\mathrm{e}\left[\epsilon_i \exp(-2\mathrm{i}\phi_i)\right]$ with ϕ_i which is the position angle of the ith galaxy with respect to the aperture centre $\boldsymbol{\theta_0}$.

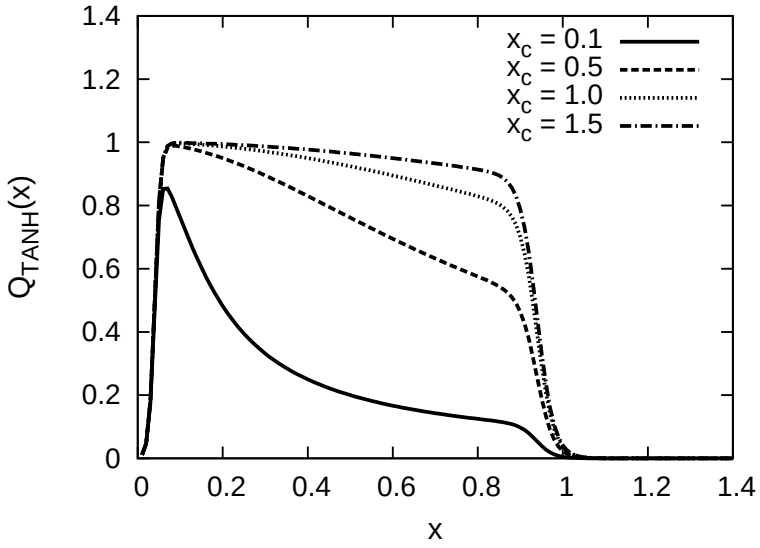

Figure 2.6: The filter function $Q_{\rm TANH}(x)$ for different values of $x_{\rm c}$. Especially for $x_{\rm c} = 0.1$ this function strongly filters the lensing signal.

Since the aperture mass provides us only with the amplitude of the filtered κ, but not of the cluster mass, it is more meaningful to use the weak lensing signal-to-noise ratio S/N of the aperture mass to obtain a measure of the significance of a mass concentration.

Assuming that the background galaxies are randomly distributed, we define the noise as the dispersion of $\hat{M}_{\rm ap}$ measured at the grid point $\boldsymbol{\theta_0}$ in the absence of lensing

$$\sigma^2\left(\boldsymbol{\theta_0}\right) = \frac{\sigma_\epsilon^2}{n^2} \sum_{i=1}^{N} Q^2\left(|\boldsymbol{\theta}_i - \boldsymbol{\theta_0}|\right) , \tag{2.29}$$

with the intrinsic ellipticity dispersion (Eq. 2.21). Thus, the weak lensing Signal-to-Noise ratio is

$$\mathrm{S/N}\left(\boldsymbol{\theta_0}\right) = \frac{\sqrt{2}}{\sigma_\epsilon} \frac{\sum\limits_{i=1}^{N} \epsilon_{{\rm t}i}\left(\boldsymbol{\theta_0}\right) Q\left(|\boldsymbol{\theta}_i - \boldsymbol{\theta_0}|\right)}{\sqrt{\sum\limits_{i=1}^{N} Q^2\left(|\boldsymbol{\theta}_i - \boldsymbol{\theta_0}|\right)}} , \tag{2.30}$$

with σ_ϵ as defined in Eq. (2.21).

2.3.2 Including individual galaxy redshifts for MS0451.6−0305

For one of the galaxy clusters studied in this work, MS0451.6−0305, individual source redshifts from photometry are available (Sect. 4.3.3). Here, I will describe how they can be included into the $\hat{M}_{\rm ap}$-statistics. For a detailed description, the reader is referred to Bartelmann & Schneider (2001).

The strength of a gravitational lensing system scales with $D_{\rm ds}/D_{\rm s}$, so that the lensing effect is stronger for sources with $z_{\rm s} \gg z_{\rm d}$ and less efficient for sources with $z_{\rm s} \gtrsim z_{\rm d}$. Often, only a mean source redshift taken from redshift probability distributions is the only information available. To assume a mean source redshift for all sources is a good solution for low-redshift clusters, but for clusters at high redshifts the influence of individual sources is more pronounced. Thus, it is appropriate to consider each source redshift individually, as far as they are known. But if individual

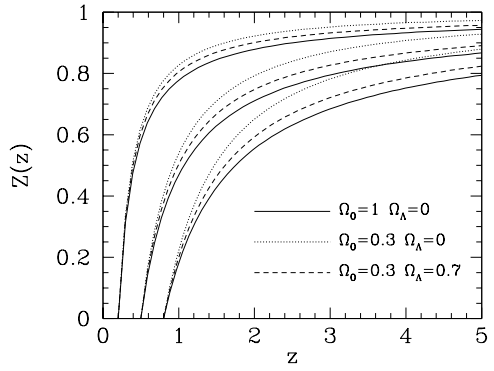

Figure 2.7: The function $Z(z)$ for three cosmological models, i.e. Einstein-de Sitter (solid), low matter universe without dark energy (dotted) and a low matter universe with dark energy (dashed). For each cosmology, $Z(z)$ is plotted for the lens redshift z_d = 0.2, 0.5, 0.8. While $Z(z)$ varies strongly for sources close to the lens, its dependence on the underlying cosmology becomes only significant for high source redshifts. For $z_\mathrm{r} \to \infty$, $Z(z) \to 1$. From Bartelmann & Schneider (2001).

source redshifts are available, the ellipticity components for those galaxies must be projected to a reference redshift z_r to obtain comparable shear values. This is done with

$$Z\left(z_\mathrm{s}\right) = \frac{D_\mathrm{ds} D_\mathrm{r}}{D_\mathrm{s} D_\mathrm{dr}} \mathrm{H}\left(z_\mathrm{s} - z_\mathrm{d}\right) , \tag{2.31}$$

whereby the Heaviside step function H(z) enters because foreground sources are not lensed. The function $Z\left(z_\mathrm{s}\right)$ describes the relative lens strength in terms of the true source redshift z_s normalised to z_r as shown in Fig. 2.7. For $z_\mathrm{r} \to \infty$, this equation approaches a maximum value $Z\left(z_\mathrm{s}\right) \to 1$.

According to Seitz & Schneider (1997) the ellipticity components $\epsilon_{1,2}$ can be normalised to z_r by rescaling,

$$\epsilon_{1,2} = \epsilon^0_{1,2} Z\left(z_\mathrm{s}\right) . \tag{2.32}$$

Provided, the redshifts of all source galaxies have errors that are smaller than the range over which Eq. (2.31) changes significantly ($\Delta z \lesssim 0.1$), we can define the *shear estimator* (Bartelmann & Schneider 2001)

$$\hat{\epsilon}_\mathrm{t} = \frac{\sum\limits_{i=1}^{N} \epsilon_{\mathrm{t}i}\, Z\left(z_{\mathrm{s},i}\right)}{\sum\limits_{i=1}^{N} Z^2\left(z_{\mathrm{s},i}\right)} \tag{2.33}$$

which is the shear at of a source scaled to z_r. This estimator maximises the weak lensing signal-to-noise ratio S/N and gives each galaxy an optimal weight according to its redshift whereby the intrinsic noise is reduced. The tangential shear $\epsilon_{\mathrm{t}i}$ in Eqs. (2.28) and (2.30) subsequently needs to be replaced by $\hat{\epsilon}$.

Figure 2.8 illustrates how the noise in shear measurements is reduced if individual source redshifts are known. It also shows that redshift information becomes more important for larger lens strengths and at low mean source redshifts, e.g. to distinguish between foreground and background galaxies. From this figure we further can predict that the noise in shear measurements and thus of the aperture mass is reduced by 20% for a cluster at the redshift of MS0451.6−0305. Hence, the signal-to-noise ratio will be increased by this fraction if individual photometric redshifts for all galaxies are included. We will learn in Chapter 6 that the expected improvement in S/N for MS0451.6−0305 is only marginal, because we have only photometric redshifts for a small fraction of our background galaxies (Sect. 4.3.3).

2.3.3 The κ-mass distribution

In weak lensing, the masses of galaxy clusters can be obtained with two different methods: Firstly, by fitting a suitable model (e.g. the NFW-profile, Navarro et al. 1997) to the tangential shear

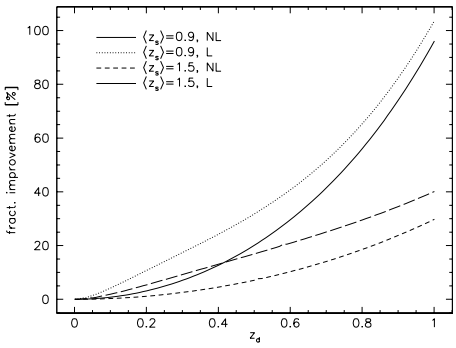

Figure 2.8: The fractional improvement of the shear estimate if individual source redshifts are known. More precisely, the ratio of the noise for sources with individual source redshifts and a mean source redshift $\langle z_s \rangle$ is plotted the mean source redshifts $\langle z_s \rangle = 0.9$ and $\langle z_s \rangle = 1.5$ and with lensing (L, $\kappa = |\gamma| = 0.3$) and without lensing (NL, $\kappa = \gamma = 0$). This figure implies that the improvement due to redshift information is higher for higher lens redshifts, since $Z(z)$ is nearly constant for low z. From Bartelmann & Schneider (2001).

measured from the source ellipticities. Secondly, the mass can be reconstructed from the reduced shear g via the surface mass density κ as defined in Eq. (2.7). Thus, it is possible to derive the projected mass density by measuring the local reduced shear, which is an unbiased estimate from weak lensing observations. By using the former method, the masses of the clusters studied in this thesis will be inferred. The latter will be used to study the mass distribution and to compare it with the aperture mass signal-to-noise ratio (Sect. 2.3.1) because the error estimation using κ is hardly feasible. In our analysis (Chapter 6) this is carried out by a publicly available code which is an application of the Seitz & Schneider (2001) finite-field method. This algorithm is based on the *Kaiser & Squires inversion* and it will be introduced in this section.

Weak lensing provides a parameter-free mass reconstruction of the projected mass distribution κ which enables to map the dark matter distribution of galaxy clusters (Kaiser & Squires 1993). Shear and surface mass density are related via a convolution of κ with a kernel $\mathcal{D} = -(\theta_1 - i\theta_2)^{-2}$ that describes a shear field as generated by a point mass

$$\gamma(\boldsymbol{\theta}) = \frac{1}{\pi} \int_{\mathbb{R}^2} \mathrm{d}^2\theta' \, \mathcal{D}(\boldsymbol{\theta} - \boldsymbol{\theta}') \, \kappa(\boldsymbol{\theta}') \; . \tag{2.34}$$

Since a convolution becomes a multiplication in Fourier space, i.e. $\hat{\gamma}(\boldsymbol{l}) = \pi^{-1} \hat{\mathcal{D}}(\boldsymbol{l}) \, \hat{\kappa}(\boldsymbol{l})$, we can invert this expression and after transformation back to real space the mass distribution can be expressed as

$$\kappa(\boldsymbol{\theta}) = \frac{1}{\pi} \int_{\mathbb{R}^2} \mathrm{d}^2\theta' \, \mathcal{R}\mathrm{e}\left[\mathcal{D}^*(\boldsymbol{\theta} - \boldsymbol{\theta}') \, \gamma(\boldsymbol{\theta}')\right] + \kappa_0 \; . \tag{2.35}$$

Here, the additional constant κ_0 enters, because a uniform surface mass density yields no shear. This implies that the observed reduced shear is invariant under the mass-sheet degeneracy, i.e.

$$g = \frac{\lambda\gamma}{\lambda(1-\kappa)} = \frac{\gamma}{1-\kappa}. \tag{2.36}$$

The mass sheet degeneracy can be broken if individual source redshifts are known (Schneider 2006b), or using magnifications (Sonnenfeld et al. 2011), or by combining strong and weak lensing (Merten et al. 2009).

In this work, the finite-field method from Seitz & Schneider (2001) was used. This method is an improved version of the Kaiser & Squires method to perform mass-reconstruction on a finite data field $\mathcal{U}$. The reduced shear can be locally related to the surface mass density due to

$$\nabla K_g(\boldsymbol{\theta}) = -\frac{1}{1 - g_1^2 - g_2^2} \begin{pmatrix} 1 - g_1 & -g_2 \\ -g_2 & 1 + g_1 \end{pmatrix} \begin{pmatrix} g_{1,1} + g_{2,2} \\ g_{2,1} - g_{1,2} \end{pmatrix} = \boldsymbol{u}_g(\boldsymbol{\theta}) \; , \tag{2.37}$$

with $K(\boldsymbol{\theta}) = \ln(1-\kappa(\boldsymbol{\theta}))$ which is a non-linear function of κ. The derivative of Eq. (2.37) yields (Seitz & Schneider 2001)

$$\nabla^2 K = \nabla \cdot \boldsymbol{u}_g \quad \text{with } \boldsymbol{n} \cdot \nabla K = \boldsymbol{n} \cdot \boldsymbol{u}_g \,, \tag{2.38}$$

with $\boldsymbol{n} \cdot \nabla K = \boldsymbol{n} \cdot \boldsymbol{u}_g$ on $\mathrm{d}\mathcal{U}$ and $\boldsymbol{n}$ is the normal vector of $\mathcal{U}$ (von Neumann boundary problem). In this derivation, the mass sheet degeneracy is not broken, which is sufficient for qualitative studies of the projected mass distribution as in this work.

Chapter 3

Galaxy clusters in X-rays

As discussed in Sect. 1.4, galaxy clusters are composed of $\sim$ 3% stars and galaxies, $\sim$ 15% intra-cluster medium and roughly $\sim$ 82% dark matter whose nature is unknown except for its gravitational interaction. The gravitational potential wells of galaxy clusters are dominated by dark matter, and the ICM subsequently is trapped in the deep potential wells and shock-heated up to temperatures of $\sim 10^7 - 10^8$ K (or $\sim 1 - 15$ keV). Hence, the ICM is sufficiently hot to emit X-rays via thermal bremsstrahlung and line emission. Temperature and luminosity of the X-ray emission are directly related to the total gravitating cluster mass because the ICM traces the dark matter distribution.

Since the atmosphere of the Earth absorbs X-ray emission from space, it was not until the beginning of the space age and the invention of space rockets that X-ray astronomy became possible. The first astronomical X-ray source that was discovered was the Sun in the late 1940's using German V-2 rockets which were captured by the USA after World War II, followed by a binary star system Sco X-1 in 1962 (Giacconi et al. 1962) which was detected with Geiger counters on an Aerobee rocket. X-ray emission from galaxy clusters was first observed in the Perseus Cluster by Mitchell et al. (1976), who concluded from the observed Fe lines that X-rays are emitted from hot plasma which is caught in the cluster potential well. Since the spectrum could be well described with thermal bremsstrahlung, Mitchell et al. (1976) concluded further that the gas is in hydrostatic equilibrium. This was later confirmed by Mushotzky et al. (1978) who also found correlations between X-ray observables and other cluster parameters. For instance, the X-ray temperature is approximately proportional to the square of the velocity dispersion of the cluster galaxies.

CCDs replaced the Geiger and proportional counters in 1993 at the launch of *ASCA* which allowed to perform spatially resolved spectroscopy and imaging up to 10 keV. The first X-ray all-sky survey was performed with *ROSAT* (1990-1999), detecting more than 10^5 X-ray sources. Its observations of galaxy clusters were then used to investigate the relation between temperature and luminosity (e.g. Arnaud & Evrard 1999) and to constrain the dark matter power spectrum and cosmological parameters such as Ω_m and σ_8 (e.g. Ikebe et al. 2002; Reiprich & Böhringer 2002). With the launch of the *XMM-Newton* and *Chandra* observatories high resolution and sensitivity observations became available which lead to improvements in determining the X-ray properties of galaxy clusters and the relations between their X-ray observables (e.g. Ettori et al. 2004; Pratt & Arnaud 2005; Zhang et al. 2006, 2008, 2010; Vikhlinin et al. 2009a,b).

In this chapter, I will give an introduction in the X-ray physics in galaxy clusters. In Sect. 3.1, I will describe emission processes and observational parameters, such as temperature and surface brightness which are crucial to calculate the total cluster mass. For a comprehensive description of the basic knowledge of the X-ray physics in galaxy clusters, I refer to e.g. Rybicki & Lightman (1979), Sarazin (1988) and Reiprich (2011). In Sect. 3.2, I will introduce scaling relations between

X-ray observables and cluster mass as cosmological application. Thereby, I will focus on the most important scaling relations which will also be investigated in this thesis.

3.1 X-ray observables and cluster properties

3.1.1 Definition of observational parameters

The *X-ray flux*, f_X, is the amount of energy dE that is emitted through an area element dA per unit time dt

$$f_\mathrm{X} = \frac{\mathrm{d}E}{\mathrm{d}A\,\mathrm{d}t}\,. \tag{3.1}$$

It is usually expressed in cgs unit, thus $[f_\mathrm{X}] = \mathrm{erg\,s^{-1}\,cm^{-2}}$. By integrating over a spherical surface with radius D_L, which refers to the luminosity distance (Sect. 1.2.3), we obtain the *X-ray luminosity*

$$L_\mathrm{X} = \frac{\mathrm{d}E}{\mathrm{d}t} = 4\pi f_\mathrm{X} D_\mathrm{L}^2\,, \tag{3.2}$$

which is the energy that is emitted isotropically in dt. Here, we directly used the luminosity distance because the galaxy clusters studied in this work are at cosmological distances. The wavelength interval we observe is redshifted since it was emitted from the source at redshift z, wherefore we have to apply a K-correction (e.g. Oke & Sandage 1968; Kim et al. 1996).

Since galaxy clusters are extended X-ray sources, we introduce the *surface brightness*, S_X, which is given by the flux measured under a solid angle Ω,

$$S_\mathrm{X} = f_\mathrm{X}/\Omega = \frac{1}{4\pi\,(1+z)^4}\int_{-\infty}^{\infty}\epsilon\,\mathrm{d}l\,. \tag{3.3}$$

The surface brightness is proportional to $D_\mathrm{A}^2/D_\mathrm{L}^2 = (1+z)^{-4}$ because at cosmological distances the *cosmological surface brightness dimming* sets in. The angular diameter distance enters via $\Omega = AD_\mathrm{A}^{-2}$. In Eq. (3.3), we introduced the *emissivity* which is defined as the energy that is emitted unit time from a given volume dV,

$$\epsilon = \frac{\mathrm{d}L_\mathrm{X}}{\mathrm{d}V}\,. \tag{3.4}$$

If the emissivity is considered as a function of frequency ν, this equation becomes $\epsilon_\nu = \mathrm{d}L_\mathrm{X}/\mathrm{d}V/\mathrm{d}\nu$ which is defined by the emission processes that will be introduced next. Hence, the emissivity determines the spectrum of an X-ray emitting source. Thus, from the X-ray spectrum of a cluster we gain information on the emission processes that take place in the plasma, such as thermal bremsstrahlung or line emission from elements. Fitting a suitable emission model to the spectrum allows us to derive the plasma temperature T_X, which is given in keV, and density. More details on spectra and temperatures will be provided in the following sections and Chapter 7.

3.1.2 Emission mechanisms

At temperatures of $k_\mathrm{B}T \gtrsim 2\,\mathrm{keV}$ and ICM metallicities of $\sim 0.1 - 1\,Z_\odot$, thermal bremsstrahlung emission (free-free emission) is the dominant process. The notation "metals" includes all elements that are heavier than He and for reasons of convenience their abundances relative to hydrogen are given in units of the solar abundance $Z_\odot$. Bremsstrahlung is emitted because the charged particles are accelerated during close encounters. In an electron-ion plasma, electrons are the prime emitters because the relative acceleration is inversely proportional to the mass that is accelerated.

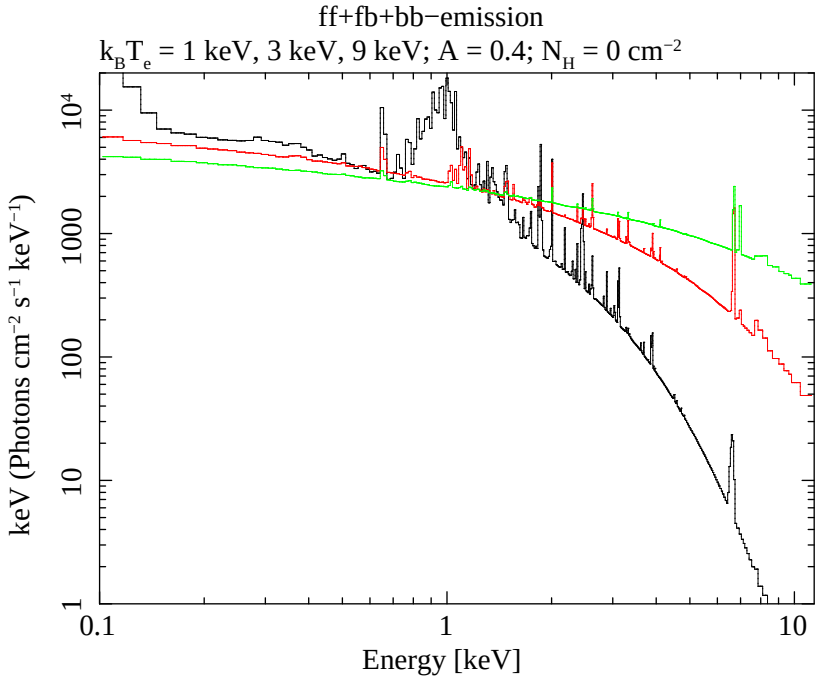

Figure 3.1: X-ray spectra emitted by plasma with temperatures of 1 keV (black), 3 keV (red) and 9 keV (green) including free-free, free-bound and bound-bound emission. At ∼ 1 keV and ∼ 6 keV line emission, especially from the iron L and K shell, becomes more pronounced than at higher temperatures. From http://www.astro.uni-bonn.de/~reiprich/act/gcs/ .

Assuming that all electrons have the same velocity v, the emissivity ϵ^{ff} is proportional to v^{-1} and to the number densities of electrons and ions, n_{e} and n_{i}, respectively. Thus, for a thermal plasma in which the electrons have a Maxwellian velocity distribution, the emissivity with respect to the electron frequency ν is given as (e.g. Sarazin 1988)

$$\epsilon_{\nu}^{\mathrm{ff}} \propto n_{\mathrm{e}} n_{\mathrm{i}} T_{\mathrm{e}}^{-1/2} \exp\left(-\frac{h\nu}{k_{\mathrm{B}} T_{\mathrm{e}}}\right), \tag{3.5}$$

whereby $\bar{v} \propto T_{\mathrm{e}}^{1/2}$. The kinetic energy of the electron has to be at least equal to the energy of the emitted photon, i.e. $1/2 m_{\mathrm{e}} v^2 \geq h\nu$. The non-relativistic, *total emissivity* of the plasma can be obtained by integrating over all frequencies,

$$\epsilon^{\mathrm{ff}} = \int_0^{\infty} \epsilon_{\nu}^{\mathrm{ff}} \mathrm{d}\nu = \frac{2^5 \pi e^6}{3 h m_{\mathrm{e}} c^3} \sqrt{\frac{2\pi k_{\mathrm{B}}}{3 m_{\mathrm{e}}}} Z^2 n_{\mathrm{e}} n_{\mathrm{i}} g_{\mathrm{B}}\,(Z, T_{\mathrm{e}})\, T_{\mathrm{e}}^{1/2}, \tag{3.6}$$

whereby Z is the ion charge and $g_{\mathrm{B}} \approx 1.2$. This value is obtained from averaging the Gaunt factor g_{ff} over all frequencies. The Gaunt factor is of the order of unity and its dependence on temperature and frequency is weak.

Further emission mechanisms are synchrotron radiation where charged particles with $v \approx c$ emit synchrotron radiation while gyrating along the magnetic field lines of the plasma, and the inverse Compton effect, in which low energy photons gain energy by penetrating a medium of energetic particles. But compared to bremsstrahlung, they only play a minor role in the X-ray emission of galaxy clusters in the $\sim 0.5 - 10$ keV energy band which almost covers the energy range that is used in this work.

Besides bremsstrahlung, recombination and line emission can become important. Line emission (bound-bound) can occur especially at $T_{\mathrm{e}} \lesssim 2$ keV, where the emission is approximately

$\epsilon \propto T_{\rm e}^{-0.6} n_{\rm e}^2$. At these temperatures, hydrogen is ionised and some heavier elements are ionised as well depending on their energy levels and the plasma temperature. The free electrons can collide with such partly ionised elements and excite them. The decay back to the previous state follows immediately. Observations of line emission in an X-ray spectrum provide information on the metal abundance and their ionisation states. Thus, hot gas is mainly composed of H and He but polluted by non-primordial elements generated in star formation and supernovae explosions. Among these, iron (Fe) is the element that preferentially contributes to line emission with its emission from the L- and K-shells, others are e.g. Si, O and N. The metallicity in galaxy clusters is peaked towards the centre which indicates that the metals are generated in the central cluster galaxies or sink down to the potential well centre (Qin & Wu 2001).

3.1.3 Universal temperature distribution for galaxy clusters

From the X-ray spectrum of a galaxy cluster, its temperature, metallicity and gas density can be derived using a combination of models for bremsstrahlung emission of hot, diffuse gas with line emission from typical elements and the absorption from Galactic hydrogen. Besides the absorption by gas, i.e. mostly hydrogen, along the line-of-sight, one has to account for instrumental effects that can distort the measurement, such as the effective area of the telescope-detector system as a function of energy and detector position, and the smearing of spectral features due to finite energy resolution. Such corrections are usually incorporated in the model by response-files for *XMM-Newton*. Yet, the best fit of $T_{\rm X}$ depends on the detector. Especially, if the plasma has two temperature components, the measured temperature will depend on the energy range in which the detector is most sensitive and in which it has the largest effective area. But if the plasma has only one $T_{\rm e}$, as one assumes for small, deprojected annuli, all detectors should measure the same $T_{\rm X}$ within statistical errors.

As long as a cluster is not merging and unless the temperature is not measured in the cluster outskirts where the gas density is low, it can be assumed that $T_{\rm e} = T_{\rm gas}$, because the mean free paths of electrons and ions are of the scale of galaxies (Sarazin 1988),

$$\lambda_{\rm e} = \lambda_{\rm i} \approx 23\,{\rm kpc} \left(\frac{T_{\rm gas}}{10^8\,{\rm K}}\right)^2 \left(\frac{n_{\rm e}}{10^{-3}\,{\rm cm}^{-3}}\right)^{-1} . \tag{3.7}$$

Thus, the ICM is non-collisional on smaller scales.

For all galaxy clusters, the temperature drops with radius because the potential well becomes shallower and the gas is less compressed. According to the measurements at small radii, the temperature profiles can be used to broadly divide the clusters into cool-core (CC) and non-cool-core (NCC) clusters (e.g. Fabian 1993; Böhringer et al. 1995). Cool-core clusters, have a temperature drop towards the centre and a low central entropy while NCCs have high entropies and high central temperatures. Since merging disturbs the X-ray emission of the ICM, it is more likely that regular clusters have cool cores than mergers as also indicated in simulations (e.g. Burns et al. 2008). Outside of the core region, the temperature profile of galaxy clusters has a universal shape as studies of the temperature distributions indicate (e.g. Markevitch et al. 1998). For example, Zhang et al. (2006) found that the temperature profiles of the REFLEX-DXL sample are nearly self-similar using high-quality *XMM-Newton* data with an almost constant temperature up to $0.3r_{500}$ (Fig. 3.2). The conclusion of the universal temperature profile is consistent among recent studies in observations (e.g. Markevitch et al. 1998; Vikhlinin et al. 2005; Zhang et al. 2006) and simulations (e.g. Borgani et al. 2004). The universal behaviour of the temperature profile in the cluster outskirts was intensively investigated and confirmed by Leccardi & Molendi (2008) using a sample of 50 clusters at low to intermediate redshifts ($0.1 < z < 0.3$). In addition, George et al. (2009), Reiprich et al. (2009) and Simionescu et al. (2011) studied the temperature profiles out to the virial radius

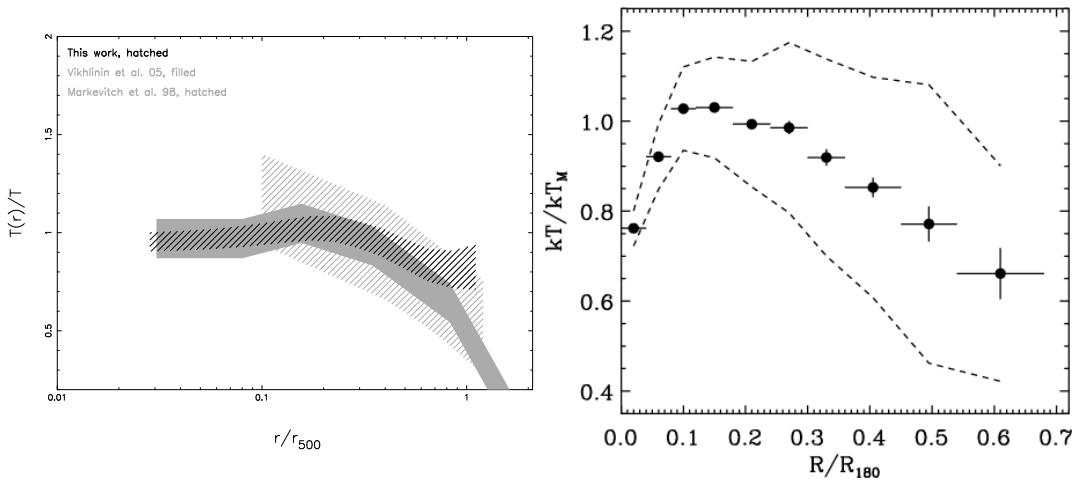

Figure 3.2: *Left:* Averaged temperature profile of the REFLEX-DXL clusters up to r_{500} (Zhang et al. 2006) which is compared to the universal temperature profiles from Markevitch et al. (1998) and Vikhlinin et al. (2005) shown as the grey hatched and the grey filled areas, respectively. From Zhang et al. (2006). *Right:* Weighted average of all temperature profiles of the sample from Leccardi & Molendi (2008). The profiles were rescaled by R_{180} and $kT_{\rm M}$. The dotted lines show the one-sigma scatter of the values around the average. Beyond $0.2R_{180}$, the averaged temperature profile declines and towards small radii the temperature drops due to the presence of cool core clusters. From Leccardi & Molendi (2008).

for individual clusters with *SUZAKU*. All these authors found that the temperature profile drops beyond $0.2r_{180}$ with a slope that is similar to those from hydrodynamical simulations.

3.1.4 ICM density and surface brightness

The intracluster gas contributes $\approx 15\%$ to the total gravitating cluster mass, which is much more than the combined mass of all cluster galaxies. The ICM is compressed and heated by shock waves. Typical central densities are $10^{-3} - 10^{-1}$ atoms cm^{-3} which is still less than the best vacuum that can be achieved in laboratories on Earth.

Simulations have shown that galaxy clusters can be considered as one-dimensional objects (*spherical cow approximation*) which is a good approximation to determine the bulk properties of most clusters (Kaiser 1986). One assumes that the density of cluster galaxies can be described by a King profile (King 1962) and that their velocity distribution is isotropic. The gas density profile is then described by a β-model,

$$\rho(R) = \rho(0)\left[1 + \left(\frac{R}{R_{\rm c}}\right)^2\right]^{-\frac{3}{2}\beta}, \tag{3.8}$$

where $R_{\rm c}$ is the *core radius* which is introduced to avoid that the density attains infinitely high values in the centre and $\rho(0)$ is the density within $R_{\rm c}$ which is assumed to be constant. The slope $\beta = \mu m_{\rm p}\sigma_v^2/k_{\rm B}T$ is the ratio between the kinetic energies of the gas and the galaxies. The β-model fits the gas density profile of galaxy clusters well (e.g. Cavaliere & Fusco-Femiano 1976; Sarazin & Bahcall 1977) and it is widely used because β is correlated with the gas temperature. For hot clusters, typically slopes are $0.7 \lesssim \beta \lesssim 0.8$.

In the energy range of $0.7 - 2\,\mathrm{keV}$, the emissivity is independent of the cluster temperature (e.g. Zhang et al. 2007) and further $\propto n_\mathrm{e}^2 \propto \rho_\mathrm{gas}^2$. Integrating Eq. (3.3) along the line-of-sight dl gives the projected surface brightness at the projected distance r from the cluster centre,

$$S_\mathrm{X}(r) \propto \int_r^\infty n_\mathrm{e}^2 \,\mathrm{d}l = S_0 \left[1 + \left(\frac{r}{r_\mathrm{c}}\right)^2\right]^{-3\beta+\frac{1}{2}} , \tag{3.9}$$

where r_c is the projected core radius.

Fitting Eq. (3.9) to the observed surface brightness profiles yields β, r_c, and the normalisation S_0. Inserting these parameters into Eq. (3.8) provides the gas density profile, with which the gas mass M_gas can be obtained by integrating $\rho_\mathrm{gas}(r)$ over a spherical volume. Here, one assumes spherical symmetry and that the ICM is isothermal with constant metallicity.

3.1.5 Hydrostatic mass estimates

Since the ICM is gravitationally bound to the cluster potential it traces the dark matter which contributes the main fraction to the cluster mass. By assuming spherical symmetry and hydrostatic equilibrium, the cluster mass can be inferred from the gradients of gas density and temperature distribution. The *equation of hydrostatic equilibrium* for a gas of density ρ and pressure P in a gravitational potential Φ can be written as

$$\frac{1}{\rho}\frac{\mathrm{d}P}{\mathrm{d}r} = -\frac{\mathrm{d}\Phi}{\mathrm{d}r} . \tag{3.10}$$

To derive an expression for the total cluster mass, we use the ideal gas equation of thermodynamics, $PV = Nk_\mathrm{B}T_\mathrm{gas}$, in which N is the number of particles, V the volume and $\rho_\mathrm{gas} = \mu m_\mathrm{p} N/V$ the gas density with $\mu = 0.62$ as the mean molecular weight per hydrogen atom which yields

$$\frac{1}{\rho}\frac{\mathrm{d}P}{\mathrm{d}r} = \frac{k_\mathrm{B}T_\mathrm{gas}(r)}{\mu m_\mathrm{p} r}\left[\frac{\mathrm{d}\ln\left(\rho_\mathrm{gas}(r)\right)}{\mathrm{d}\ln(r)} + \frac{\mathrm{d}\ln\left(T_\mathrm{gas}(r)\right)}{\mathrm{d}\ln(r)}\right] , \tag{3.11}$$

where we used $\mathrm{d}x = x\,\mathrm{d}\ln x$. The right-hand side of Eq. (3.10) relates the gravitational potential to the total mass density ρ_tot via the Poisson equation $\nabla^2\Phi = 4\pi G\rho_\mathrm{tot}$ and the Gauss divergence theorem. Integrating over a spherical volume yields

$$\frac{\mathrm{d}\Phi}{\mathrm{d}r} = \frac{GM_\mathrm{tot}(<r)}{r^2} . \tag{3.12}$$

By combining Eq. (3.11) and Eq. (3.12) we obtain the *hydrostatic mass equation*

$$M_\mathrm{tot}(<r) = -\frac{k_\mathrm{B}T_\mathrm{gas}(r)r}{G\mu m_\mathrm{p}}\left[\frac{\mathrm{d}\ln\left(\rho_\mathrm{gas}(r)\right)}{\mathrm{d}\ln(r)} + \frac{\mathrm{d}\ln\left(T_\mathrm{gas}(r)\right)}{\mathrm{d}\ln(r)}\right] . \tag{3.13}$$

To the ICM temperature T_gas we henceforth refer to as the X-ray temperature T_X, which can be obtained from the spectra, and to M_tot as the X-ray hydrostatic mass M_X. With the gas density profile (Eq. 3.8) and the temperature as a function of radius, the total hydrostatic X-ray mass can be re-expressed as

$$M_\mathrm{X}(<r) = \frac{r^2}{G\mu m_\mathrm{p}}\left[\frac{3\beta r}{r_\mathrm{c}^2 + r^2} + \frac{\mathrm{d}k_\mathrm{B}T(r)}{\mathrm{d}r}\right] , \tag{3.14}$$

where $T(r)$ is the function that models the temperature profile (Sect. 7.2.1). Thus, the mass depends primarily on the gas density and temperature gradients, and the gas temperature.

The hydrostatic mass equation still provides unbiased mass estimates if clusters are not exactly spherical. It was shown in N-body plus hydrodynamical simulations (e.g. Schindler 1996; Evrard et al. 1996) and via gravitational lensing (Oguri et al. 2010) that the unbiased mass estimates have a scatter of less than 30% between measured and true mass of non-merging clusters. For mergers, however, the assumption of hydrostatic equilibrium is violated but still within 30% scatter (Rasia et al. 2012).

With Eq. (3.14), the mass inside any given radius can be calculated. In X-rays, hydrostatic masses are usually calculated within r_{2500}, r_{1000} and r_{500} which correspond to the cluster overdensities $\Delta = 2500$, 1000 and 500. Assuming spherical symmetry, the overdensity can be expressed as

$$\Delta(< r) = \frac{3M(< r)}{4\pi r^3 \rho_{\rm cr}(z)}\,, \tag{3.15}$$

where

$$\rho_{\rm cr}(z) = \rho_{\rm cr,0} E^2(z) \tag{3.16}$$

is the critical density at the cluster redshift z for a flat universe.

3.1.6 X-ray background components

For accurate photon statistics one has to account for the radiation that does not come from the galaxy cluster itself but also from the cosmic background or the instrument by reactions with high-energy cosmic particles. Following Snowden et al. (2008) and Zhang et al. (2009) I will briefly discuss the most important background components.

1. Quiescent and fluorescent particle background (QPB & FXB)

The quiescent particle background is a continuum emission that is produced by the interaction of high energy particles that penetrate the detectors. This also includes the fluorescent X-ray background (FXB) which is produced by the flux from particles that with the metals the detector is made of. For the MOS-detectors of *XMM-Newton* (Sect. 4.4.1), the fluorescent X-rays are dominated by lines, such as Al Kα at $E \sim 1.49$ keV and Si Kα at $E \sim 1.75$ keV, additional to higher energy lines from elements, such as Au, Cr, Mn, Fe, Ni, Zn. The continuum QPB dominates at energies $\gtrsim$2 keV and $\lesssim$1.2 keV.

According to De Luca & Molendi (2004), a simple renormalisation of the QPB using only the high energy band (8 – 12 keV) may produce systematic errors in both the continuum and the line contribution of the spectrum. Zhang et al. (2009) found that this problem can be solved by including lower energies, i.e. 3 – 10 keV.

2. Soft proton background (SPB)

Protons with energies less than a few 100 keV travel down the telescope light path and deposit their energy directly in the detectors producing undesired events. This effect is highly variable and significant peaks in the lightcurve are called *soft proton flares*. The spectrum of these protons varies in magnitude and slope of the light curve and be described by a power law. By inspecting the light curve of the data, these flares can be excised (Sect. 4.4.2).

3. Cosmic X-ray background (CXB)

The cosmic X-ray background is a superposition of Galactic emission from multiple sources, the Galactic halo and probably from even more distant sources. Its diffuse thermal spectrum governs

the energy range below $\sim$ 1 keV and is dominated by emission lines. This emission is highly variable over the whole sky and it becomes dominant with increasing radial distance from the cluster centre where the cluster emission becomes low. For these reasons, the CXB should be estimated by statistical means from the cluster outskirts if there is sufficient area for good photon statistics.

The unresolved emission of the CXB is from the superposition of cosmological objects like e.g. AGN (Hickox & Markevitch 2007), which dominates at higher energies, and Galactic stars with only small contribution at lower energies (e.g. Kuntz & Snowden 2001). The average spectrum of the cosmological emission is predominantly a power-law continuum with a typical index $\sim$ 1.4 and possible change in slope at lower energies. A true cosmic variation of magnitude on the sky is further assumed but there is also the obvious variation caused by the excision of point sources to various levels.

Zhang et al. (2009) showed that the CXB can be well described by a combined model "mekal+wabs*(mekal+powerlaw)" where the power-law accounts for unresolved point sources, "wabs" models the absorption by Galactic hydrogen while "mekal" models the CXB thermal emission. A description of these models will be provided in Sect. 7.2.1 where we will discuss the spectral analysis.

4. Solar wind charge exchange emission (SWCX)

This type of emission is produced by solar wind flows in which highly ionised atoms interact with neutral material in the solar system coming from the Local Cloud (Lallement 2004) or exospheric material at the magnetosheath of the Earth (Robertson & Cravens 2003). The SWCX causes line emission at energies less than $\sim$1.3 keV from CVI, OVII, OVIII, NEIX and MGXI in the MOS energy band. Magnitude and line strengths of the SWCX are strongly variable.

3.2 Scaling relations

Since the X-ray emission of galaxy clusters is tightly correlated with their total mass, they can be used for cosmological studies in which cosmological parameters are constrained via the cluster mass function or to study the large-scale structure. For this purpose, scaling relations between the X-ray observables related to the total gravitating mass have to be calibrated. Since the correlations between X-ray observables and mass can only be as precise as these observables can be estimated, the errors of the scaling relations affect the accuracy of cosmological parameters. Hence, an accurate calibration of scaling relations is crucial for cluster cosmology.

All clusters share self-similar structure. In other words, they appear the same after normalised to their characteristic scales (e.g. r_{500}) and masses (Kaiser 1986). Such scaled profiles of X-ray properties probe the regularity in galaxy clusters because they allow us to study the cluster structure, its morphology and thermodynamics as well as the evolution of the ICM-properties. If the scaling relations deviate from the self-similar predictions, non-gravitational mechanisms, merging or substructures may be responsible for that. The structure formation on various scales is correlated due to the large-scale environment dependence of galaxy formation and evolution. In turn, galaxy feedback affects the evolution of the large-scale environment which can be well investigated with galaxy clusters. This also allows us to study the structure formation history via scaling relations (e.g. Haines et al. 2009; Smith et al. 2010; De Lucia et al. 2011).

In general, scaling relations are parametrised by a power law, $Y = Y_0 X^\gamma$, and some may evolve as a function of redshift (e.g. Voit 2005). According to the hierarchical structure formation scenario, halos form via gravitational collapse when a matter overdensity exceeds the critical density at that redshift. Due to cosmic expansion, the critical density is high towards high redshift. As

a consequence, gravitational collapses at higher redshifts happen at higher densities. The redshift evolution correction (Eq. 1.16) accounts for the redshift dependence of scaling relations.

Scaling relations were mostly studied for clusters at low redshifts (e.g. Arnaud et al. 2007; Vikhlinin et al. 2006; Zhang et al. 2007, 2008). For studies at higher redshifts mostly relaxed, homogeneous samples were used (e.g. Maughan et al. 2006, 2008). Scaling relations likely deviate for clusters with irregular morphology. In this thesis, the scaling relations for an inhomogeneous sample of non-regular clusters at higher redshifts will be investigated and any differences from the well-known behaviour will be discussed.

3.2.1 Mass-temperature ($M_{\rm tot} - T_{\rm X}$) relation

The $M_{\rm tot} - T_{\rm X}$ relation scales as $M_{\rm tot} \propto T_{\rm X}^{3/2}$, because of the correlation of mass and radius from the spherical collapse model, $M_{\rm tot} \propto r^3$, and the correlation between mass and temperature from the virial theorem, $T_{\rm X} \propto M_{\rm tot}/r$. This behaviour was confirmed observationally for nearby clusters by e.g. Arnaud et al. (2005). The $M_{\rm tot} - T_{\rm X}$ relation is sensitive to merging clusters, while it has low scatter for relaxed ones (e.g. Zhang et al. 2008). For precision cosmology, mass-observable relations with low scatter are preferred. For example, the error on σ_8 is dominated by the scatter of the $M_{\rm tot} - T_{\rm X}$ relation (Pierpaoli et al. 2001). The calibration of mass-observable relations with reliable mass measurements is crucial for constructing the cluster mass function (e.g. Stanek et al. 2010).

Zhang et al. (2007) found no evident evolution in the $M_{\rm tot} - T_{\rm X}$ relation for the pilot LoCuSS sample compared to the higher redshift samples (e.g. Ettori et al. 2004) or low-redshift samples (e.g. Arnaud et al. 2005) within the scatter.

3.2.2 Luminosity-temperature ($L_{\rm X} - T_{\rm X}$) and luminosity-mass ($L_{\rm X} - M_{\rm tot}$) relation

Only if a sufficiently large number of X-ray photons are detected ($\sim 10^3 - 10^4$), cluster masses can be inferred with Eq. (3.14), because good statistics are required to calculate temperature and gas density profiles. Yet, with $\sim 10^1 - 10^2$ photons, the X-ray luminosity can be measured with satisfying accuracy. Since the surface brightness scales with $(1+z)^{-4}$, long exposure times are required for clusters at $z > 0.5$ with the currently available detectors.

Using scaling relations, the observable $L_{\rm X}$ (but also $T_{\rm X}$), can give an estimate of cluster masses that are not accessible from shallower exposures. Due to $M_{\rm gas,500} \propto T_{\rm X}^{3/2}$ and $M_{500} \propto r_{500}^3$, the relation between luminosity and temperature is expected to scale as $L_{\rm X} \propto M_{\rm gas}^2 T_{\rm X}^{1/2} r_{500}^{-3} \propto T_{\rm X}^2$. Since the gas-mass fraction of the ICM depends on the cluster temperature, this relation becomes steeper ($L_{\rm X} \propto T_{\rm X}^{2.6}$) as found in observations (e.g. Neumann & Arnaud 2001). Empirically, the mass scales rather with $M_{\rm gas} \propto T_{\rm X}^{1.8}$. For nearby clusters, the $L_{\rm X} - T_{\rm X}$ relation has already been intensively studied (e.g. Markevitch et al. 1998; Reiprich & Böhringer 2002; Ikebe et al. 2002; Chen et al. 2007). With deep *XMM-Newton* imaging spectroscopic data Zhang et al. (2007) found that the $L_{\rm X} - T_{\rm X}$ relation shows no strong evolution compared to those samples, despite their deviation from the self-similar prediction $L_{\rm X} \propto T_{\rm X}^2$.

The luminosity-mass relation scales as $L_{\rm X} \propto M^{1.33}$ because of $M_{\rm tot} \propto T_{\rm X}^{3/2}$ and $L_{\rm X} \propto T_{\rm X}^2$. Using the observed scaling relations from Reiprich & Böhringer (2002), $L_{0.1-2.4{\rm keV}} \propto T^{2.6}$ and $L_{\rm bol} \propto T_{\rm X}^{2.98}$, this gives $L_{0.1-2.4{\rm keV}} \propto M_{\rm tot}^{1.73}$ and $L_{\rm bol} \propto M_{\rm tot}^{1.99}$, respectively (Zhang et al. 2007). Here, the bolometric luminosity $L_{\rm bol}$ is the luminosity which is emitted by a source in the 0.1 – 100 keV energy band. The $L_{\rm X} - M_{\rm tot}$ relation of the LoCuSS sample at $z \sim 0.2$ sample agrees with those of the nearby HIFLUGCS sample at $z < 0.15$ (Reiprich & Böhringer 2002; Chen et al. 2007), the REXCESS sample (Pratt et al. 2009) and the more distant REFLEX-DXL sample (Zhang et al. 2006). Thus, this relation shows no strong evolution at redshifts below $z \sim 0.3$ (Zhang et al. 2007).

Since these samples are too close with respect to their redshifts and the smallness of their redshift bins, an evolution of the scaling relations can hardly be observed. For this reason, samples at higher redshifts and with a broader redshift range such as the sample that is analysed in this work are expected to reveal evolution effects in the mass-observable scaling relations. Calibrating the $L_X - M_{tot}$ relation can help to understand scatter and sources of systematic errors that should be included in the cluster luminosity function (Stanek et al. 2010). This would allow to use the global luminosity as cluster mass indicator (e.g. Reiprich & Böhringer 2002).

3.2.3 Weak lensing and X-ray masses

Since some X-ray observables, e.g. the temperature, are probably auto-correlated with the X-ray hydrostatic mass M_X, the calibration of the scaling relations using the X-ray data alone can be biased. With mass estimates from approaches that are independent from X-ray, such as e.g. weak lensing masses M_{wl}, this bias can be cross-checked. Those independent mass estimates further allow us to check other systematics in cluster mass estimates and the normalisation of the mass-observable relations (Wu et al. 1998; Mahdavi et al. 2008; Zhang et al. 2008, 2010). The comparison between X-ray and weak lensing mass estimates can be affected by the assumptions made in both approaches. Investigations of small cluster samples at $z \sim 0.2$ with $T_X > 3.5\,\mathrm{keV}$ (e.g. Smith et al. 2005; Bardeau et al. 2007; Hoekstra 2007; Zhang et al. 2007, 2008) indicate that the scaling relations with weak lensing and X-ray masses agree within their scatter and that the morphology dependence is stronger using lensing masses than using X-ray masses. Furthermore, the scatter of those scaling relations is ~ 2 times larger if weak lensing masses are used instead of X-ray hydrostatic masses.

Since the X-ray emission can only be measured up to r_{500} with the current instruments, masses are better compared only out to this radius. At larger radii, the X-ray hydrostatic mass estimate is derived by extrapolation. Recent studies indicate an offset between M_X and M_{wl}. For instance, Zhang et al. (2008) found $M_{wl}/M_X = 1.09 \pm 0.08$ for r_{500} and the agreement between both mass estimates improves towards higher overdensities (Zhang et al. 2010). Considering individual clusters, the scatter between M_X and M_{wl} can be large because lensing masses are sensitive to projection effects (Pratt et al. 2005; Zhang et al. 2005).

Chapter 4

Sample and data preparation

In this chapter, I will discuss known characteristics of the galaxy clusters which are analysed in this thesis and describe the used data. The cluster sample is introduced in Sect. 4.1. Section 4.2 describes the high-resolution space-based data that was used to measure source ellipticities. I will briefly outline telescope properties, data reduction and how the effective mean source redshifts were obtained from these data. Section 4.3 follows the same scheme for the multi-colour data from ground facilities that were used to estimate the photometric redshifts for MS0451.6−0305. The *XMM-Newton* data for three clusters of the sample are described in Sect. 4.4.

4.1 Cluster sample

The cluster sample consists of three high- and two intermediate-redshift clusters. They were originally selected to study the kinematics of cluster galaxies and their evolution with respect to the ICM (Ziegler et al. 2003; Jäger et al. 2004). For this reason, these clusters exhibits striking and interesting properties (Table 4.1) which makes the sample attractive for a thorough comparison between weak lensing and X-ray masses. Here, I describe what is known from previous observations.

4.1.1 CL0015.9+1609

CL0015.9+1609 at $z_d = 0.541$ is one of the most studied galaxy clusters. It was observed in different wavelength ranges, such as in the optical (Tanaka et al. 2005), radio (Giovannini & Feretti 2000), and in X-rays with *ROSAT* (Neumann & Böhringer 1997) and *XMM-Newton* (Kotov & Vikhlinin 2005; Worrall & Birkinshaw 2003) among others. Further studies were performed by Bonamente et al. (2008) using the Sunyaev-Zeldovich effect and by Clowe et al. (2000) using weak lensing measurements from ground-based data.

The HST-image in Fig. 4.1 shows that the cluster can be identified by three bright galaxies aligned from northeast to southwest. Because of these galaxies, the light in the central part of CL0015.9+1609 has elliptical isophotes such that the major axis of this ellipse coincides with the connection line of these galaxies (Clowe et al. 2000). In a circular area around the BCG, which is the luminous galaxy in the middle of this bar-like structure, a large number of fainter galaxies are distributed with a slight overdensity to the West of the BCG.

Optical observations revealed that CL0015.9+1609 is embedded in a large filamentary structure extending over 20 Mpc from North to South and another filament in east-west direction (Tanaka et al. 2005). A strong radio halo indicates that CL0015.9+1609 is in the process of merging (Giovannini & Feretti 2000). Evidence for merging was also found by Solovyeva et al. (2007)

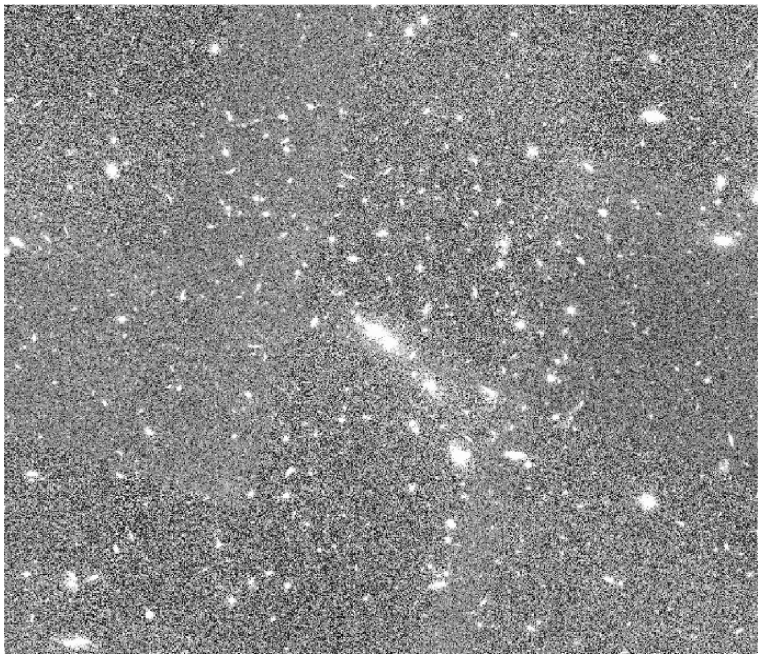

Figure 4.1: HST-mosaic of CL0015.9+1609 showing a $\sim 3\farcm5 \times 3\farcm0$ zoom into the cluster centre which can be identified as the diagonal bar-like structure in the middle of the image.

who detected temperature perturbations of the cluster gas and a luminosity of $L_X = (51 \pm 1) \times 10^{44}\,\mathrm{erg\,s^{-1}}$ in the 0.3–4.5 keV band with *XMM-Newton*. This luminosity is two times brighter than predicted from the $L_X - T_X$ relation but consistent with $L_X = 14.6 \times 10^{44}\,\mathrm{erg\,s^{-1}}$ in the 0.3–3.5 keV band using *Einstein*-data (Luppino et al. 1999) and $L_X = (19.6 \pm 0.3) \times 10^{44}\,\mathrm{erg\,s^{-1}}$ in the 0.1–2.4 keV band using *Chandra*-data (Ebeling et al. 2007). *Chandra*-studies show that CL0015.9+1609 is among the hot clusters because of $T_X = 9.3^{+0.5}_{-0.3}\,\mathrm{keV}$ (Balestra et al. 2007), $T_X = (9.4 \pm 0.3)\,\mathrm{keV}$ (Ebeling et al. 2007), and more recently $T_X = (10.5 \pm 0.6)\,\mathrm{keV}$ (Bonamente et al. 2008).

4.1.2 CL0413−6559

While CL0015.9+1609 is the most studied cluster in the sample, CL0413−6559 located at $z_d = 0.51$ is the least studied one. In the literature it is also known as FT1557.19TC. It has a high fraction of spiral galaxies and no red sequence (Ziegler et al. 2003). This is untypical for galaxy clusters because according to prevalent theories of galaxy formation, cluster galaxies lose their gas due to encounters with other cluster members and merge to elliptical galaxies (Sect. 1.4.1). The low X-ray luminosity $L_X = 0.11 \times 10^{44}\,\mathrm{erg\,s^{-1}}$ in the 0.3–3.5 keV band measured from *ROSTA*-data (Smail et al. 1997) also indicates a shallow gravitational potential and less rich intra-cluster gas which provides evidence that this cluster is still in the process of forming.

Cl0413−6559 is the only cluster in our sample that does not exhibit strong lensing features. Figure 4.2 shows an HST-image of the cluster in which the cluster centre is between the two bright stars and the luminous spiral galaxy in the foreground.

4.1.3 MS0451.6−0305

The galaxy cluster MS0451.6−0305 is the most X-ray luminous cluster of the Einstein Medium Sensitivity Survey (EMSS) residing at $z_d = 0.55$. As an X-ray source, this cluster is known since

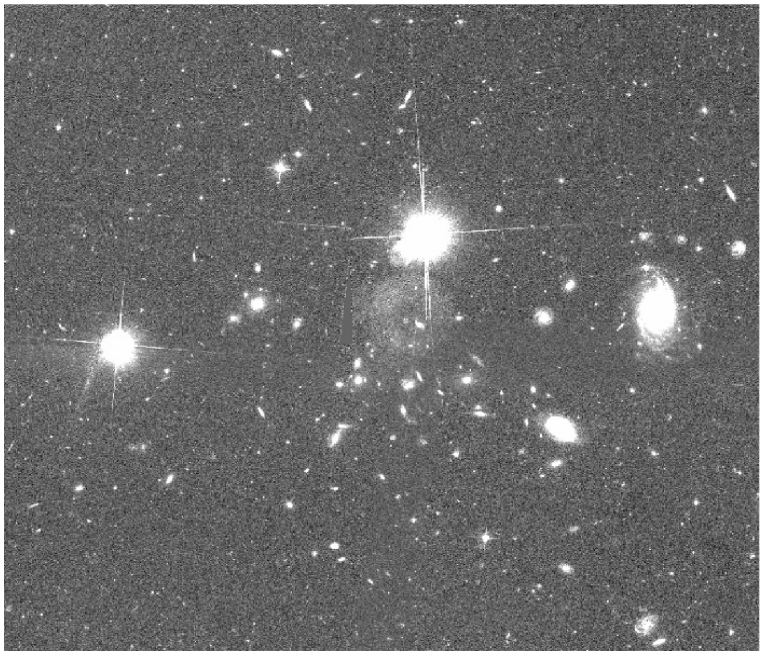

Figure 4.2: HST-mosaic of CL0413−6559 showing a $\sim 3\farcm0 \times 2\farcm5$ zoom into the cluster centre. The cluster is between the two bright stars and the luminous spiral galaxy in the centre of the image.

Table 4.1: HST data properties: Coordinates are in the J2000-system. The number density n is given in sources/arcmin^2. FOV is the field-of-view, and $\langle D_{\rm ds}/D_{\rm s}\rangle$ and $\langle z_{\rm s}\rangle$ are the mean distance ratios and effective mean source redshifts, respectively. The values for the effective mean source redshift do not depend only on n but also on the cluster coordinates. References for coordinates and redshifts: (1) Stocke et al. (1991), (2) Ellis et al. (1997), (3) Gioia & Luppino (1994).

Cluster	$\alpha_{\rm J2000}$	$\delta_{\rm J2000}$	$z_{\rm d}$	Exptime [s]	n	FOV	$\langle D_{\rm ds}/D_{\rm s}\rangle$	$\langle z_{\rm s}\rangle$
CL0015.9+1609	00:18:33.3	16:26:36	$0.541^{(1)}$	2240	43	$8.05' \times 6.95'$	0.398	1.725
CL0413−6559	04:12:54.7	−65:50:58	$0.51^{(2)}$	2596	73	$7.05' \times 7.05'$	0.463	1.880
MS0451.6−0305	04:54:10.9	−03:01:07	$0.55^{(3)}$	2036	82	$22' \times 22'$	0.383	1.645
MS1008.1−1224	10:10:34.1	−12:39:48	$0.301^{(1)}$	2232	55	$7.55' \times 7.05'$	0.603	1.644
MS2137.3−2353	21:40:12.8	−23:39:27	$0.313^{(1)}$	2240	59	$7.05' \times 7.05'$	0.598	1.665

1989, which is why its name is based on the coordinate system of 1950. Thus, its current right ascension deviates from the former value as given in its name by three minutes due to precession. It was during the mission of the *Einstein* satellite that MS0451.6−0305 was identified as a galaxy cluster (Stocke et al. 1991).

The luminosity was measured to be $L_{\rm X} = 19.98 \times 10^{44}\,{\rm erg\,s^{-1}}$ in the 0.3 – 3.5 keV band with *Einstein*-data (Luppino et al. 1999). Using *Chandra*-data, more recent results for luminosity and temperature are $L_{\rm X} = 8.87 \times 10^{44}\,{\rm erg\,s^{-1}}$ in the 0.1 – 2.4 keV band and $T_{\rm X} = 10.6^{+1.6}_{-1.3}$ keV using "wabs+mekal"[1] (Donahue et al. 2003), $T_{\rm X} = 8.2^{+0.4}_{-0.3}$ keV (Balestra et al. 2007), $L_{\rm X} = (16.8 \pm 0.6) \times 10^{44}\,{\rm erg\,s^{-1}}$ and $T_{\rm X} = (7.5 \pm 1.0)$ keV in the 0.1 – 2.4 keV band (Ebeling et al. 2007) and $T_{\rm X} = 9.9^{+0.8}_{-0.7}$ keV (Bonamente et al. 2008).

The cluster centre is indicated by a large bar of galaxies extending from northwest to southeast (Fig. 4.3). In the middle of it is the BCG. Due to a luminous spiral galaxy in the foreground, it is not the brightest object in this region. Clowe et al. (2000) observed that the X-ray emission traces the bar-like structure of galaxies, but less extended. Most galaxies either are located near the southeast or the northwest of the BCG.

[1]The spectral model "wabs+mekal" will be explained in Sect. 7.2.1.

Figure 4.3: HST-mosaic of MS0451.6−0305 showing a $\sim 7\farcm0 \times 6\farcm0$ zoom into the cluster centre. The cluster centre is indicated by a large bar of galaxies extending from northwest to southeast.

4.1.4 MS1008.1−1224

With 112 cluster galaxies, the EMSS galaxy cluster MS1008.1−1224 is a rich strong-lensing cluster at $z_\mathrm{d} = 0.301$ with a low X-ray luminosity of $L_\mathrm{X} = 4.49 \times 10^{44}\,\mathrm{erg\,s^{-1}}$ as measured from *Einstein*-data in the $0.3-3.5\,\mathrm{keV}$ band (Luppino et al. 1999). Lensed arclets were found north and east near the cluster centre which is defined by the central cD-galaxy, but no giant arcs have been detected so far (Le Fevre et al. 1994). The galaxies are distributed approximately circular around the cluster centre but with an elongation in the north-south direction (Fig. 4.4, Mayen & Soucail 2000). To the North of the cluster centre, a further clump of galaxies is located (Gioia & Luppino 1994).

Observations in X-ray and optical light as well as the weak lensing mass distribution reveal substructures that indicate merger processes (Athreya et al. 2002). Thus, the ICM may not be in hydrostatic equilibrium with the cluster potential. With $T_\mathrm{X} = 7.3^{+1.2}_{-0.8}\,\mathrm{keV}$ determined from *ROSAT*-observations (Lewis et al. 1999), or more recently $T_\mathrm{X} = 5.8^{+0.3}_{-0.2}\,\mathrm{keV}$ (Balestra et al. 2007), MS1008.1−1224 is moderately hot.

MS1008.1−1224 is an excellent example for cluster-cluster lensing. Athreya et al. (2002) detected a lensed background cluster at redshift $z = 0.9$ with an image position of $30''$ southwest from the central cD-galaxy. Since this background cluster is magnified due to gravitational lensing, MS1008.1−1224 allows to study this high-redshift cluster in more detail.

4.1.5 MS2137.3−2353

The strong lensing cluster MS2137.3−2353 at $z_\mathrm{d} = 0.313$ was detected with *Einstein* (Stocke et al. 1991). Exhibiting several arclets, a radial and a giant arc embedded in the halo of the bright cD-galaxy (Fort et al. 1992), it has the most impressive strong lensing features in the cluster sample. Further strong lensing observations of this cluster were performed by Gioia et al. (1996), Hammer et al. (1997) and Gavazzi et al. (2003) among others. Merten et al. (2009) analysed the cluster combining strong and weak lensing.

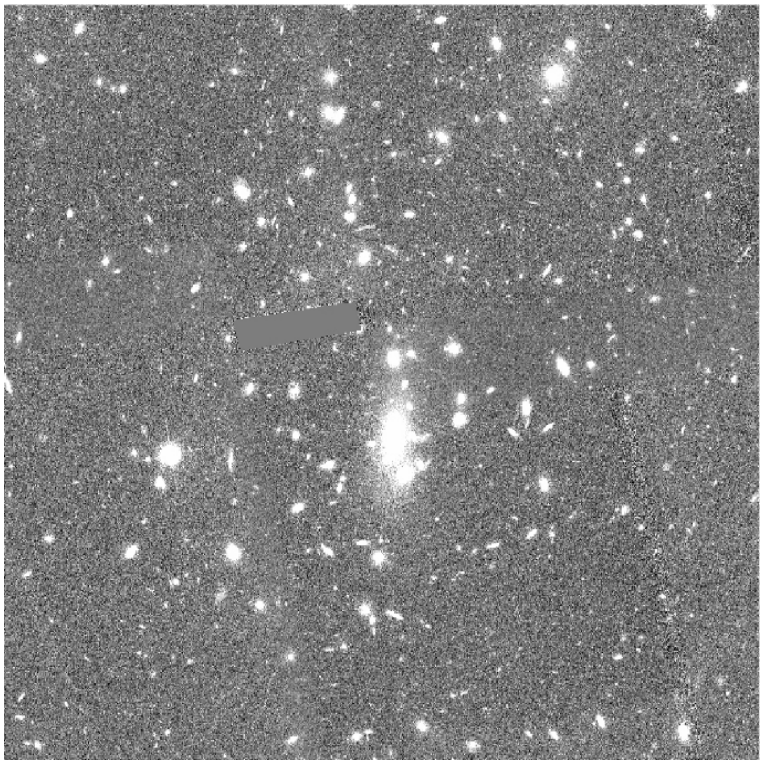

Figure 4.4: HST-mosaic of MS1008.1−1224 showing a $\sim 3\farcm0 \times 3\farcm0$ zoom into the cluster centre. The bright peak in the centre of the image is the cD-galaxy which is surrounded elliptically distributed cluster galaxies. The major axis of this galaxy distribution is aligned in North-South direction.

The luminous cD-galaxy dominates the cluster centre (Fig. 4.5) and contributes much to the high X-ray luminosity of $L_X = 15.62 \times 10^{44}\,\mathrm{erg\,s^{-1}}$ in the $0.3 - 3.5\,\mathrm{keV}$ band measured from *Einstein*-data (Luppino et al. 1999). With *Chandra*, the cluster was observed by Allen et al. (2001) who measured $T_X = 5.56^{+0.46}_{-0.39}\,\mathrm{keV}$ and more recently by Balestra et al. (2007) and Ebeling et al. (2010) who measured $T_X = (4.96 \pm 0.11)\,\mathrm{keV}$ and $T_X = (4.67 \pm 0.43)\,\mathrm{keV}$, respectively. Despite its high luminosity ($L_X = (11.1 \pm 0.4) \times 10^{44}\,\mathrm{erg\,s^{-1}}$ in the $0.1 - 2.4\,\mathrm{keV}$ band, Ebeling et al. 2010), the cluster is not moderately hot.

The mass distribution is elliptical and matches the elliptical distribution of both optical light and X-rays wherefore MS2137.3−2353 is likely relaxed (Hammer et al. 1997). Furthermore, the dark matter density profile is much flatter than those of the visible matter which implies large magnification effects (Hammer et al. 1997).

4.2 HST-data

4.2.1 The instrument

To investigate the lensing properties of the cluster sample, we used high-quality from the ACS/WFC detector of the Hubble Space Telescope. The HST is a 2.4m f/24 Ritchey-Chrétien Cassegrain telescope named after the famous US astronomer Edwin Hubble. It is jointly operated by NASA and ESA at an altitude of 590 km from the ground taking 96 minutes per orbit. Although it was launched in April 24 in 1990, it still provides splendid images from deep space.

The Advanced Camera for Surveys (ACS) was installed during the 3rd Servicing Mission in March 2002. It consists of three detectors that cover a spectral range of $1200 - 11000$ Å in total. Its

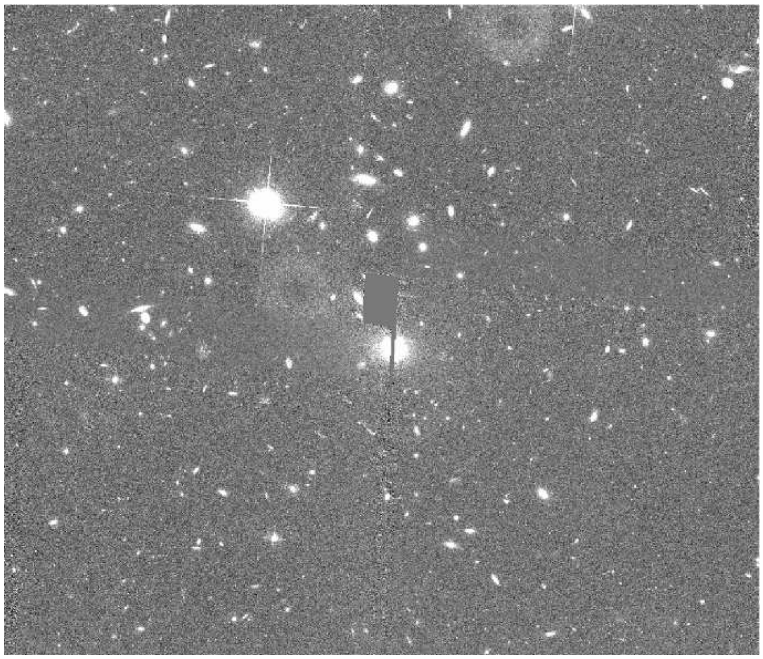

Figure 4.5: HST-mosaic of MS2137.3−2353 showing a $\sim 3\farcm5 \times 3\farcm0$ zoom into the cluster centre. The bright peak in the centre of the image is the luminous cD-galaxy.

purpose is to study the formation of planetary systems, galactic nuclei and to perform deep imaging surveys of galaxy clusters. The cluster data was taken with the Wide Field Channel detector (WFC) which has a resolution of 0.05 arcsec/pixel[2]. With $202'' \times 202''$ it has the largest field-of-view (FOV) and the highest sensitivity of all HST-detectors. The infalling light is collected by two thinned and backside-illuminated CCD-chips with 2048×4096 pixel ($6.88{\times}3.46\,\mathrm{cm}^2$) which are sensitive in the spectral range 3500 – 11000 Å (Fig. 4.6). To make sure that the CCDs remain flat, both are mounted on a thick ceramic holder[2].

Except for MS0451.6−0305, all clusters were observed as 4-pointing mosaics in the filter F606W as part of the GO-program #10635 (PI: Bodo Ziegler). Archival data from program #9836 (PI: Richard Ellis) forming a 41-pointing mosaic observed in F814W was used for MS0451.6−0305. The filter curves and the total throughput are shown in Fig. 4.6.

4.2.2 Data reduction and galaxy selection

The ACS data reduction and weak lensing catalogue creation was done by Tim Schrabback (Schrabback et al. 2007, 2010). Thus, we only summarise details relevant for our analysis.

The data reduction pipeline employs a customised version of `MultiDrizzle` (Koekemoer et al. 2002) for cosmic ray removal, distortion correction and stacking. It also features optimised bad pixel masking and weighting, as well as a careful refinement of shifts and rotations. The shape measurements are based on the Erben et al. (2001) implementation of the KSB+ formalism (Kaiser 1995; Luppino & Kaiser 1997; Hoekstra et al. 1998). The F606W-data was reduced with the Schrabback et al. (2007) pipeline, which employs a large library of stellar-field PSF templates to model the temporally and spatial varying ACS Point Spread Function (Sect. 2.2). Schrabback et al. (2010) implemented a revised version of this interpolating scheme for F814W based on a principal component analysis, which was utilised for the MS0451.6−0305 data. For all clusters parametric corrections for spurious ellipticities caused by charge-transfer-inefficiency were

[2]The details of the telescope and the ACS-camarea are taken from http://acs.pha.jhu.edu

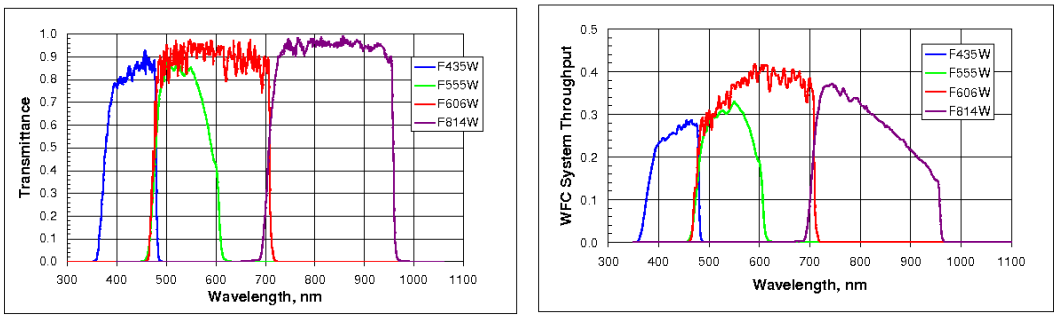

Figure 4.6: The broad-band filter set of the ACS camera. *Left*: Filter transmittance. *Right*: Total system throughput. The shear catalogues are taken in the filters F606W and F814W, operating in the red and IR, respectively. From http://acs.pha.jhu.edu/instrument/filters .

used (Schrabback et al. 2010). Also, the shear estimation based on image simulations from the STEP-project (Heymans et al. 2006; Massey et al. 2007) was recalibrated. Following Hartlap et al. (2009), a mean calibration correction (7%) combined with conservative galaxy selection criteria ($S/N^{KSB} > 2.3$) was used, whereby S/N^{KSB} includes the KSB weight function (Erben et al. 2001), for the F606W-data. An updated signal-to-noise-ratio dependent correction has been derived by Schrabback et al. (2010), which was employed in the analysis of MS0451.6−0305. This allows to include noisier galaxies ($S/N^{KSB} > 2.0$).

The S/N-cuts were done differently, because for F606W the sky background is higher in many of the exposures than for F814W. Since the brightness of the sky background is a function of the ecliptic latitude and longitude of the observations due to zodiacal light, the number density n of background sources and their effective mean source redshift $\langle z_s \rangle$ vary among the clusters. For instance, CL0413−6559 has a higher n and a larger $\langle z_s \rangle$ than CL0015.9+1609 (Table 4.1), which is not only due to the longer exposure time but also to the higher ecliptic latitude. Furthermore, the simplistic 2-position dither pattern that was used for the F606W observations leads to the presence of some uncorrected hot pixels in the stacked image, which increases the noise.

Both pipeline incarnations have been successfully applied to cosmic shear data (GEMS and COSMOS), with substantially stricter correction requirements for weak lensing shape systematics than the weak lensing cluster analysis in this thesis.

4.2.3 Mean distance ratios

As a geometric measure, the strength of the weak lensing signal depends on the angular diameter distances between observer, lens and sources. Therefore, the redshift distribution of the source galaxies must be accurately determined. If no photometric redshifts are available for the studied cluster fields, the redshift distribution must be derived from external fields.

To estimate the redshift distribution from the magnitude distribution of our sources, we used the magnitude-dependent parametrisation by Schrabback et al. (2007) from the GOODS-MUSIC photometric redshift catalogue (Grazian et al. 2006) for the clusters observed in F606W. For F814W, we used the Schrabback et al. (2010) parametrisation which is based on the COSMOS-30 photometric redshift catalogue by Ilbert et al. (2009).

It is convenient to parametrise the redshift distribution as (e.g. Brainerd et al. 1996)

$$p(z) \propto \left(\frac{z}{z_0}\right)^{\alpha} \exp\left[-\left(\frac{z}{z_0}\right)^{\beta}\right] . \tag{4.1}$$

For this thesis, the extended versions of this equation given by Schrabback et al. (2007) for F606W and those given by Schrabback et al. (2010) for F814W were used. The parameters α and β were

fitted with a linear relation between the magnitude and redshift of a galaxy. The source magnitude distribution of an observed field has a characteristic shape. Hence, one can easily derive the corresponding redshift distribution.

For F606W, the redshift distribution is (Schrabback et al. 2007)

$$p(z, i_{606}) = \frac{\beta}{z_0 \Gamma\left(\frac{1+\alpha}{\beta}\right)} \left(\frac{z}{z_0}\right)^{\alpha} \exp\left[-\left(\frac{z}{z_0}\right)^{\beta}\right], \tag{4.2}$$

with $(\alpha, \beta, a, b) = (0.563, 1.716, 0.299, 0.310)$. The linear relation between the magnitude m_{606} measured in F606W and the median redshift z_m of a background source is given as

$$z_\mathrm{m} = r z_0 = a\,(i_{606} - 22) + b\,. \tag{4.3}$$

Here, $r(\alpha,\beta)$ was calculated from numerical integration of Eq. (4.2), which gives the redshift probability distribution for a galaxy with magnitude i_{606}.

For MS0451.6−0305 which was observed in F814W, we used a modified version of Eq. (4.2) which reproduces the galaxy redshift distribution for the Cosmos-field better than Eq. (4.2),

$$p(z, i_{814}) \propto \left(\frac{z}{z_0}\right)^{\alpha} \left(\exp\left[-\left(\frac{z}{z_0}\right)^{\beta}\right] + c u^{d} \exp\left[-\left(\frac{z}{z_0}\right)^{\gamma}\right]\right), \tag{4.4}$$

with $(\alpha, \beta, c, d, \gamma) = (0.678, 5.606, 0.581, 1.851, 1.464)$ and $u = \max[0, (i_{814} - 23)]$ (Schrabback et al. 2010). To account for the correlation between redshift and i_{814}, the magnitude-redshift distribution is subdivided into two magnitude bins:

$$z_0 = \begin{cases} 0.446(i_{814} - 23) + 1.235 & 22 < i_{814} < 23 \\ \sum_{j=0}^{7} a_j [(i_{814} - 23)/4]^j & 23 < i_{814} < 27\,, \end{cases} \tag{4.5}$$

with $(a_0, \ldots, a_7) = (1.237,\ 1.691,\ -12.167,\ 43.591,\ -76.076,\ 72.567,\ -35.959,\ 7.289)$.

With the parametrisations in Eqs. (4.2) and (4.4), the mean distance ratio for a lens redshift z_d can then be calculated from the magnitude distributions with

$$\frac{D\,(z_\mathrm{d}, \langle z_\mathrm{s}\rangle)}{D\,(\langle z_\mathrm{s}\rangle)} \equiv \left\langle \frac{D_\mathrm{ds}}{D_\mathrm{s}} \right\rangle = \int_0^\infty p(z) \frac{D_\mathrm{ds}(z_\mathrm{d}, z)}{D_\mathrm{s}(z)}\, \mathrm{d}z\, \mathrm{H}\,(z - z_\mathrm{d})\ . \tag{4.6}$$

Here, $D_\mathrm{ds}(z_\mathrm{d}, z)$ is the angular diameter distance between the lens and a galaxy at redshift z and $D_\mathrm{s}(z)$ is the angular diameter distance between the observer and this galaxy. The Heaviside step function indicates that sources with $z > z_\mathrm{d}$ are lensed. To reduce the contamination by foreground galaxies, we select faint (and preferentially background) galaxies with magnitude cuts. These cuts have been chosen at the F606W (F814W) magnitudes from Schrabback et al. (2007) (Schrabback et al. 2010), i_{606} (i_{814}), where the median (medium) redshift equals 0.4 for the intermediate redshift clusters and 0.6 for the high-redshift clusters, respectively. From Eq. (4.6) we determined the effective source redshift $\langle z_\mathrm{s}\rangle$ which is indicated by putting z_s in angular brackets on the left-hand side. Mean distance ratios $\langle D_\mathrm{ds}/D_\mathrm{s}\rangle$ and effective mean source redshifts $\langle z_\mathrm{s}\rangle$ are listed in Table 4.1. The redshift distributions normalised to $\int_0^\infty p(z)\mathrm{d}z = 1$ are plotted in Fig. 4.7.

Our magnitude cuts exclude bright galaxies disregarding whether they are foreground galaxies or not. Furthermore, small and faint cluster and foreground galaxies may possibly be interpreted as background galaxies by the pipeline. For these reasons, our HST-catalogues will not exclusively be composed of background galaxies.

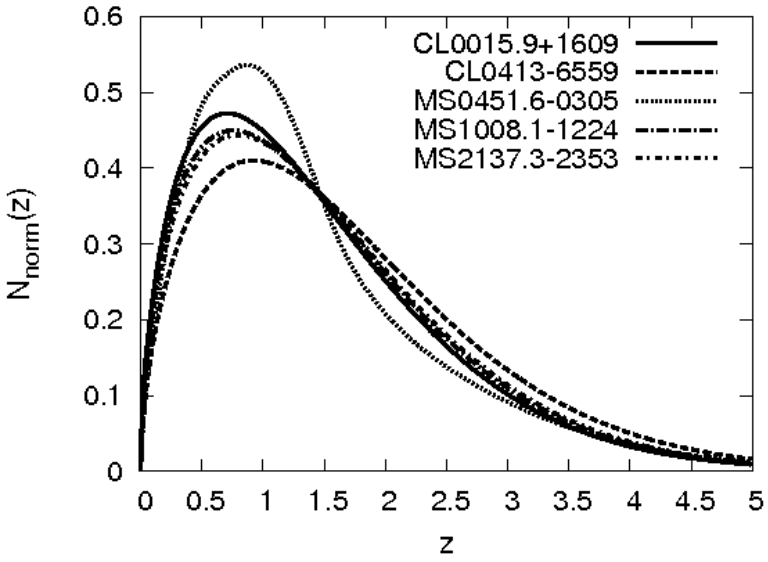

Figure 4.7: Estimated redshift distributions for the cluster sample normalised to $\int_0^\infty p(z)\mathrm{d}z = 1$. While the redshift distributions of the four clusters observed in F606W only differ with respect to their amplitude, the shape of the redshift distribution for MS0451.6−0305 differs notably.

For MS0451.6−0305, we create two catalogues which will be analysed in parallel. For both the magnitude selection has been applied: (1) In $\mathrm{MS0451_{ACS}}$ we used the effective mean source redshift $\langle z_s \rangle = 1.645$ as inferred from Eq. (4.6) for all sources. We used this catalogue to directly compare this cluster to the other clusters. (2) In $\mathrm{MS0451_{zphoto}}$ we included photometric redshifts for those galaxies to which we could assign them and calculate $\langle z_s \rangle$ for galaxies without photo-z. We used this catalogue to study the effect of using individual source redshifts compared to an effective mean source redshift for all sources. The photometric redshift estimation will be discussed in Sect. 4.3.3.

4.3 Multi-colour data

For MS0451.6−0305, multi-colour data from two ground-facilities were used to estimate the photometric redshifts of the HST-data, to remove foreground and background galaxies and to demonstrate the effect of using photometric redshifts in the weak lensing analysis compared to using a mean redshift for all sources. In particular, data from MegaPrime@CFHT and Suprime-Cam@SUBARU both seated on Mauna Kea, Hawaii at an altitude of 4200 metres above sea level (Fig. 4.8) were used for this study[3]. In this section both data sets will be briefly introduced. Table 4.2 gives a technical overview.

4.3.1 MegaPrime@CFHT

The Canadian-France-Hawaii Telescope (CFHT) is a 3.6m-telescope consisting of several optical and infrared instruments for wide-field imaging or spectroscopic purposes among others. MegaPrime is a wide-field optical imaging facility which was built by CEA[4] in France. Since

[3]The details of the telescopes and instruments are taken from http://www.cfht.hawaii.edu and http://www.www.naoj.org for CFHT and SUBARU, respectively.

[4]Consumer Electronics Association

Figure 4.8: The CFHT telescope (*upper panel*) and the SUBARU telescope (*lower panel*) both on top of Mauna Kea, Hawaii in 4200 m above sea level. From http://www.cfht.hawaii.edu and http://www.www.naoj.org .

its field-of-view is $1° \times 1°$, MegaPrime is able to observe a large number of faint objects simultaneously. It has a resolution of 0.187 arcsec/pixel which allows to sample properly the seeing at Mauna Kea which has a median value of $0\farcs7$. The instrument has a 9×4 CCD-array with 2048×4162 pixels/CCD. At the time when it was launched in January 2003, it was the largest astronomical CCD-mosaic ever built. Since then and for many years that followed, MegaPrime represented a major upgrade of the telescope upper-end.

In a period of 15 to 18 days centred on the New Moon, MegaPrime operates at a temperature of $-120°$C in five broad-band filters u^*, g′, r′, i′ and z′. Except for u^*, all filters were designed to match the SDSS-filters of the Apache Point telescope. Since the UV-extinction on Mauna Kea is smaller than on the Apache Point, the u^*-filter was designed in addition and is therefore denoted with an asterisk.

Gain and quantum efficiency vary among the CCDs with a dispersion of 0.2 e^-/ADU. The zero point magnitudes arise from photometric frames which were processed by the data reduction pipeline `Elixir` (Magnier & Cuillandre 2004) including corrections for scattered light on the order of 0.1 mag. Furthermore, the zero point magnitudes are normalised during flat-fielding such that the exposure is uniformly shaped, but this has the disadvantage that the detection limit varies over the CCDs due to differences in quantum efficiency and read-out noise. The transmission curves and the mean quantum CCD efficiency are shown in Fig. 4.9.

The data were calibrated and processed by Thomas Erben with the `GaBoDS/THELI` image processing pipeline (Erben et al. 2005). The quality of the images was thoroughly checked against the Sloan-Digital-Sky Survey (SDSS) and already public high-end CFHTLS data products. More details of the data reduction can be found in Erben et al. (2009).

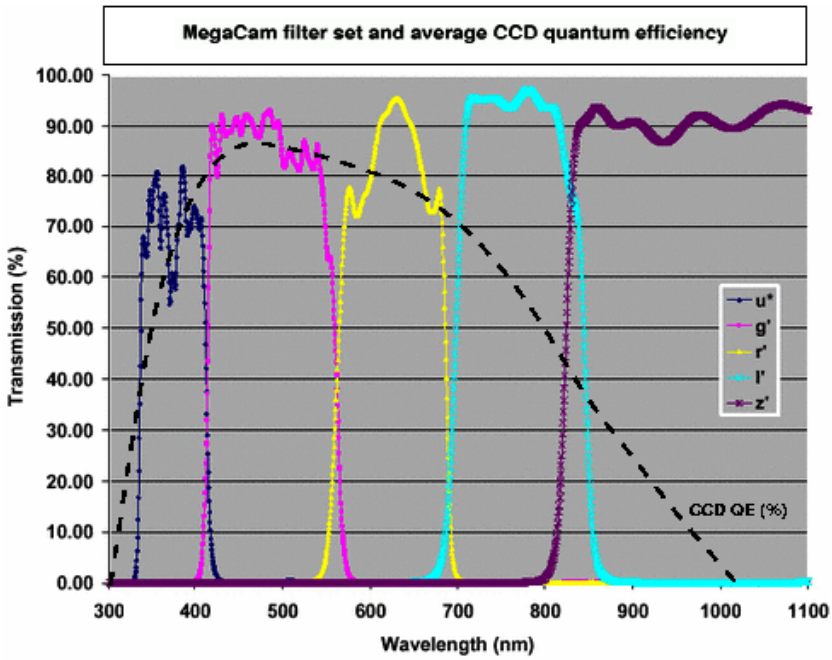

Figure 4.9: Transmission of the MegaCam-filters and the average CCD quantum efficiency [%] (*dashed line*). From http://www.cfht.hawaii.edu .

4.3.2 Suprime-Cam@SUBARU

Suprime-Cam is mounted on the 8.2m SUBARU telescope on Mauna Kea at an altitude of 4139 m near the CFHT. It is an optical instrument consisting of 5×2 CCDs that cover an area of $34' \times 27'$

comparable to the size of the full Moon. It has a resolution of 0.202 arcsec/pixel. The large pixel size of the instrument and light gathering power of the primary mirror produce high count rates per pixel. Since even at high Galactic latitudes a number of bright stars is always present in the large field-of-view, a saturation of pixels is inevitable.

SUBARU is the only 8m-class telescope in the world on which an instrument can be mounted at the prime focus. This allows to perform deep imaging of a large area of the sky because the shorter focal length of the prime focus provides a field-of-view which is five times wider than the Cassegrain focus. Apart from the wide-field imaging of galaxy clusters, the instrument is an effective tool to detect small objects at the outskirts of the solar system, study the birth and evolution of galaxies, and probe large-scale structures of our Universe.

Observations of MS0451.6−0305 were carried out in the broad-band filters B, V, R_c, I_c and z′. The data reduction was done by Mischa Schirmer using the `GaBoDS/THELI` image processing pipeline (Erben et al. 2005), but with some deviations which are given by Schirmer et al. (2010) in more detail. Here, we only list the most important: When the observation was performed in 2001, Suprime-Cam had one broken CCD and individual gain settings. Lateron, the broken CCD and three others were replaced and the gains were homogenised. For our data, all chips had to be adjusted to the same gain. Area lost due to blooming could be recovered because the images were taken with two different sky position angles. Without extensive dithering of photometric standard fields, a correction of scattered light in the flat-field images was not possible for this data. Furthermore, only parts of the data were taken in photometric conditions with relative zeropoint variations up to 0.1 mag. Fig. 4.10 shows the SUBARU I-band image overlaid with the HST mosaic pattern.

Table 4.2: The multi-colour data used to estimate the photometric redshifts of MS0451.6−0305: We show observational properties such as limiting magnitude $M_{\rm lim}$ derived from apertures of 3″, seeing and the total exposure time (Exptime) as well as the central wavelength λ of each passband. $M_{\rm lim}$ are the limiting AB magnitudes (50% completeness level) for 10σ point sources and are ∼ 0.8 mag brighter for extended objects. For more details, see Schirmer et al. (2010).

Filter	Instrument	Exptime [s]	seeing	$M_{\rm lim}$	λ [nm]
u*	MegaPrime	5215	0.″87	25.7	374
g′	MegaPrime	3400	0.″85	26.0	487
r′	MegaPrime	14852	0.″71	26.2	625
i′	MegaPrime	1280	0.″71	23.7	770
z′	MegaPrime	1440	0.″70	22.4	882
WJB (B)	Suprime-Cam	12240	0.″82	26.7	446
WJV (V)	Suprime-Cam	5040	0.″94	26.0	548
WCRC (R_c)	Suprime-Cam	11400	0.″84	26.6	653
WCIC (I_c)	Suprime-Cam	4920	0.″92	25.9	795
WCZ (z′)	Suprime-Cam	4380	0.″76	25.1	904

4.3.3 Photometric redshifts

The photometric redshifts for MS0451.6−0305 were determined with the public code `Bayesian Photometric Redshifts` (`BPZ`, Benítez 2000). The code is based on an SED-template fitting with a prior, which carries information about the spectral energy distributions of six types of galaxies in redshift. Thus, `BPZ` estimates the most likely redshift of a galaxy using the magnitudes measured in a set of passbands according to the prior information.

Comparing to the analysis using externally calibrated redshift distributions (Sect. 4.2.3), the one using individual redshift estimates has two advantages in deriving weak lensing masses: First, it enables the selection of individual background galaxies, whose shear estimates can be weighted according to their geometric lensing efficiencies to boost the signal-to-noise (Sect. 2.3.2). Second,

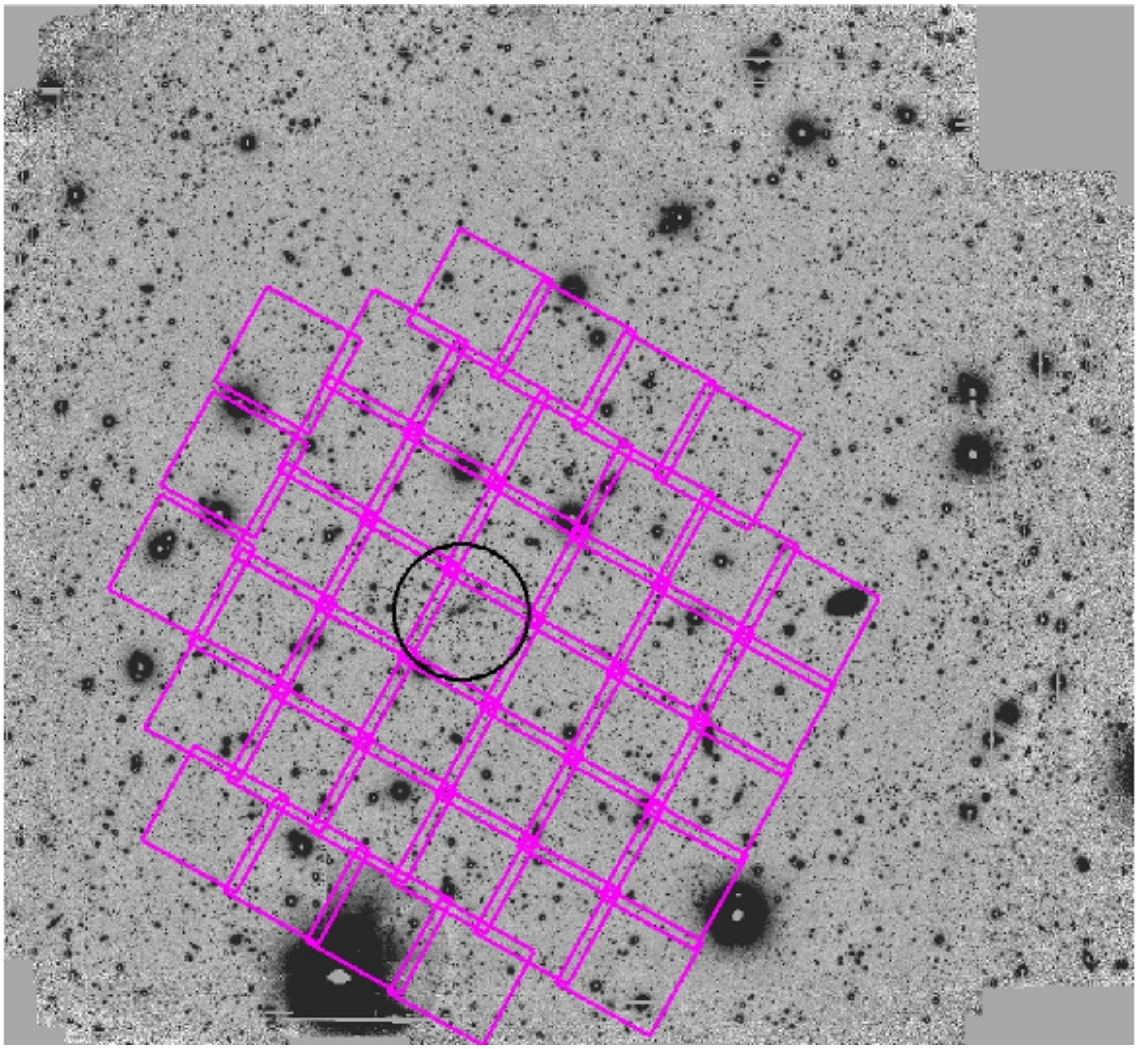

Figure 4.10: Optical image of MS0451.6−0305 in the I-filter of Suprime-Cam (WCIC) overlaid with the contours of the HST-mosaic (solid magenta lines) to demonstrate the coverage of both data sets. The black circle indicates the central cluster region inside which the diagonal bar of galaxies can be identified with the cluster centre. The field-of-view is $\approx 39' \times 34'$.

it allows for a robust removal of foreground and cluster galaxies which have otherwise to be excluded by a magnitude cut, but this is less accurate since it may also remove luminous background galaxies and keep faint foreground galaxies. If there is contamination from foreground galaxies, the shear signal is diluted and those galaxies can be removed statistically. Imaging data of similar depth using this filter set yield excellent photometric redshifts for bright galaxies with $z \lesssim 1.3$ (Hildebrandt et al. 2012).

We used the photo-z catalogue from by Schirmer et al. (2010) based on the methods from Hildebrandt et al. (2009, 2012) in which photometric redshifts were selected according to:

- if $z_{\mathrm{photo}} < 0.4$, only CFHT-redshifts,
- if $z_{\mathrm{photo}} > 0.7$, only SUBARU-redshifts,
- if $0.4 < z_{\mathrm{photo}} < 0.7$, the average of CFHT- and SUBARU-redshifts weighted by the estimation confidence (ODDS-parameter in BPZ),
- z_{photo} from CFHT or SUBARU, whichever has the higher ODDS,
- all photometric redshifts are limited to those with more than 80% confidence (ODDS ≥ 0.8).

Schirmer et al. (2010) found that these criteria well serve the multi-colour data of MS0451.6 −0305 because: (1) The PSFs in the CFHT- and the SUBARU-data give varying fluxes for a galaxy observed in similar passbands, e.g. r′ and R_c. (2) The CFHT-data are shallower than the SUBARU-data. They show 2-3 times as much scatter for $z \gtrsim 0.6$ as SUBARU and fail for fainter galaxies, because of marginal depth in the i′- and z′-band, but provide better constraints for galaxies at lower redshifts. In contrast, the SUBARU-data yield more accurate redshifts for distant galaxies, but are highly unreliable for $z \lesssim 0.3$ due to the lack of u-band data. Without the u-band, BPZ assigns a significant fraction of lensed galaxies to the foreground. (3) The SUBARU-data show scattered light in the flat-field images and thus the photometric zero-point is not continuous over the image with a variation of 0.1 mag. Schirmer et al. (2010) left this effect uncorrected, because it was not possible to model it. For details see Schirmer et al. (2010).

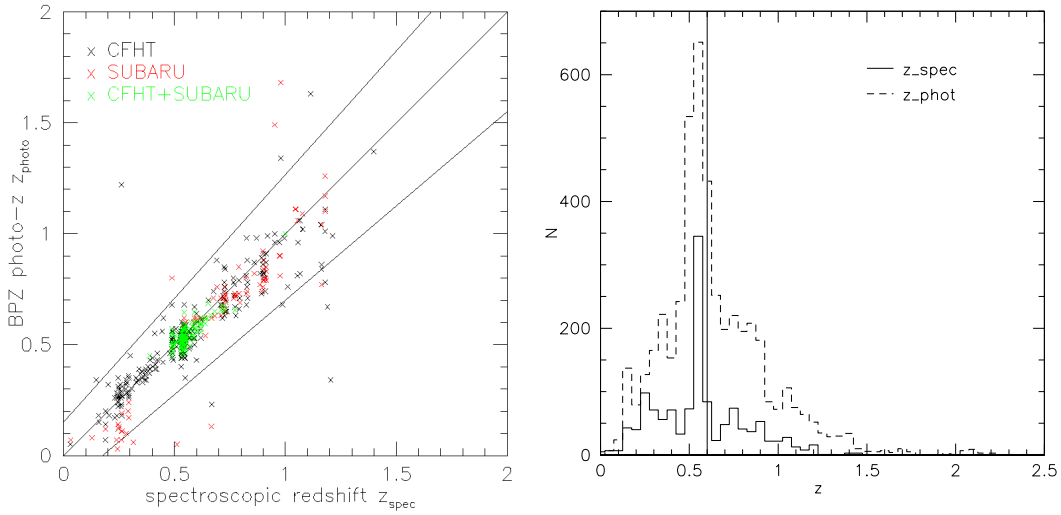

Figure 4.11: *Left panel:* Photometric redshifts of MS0451.6−0305 plotted versus the spectroscopic redshifts from DEIMOS@Keck-II from Moran et al. (2007). *Right panel:* Histogram of the estimated photometric redshifts *(dashed)* and of the spectroscopic redshifts *(solid)* in bins of dz = 0.05. The vertical line at $z = 0.6$ distinguishes between foreground and background galaxies.

The photometric redshifts were calibrated against 1561 spectroscopic redshifts taken with DEIMOS@Keck-II (Fig. 4.11, *left*). These spectroscopic redshifts were originally used in a wide-field survey by Moran et al. (2007).

We defined outliers with a cut of

$$\Delta z = \left| \frac{z_{\rm photo} - z_{\rm spec}}{1 + z_{\rm spec}} \right| > 0.15 \tag{4.7}$$

and the outlier rate η is the fraction of galaxies with $\Delta z > 0.15$. The standard deviation of Eq. (4.7), σ_z, is a mean error of the estimated photometric redshifts. Applying ODDS ≥ 0.8 and $\Delta z < 0.15$ gave $\sigma_z = 0.035$ and $\eta = 1.57\%$.

The histograms of photometric and spectroscopic redshifts are plotted in the right panel of Fig. 4.11. The number of spectroscopic redshifts is smaller than the number of available photo-*z*, because the spectroscopic redshifts are limited to $i < 23.0$. We used the spectroscopic redshifts to calibrate the zero-points and templates in the photo-*z* estimations (Schirmer et al. 2010). The consistency between spectroscopic and photometric redshifts suggests reliable photo-*z* estimates for the nearby and bright galaxies ($z \leq 1.2$) with less than $\sigma_z = 0.035$ scatter. We used the photometric redshifts for distant galaxies ($1.2 \leq z \leq 2.2$) only if we could estimate them with more than 80% confidence.

We defined background galaxies as those with $z_{\rm photo} \geq 0.6$. This cut is more conservative than the redshift of MS0451.6−0305, $z_{\rm d} = 0.55$, plus the scatter, $\sigma_z = 0.035$, because σ_z arises from the comparison of photo-*z*s with the spectroscopic redshifts for bright galaxies ($i < 23.0$).

The HST-data is deeper than the ground-data. Only $\sim 5\%$ of the sheared sources located at the bright end of the HST-magnitude distribution have photometric redshifts, after applying the magnitude cut at $z = 0.6$. Figure 4.12 shows histograms of the HST-magnitudes measured in F814W i_{814} of all sheared sources (*left*) and of those 5% of sources which have also photometric redshifts (*right*). The distribution of the latter has its peak at $i_{814} = 28$ which is two magnitudes brighter than the magnitude distribution of all HST-sources. For the remaining galaxies we assigned an effective mean source redshift (Sect. 4.2.3) and their treatment will be further discussed in Sect. 6.2.3.

For a larger coverage of photometric redshifts for the data, deeper observations would be required.

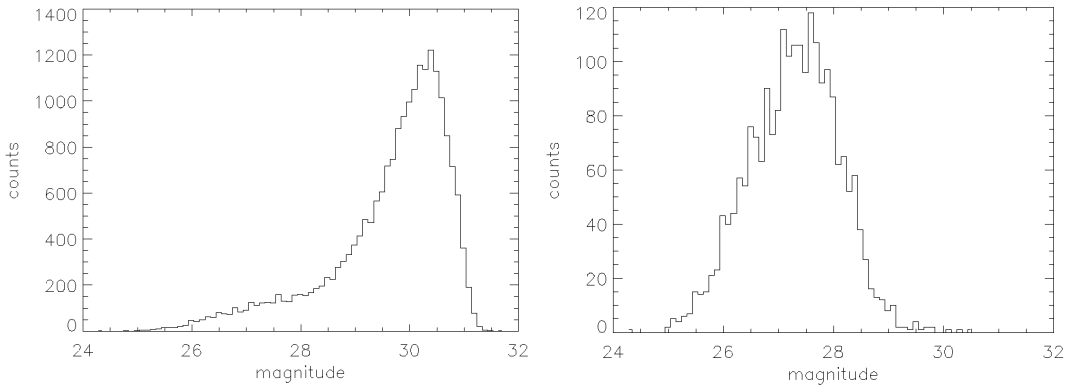

Figure 4.12: *Left panel:* HST magnitude distribution of all our lensed background sources. *Right panel:* HST magnitude distribution those 5% sources which have photometric redshifts. In both histograms, "magnitude" is the magnitude measured in the F814W-filter i_{814}.

4.4 X-ray data

4.4.1 XMM-Newton

The X-ray Multi-Mirror Mission (*XMM-Newton*) from ESA was launched by an Ariane 504 on December 10th 1999. The satellite carries three high-throughput X-ray telescopes with the largest effective area up to date. *XMM-Newton* can take imaging spectroscopy and grating spectroscopy simultaneously.

The European Photon Imaging Camera (EPIC) was designed to perform extremely sensitive observations over a whole field of view of $\sim 30'$ in diameter in the energy range $0.15 - 15\,\mathrm{keV}$. EPIC has a spectral resolution of $E/\Delta E \sim 20-50$ and an angular resolution which is of the size of the Point Spread Function ($30''$) with a full width at half maximum of $6''$. EPIC consists of three X-ray CCD cameras. Two of these cameras are Metal Oxide Semi-conductor CCD-arrays (MOS1 and MOS2). Since they are installed behind the X-ray telescopes such that the light has to pass the gratings of the Reflection Grating Spectrometers (RGS) first, only 50% of the incident flux reaches the MOS cameras[5]. Each MOS camera consists of seven front-illuminated CCDs, which are mounted in the focal plane of the cameras. The central CCD is at the focal point on the optical axis of the telescope while the outer six are stepped towards the mirror by 4.5 mm to follow approximately the focal plane curvature, which improves the focus for off-axis sources. The physical imaging area of one CCD is $\sim 2.5 \times 2.5\,\mathrm{cm}^2$ which corresponds to a $28.4'$ coverage of the total focal plane. The readout register is split into two sections with readout nodes, such that the full CCD image can be read out using either one readout node or both nodes simultaneously, which halves the readout time. The quantum efficiency of the MOS-cameras is reasonably good from $0.2 - 10\,\mathrm{keV}$ (Fig. 4.13) for observations. Below 700 eV, the energy response is low, because of absorption in the electrode structure. To provide a detector region with a high transmission for very soft X-rays that would otherwise be absorbed by the electrodes, one of the three electrodes has been enlarged to occupy a greater fraction of each pixel, and holes have been etched through this enlarged electrode to the gate oxide.

The third EPIC instrument is composed of twelve $3 \times 1\,\mathrm{cm}$ pn-CCDs (pn) with a physical area of $6 \times 6\,\mathrm{cm}^2$ which cover $\sim 97\%$ of the field-of-view on a single wafer and has an undisturbed beam. The CCDs are arranged for reasons of redundancy in four quadrants. The three pn-CCDs in each quadrant can be operated in parallel. Since $6\,\mathrm{cm}^2$ of the sensitive area are outside the FOV, they are used for background studies. X-rays hit the detector from the rear side and interact with the silicon atoms such that the generated electron and hole numbers are proportional to the energy of the incident photon. The average energy required to create an electron-hole pair is 3.7 eV at $-90°\mathrm{C}$. To provide a recombination of electrons and holes, pn consists of strong electric fields that draw charges to the electrodes. Due to its larger effective area, the number of counts in pn is two times larger than for one of the MOS detectors for the same exposure time.

All EPIC CCDs operate in photon counting mode with a fixed, mode-dependent frame read-out frequency. The data is read-out into event lists, which are tables with one entry-line per received event that lists their energy, time and position at which they were registered.[6]

4.4.2 Data reduction

The galaxy clusters CL0015.9+1609, MS0451.6−0305 and MS2137.3−2353 were observed with *XMM-Newton*. We used *Chandra*-data for MS1008.1−1224 because no *XMM-Newton* data was available. This data was reduced by Helen Eckmiller and I therefore refer to Eckmiller et al. (2011)

[5] After taking structural obscuration into account, actually only $\sim 40\%$ of the incident flux reaches the MOS cameras.
[6] The details of *XMM-Newton* and the instruments are taken from http://xmm.esac.esa.int .

Table 4.3: Overwiev of the archival X-ray data we used for the analysis of our cluster sample. We list the instrument with which the data was taken, exposure times, observational ID, who was Principal Investigator PI and the date at which the clusters were observed.

Cluster	Instrument	Exptime [s]	OBSID	PI	obs. date
CL0015.9+1609	*XMM-Newton*	28372	0111000101	M. Watson	2000 – 12 – 29
CL0413−6559					
MS0451.6−0305	*XMM-Newton*	22253	0205670101	D. Worrall	2004 – 09 – 16
MS1008.1−1224	*Chandra*	44740	926	E. Ellingson	2000 – 06 – 11
MS2137.3−2353	*XMM-Newton*	11311	0008830101	S. Allen	2001 – 04 – 29

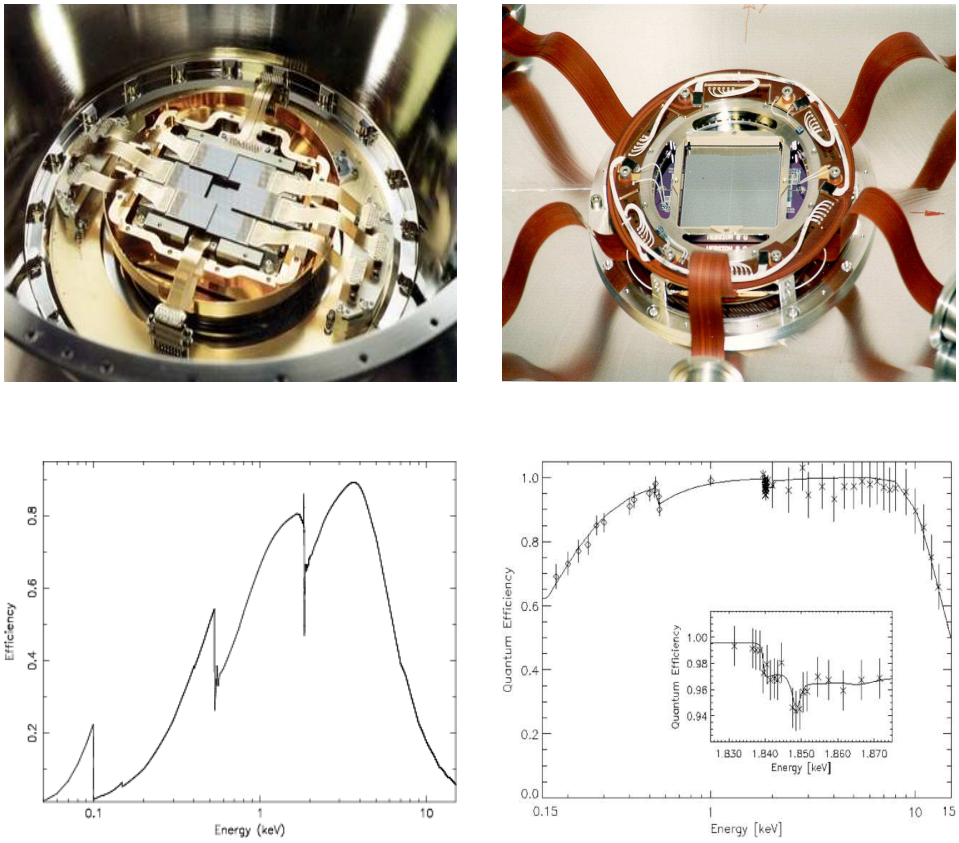

Figure 4.13: *Upper left:* One of the MOS cameras inside the cryostat. The camera consists of seven CCDs covering a field of view of ∼ 30′ in diameter in the energy range 0.15 – 15 keV. From http://xmm.esac.esa.int . *Lower left:* The quantum efficiency of MOS. From Turner et al. (2001). *Upper right:* The pn camera consisting of twelve CCDs. Since its effective area is larger than that of MOS, the number of counts in pn is ∼ 2 times larger than for one of the MOS detectors for the same exposure time. From http://xmm.esac.esa.int . *Lower right:* The quantum efficiency of pn. From Strüder et al. (2001).

for details of the reduction. For CL0413−6559 currently no archival X-ray data are available, except for a 20 ks *ROSAT* PSPC-observation with ∼ 70 source counts which are not sufficient for our purpose. Details of the data are summarised in Table 4.3.

The observations were carried out with the European Photon Imaging Camera (EPIC) in full frame (FF) mode for MOS and extended full frame (EFF) for pn. This gives a fraction of 2.32% of out-of-time (OOT) events for pn. For all three detectors, the thin filter was used. We performed the data reduction using the *XMM-Newton* `Science Analysis System (SAS 8.0.0)`. We used $FLAG = 0$ and $PATTERN < 12$ for MOS and $PATTERN < 4$ for pn, because larger thickness of pixels leads to higher sensitivity to the particle flux.

The data reduction of this work follows that of CL0024+17 (Zhang et al. 2005). For pn we created an OOT event file to statistically remove the OOT effect. Since the effective area is low at photon energies above 10 keV and 12 keV for MOS and pn respectively, the particle background dominates at that energies. Therefore, we used these high energy bands to excise periods with high flux from high energy protons as follows. We binned the light curve in the $10 - 12$ keV ($12 - 14$ keV) energy range for MOS (pn) with a 100 s interval. Since there are also protons at lower energies, we further used the $0.3 - 10$ keV energy range to exclude such soft proton flares (e.g. De Luca & Molendi 2004). Here, we binned the light curve with a 10 s interval to provide a similarly photon statistic as that of the hard band ($10 - 12$ keV for MOS and $12 - 14$ keV for pn, respectively).

From each light curve, we determined the average and variance σ by fitting a gaussian to the count rate histogram. We defined Good Time Intervals (GTIs) as those intervals, where the count rate is below 3.3σ above the quiet average and then created GTI events files. We used those GTI files to clean the data from proton flares both in the hard and the soft band, respectively.

The vignetting correction to effective area for off-axis observations and the bad-pixel correction were performed with the `SAS`-command “eviweight”.

Chapter 5

Simulations for MS0451.6−0305

To estimate the quality of scientific results, simulations can be used. Since MS0451.6−0305 is special in this thesis due to its photometric redshifts, issues that are not of interest for the other clusters have to be considered. In this chapter, two simulations will be performed to estimate the gain of using photometric redshifts in a weak lensing analysis. In Sect. 5.1, the accuracy with which photometric redshifts can be obtained from the multi-colour data (Table 4.2) will be estimated. This simulation will serve as an independent cross-check of calibrating the photometric redshifts against the spectroscopic redshifts from DEIMOS@Keck-II (Moran et al. 2007, Sect. 4.3.3). In Sect. 5.2, we will simulate the effect 5% photometric redshifts have on the errors on the parameters of our mass models which will be introduced in Sect. 6.2.

5.1 Simulations for photometric redshifts

To cross-check the photometric redshifts estimated with `BPZ` (Sect. 4.3.3), simulations with `Stuff 1.19` – throughout this paper denoted as `STUFF` – and `SkyMaker` both developed by E. Bertin were performed and are discussed in this section. `STUFF` generates galaxy catalogues with a realistic galaxy population in redshift, without errors in magnitude and redshift, and `SkyMaker` produces the corresponding fits-images from which magnitudes and their errors can be measured. The simulations were done for both idealised data, for which the magnitudes are measured without errors, and mock data generated with the properties of our multi-colour data (Tab. 4.2).

5.1.1 Photometric redshifts for idealised conditions

Under idealised conditions the photometric redshifts that are estimated from the `STUFF`-simulation are expected to be very accurate, i.e. $z_{\mathrm{photo}} \approx z_{\mathrm{stuff}}$. To estimate photometric redshifts from generated data without magnitude errors cross-checks whether the spectral templates for galaxy types, filter curves and extinction in `STUFF` and `BPZ` are equal. This test further allows us to study the effect that filters of the CFHT- and SUBARU-data have on the photometric redshift estimation. We combined the filter sets of both instruments before `BPZ` is run, because we do not have to account for varying fluxes due to different PSFs or scattered light in the flat-field images as we have for the real data (Schirmer et al. 2010).

We created catalogues for the CFHT- and SUBARU-filters for a field of 2048×2048 pixel using `STUFF` and fed both into `BPZ` separately. In addition, a third catalogue comprising all ten filters was generated from which the photometric redshifts were estimated. The same spectral templates, filter curves and extinction coefficients were used for both `STUFF` and `BPZ`. An illustration of the spectral templates of the galaxy types used in `BPZ` is shown Fig. 5.2.

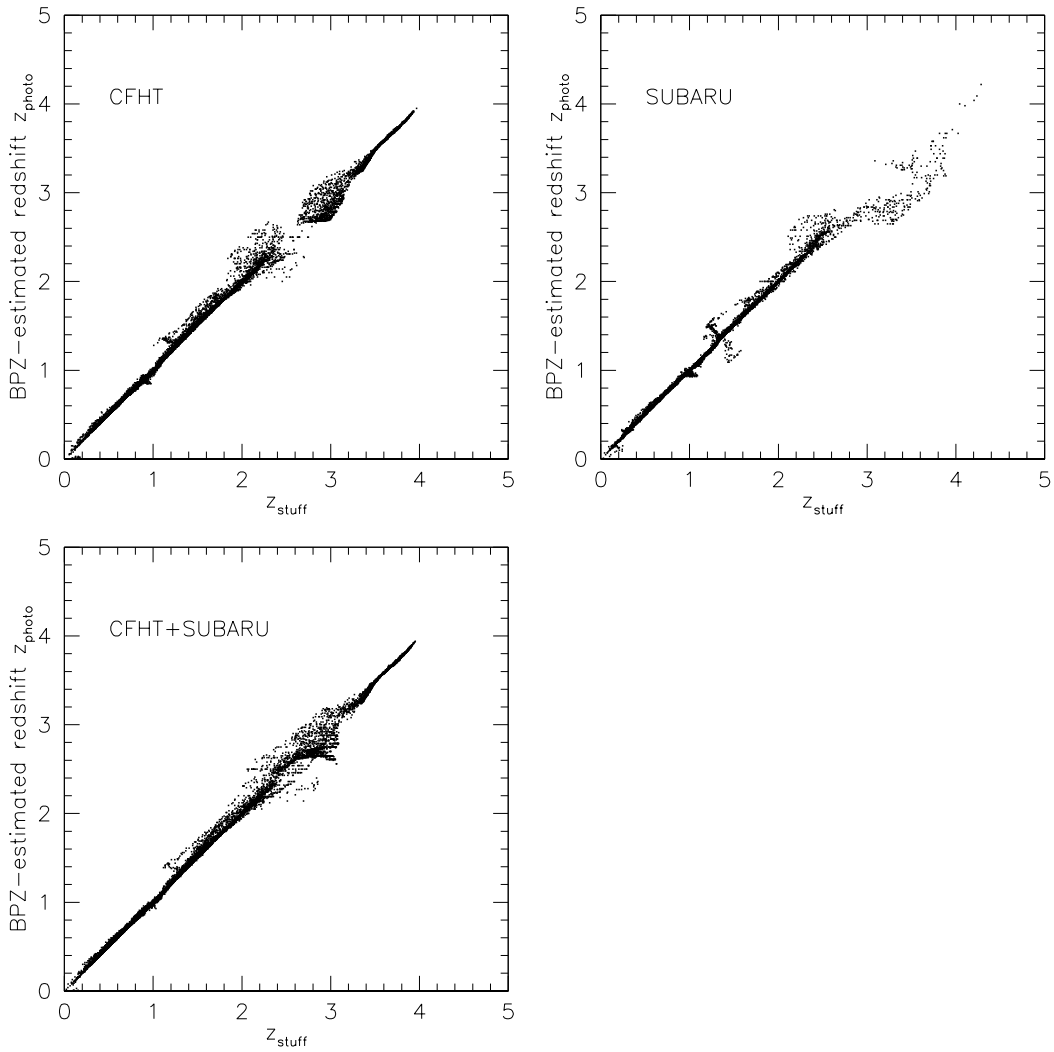

Figure 5.1: Photometric redshifts z_{photo} versus STUFF-redshifts z_{stuff} for different filter combinations and ODDS ≥ 0.8. We show the results for the CFHT-filters u*, g′, r′, i′and z′(*upper left panel*), the SUBARU-filters B, V, R, I, Z (*upper right panel*) and for both filter sets (*lower panel*). The UV-filter improves the agreement between z_{photo} and z_{stuff}.

According to Sect. 4.3.3, only photometric redshifts with more than 80% estimation confidence (ODDS ≥ 0.8) were used for the further analysis. We did not calculate outlier fraction η and scatter σ_z for this simulation because this simulation only qualitatively checks the combination of the CFHT- and SUBARU-filters.

The results of these simulations are plotted in Fig. 5.1. This figure shows that we have $z_{photo} \approx z_{stuff}$ at $0 \lesssim z_{stuff} \lesssim 2$ for the CFHT data and at $0.2 \lesssim z_{stuff} \lesssim 1.4$ for the SUBARU data, respectively. The redshift range for which $z_{photo} \approx z_{stuff}$ is smaller for the SUBARU filters because it has no UV-filter. Without this filter, elliptical galaxies at low redshifts will be assigned to higher redshifts because the 4000 Å-break of elliptical galaxies at low redshifts would be misinterpreted as Lyα-break of spiral galaxies at high redshifts.

Since there is no useful IR-data available, $z_{photo} \not\approx z_{stuff}$ at $2 \lesssim z_{stuff} \lesssim 3.5$ because the 4000 Å-break moves from the optical into the IR. Combining both filter-sets provides a smooth distribution of redshifts from $0 \lesssim z_{stuff} \lesssim 2.2$, which corresponds to the redshift range of the multi-colour data for MS0451.6−0305. Thus, we can ignore the broad scatter at $z \gtrsim 2.2$ due to the lack of the IR-filter.

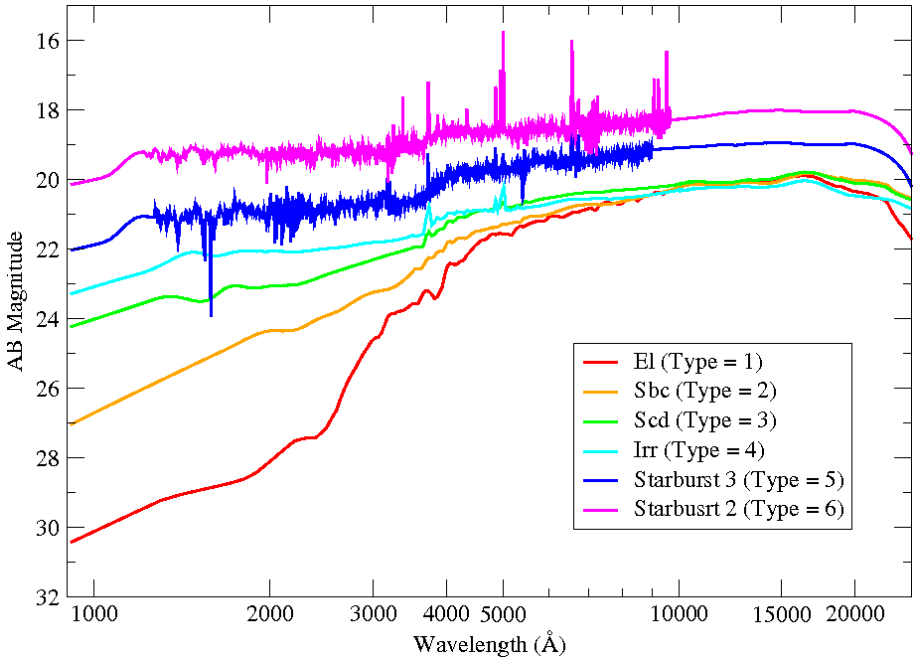

Figure 5.2: Templates for different spectral galaxy types in the local Universe that are used in BPZ. Early-type galaxies are faint at short wavelengths, since they consist of old stellar populations and a small gas content. In contrast, starburst galaxies have a dense sequence of strong emission and absorption lines in their spectrum because of their high gas content, and a large amount of young and massive stars (Mobasher et al. 2007).

This simulation qualitatively shows that the given set of CFHT and SUBARU filters can produce accurate redshifts within the range $0 \lesssim z_{\rm stuff} \lesssim 2.2$ which is the redshift range for which we have photometric redshifts for MS0451.6−0305. In the next simulation, we will investigate how accurate the photometric redshifts are with respect to the properties of the multi-colour data which are given in Table 4.2.

5.1.2 Photometric redshifts for realistic conditions

In this simulation, mock data with the properties of the multi-colour data such as exposure time, seeing, limiting magnitudes etc. (Table 4.2) were generated from a STUFF-catalogue comprising all ten filters using SkyMaker. To make the images comparable and to account for seeing that affects the magnitudes, the images in all bands were corrected with respect to the image from the V-band which has the worst seeing as follows. Seeing changes the brightness distribution of an object and it is assumed to be Gaussian with width σ. For worse seeing, the width is larger. If the seeing has the width σ_1 for the observation with smaller seeing and σ_2 for the observation with the worse seeing, i.e. $\sigma_2 > \sigma_1$, the convolution of both Gaussians gives $\sigma_3 = \sqrt{\sigma_1^2 + \sigma_2^2}$ which is then the seeing to which we correct our images.

The source magnitudes were determined in SExtractor (Bertin & Arnouts 1996) with respect to the r′-band. This filter is a good compromise between the drop-out of objects in filters operating at shorter wavelengths and a high sky background at longer wavelenghts which prohibits the detection of faint objects. We defined objects as neighbouring pixels with DETECT_MINAREA $\geq$ 3 and DETECT_THRESH $\geq$ 2. To account for individual objects shapes, we extracted the isophotal magnitudes MAG_ISO which were determined by SExtractor and fed them into BPZ. The parameter MAG_ISO defines objects as a set of pixels with isophotal magnitudes which fulfil DETECT_MINAREA and DETECT_THRESH. Alternative magnitude definitions are the aper-

Table 5.1: Outlier fraction η and scatter σ_z for ODDS $\geq$ 0.8 and $\Delta z < 0.15$ for CFHT, SUBARU, CS and their combination, CS_{select} according to the criteria for the real data (Sect. 4.3.3).

		CFHT	SUBARU	CS	CS_{select}
all	η	4.92	3.16	2.99	3.42
	σ	0.0438	0.0374	0.0363	0.0376
$z \leq 0.6$	η	2.46	1.93	1.76	2.10
	σ	0.0390	0.0319	0.0320	0.0372
$z \geq 0.6$	η	1.76	0.53	0.53	0.57
	σ	0.0480	0.0395	0.0391	0.0386

ture magnitudes MAG_APER which defines objects fulfilling the criteria DETECT_MINAREA and DETECT_THRESH within fixed apertures and MAG_AUTO which uses flexible elliptical apertures.

Similar to Sect. 5.1.1, we run BPZ over the CFHT- and SUBARU-filters separately and over both filter sets together. To these samples, we refer as CFHT, SUBARU and CS, henceforth. In addition, the photometric redshifts of CFHT and SUBARU that were estimated separately were combined according to the criteria in Sect. 4.3.3. We refer to this sample as CS_{select}, henceforth. We do not expect a significant difference between CS and CS_{select} because compared to the multi-colour data the simulations are free of the problems discussed in Sect. 4.3.2 and Schirmer et al. (2010). For this reason we used CS_{select} to cross-check systematics in the selection of photometric redshifts for the real data. The results are plotted in Fig. 5.3 for $\Delta z < 0.15$ and ODDS $\geq$ 0.8 and listed in Table 5.1. Figure 5.4 shows the histograms of the photometric redshifts for CFHT, SUBARU and CS. The redshift distributions for those three cases show only marginal difference.

We qualitatively analysed the simulated objects with respect to galaxy type, magnitude and z_{stuff} for $\Delta z < 0.15$ and ODDS $\geq$ 0.8 whereby we discriminated between foreground and background galaxies by $z \leq 0.6$ and $z \geq 0.6$, respectively. This redshift cut conforms to the magnitude cut for MS0451.6−0305 (Sect. 4.2.3). We have $\sim$ 3% fewer outliers and 4 – 20% higher scatter for background than for foreground objects. With the available filters, $\sim$ 68% of all outliers are late-type galaxies such as spirals and starburst galaxies because compared to elliptical galaxies they do not have a well-defined colour-magnitude sequence which is very pronounced for elliptical galaxies due to their old stellar population. In late-type galaxies, in contrast, there is still star formation which causes more absorption and emission features in their spectra (Fig. 5.2). Yet, spiral galaxies have a smaller spread in z_{photo} than elliptical galaxies, because their Lyα-line is more significant than the 4000Å-break of the elliptical galaxies.

We list outlier fraction and scatter for the photometric redshifts estimated from CFHT, SUBARU, CS and CS_{select} in Table 5.1 and plot z_{photo} versus z_{stuff} in Fig. 5.3. Due to its higher depth compared to the CFHT data, the SUBARU data provide $\sim$ 2% fewer outliers and $\sim$ 15% less scatter. Photometric redshifts for CS and CS_{select} produces 3 – 17% less scatter and 0.17 – 1.93% outliers $0 \lesssim z_{spec} \lesssim 2.5$ (Table 5.1) compared to using only either the CFHT or the SUBARU filters. CS has 0.43% fewer outliers and 3% less scatter than CS_{select}. Thus, our simulation confirms that the CFHT and SUBARU data are better for foreground and background objects, respectively.

From the simulation, we expect 2% and 1% outliers in the foreground and background galaxy population, respectively, with a scatter of $\sigma_z \approx 0.037$ and $\sigma_z \approx 0.039$ for each.

5.1.3 Comparison with the multi-colour data

We compared the simulations with the multi-colour data, in which the estimated photometric redshifts were calibrated against 1561 spectroscopic redshifts from DEIMOS@Keck-II (Moran et al. 2007). With ODDS > 0.8 and $\Delta z < 0.15$ we obtained $\sigma_z = 0.035$ and $\eta = 1.57\%$ (Sect. 4.3.3).

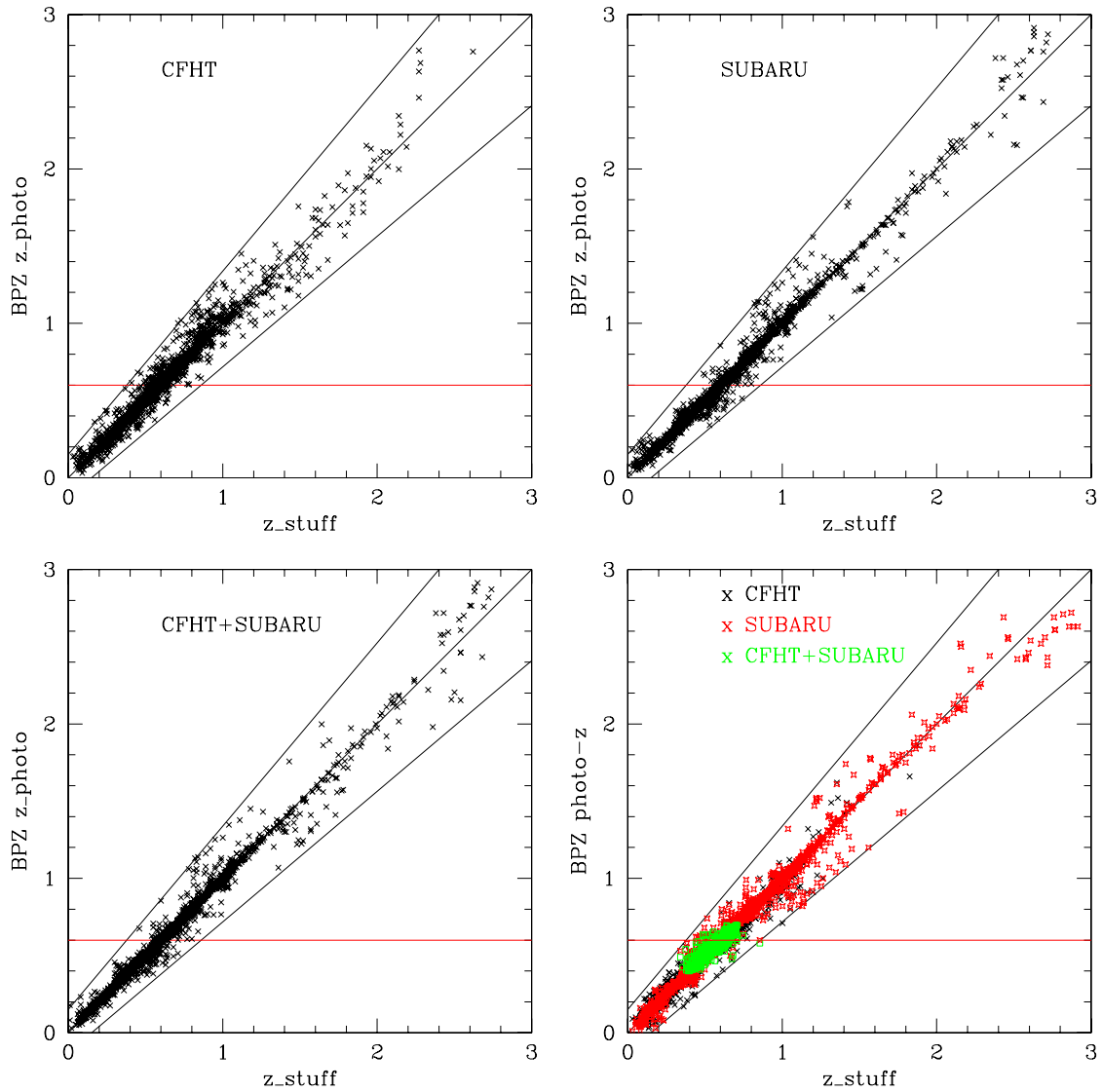

Figure 5.3: Photometric redshifts z_{photo} estimated with BPZ versus STUFF-redshifts z_{stuff} for ODDS ≥ 0.8 and $\Delta z < 0.15$. We show the results for the CFHT-filters (*upper left*), the SUBARU-filters (*upper right*), CS (*lower left*) and $\mathrm{CS}_{\mathrm{select}}$ (*lower right*). The black, red and green data points for $\mathrm{CS}_{\mathrm{select}}$ denote photometric redshifts from CFHT, SUBARU and CS due to the selection criteria in Sect. 4.3.3 according to which CFHT-galaxies and SUBARU-galaxies are also at $z_{\mathrm{photo}} > 0.4$ and $z_{\mathrm{photo}} < 0.7$ depending on their ODDS.

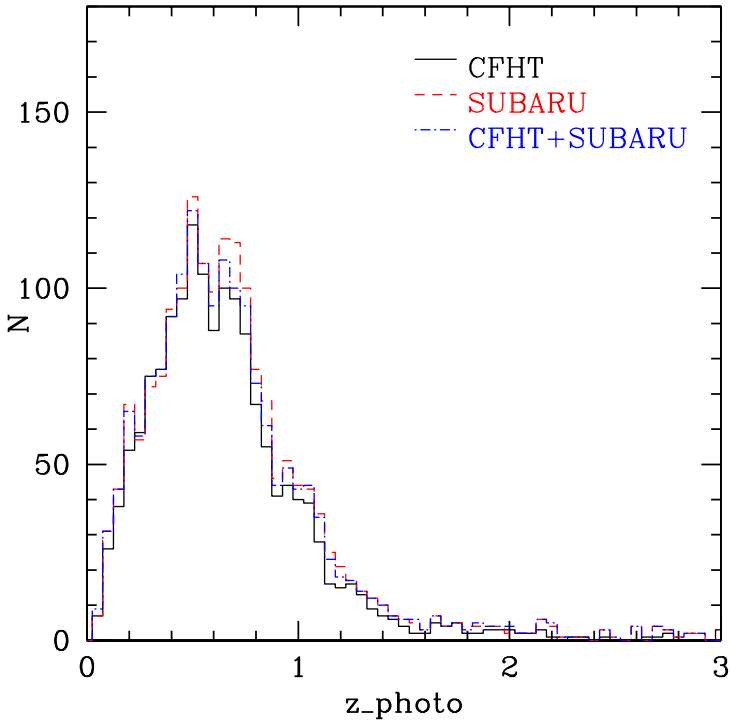

Figure 5.4: Histogram of photometric redshifts from the simulations. The solid black, dashed red and dashed-dotted blue lines show the $z_{\rm photo}$-distribution for CFHT, SUBARU and CS, respectively.

The outlier fractions for foreground and background galaxies are both $\sim 1.60\%$. For the real data η is $\sim 0.5\%$ lower for the foreground galaxies and $\sim 1\%$ higher for background galaxies than in the simulation. Most outliers of the real data are assigned to $z_{\rm photo} \lesssim 1.6$. Compared to the simulation, there are only few objects in $0 \lesssim z \lesssim 0.2$. At the redshift of the cluster, there is further a cumulation of objects in the real data.

We find η and σ_z consistent with the simulations. The scatter is only 6% and 10% higher for foreground and background galaxies, respectively and η is only $\sim 0.6\%$ lower for the foreground and $\sim 0.4\%$ higher for the background. Thus, our simulations predict quite precisely the outlier fraction and scatter of the photometric redshifts which were estimated for MS0451.6−0305.

5.2 Simulations for Weak Lensing

To estimate how individual source redshifts affect a weak lensing analysis, we generated a shear field with the properties of MS0451.6−0305. We conducted a χ^2-minimisation and determined the 1σ-errors of the fit parameters (Sect. 6.2.2) with respect to both an effective mean source redshift and the inclusion of 5% of photometric redshifts.

5.2.1 Shear field generation

We created a shear field of $22' \times 22'$ with a random galaxy distribution and a number density of $n = 82$ galaxies/arcmin^2 (Table 4.1). The galaxies have random intrinsic ellipticities $\chi^{(2)}$ drawn from a Gaussian distribution centred at zero and an intrinsic ellipticity dispersion of $\sigma_\epsilon = 0.3$. We used Eq. (2.17) to define the complex ellipticities, because this definition accounts for strong lensing effects. We sheared the galaxies with an NFW-lens (Sect. 6.2.1) at $z_{\rm d} = 0.55$ with $r_{200} =$

2239 kpc and $c_{200} = 3.5$ from the best fit NFW-model for MS0451$_{\rm ACS}$ (Table A.3). We did not apply a boost-correction as for the real data (Sect. 6.2.3), because we simulated only background galaxies.

Unlike for real data where the superposition of intrinsic ellipticities $\chi^{(\rm s)}$ and the distortion χ is directly obtained from measuring the shear, the reduced tangential shear χ_t has to be decomposed into both quantities by inverting Eq. (2.17),

$$\chi = \frac{\chi^{(\rm s)} + 2g + g^2\chi^{(\rm s)*}}{1 + |g|^2 + 2\mathcal{R}\mathrm{e}\left(g\chi^{(\rm s)*}\right)} \,. \tag{5.1}$$

Here, the measured complex ellipticities can be expressed as

$$\begin{aligned} \chi_1 &= \mathcal{R}\mathrm{e}\left(\chi\right) = \frac{\chi_1^{(\rm s)}\left(1 + g_1^2 - g_2^2\right) + 2g_1\left(1 + g_2\chi_2^{(\rm s)}\right)}{1 + |g|^2 + 2\left(g_1\chi_1^{(\rm s)} + g_2\chi_2^{(\rm s)}\right)} \\ \chi_2 &= \mathcal{I}\mathrm{m}\left(\chi\right) = \frac{\chi_2^{(\rm s)}\left(1 - g_1^2 + g_2^2\right) + 2g_2\left(1 + g_1\chi_1^{(\rm s)}\right)}{1 + |g|^2 + 2\left(g_1\chi_1^{(\rm s)} + g_2\chi_2^{(\rm s)}\right)} \,. \end{aligned} \tag{5.2}$$

The components of the reduced tangential shear were calculated with Eq. (2.11). The reduced tangential shear χ_t and its cross component $\chi_\times$ were calculated via χ_1 and χ_2 by decomposing Eq. (2.22) into its components.

We created three catalogues: Cat1 has $n = 82$ galaxies/arcmin^2 and all galaxies at $\langle z_{\rm s}\rangle = 1.645$ (Table 4.1) similar to MS0451$_{\rm ACS}$. Cat2 has $n = 77$ galaxies/arcmin^2, 5% individual source redshifts drawn from the redshift distribution of MS0451.6−0305 and 95% of galaxies at $\langle z_{\rm s}\rangle = 1.647$ similar to MS0451$_{\rm zphoto}$ (Table 4.1). Cat3 has $n = 77$ galaxies/arcmin^2 and $\langle z_{\rm s}\rangle = 1.645$ to investigate the effect of a smaller number density on the errors.

The analysis of the three catalogues was carried out as for MS0451$_{\rm ACS}$ and MS0451.6$_{\rm zphoto}$ in Sect. 6.2. For Cat2, we scaled all redshifts to $z_{\rm r} = 1.647$ with Eq. (2.31) and calibrated the sources with an effective mean source redshift on the sources with individual redshifts according. This process will be described in Sect. 6.2.3. As for the real data, we fitted NFW- and SIS-models to the catalogues and studied how the errors on the free parameters r_{200}, c_{200} and σ_v change with respect to number density, photometric redshifts and different numbers of fit parameters. We expected the largest errors for Cat3 because it has no photometric redshifts and a smaller n than Cat1 and Cat2.

5.2.2 Results

The tangential shear profiles of the three simulated catalogues are plotted in Fig. 5.5 and the fit parameters are listed in Table 5.2, whereby $M_{\rm SIS}$ is truncated at r_{200} from the NFW-model. We plot the likelihood contours of the fit-parameters and the tangential shear profiles for the three catalogues in the upper and lower panel of Fig. 5.5, respectively.

Cat1 predicts $\Delta r_{200}/r_{200} \approx 5\%$, $\Delta c_{200}/c_{200} \approx 12\%$ and $\Delta\sigma_v/\sigma_v \approx 3\%$ for MS0451$_{\rm ACS}$. This is consistent with our weak lensing analysis although the errors on c_{200} are $\approx 15\%$ for the NFW-profile (Table A.3). For MS0451$_{\rm zphoto}$ the predictions from Cat2 are $\Delta r_{200}/r_{200} \approx 8\%$, $\Delta c_{200}/c_{200} \approx 20\%$ and $\Delta\sigma_v/\sigma_v \approx 5\%$ which is consistent with Table A.3. The errors on σ_v are ~ 4 times larger for Cat2 than for MS0451$_{\rm zphoto}$ because we did not simulate an SIS-lens. Cat3 predicts $\Delta r_{200}/r_{200} \approx 5\%$, $\Delta c_{200}/c_{200} \approx 13\%$ and $\Delta\sigma_v/\sigma_v \approx 3\%$ if only the number density would drop.

The model parameters and their errors are consistent with the results for MS0451$_{\rm ACS}$ and MS0451$_{\rm zphoto}$ (Sect. 4.1.3 and Table A.3). Thus, the simulation confirms our results for MS0451$_{\rm ACS}$

Table 5.2: Results of the weak lensing simulation.

	Cat1	Cat2	Cat3
NFW:			
r_{200} [kpc]	2206^{+100}_{-101}	2216^{+174}_{-170}	2195^{+106}_{-103}
c_{200}	$4.6^{+0.6}_{-0.5}$	$3.2^{+0.7}_{-0.6}$	$4.6^{+0.6}_{-0.6}$
M_{200} [$10^{14} M_{\odot}$]	$22.45^{+3.05}_{-3.08}$	$22.76^{+5.36}_{-5.24}$	$22.12^{+3.20}_{-3.11}$
SIS:			
σ_v [km/s]	1295^{+38}_{-40}	1182^{+49}_{-58}	1287^{+39}_{-42}
$M_{\rm SIS}$ [$10^{14} M_{\odot}$]	$17.20^{+1.01}_{-1.06}$	$14.39^{+1.19}_{-1.41}$	$16.90^{+1.02}_{-1.10}$

and $\mathrm{MS0451}_{\rm zphoto}$. The errors on the fit parameter of Cat3 and Cat1 are consistent. We find only marginal difference in the expected errors if photometric redshifts are included because the smaller number density compensates the effect of the 5% of photometric redshifts. To make a meaningful statement about the effect of photometric redshifts on mass uncertainty in a weak lensing analysis, photometric redshifts for a larger fraction of sources would be required.

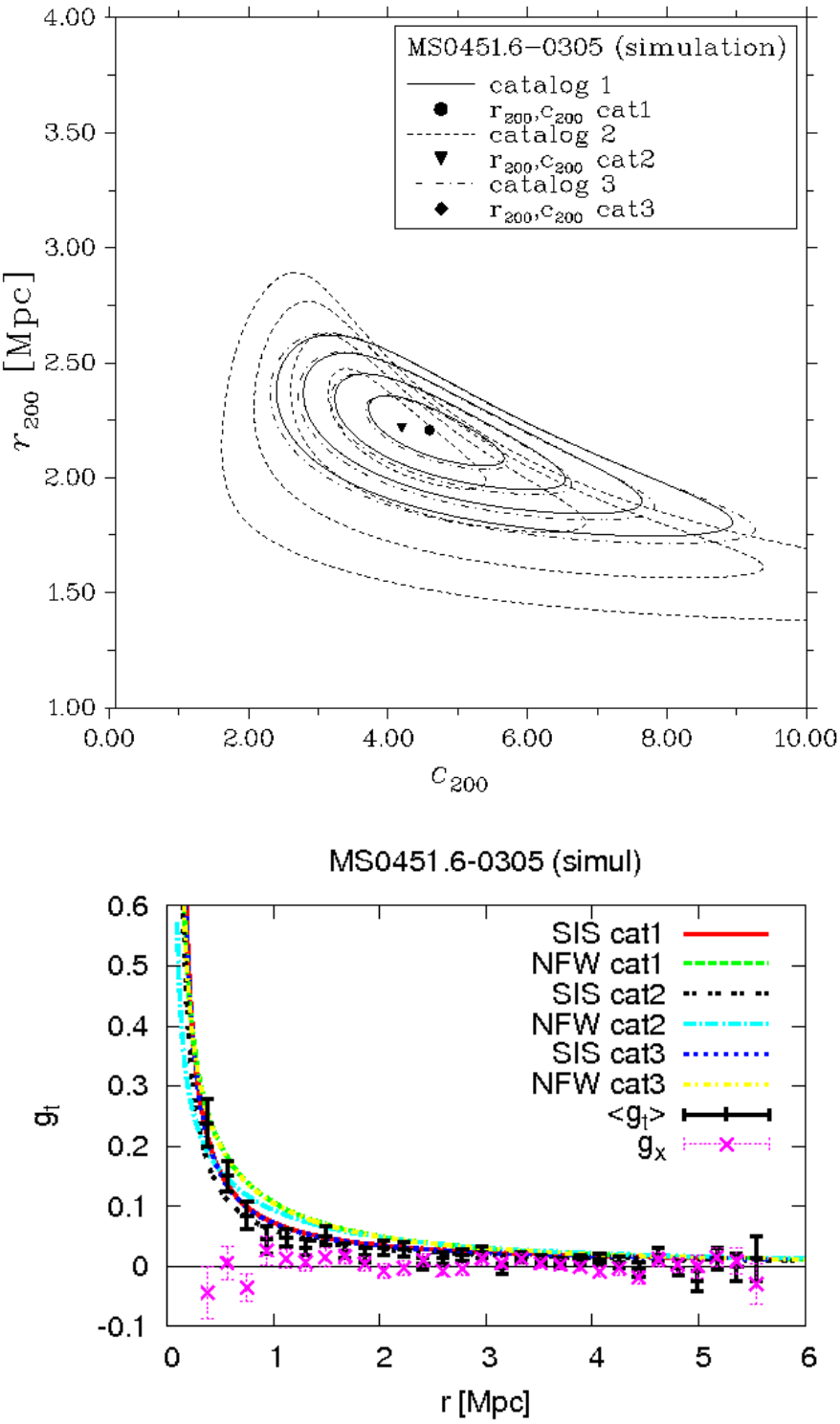

Figure 5.5: *Upper panel:* Likelihood contours for the NFW-models of cat1, cat2 and cat3 for the best-fit parameters r_{200} and c_{200}. We show the 1-,2-,3- and 4σ confidence regions. *Lower panel:* Tangential shear profiles of cat1, cat2 and cat3 for the NFW- and the SIS-model assuming an NFW-lens. For reasons of visualisation the tangential shear was binned which is shown as the black data points with the errors bars which are the standard deviation of g_t in each bin. The crosses with the thin, dotted error bars display the cross component $g_\times$. Due to the high number density of sources, the error bars are small. As for MS0451.6−0305, we cut out the innermost 17″.

Chapter 6

Weak lensing analysis

In this chapter, I will present the weak lensing analysis for the cluster sample studied in this work and discuss the results with respect to the cluster properties such as dynamical state, morphology, projected 2d-morphology and merger processes as well as to results from previous studies. Section 6.1 describes how the aperture mass statistics (Sect. 2.3.1) are applied to the cluster centre. I will define the cluster centre as the position at which the weak lensing signal-to-noise ratio reaches a maximum, $(S/N)_{max}$, and confirm its position and amplitude with simulations. I will also show that this centre is consistent with the BCG position and optical and X-ray centres from previous studies. In Sect. 6.2, the mass models used in this study and their error analysis will be introduced (Sects. 6.2.1 and 6.2.2, respectively) and I will discuss possible issues such as the contamination of cluster galaxies and the influence of large-scale-structure (Sect. 6.2.3). In Sect. 6.3, I will present and discuss the results.

6.1 Signal-to-Noise and surface mass density

6.1.1 Detection significance

The aperture mass signal-to-noise ratio S/N (Eq. 2.30) depends on the position of the aperture $\boldsymbol{\theta}_0$ and the number of objects inside the aperture radius θ_{ap}. Its amplitude depends also on the cluster redshift z_d and mass as we will see in the following. For a cluster with given mass, redshift and number density of lensed sources, however, S/N varies only with respect to the grid position and θ_{ap}. At the position of the cluster centre, it reaches a maximum, $(S/N)_{max}$, because ideally the shapes of the source galaxies are tangentially aligned around a mass concentration.

To determine the significance of a mass concentration, the aperture must be optimised. We calculated S/N on a finite grid as a function of θ_{ap}. For the grid constant we chose $\Delta = 18''$ which is a good compromise between coarse grids and long computation times. The aperture radius has to be chosen carefully: Small θ_{ap} reduce the measured S/N due to ignoring galaxies at larger projected distances from the centre of the aperture which still carry a significant lensing signal. On the other hand, large θ_{ap} may include regions where the lensing signal is depleted by noise or even influenced by cosmic shear from the LSS. Thus, S/N as a function of θ_{ap} increases with aperture radius and drops after attaining its maximum value $(S/N)_{max}$. To find $(S/N)_{max}$, we increased θ_{ap} by $30''$ and around a maximum by $3''$ to determine $(S/N)_{max}$ more precisely. We refer to the grid position of $(S/N)_{max}$ as the S/N-peak or the weak lensing cluster centre.

Significances, aperture radii and coordinates of the peaks are listed in Table 6.1. Figure 6.1 shows S/N as a function of θ_{ap} for the cluster sample. We determined $(S/N)_{max}$ for both $MS0451_{ACS}$ and $MS0451_{zphoto}$ (Sect. 4.2.3) to investigate how the inclusion of photometric redshifts affects the signal-to-noise ratio. For $MS0451_{zphoto}$, $(S/N)_{max}$ is 4% higher than for $MS0451_{ACS}$ which

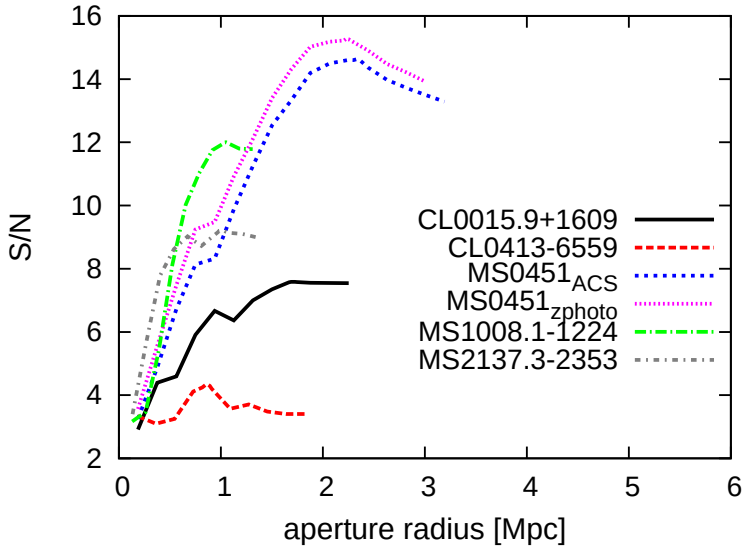

Figure 6.1: Weak lensing signal-to-noise ratio as a function of aperture radius $\theta_{\rm ap}$.

is much smaller than predicted by Bartelmann & Schneider (2001) due to the small fraction of sources with photometric redshifts. $(S/N)_{\rm max}$ is correlated with cluster mass and redshift as well as with the number density n of the background galaxy population. Thus, $(S/N)_{\rm max}$ decreases towards higher redshifts and increases with mass.

A more detailed discussion will follow for each of the clusters.

6.1.2 S/N- and Surface Mass Maps

Having S/N calculated for each grid position, S/N-contour maps can be constructed. With weak lensing mass reconstructions the projected mass distribution κ could be constructed (Sect. 2.3.3). The morphology of the surface mass distribution can distinguish relaxed clusters from merging systems. The mass reconstruction was provided by Holger Israel, who applied a freely available code[1] based on the Seitz & Schneider (2001) finite-field method for the HST-data. The dimensionless surface mass $\kappa = \Sigma/\Sigma_{\rm crit}$ was calculated on a regular grid with $\sim 15''$ mesh size[2]. A Gaussian smoothing filter with a full-width at half-maximum of $0.555\,R_{\rm s}$ accounting for all sources within the scale radius $R_{\rm s} = 1'$ was used for the shear field. We left κ unnormalised because we are only interested in the comparison with the S/N-contours.

The resulting κ-contours and the S/N-contours are plotted for each cluster in Figs. 6.2– 6.6. Both S/N and κ agree for each cluster. Starting at S/N= 1, we plot the S/N-contours in steps of $\Delta(S/N) = 2$ for MS0451.6−0305 and $\Delta(S/N) = 1$ for the other clusters as the thin, orange curves. The S/N-peak is denoted as the orange cross. Starting at $\kappa = 0.02$, we plot surface mass contours in steps of $\Delta\kappa = 0.02$ as the thick, green curves. We show the contours for both $\mathrm{MS0451}_{\rm ACS}$ and $\mathrm{MS0451}_{\rm zphoto}$ to investigate whether the mass distribution and the signal-to-noise ratio are sensitive to the inclusion of individual source redshifts. The morphology in the κ-maps agrees with the S/N-contours with respect to the peak positions.

The S/N- and κ-contours will be interpreted using former studies of these clusters in the following.

[1] www.astro.uni-bonn.de/~mischa/download/massrec.tar

[2] The actual mesh constants vary between $14\farcs73$ and $14\farcs95$, because the code demands an integer number of grid cells.

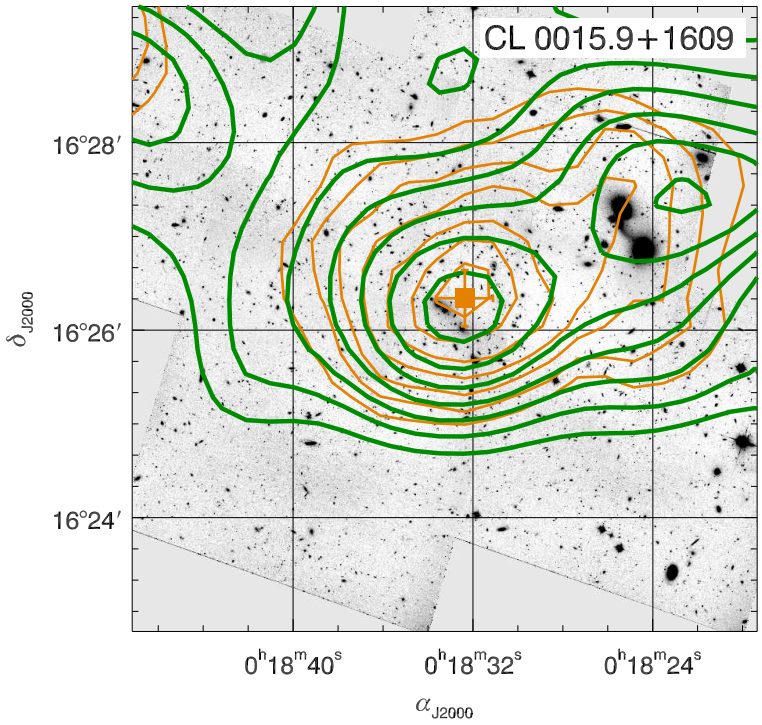

Figure 6.2: Weak lensing Signal-to-Noise and κ-contours of CL0015.9+1609. We plot the S/N-contours from S/N= 1 in steps of $\Delta(S/N) = 1$ as the thin, orange curves and surface mass contours from $\kappa = 0.02$ in steps of $\Delta\kappa = 0.02$ as the thick, green curves. The S/N-peak (orange cross) has a significance of 7.59σ (Table 6.1).

CL0015.9+1609

The S/N and κ-contours are plotted in Fig. 6.2. The orange cross which denotes the S/N-peak is close to the diagonal bar of galaxies which defines the optical cluster centre (Sect. 4.1.1).

The radio study by Giovannini & Feretti (2000) and the X-ray analysis by Solovyeva et al. (2007) indicate that CL0015.9+1609 is a merger. The double-peak structure in the κ-map in the North-East may thus be interpreted as infalling galaxies from a filament. This structure is also close to the edge of the field-of-view where the S/N is affected by noise. To find out whether this structure, shown in the S/N-map as elongated contours, belongs to a true mass concentration, one requires data that cover a larger field-of-view than the existing data. In the Northwest, the κ-contours indicate another filament which is not visible in the S/N-contours. According to Tanaka et al. (2005), the cluster is embedded in a filament extending from East to West and in another extending from North to South. Our observation gives evidence for the filament in East-West direction.

CL0413−6559

CL0413−0305 is a low-mass cluster (Girardi & Mezzetti 2001; Smail et al. 1997), wherefore the S/N- and κ- peaks are less distinct than for the other clusters. For the same reason, our detection significance 4.34σ is low for space-data which would be typical for ground-based data.

In the Southeast and Southwest of the CL0413−6559, we detected two 2σ-peaks, which can be associated to the cluster according to the κ-map (Fig. 6.3). Since the high fraction of spiral galaxies indicates that the cluster is still in the process of forming (Sect. 4.1.2), the κ- and S/N-

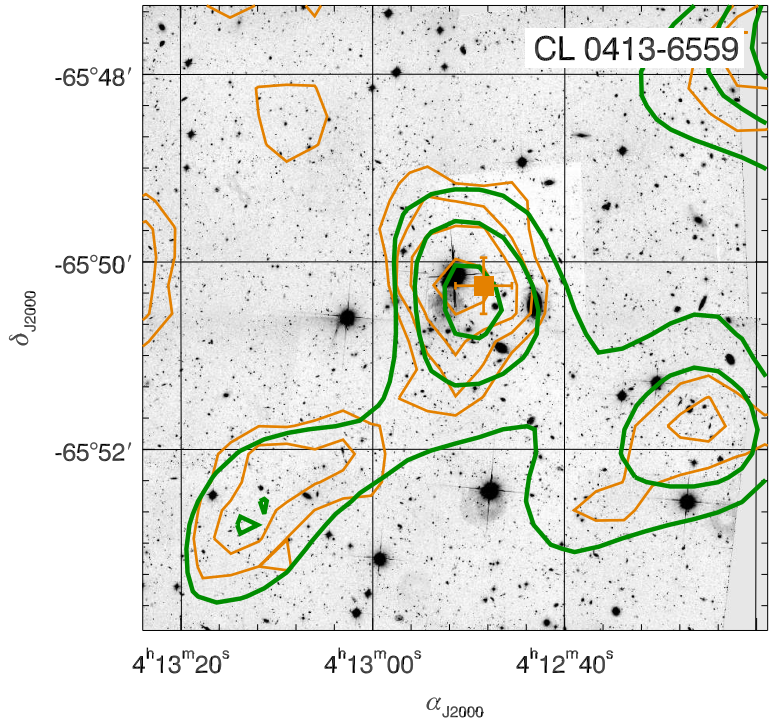

Figure 6.3: Weak lensing Signal-to-Noise and κ-contours of CL0413−6559. We plot the S/N-contours from S/N= 1 in steps of $\Delta(S/N) = 1$ as the thin, orange curves and surface mass contours from $\kappa = 0.02$ in steps of $\Delta\kappa = 0.02$ as the thick, green curves. The S/N-peak (orange cross) has a significance of 4.34σ (Table 6.1).

contours may give evidence that these peaks are low-mass systems which are merging with the cluster.

MS0451.6−0305

The contours of MS0451.6−0305 are nearly circular around the S/N-peak but are elongated in the Southeast towards larger projected distances to the cluster centre. Since this cluster is supposed to be massive (Sect. 4.1.3) and due to its high number density (Table 6.1) we measure a high detection significance of 14.60σ and 15.24σ for $\mathrm{MS0451_{ACS}}$ and $\mathrm{MS0451_{zphoto}}$, respectively. In the central region, the κ-contours are approximately circular as well.

Since only 5% of the background sources have photometric redshifts, the S/N-peak $(S/N)_{max}$ of $\mathrm{MS0451_{zphoto}}$ is only 4% higher than the one of $\mathrm{MS0451_{ACS}}$. Furthermore, the inclusion of photometric redshifts does not affect much the S/N- and κ-contours (Fig. 6.4).

Apart from that, the S/N- and κ-contours do not indicate that this cluster is associated to other structures such as filaments or small groups of galaxies. A higher fraction of photometric redshifts would reveal if and how strongly the contours are affected by individual source redshifts.

MS1008.1−1224

The galaxy distribution of MS1008.1−1224 is elongated from North to South (Mayen & Soucail 2000) which is also reflected in the S/N- and κ-contours, because the cluster galaxies trace the dark matter distribution and thus they roughly reflect the total mass distribution. The significance of 12.00σ is high because the cluster is massive and at an intermediate redshift ($z_d = 0.301$).

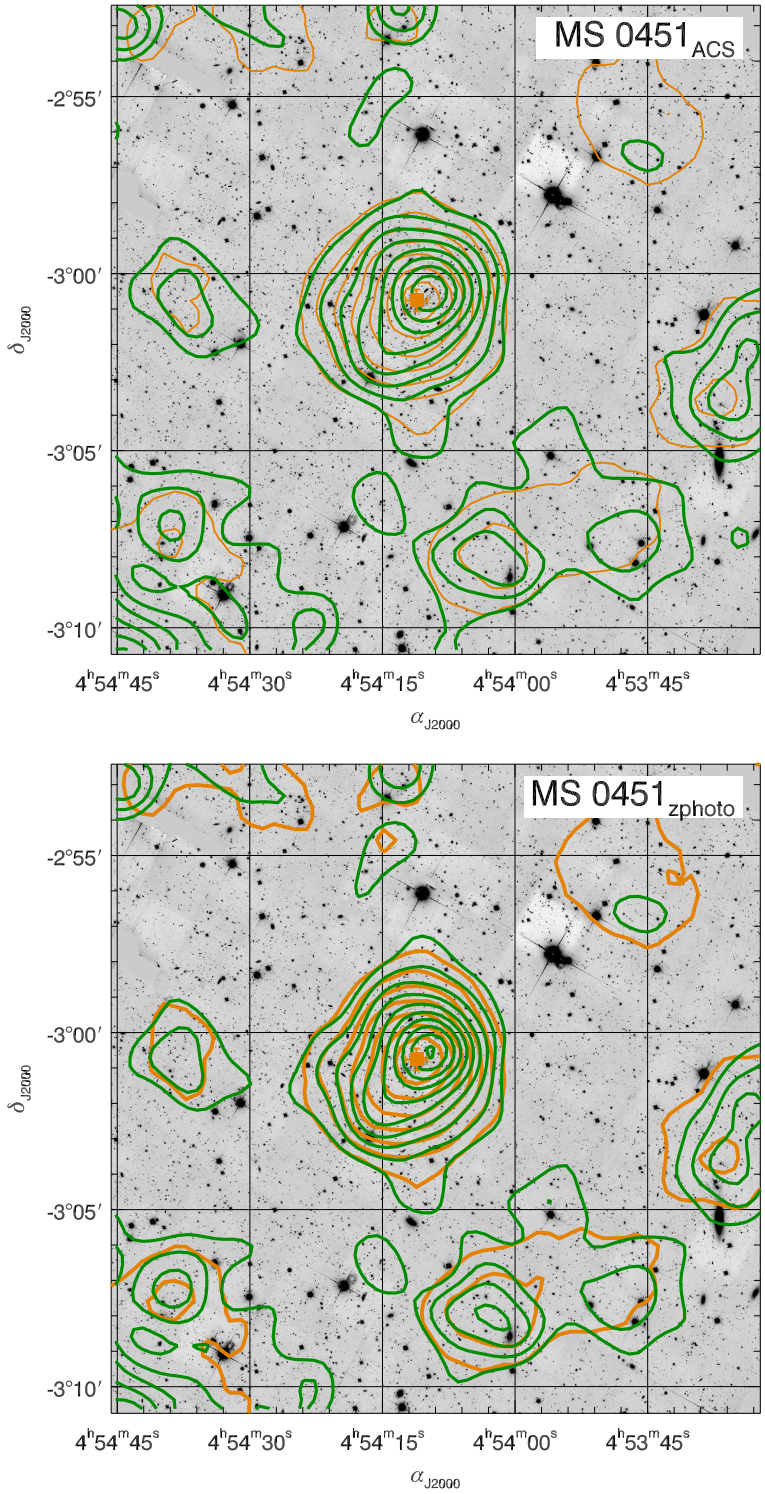

Figure 6.4: Weak lensing Signal-to-Noise and κ-contours of MS0451$_{\rm ACS}$ (*upper panel*) and MS0451$_{\rm zphoto}$ (*lower panel*). We plot the S/N-contours from S/N= 1 in steps of Δ(S/N) = 2 as the thin, orange curves and surface mass contours from κ = 0.02 in steps of $\Delta\kappa$ = 0.02 as the thick, green curves. The S/N-peak (orange cross) has a significance of 14.60σ for MS0451$_{\rm ACS}$ and 15.24σ for MS0451$_{\rm zphoto}$ (Table 6.1).

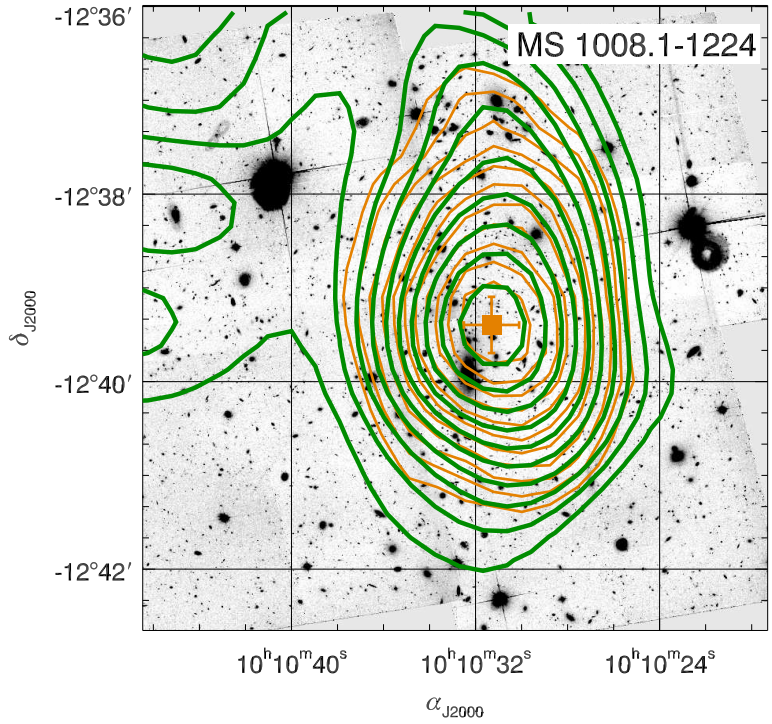

Figure 6.5: Weak lensing Signal-to-Noise and κ-contours of MS1008.1−1224. We plot the S/N-contours from S/N= 1 in steps of $\Delta(S/N) = 1$ as the thin, orange curves and surface mass contours from $\kappa = 0.02$ in steps of $\Delta\kappa = 0.02$ as the thick, green curves. The S/N-peak (orange cross) has a significance of 12.00σ (Table 6.1).

The κ-contours indicate an associated filament in the East which does not appear in the S/N-contours. Since this structure is extended over a large area it is likely not caused by noise.

MS2137.3−2353

Previous observations (e.g. Hammer et al. 1997) indicate that MS2137.3−2353 has spherical symmetry and is relaxed. This agrees with the nearly circular κ- and S/N-contours (Fig. 6.6). Only in the outskirts, the S/N- and κ-contours deviate from circularity. The κ-map indicate filamentary structures in the North and in the Southeast which would explain why both the S/N- and κ-contours show distortions in the cluster outskirts.

Although this cluster is less massive than MS0451.6−0305 and the mergers, $(S/N)_{max}$ is high because of the geometry and the dynamical state of the cluster as well as because of the cluster redshift $z_d = 0.313$.

6.1.3 Monte-Carlo simulation of the amplitude of the S/N-peak

In lensing, the image shapes of background galaxies are tangentially aligned, but they attain a random orientation if they are not distorted by a mass concentration and thus the estimator of the aperture mass vanishes, $\langle \hat{M}_{ap} \rangle = 0$.

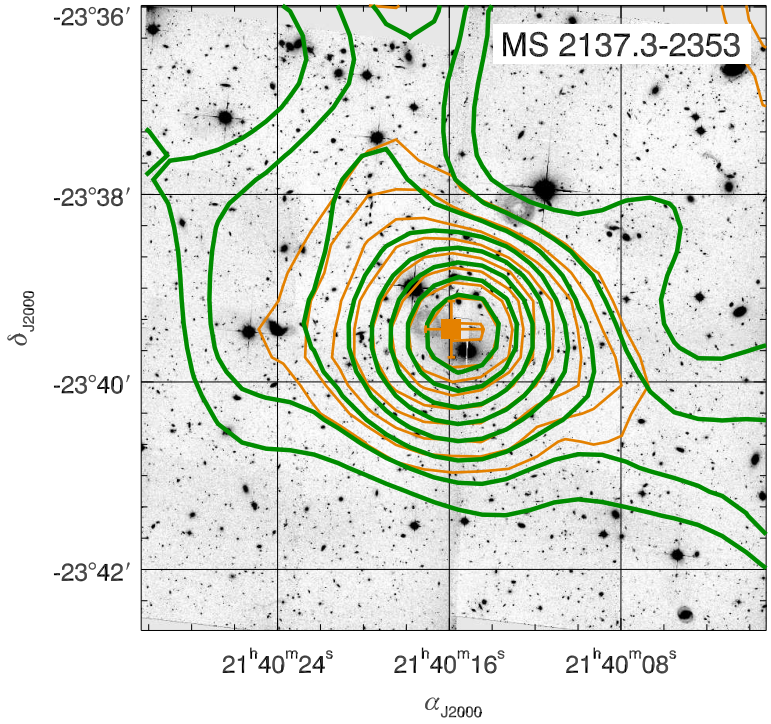

Figure 6.6: Weak lensing Signal-to-Noise and κ-contours of MS2137.3−2353. We plot the S/N-contours from S/N= 1 in steps of $\Delta(S/N) = 1$ as the thin, orange curves and surface mass contours from $\kappa = 0.02$ in steps of $\Delta\kappa = 0.02$ as the thick, green curves. The S/N-peak (orange cross) has a significance of 9.22σ (Table 6.1).

The amplitudes of our $(S/N)_{max}$ were cross-checked using a Monte-Carlo simulation. The absence of lensing was modelled by assigning random angles φ_{rand} to the ellipticity components $\epsilon_{1,2}$

$$\begin{aligned} \epsilon_1 \rightarrow \epsilon_{1,rand} &= \sqrt{\epsilon_1^2 + \epsilon_2^2}\cos(2\varphi_{rand}) \\ \epsilon_2 \rightarrow \epsilon_{2,rand} &= \sqrt{\epsilon_1^2 + \epsilon_2^2}\sin(2\varphi_{rand}) \ , \end{aligned} \tag{6.1}$$

of each source.

We calculated the aperture mass at the grid positions of $(S/N)_{max}$ for $n = 10^6$ randomisations. The randomised ellipticities provide a Gaussian distribution of the aperture mass $\hat{M}_{ap,rand}$ around zero, with a standard deviation $\sigma_{M_{ap,rand}}$. This yields an independent estimate for the signal-to-noise ratio

$$(S/N)_{MC} = \frac{M_{ap}(S/N_{max})}{\sigma_{M_{ap,rand}}} \ . \tag{6.2}$$

Here, $M_{ap}(S/N_{max})$ is the aperture mass calculated on the grid coordinates of $(S/N)_{max}$ (Sect. 6.1.1). The deviation $|\Delta_{S/N}|$ between $(S/N)_{MC}$ and $(S/N)_{max}$ is given in Table 6.1. Ideally, $|\Delta_{S/N}| = 0$, in practice $|\Delta_{S/N}| \approx 1\%$ because our measurements of $(S/N)_{max}$ included the Q-filter which weights the galaxies depending on their projected distance from the cluster centre (Sect. 2.3.1). The orientation of those galaxies is randomised which, however, affects the S/N. The results from the Monte-Carlo simulation agree with our measurements from Sect. 6.1.1.

$|\Delta_{S/N}|$ is 0.3% smaller for $MS0451_{zphoto}$ than for $MS0451_{ACS}$, because the shear estimates of the galaxies with photometric redshifts were weighted according to the geometric lensing efficiencies. Except for MS2137.3−2353, we obtained the smallest $|\Delta_{S/N}|$ for MS0451.6−0305 because

Table 6.1: Results from the weak lensing analysis. The coordinates α_{J2000} and δ_{J2000} are given in world coordinates. θ_{ap} is the aperture for which we measure the S/N-peak $(S/N)_{max}$ in kpc. The number density n is given in sources/arcmin^2. For MS0451$_{zphoto}$, n is smaller than for MS0451$_{ACS}$ because we removed faint and small foreground galaxies using photometric redshifts. $|\Delta_{S/N}|$ is difference between $(S/N)_{max}$ and $(S/N)_{MC}$ from the Monte-Carlo simulation in [%]. σ_{pos} is the radial uncertainty of the S/N-peak from bootstrapping. We also list the projected distances to the BCG, Δ_{BCG}, and to the optical and X-ray centres from previous analyses, Δ_{opt} and Δ_{X-ray}, respectively. The small numbers in brackets refer to the following references: Gioia & Luppino (1994) (1), Lewis et al. (1999) (2), Smail et al. (1997) (3), Allen et al. (2008) (4).

Cluster	θ_{ap} [kpc]	n	$(S/N)_{max}$	$\lvert\Delta_{S/N}\rvert$	α_{J2000}	δ_{J2000}	σ_{pos}	Δ_{BCG}	Δ_{opt}, Δ_{X-ray}
Cl0015.9+1609	1708	43	7.59	1.45	00:18:32.9	16:26:11	10.″5	9.″4	5.″4$^{(1)}$, 7.″9$^{(2)}$
Cl0413−6559	855	73	4.34	0.70	04:12:49.9	−65:50:25	21.″3	20.″6	12.″7$^{(3)}$
MS0451$_{ACS}$	2347	82	14.60	0.81	04:54:11.2	−03:00:55	8.″3	8.″6	5.″4$^{(1)}$, 12.″2$^{(2)}$
MS0451$_{zphoto}$	223	77	15.24	0.50	04:54:11.2	−03:00:55	8.″9	8.″6	5.″4$^{(1)}$, 12.″2$^{(2)}$
MS1008.1−1224	1049	55	12.00	1.03	10:10:32.5	−12:39:36	9.″2	17.″5	19.″9$^{(1)}$, 5.″3$^{(2)}$
MS2137.3−2353	1011	59	9.22	0.40	21:40:15.2	−23:39:35	9.″2	5.″0	4.″4$^{(1)}$, 5.″0$^{(4)}$

this cluster has the highest number density of background sources[3]. $|\Delta_{S/N}|$ of MS2137.3−2353 is only the lowest because this cluster is spherically and relaxed which is in contrast with the highest uncertainties for the merging clusters CL0015.9+1609 and MS1008.1−1224.

6.1.4 Bootstrapping to confirm the cluster centre

Since S/N (Eq. 2.30) is also a function of position and number density, the cluster centre varies between neighbouring grid positions for different θ_{ap}. Though this effect is small using large apertures, the position of $(S/N)_{max}$ can only be located up to an uncertainty which is of the order of the grid constant, i.e. a few arcseconds.

This uncertainty was estimated with a bootstrap-simulation in which the source catalogues with a total number of N galaxies were randomised by choosing N galaxies with replacement. We simulated 10^6 mock catalogues and we determined the position of $(S/N)_{max}$, which varies due to the different constellation of galaxies for each. The significances of the simulated S/N-peaks have mean values that deviate $\sim 0.5\sigma$ from our measured $(S/N)_{max}$ with a standard deviation of $\sim 1\sigma$. For each simulated S/N-peak we calculated the distance to the "true" peak position at which $(S/N)_{max}$ was measured. The discrete distribution of all simulated peaks around the "true" peak has a standard deviation σ_{pos} which we interpreted as the uncertainty with which the position of $(S/N)_{max}$ can be located.

In the last two columns of Table 6.1, we compare the position of $(S/N)_{max}$ with the BCG position, optical centres (Gioia & Luppino 1994; Smail et al. 1997) and X-ray centres (Lewis et al. 1999; Allen et al. 2008). Except for MS1008.1−1224, which is a merger, the projected distance between BCG and S/N-peak is equal or smaller than σ_{pos}. The same holds for at least one published X-ray or opitcal centre for each cluster. Those with deviations of more than σ_{pos} can be explained as follows: The X-ray centre of MS1008.1−1224 (Lewis et al. 1999) is $\sim 15''$ from the optical centre (Gioia & Luppino 1994) because of a clump of galaxies north to the centre. Our centre is closer to the X-ray centre than to optical centre. For MS0451.6−0305, the X-ray centre (Lewis et al. 1999) differs from the optical centre (Gioia & Luppino 1994). This is due to multiple peaks and elongations in NS- and EW-directions of the X-ray emission (Lewis et al. 1999). For this cluster, our centre agrees better with the optical one than with the X-ray centre. For MS2137.3−2353, the offset to the centres from Gioia & Luppino (1994) and Allen et al. (2008) is smallest because the cluster is relaxed.

[3]The number density of MS0451.6−0305 is larger because of different selection criteria for F814W and F606W and the different sky background (Sect. 4.2.2).

From the above, we concluded that the S/N-peak can define the cluster centre well. This is also expected since the tangential alignment is maximised around the centre of a mass concentration. We found that large $(S/N)_{max}$ values have small σ_{pos} values and that σ_{pos} increases with cluster redshift.

The systematic uncertainty in the cluster centre will be included in the mass error by centering our tangential shear profiles at the X-ray and optical centres as well as the BCG positions. We will show later that all those mass estimates at different centres are consistent.

6.2 Mass modelling

6.2.1 Models for gravitational lenses

By assuming a spherically-symmetric mass distribution, simple models for describing the lensing properties of a galaxy cluster can be considered. In the case of spherical symmetry, the lens equation reduces to one dimension, because the projected mass distribution is axially symmetric. Therefore, the following mass models provide immediately the tangential component of the reduced shear g_t, while its cross component vanishes ($g_\times = 0$).

The Singular Isothermal Sphere (SIS)

The Singular Isothermal Sphere (SIS) is a zero-order model for describing the lensing properties of galaxy clusters. It is motivated by the flat rotation curves of spiral galaxies, which are embedded in a dark matter halo with a density profile of

$$\rho(r) = \frac{\sigma_v^2}{2\pi G r^2}\,. \tag{6.3}$$

For an SIS-lens, the only free parameter is the velocity dispersion σ_v of the cluster galaxies. Equation (6.3) is a special solution of the equation-of-state $P = \rho k_B T/m$ for a set of self-gravitating particles of mass m that behave like an ideal gas with temperature T. To solve the equation-of-state, the equation of hydrostatic equilibrium and the mass continuity equation have to be employed.

With the Einstein angle $\theta_E = 4\pi\left(\sigma_v^2/c^2\right) D_{ds}/D_s$, the reduced tangential shear g_t for a galaxy at radial distance θ can be expressed in terms of σ_v,

$$\begin{aligned} g_{SIS}(\theta) &= \frac{\gamma(\theta)}{1-\kappa(\theta)} = \left(\frac{2|\theta|}{\theta_E} - 1\right)^{-1} \\ &= \left(\frac{\theta c^2}{2\pi\sigma_v^2 D_{ds}/D_s} - 1\right)^{-1}\,. \end{aligned} \tag{6.4}$$

We calculated the cluster mass by integrating Eq. (6.3) in spherical polar coordinates

$$M_{SIS}(r) = \frac{2\sigma_v^2}{G} r\,. \tag{6.5}$$

The Navarro-Frenk-White profile (NFW)

Since dark matter halos are the result of a generic dissipationless collapse of spherical overdensities, they are assumed to be virialised with an overdensity which is 200 times above the critical density (Sect. 1.3.2). In N-body simulations, Navarro et al. (1996) found that the density profile of such halos has a universal shape, given as the *NFW-density profile*

$$\rho(r) = \frac{\delta_{cf}\rho_{cr}(z_d)}{(r/r_s)(1+r/r_s)^2}\,. \tag{6.6}$$

Here, $\rho_{\rm cr}(z_{\rm d}) = 3H^2(z_{\rm d})/8\pi G$ is the critical overdensity at the halo redshift $z_{\rm d}$ (Sect. 1.2.2) and $\delta_{\rm cr}$ is the *characteristic overdensity* of the halo defined. It is related to the *concentration parameter* $c_{200} = r_{200}/r_{\rm s}$ by

$$\delta_{\rm cr} = \frac{200}{3}\frac{c_{200}^3}{\ln(1+c_{200}) - c_{200}/(1+c_{200})}\,. \tag{6.7}$$

The concentration parameter is a dimensionless measure for the amount of mass concentrated towards the centre and r_{200} is the radius inside which the mean density of the halo is about $200\rho_{\rm cr}$. Both r_{200} and c_{200} can be treated as free parameters or an externally calibrated relation can be used to reduce the NFW model to an effective one-parameter model (Sect. 6.2.1). At the scale radius $r_{\rm s}$ the NFW-profile changes its slope according to

$$\rho(r) \propto \begin{cases} r^{-1} & r \ll r_{\rm s} \\ r^{-3} & r \gg r_{\rm s}\,. \end{cases} \tag{6.8}$$

Thus, the NFW-profile is on large scales steeper than the SIS and shallower on small scales.

Assuming an NFW-model, the total cluster mass is defined as

$$M_{200} = \frac{4\pi}{3} r_{200}^3 200\rho_{\rm cr}(z_{\rm d})\,. \tag{6.9}$$

The lensing properties of NFW-mass distributions are described by Wright & Brainerd (2000) in the thin lens approximation via convergence κ and tangential shear γ. By integrating Eq. (6.6) along the line-of-sight, the surface mass density $\Sigma_{\rm NFW}$ can be inferred. Dividing $\Sigma_{\rm NFW}$ by the critical surface mass density $\Sigma_{\rm cr}$ provides the convergence for an NFW-lens

$$\kappa_{\rm NFW}(x) = A \begin{cases} \frac{2}{x^2-1}\left[1 - \frac{2}{\sqrt{1-x^2}}\,\mathrm{arctanh}\,\sqrt{\frac{1-x}{1+x}}\right] & x < 1 \\ \frac{2}{3} & x = 1 \\ \frac{2}{x^2-1}\left[1 - \frac{2}{\sqrt{x^2-1}}\arctan\sqrt{\frac{x-1}{1+x}}\right] & x > 1\,. \end{cases} \tag{6.10}$$

Here, we defined $A = r_{\rm s}\delta_{\rm cr}\rho_{\rm cr}/\Sigma_{\rm cr}$ and x is the projected distance to the cluster centre in units of the scale radius, $x = R/r_{\rm s}$. Due to spherical symmetry, the tangential shear is

$$\gamma_{\rm NFW}(x) = A \begin{cases} \frac{8\,\mathrm{arctanh}\sqrt{\frac{1-x}{1+x}}}{x^2\sqrt{1-x^2}} + \frac{4}{x^2}\ln\left(\frac{x}{2}\right) + \frac{2}{(x^2-1)} + \frac{4\,\mathrm{arctanh}\sqrt{\frac{1-x}{1+x}}}{(x^2-1)(1-x^2)^{1/2}} & x < 1 \\ \frac{10}{3} + 4\ln\left(\frac{1}{2}\right) & x = 1 \\ \frac{8\arctan\sqrt{\frac{x-1}{1+x}}}{x^2\sqrt{x^2-1}} + \frac{4}{x^2}\ln\left(\frac{x}{2}\right) + \frac{2}{(x^2-1)} + \frac{4\arctan\sqrt{\frac{x-1}{1+x}}}{(x^2-1)^{3/2}} & x > 1 \end{cases} \tag{6.11}$$

and thus $g_{\rm NFW} = \gamma_{\rm NFW}/(1-\kappa_{\rm NFW})$ can be calculated.

Truncated NFW

The NFW-profile well describes the mass distribution of galaxy clusters within r_{200} while its usefulness beyond that scale is debated (Takada & Jain 2003a,b; Binney & Tremaine 2008; Oguri & Hamana 2011). Sources with projected distances of $r > r_{200}$ from the cluster centre might distort the result when they are fitted by an NFW-profile.

Since the r_{200} of CL0413−6559 and MS0451.6−0305 are inside the field-of-view, we tested with both clusters how well the NFW-model can be applied beyond this radius by comparing the results of the NFW-profile to a simplified truncated NFW-profile (NFW&PS, henceforth). The

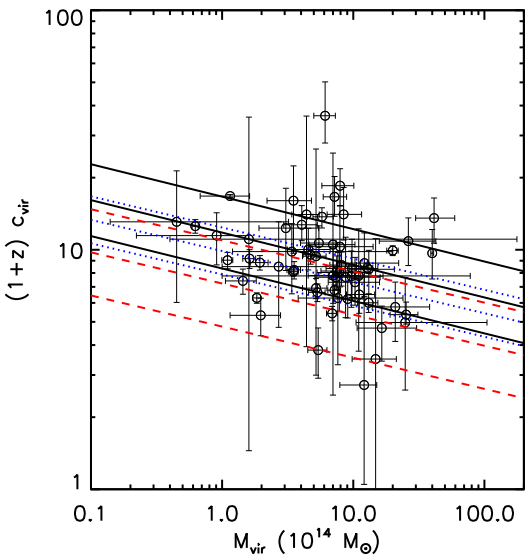

Figure 6.7: Observed cluster concentrations and virial masses of the 62 galaxy clusters from Comerford & Natarajan (2007). The middle black solid line denotes the best-fitting power law for which Eq. (6.13) was employed and the outer two solid black lines denote the 1σ scatter $\Delta(\log c_{\rm vir}) \sim 0.15$. Comerford & Natarajan (2007) compare their results with the simulations from Bullock et al. (2001) (dashed red line) and Hennawi et al. (2007) (dotted blue line) but they point out that a direct comparison is not possible because of differing systematics. From Comerford & Natarajan (2007).

latter is defined such that for $r < r_{200}$ the NFW-model applies and for $r > r_{200}$ the reduced tangential shear behaves as for a point mass lens,

$$g_{\rm PS}(\theta) = g_{\rm NFW}(\theta_{200}) \left(\frac{r_{200}}{r}\right)^2 , \tag{6.12}$$

with all mass inside r_{200}.

NFW&PS serves only as cross-check because it is not a physical model. Israel et al. (2010) found only marginal difference between NFW and NFW&PS for the galaxy cluster CL0030+2618. If there is a significant discrepancy between the two models, we expect to find it at least for MS0451.6−0305 because this cluster has the largest field-of-view coverage.

Mass-concentration relation

The concentration parameter c_{200} is poorly constrained by the NFW-model for merging clusters. For two such clusters, CL0015.9+1609 and MS1008.1−1224, we obtained $c_{200} = 1.2^{+1.0}_{-1.1}$ (Table A.1) and $c_{200} = 2.2^{+0.8}_{-0.7}$ (Table A.4), respectively. To check any systematic caused by poorly determined concentrations, we also applied an NFW-profile with fixed concentration $c_{\rm NFW}$ (*Mc*-model, henceforth) to the tangential shear profiles. In this model, r_{200} is the only free parameter.

The fixed $c_{\rm NFW}$ were calculated according to Bullock et al. (2001) who found an empirical relation between mass and concentration using numerical simulations for dark matter halos,

$$c_{\rm NFW} = \frac{c_{\rm NFW,0}}{1+z_{\rm d}} \left(\frac{M_{200}}{M_*}\right)^{\alpha} . \tag{6.13}$$

with $M_* = 1.3 \times 10^{13} h^{-1} M_\odot$. Comerford & Natarajan (2007) fitted a sample of 62 galaxy clusters with given masses and concentrations and obtained $c_{\rm NFW,0} = 14.5 \pm 6.4$ and $\alpha = -0.15 \pm 0.13$ (Fig. 6.7). We calculate $c_{\rm NFW}$ with Eq. (6.13) using Eq. (6.9).

Since this relation is based on the scenario of hierarchical clustering, low-mass halos are expected to be more compact than high-mass halos, because they have collapsed at earlier times when the Universe was denser. Thus, the concentration depends on the assembly history of a cluster as well as on the redshift and on $\rho_{\rm crit}(z_{\rm d})$, wherefore it provides an important probe of the mean density of the Universe at the time the cluster has formed.

This relation is, of course, a mean relation for a large sample of galaxy clusters. Individual clusters may deviate significantly from Eq. (6.13) due to effects of halo triaxiality, substructures along the line-of-sight or merging. In Sect. 6.3, we will test this effect for our merging clusters, for which Eq. (6.13) provides too high concentrations ($c_{\rm NFW} \sim 7$) and consequently too low masses. On the other hand, the mass-concentration relation provides us with reasonable concentrations for relaxed clusters, e.g. MS2137.3−2353.

6.2.2 Likelihood parameter estimation

The free parameters r_{200}, c_{200} and σ_v and their uncertainties were estimated by minimising the merit function

$$\chi^2_{\rm model} = \sum_{i=1}^{N} \frac{\left[g_{\rm model}\left(\theta\right) - \epsilon_{{\rm t},i}\left(\theta\right)\right]^2}{\sigma^2_\epsilon \left(1 - |g_{\rm model}\left(\theta\right)|^2\right)^2} \,. \tag{6.14}$$

Here, σ_ϵ is the intrinsic ellipticity dispersion (Eq. 2.21) and $g_{\rm model}$ is the assumed mass model (Sect. 6.2.1). The second order term $(1-|g_{\rm model}\left(\theta\right)|^2)$ takes into account how the noise depends on the shear itself and it thus improves the estimate of the error in individual shear estimates (Schneider et al. 2000).

We used Eq. (6.14) to fit r_{200} and c_{200} for NFW and NFW&PS (Fig. 6.8). For CL0015.9+1609 and MS1008.1−1224, the best fit values for NFW and NFW&PS are the same because r_{200} is fitted outside the field-of-view. For MS1008.1−1224, also the likelihood contours of both models agree with each other which may be due to that r_{200} exceeds the field-of-view by almost 1 Mpc, while it is only 200 kpc for CL0015.9+1609. The contours of MS2137.3−2353 are likely the same for both models because this cluster is spherical and relaxed. The differences between both NFW-models show the strongest deviation for $\mathrm{MS0451}_{\rm ACS}$ and $\mathrm{MS0451}_{\rm zphoto}$, respectively, but only with respect to the position and not to the shape of the contours.

For the case of using the SIS-model or the *Mc*-model, we only fitted σ_v or r_{200}. The best fit parameters are the maximum likelihood values for which Eq. (6.14) reaches a minimum. The reduced $\chi^2_{\rm model}$, $\chi^2_{\rm dof}$, for the best fit parameters, will be $\chi^2_{\rm dof} \lesssim 1$, because in the mass-less case ($g_{\rm model} = 0$) we have

$$\chi^2_{\rm dof} = \frac{1}{N} \sum_{i=1}^{N} \frac{\left[\epsilon_{{\rm t},i}\left(\theta\right)\right]^2}{\sigma^2_\epsilon} = 1 \tag{6.15}$$

due to $\sigma^2_{\epsilon_{\rm t}} = (\sigma^2_{\epsilon_1} + \sigma^2_{\epsilon_2})/2$. Any model that minimises Eq. (6.15) will provide a better fit to the data with $\chi^2_{\rm dof} < 1$.

The errors on the model parameters were estimated at the 1σ-level which is $\Delta\chi^2 = 1.0$ for the one-parameter models SIS and *Mc*, and at $\Delta\chi^2 = 2.3$ for the two-parameter models NFW and NFW&PS. Since r_{200} and c_{200} are correlated with each other, we had to determine the errors of each parameter with respect to the other. Thus, we calculated the upper and lower errors on r_{200} (c_{200}) by fixing c_{200} (r_{200}) and integrated over the corresponding area for which $\Delta\chi^2 = 2.3$.

This method allows us to estimate the errors of our fit parameters and their interdependence in arbitrary σ-intervals simultaneously. This has the advantage over fitting tools which require start values and approach the minimum iteratively, like e.g. the Levenberg-Marquardt method. Especially for the NFW-model this is important because the interdependence between r_{200} and c_{200} provides poor constraints on c_{200} if estimated with the iterative approach of conventional fitting tools.

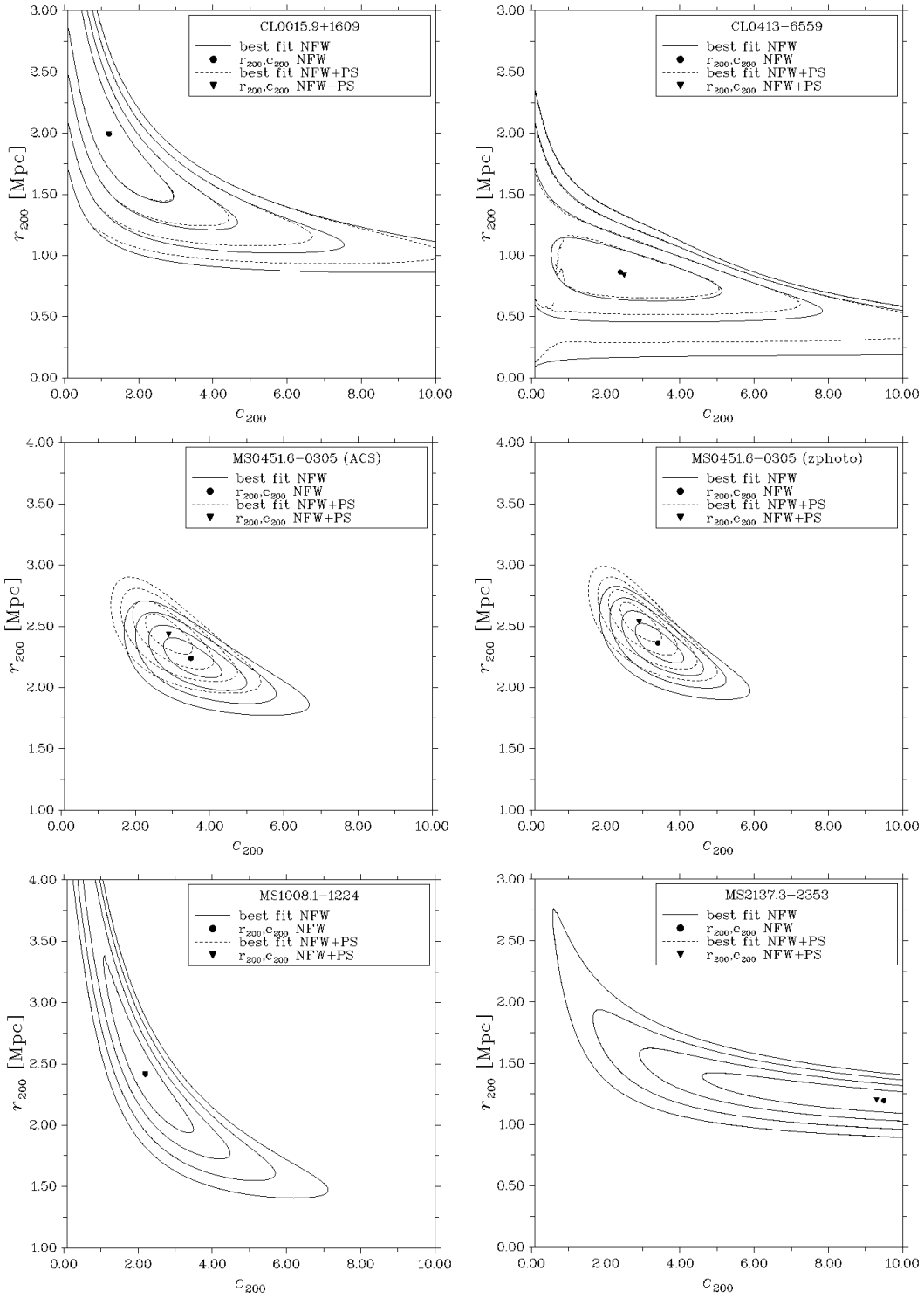

Figure 6.8: Likelihood contours for the NFW-model and the truncated NFW (NFW&PS) for the best-fit parameters r_{200} and c_{200}. We show the 1-,2-,3- and 4σ confidence regions. For MS1008.1−1224 and MS2137.3−2353, the contours of both models are the same.

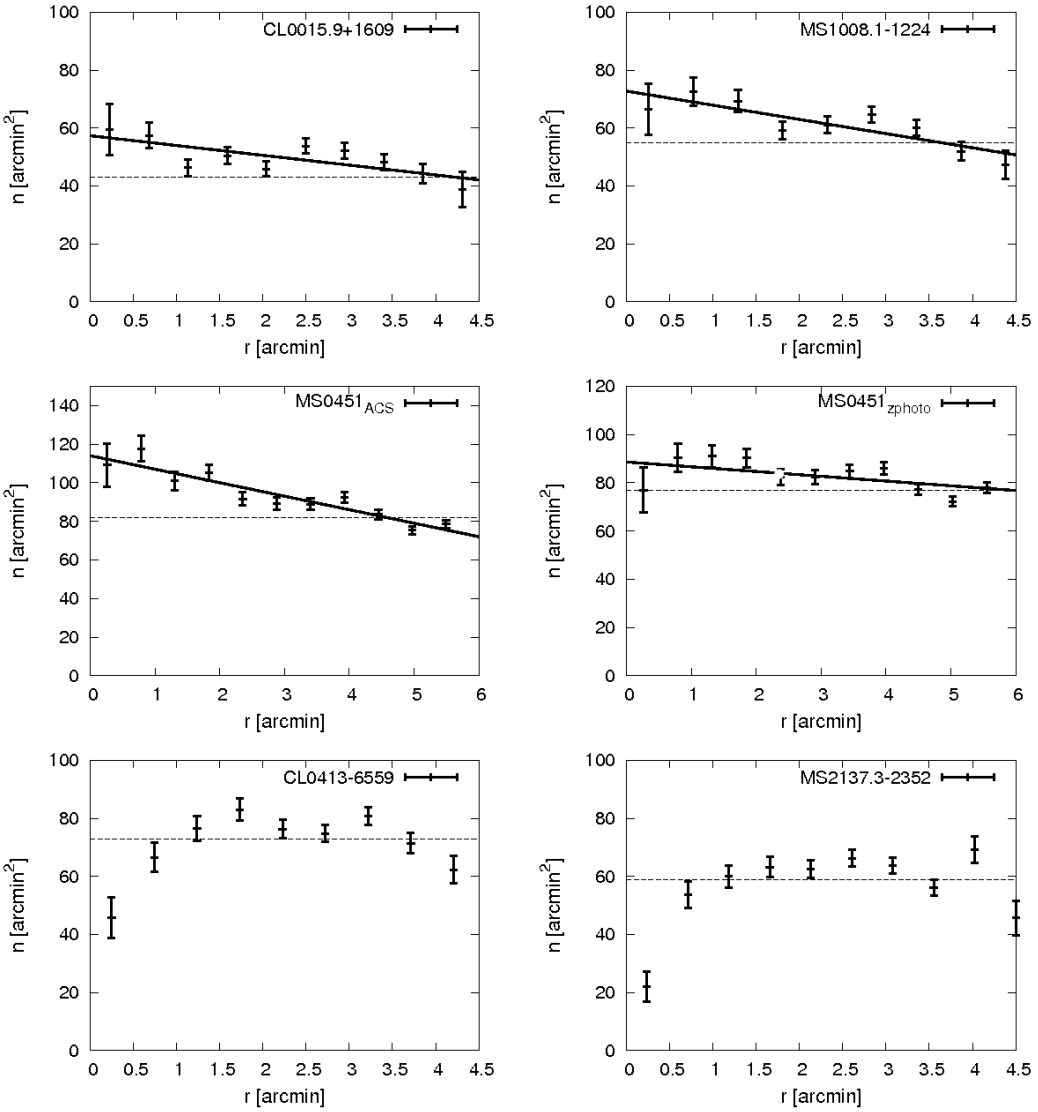

Figure 6.9: Radial profiles of the number density of galaxies. The dashed horizontal line denotes the mean number density n (Table 6.1). For CL0413−6559 and MS2137.3−2353, n is constant within the statistical errors, except the inner bin and in the case of CL0413−6559 also the outmost bin. The drop of n in the inner two bins of both is caused by bright objects in their central regions and the drop of n in the outer bin of CL0413-6559 results from few objects in that area. The excess in n caused by cluster galaxies is modelled with a linear relation for CL0015.9+1609, MS0451.6−0305 and MS1008.1−1224.

6.2.3 Issues for mass modelling

Contamination by cluster galaxies

Due to lack of redshift information, we cannot reliably distinguish lensed sources from cluster galaxies for distant clusters. Our weak lensing pipeline is designed for small and faint galaxy images, while it excludes bright and very extended ones. For this reason, the low-mass and low-luminosity end of cluster members may contaminate the background galaxy catalogue and dilute the lensing signal.

To account for this, we used a statistical approach, which boosts the observed tangential shear by a factor of $1 + f_{\rm cg}(\theta)$. Here, $f_{\rm cg}$ is the estimated fraction of cluster galaxies at projected

angular distance θ from the cluster centre (*boost-correction*, Hoekstra 2007). We calculated the radial profile of the source number density n in 10 radial bins for the clusters with 4-pointing mosaics and in 30 bins for the 41-pointing mosaic of MS0451.6−0305. Here, we accounted for both the masked areas and border effects. If the lensing catalogue is not contaminated by cluster galaxies, the number density in each radial bin is consistent with n from Table 6.1. If the catalogue is contaminated by cluster galaxies, n increases towards the cluster centre. The radial profiles $n(r)$ are plotted in Fig. 6.9 with their statistical errors. We only corrected for cluster galaxies if $n(r)$ shows an excess towards the centre.

We fit $f_{\rm cg}(\theta) = a + b\theta$ to CL0015.9+1609, MS0451.6−0305 and MS1008.1−1224 because the excess is approximately linear. For MS0451$_{\rm zphoto}$ the excess is significantly smaller compared to that for MS0451$_{\rm ACS}$, because we excluded cluster galaxies using the photometric redshifts. Since for MS0451.6−0305 we are already in the cluster outskirts at $r = 6'$ ($\sim r_{200}$), we apply the boost-correction only up to that scale which leaves us 11 of the 30 bins from the full field-of-view.

We did not apply a boost-correction to CL0413−6559 and MS2137.3−2353, because at small radii n is significantly affected by two bright stars and a luminous foreground galaxy for CL0413−6559 and by the bright cD-galaxy of MS2137.3−2353. For both clusters there are only a few background sources in the central regions. The drop of n in the outer bin of CL0413−6559 is also due to too few objects in that area.

Modified mass models for MS0451$_{\rm zphoto}$

Only 5% of the source galaxies from the HST-data of MS0451.6−0305 have photometric redshifts (Sect. 4.3.3). We took those 5% of galaxies with photometric redshifts as the sub-sample henceforth and the other galaxies as the main-sample and calibrate the main-sample on the photometric redshifts of the sub-sample. Thereby, we rescaled the ellipticities of the sub-sample with Eq. (2.32). For the main-sample we introduced an additional parameter α which substitutes $Z(z_{{\rm s},i})$ in the χ^2-minimisation for MS0451$_{\rm zphoto}$

$$\begin{aligned}\chi^2 &= \sum_{i=1}^{N_{\rm zphoto}} \frac{\left[Z(z_{{\rm s},i})g_{\rm model}(\theta) - \epsilon_{{\rm t,i}}(\theta)\right]^2}{\sigma_\epsilon^2\left(1 - Z(z_{{\rm s},i})^2|g_{\rm model}(\theta)|^2\right)^2} \\ &+ \sum_{j=1}^{N_{\rm zmean}} \frac{\left[\alpha g_{\rm model}(\theta) - \epsilon_{{\rm t,j}}(\theta)\right]^2}{\sigma_\epsilon^2\left(1 - \alpha^2|g_{\rm model}(\theta)|^2\right)^2}\,.\end{aligned} \tag{6.16}$$

Here, $N_{\rm zphoto}$ refers to the number of galaxies in the sub-sample and $N_{\rm zmean}$ to the number of galaxies in the main-sample.

This approach was applied because the sub-sample consists of bright source galaxies. Thus, we could not extrapolate their magnitude distribution to those of the main-sample. Instead we used an approach which is motivated as follows: The mean distance ratio of the main-sample $\langle D_{\rm ds}/D_{\rm s}\rangle = 0.384$[4] provides us with a mass profile $\kappa(r)$ that is defined except for its amplitude. Since the amplitude depends on $D_{\rm ds}/D_{\rm s}$, we can better determine the surface mass density $\Sigma(r) = \kappa(r)\Sigma_{\rm cr}$ using photo-zs than an effective mean source redshift.

Since the main-sample consists of 95% of all sources we expect α close to $Z(\langle z_{\rm s}\rangle) = 0.658$ with $\langle z_{\rm s}\rangle = 1.647$ which is the effective mean source redshift of the main-sample. This value is slightly higher than $\langle z_{\rm s}\rangle = 1.645$ for MS0451$_{\rm ACS}$ because we removed foreground galaxies from the data.

[4] $\langle D_{\rm ds}/D_{\rm s}\rangle$ for the main-sample of MS0451$_{\rm zphoto}$ is slightly higher than that of MS0451$_{\rm ACS}$ ($\langle D_{\rm ds}/D_{\rm s}\rangle = 0.383$) because it does not include the bright galaxies to which photometric redshifts could be assigned.

Table 6.2: Large-scale-structure error for MS0451.6−0305. The first column gives the error on M for an NFW-profile with fixed concentration and second and third column give the errors on M and c_{200} for a two-parameter NFW-model. The errors on M are given in units of $10^{14} M_\odot$.

	σ_M (c_{200} fixed)	σ_M	$\sigma_{c_{200}}$
LSS only	0.20	0.27	0.70
total	0.34	0.43	1.59

We found $\alpha = 0.698 \pm 0.054$ which is consistent with $Z(\langle z_s \rangle) = 0.658$. Thus, we can also directly use $Z(\langle z_s \rangle)$ for the main-sample.

Large-scale structure influence

At $r > 10'$ from the cluster centre, the large-scale structure (LSS) starts to dominate over the lensing signal and reduces the accuracy of weak lensing masses by inducing noise (e.g. Hoekstra 2003). Furthermore, the weak lensing signal is sensitive to any matter along the line-of-sight. Hoekstra (2003) showed that uncertainties in M_{200} and c_{200} are ~ 2 times larger, depending on cluster mass, when distant large-scale structure is not taken into account in the error budget of weak lensing masses. MS0451.6−0305 is the only cluster for which we can measure the tangential shear profile out to $\sim 16'$. We thus consider LSS-errors for this cluster. We did not account for LSS-influence for the other clusters because with our data their shear signal is only measurable out to $\sim 5'$.

We estimated the error from large-scale-structure $\sigma_{\rm LSS}$ for MS0451.6−0305 from Hoekstra et al. (2011) who determined the LSS-error on mass and concentration for a simulated cluster with virial mass $M_{\rm vir} = 10^{15} M_\odot$ at $0.05 < z < 0.6$ inside annuli of $10'$ and $25'$. Hoekstra et al. (2011) assumed a two-parameter NFW-model and an NFW-model with a fixed concentration. Because our field-of-view is $\sim 16'$ we used the mean of the errors for $10'$ and $25'$ as crude approximation.

Since Hoekstra et al. (2011) used a default mass, we adapted these errors for a cluster as massive as MS0451.6−0305. In our analysis, MS0451.6−0305 has $15 \times 10^{14} M_\odot \lesssim M \lesssim 35 \times 10^{14} M_\odot$ (Table A.3) depending on the mass model and whether we included photometric redshifts. For an optimistic estimate for MS0451.6−0305 we assumed that the error only depends on LSS, while for a conservative estimate the total error limits the LSS-errors reasonably. Thus, we use the total errors in Table 6.2 as second upper and lower errors for M_{200} and c_{200} in Table A.3. We used σ_M from the one-parameter NFW-model also for the cases using the SIS-model and Mc.

6.3 Results

The weak lensing cluster masses centred on the S/N-peak are consistent with those for the optical centres (Gioia & Luppino 1994; Smail et al. 1997), X-ray centres (Stocke et al. 1991; Lewis et al. 1999) and the BCG position which is shown in Fig. 6.10 (*lower left*). We show the tangential shear profiles centred on the S/N-peak in Figs. 6.11–6.15, where we also plot the cross-component $g_\times$. We fitted the mass models to all sources and calculated the mean tangential shear with the same binning as in Sect. 6.2.3. For each cluster we excluded the innermost arcseconds individually. In the following, we only focus on our results centred on the S/N-peak, but we summarise all results in Tables A.1-A.5 in the appendix. We refer to the best fit model as the mass model centred on the S/N-peak which gives the smaller $\chi^2_{\rm dof}$ compared to the other mass models.

We compared our mass estimates with those from previous studies which have a large overlap with our sample and are most recent (Fig. 6.10, *lower right*) to check for possible systematics in our method because our mass estimates centred on different cluster centres are obtained with the

same method. The consistency between the mass estimates for different cluster centres confirms that the S/N-peak can be used as an alternative definition of the cluster centre. Yet, this does not give rise to systematics. Our cluster masses are also consistent for different mass models except the SIS-model for MS0451.6−0305 (Fig. 6.10, *upper panels*).

Most clusters have already been analysed with several methods, e.g. X-ray observations (XRAY), dynamical estimates (DYN), where the line-of-sight velocity dispersion of the cluster galaxies is measured, or Sunyaev-Zeldovich effect (SZE) observations, which consider the energy gain of CMB-photons due to scattering with the ICM. Some clusters were already studied with weak (WL) or strong (SL) lensing approaches. If the cosmologies used in previous analyses differ from our ΛCDM ($\Omega_m = 0.27$, $\Omega_\Lambda = 0.73$ and $h = 0.72$), we transformed their results to our cosmology and listed them in Table 6.4. We compared the results from other studies at our best fit r_{200}, except for XRAY and SZE where we compared the masses at r_{500} and r_{2500} instead because it is too unreliable to extrapolate them to r_{200} (Table 6.3). Compared to these previous studies done with different methods, our results using the same method are more suitable for mass calibration studies. For a detailed comparison with hydrostatic mass estimates, X-ray masses obtained with the same method for all clusters would also be more suitable for the same reason.

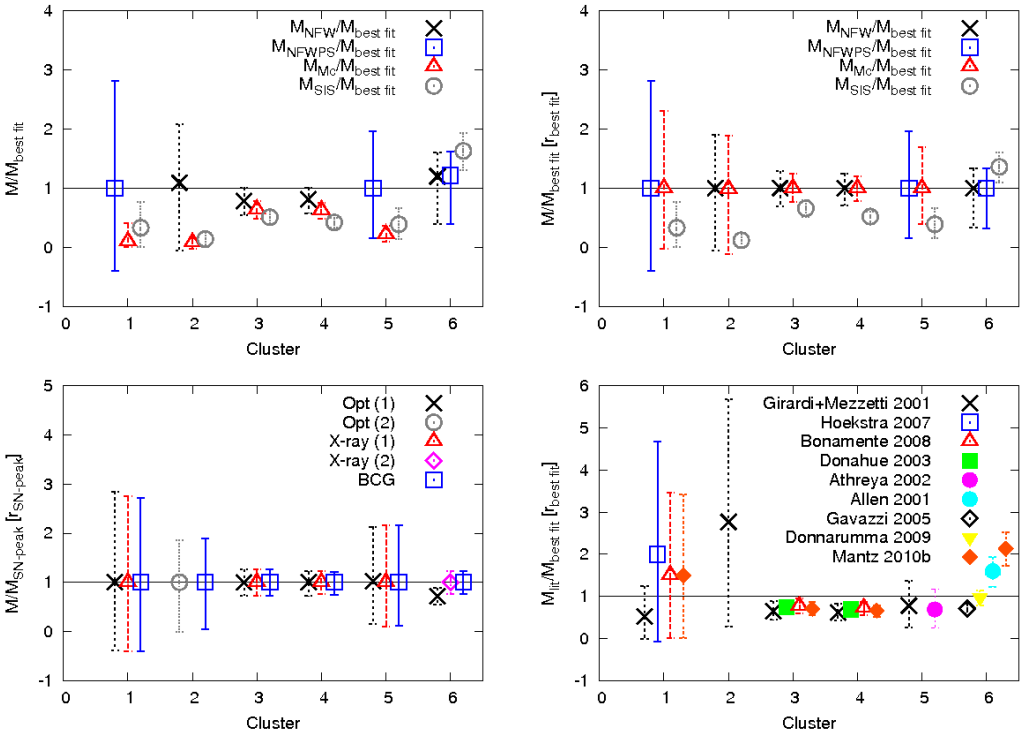

Figure 6.10: Mass ratios for CL0015.9+1609 (1), CL0413−6559 (2), $MS0451_{ACS}$ (3), $MS0451_{zphoto}$ (4), MS1008.1−1224 (5) and MS2137.3−2353 (6). *Upper left:* Cluster masses for different mass models versus the best fit model centred on the S/N-peak. *Upper right:* The same as in the upper left panel but the masses are normalised to the cluster radius of the best fit model. *Lower left:* Best fit cluster mass centred on the S/N-peak versus cluster masses of the same mass model at other cluster centres. *Lower right:* Best fit cluster masses centred on the SN-peak versus cluster masses from the literature. Our mass is calculated at r_{500} and r_{2500} for those studies who give masses at those radii.

6.3.1 CL0015.9+1609

The tangential shear profile centred on the S/N-peak is plotted in Fig. 6.11 and the masses and parameters are summarised in Table A.1 in the appendix. The tangential shear profile is disturbed due

Table 6.3: Masses for CL0015.9+1609, MS0451.6−0305 and MS2137.3−2353 compared at the radii of those previous studies which used higher overdensities, i.e. Allen et al. 2001 (A01), Donahue et al. 2003 (D03), Bonamente et al. 2008 (B08) and Mantz et al. 2010a (M10). The masses from the NFW-profile and the truncated NFW, $M_{\rm NFW}$ and $M_{\rm NFW\&PS}$, respectively, are the same for CL0015.9+1609 because r_{200} exceeds the field-of-view. For MS0451.6−0305, we neglect the contribution from large-scale-structure for reasons of simplicity.

	r [kpc]	$M_{\rm NFW}$ $[10^{14}M_\odot]$	$M_{\rm NFW\&PS}$ $[10^{14}M_\odot]$	M_{Mc} $[10^{14}M_\odot]$	$M_{\rm SIS}$ $[10^{14}M_\odot]$
CL0015.9+1609	$507^{(B08)}$	$2.19^{+2.83}_{-2.17}$	$2.19^{+2.83}_{-2.17}$	$1.06^{+0.28}_{-0.25}$	$1.37^{+0.18}_{-0.20}$
	$1470^{(M10)}$	$11.09^{+14.31}_{-10.95}$	$11.09^{+14.31}_{-10.95}$	$4.59^{+0.43}_{-0.46}$	$3.97^{+0.52}_{-0.58}$
$MS0451_{\rm ACS}$	$1319^{(D03)}$	$14.40^{+2.61}_{-2.89}$	$16.26^{+3.05}_{-3.09}$	$13.19^{+1.40}_{-1.47}$	$9.11^{+0.28}_{-0.32}$
	$526^{(B08)}$	$4.81^{+1.04}_{-1.15}$	$4.94^{+0.93}_{-0.94}$	$4.96^{+0.52}_{-0.55}$	$3.63^{+0.11}_{-0.13}$
	$1310^{(M10)}$	$14.30^{+2.59}_{-2.87}$	$16.13^{+3.02}_{-3.06}$	$13.11^{+1.39}_{-1.46}$	$9.05^{+0.55}_{-0.64}$
$MS0451_{\rm zphoto}$	$1319^{(D03)}$	$15.91^{+2.67}_{-3.13}$	$17.61^{+2.66}_{-3.14}$	$14.26^{+1.30}_{-1.38}$	$8.03^{+0.22}_{-0.25}$
	$526^{(B08)}$	$5.16^{+0.87}_{-1.02}$	$5.27^{+0.80}_{-0.94}$	$5.29^{+0.48}_{-0.51}$	$3.20^{+0.09}_{-0.19}$
	$1310^{(M10)}$	$15.79^{1.39}_{-3.11}$	$17.47^{2.64}_{-3.12}$	$14.17^{+1.29}_{-1.37}$	$7.98^{+0.43}_{-0.49}$
MS2137.3−2353	$460^{(A01)}$	$1.43^{+0.42}_{-0.93}$	$1.44^{+0.42}_{-0.94}$	$1.18^{+0.19}_{-0.20}$	$1.44^{+0.14}_{-0.14}$
	$1060^{(M10)}$	$2.57^{+0.75}_{-1.66}$	$2.59^{+0.75}_{-1.70}$	$2.21^{+0.31}_{-0.37}$	$3.31^{+0.31}_{-0.32}$

Table 6.4: Literature masses for the cluster sample. Allen et al. (2001) and Bonamente et al. (2008) calculated their masses at r_{2500}, Donahue et al. (2003) and Mantz et al. (2010a) at r_{500}. We compared our results to the radii of these studies and transformed the masses from the other studies to the radius of our best fit model.

Cluster	Method	r [kpc]	M $[10^{14}M_\odot]$	c_{200}	σ_v [km s^{-1}]	Reference
CL0015.9+1609	DYN	1208	$5.28^{+1.92}_{-1.67}$		984^{+130}_{-95}	Girardi & Mezzetti (2001)
	WL	2083	$37.5^{+12.6}_{-11.8}$		1164^{+151}_{-173}	Hoekstra (2007)
	XRAY&SZE	507	3.3 ± 0.4			Bonamente et al. (2008)
	XRAY	1470	16.5 ± 2.5			Mantz et al. (2010a)
CL0413−6559	XRAY		0.40 ± 0.69			Smail et al. (1997)
	DYN	861	$3.36^{+2.67}_{-2.01}$		681^{+256}_{-185}	Girardi & Mezzetti (2001)
MS0451.6−0305	DYN	1625	$12.58^{+3.92}_{-3.71}$		1317^{+122}_{-103}	Girardi & Mezzetti (2001)
	XRAY	1319	12.15			Donahue et al. (2003)
	XRAY&SZE	526	3.8 ± 0.5			Bonamente et al. (2008)
	XRAY	1310	11.5 ± 1.5			Mantz et al. (2010a)
MS1008.1−1224	DYN	1639	$11.92^{+3.99}_{-3.83}$		1033^{+115}_{-105}	Girardi & Mezzetti (2001)
	WL	500	3.19 ± 0.69		900	Athreya et al. (2002)
MS2137.3−2353	XRAY&SL	460	$1.89^{+0.25}_{-0.31}$			Allen et al. (2001)
	SL&WL	1890	$7.72^{+0.47}_{-0.24}$	$11.73^{+0.55}_{-0.55}$		Gavazzi (2005)
	XRAY&SL	1410	4.4 ± 0.3	$8.7^{+0.7}_{-0.9}$		Donnarumma et al. (2009)
	XRAY	1060	4.7 ± 0.6			Mantz et al. (2010a)

to merging, and infalling galaxies from filaments may be responsible for it. Because of merging, CL0015.9+1609 is not highly concentrated towards the centre. Correspondingly, we measured a low concentration $c_{200} = 1.2^{+0.9}_{-1.1}$.

The SIS, which is steeper on scales $r < r_{200}/c_{200}$ than the NFW-profile, and the one-parameter NFW-model with fixed concentration, Mc, which overpredicts the concentration with $c_{\rm NFW} = 6.8$, do not provide good fits to the shear profile. For a relaxed cluster with the same mass and redshift, $c_{\rm NFW}$ can be appropriate, but it provides a too small r_{200}. With $\sigma_v = 762^{+50}_{-55}$km s^{-1} and $M_{\rm SIS} = 5.38^{+0.71}_{-0.78} \times 10^{14} M_\odot$ inside r_{200}, the SIS underpredicts the cluster mass. The velocity dispersion from DYN is measured from galaxy spectra but infalling galaxies can show large line-of-sight velocities. On the other hand, σ_v is a poor estimate of the tangential shear fitted to an SIS.

The NFW-model fits best with $r_{200} = 1993^{+857}_{-656}$ kpc, $c_{200} = 1.2^{+0.9}_{-1.1}$ and $M_{200} = 16.39^{+21.14}_{-16.18} \times 10^{14} M_\odot$. Large errors on r_{200} and subsequently on M_{200} are due to: (1) the cluster is a merger and (2) r_{200} is outside the field-of-view. Because of the latter, our results for NFW and NFW&PS are identical.

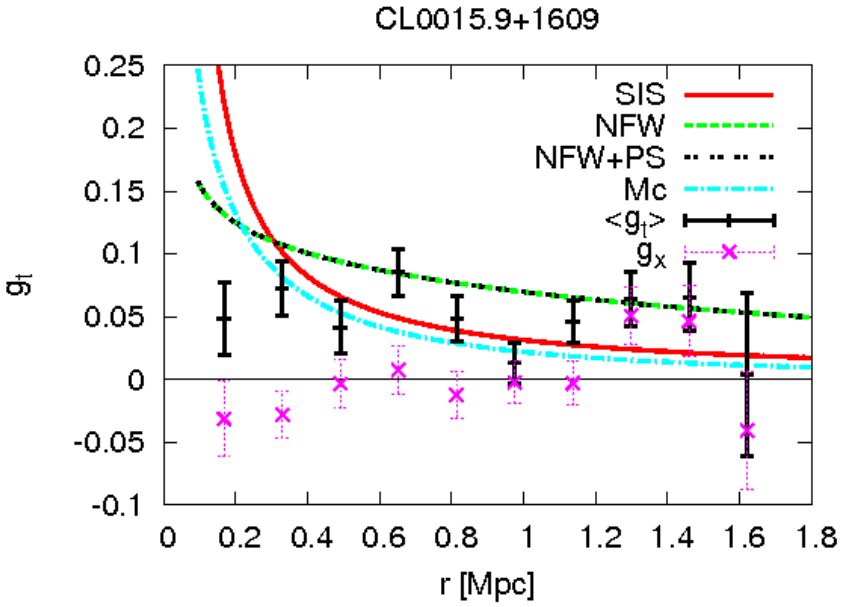

Figure 6.11: Tangential shear profile for CL0015.9+1609 centred on the S/N peak. We fitted the two parameter models NFW and the truncated NFW (NFW&PS) and the one parameter models SIS and the *Mc*-model to the tangential shear of all sources. We cut out the innermost 14″. Note that the shear profile is not very steep and disturbed due to effects of merging.

Our best fit model is consistent with previous studies (Fig. 6.10 *lower right*, Tables 6.4 and 6.3).

6.3.2 CL0413−6559

The tangential shear profile is plotted in Fig. 6.12 and the masses and model parameters are summarised in Table A.2 in the appendix.

Our detection significance 4.34σ is low for space-based data. Since S/N is correlated with mass we inferred a small total mass that is not highly concentrated towards the centre. The *Mc*-model does not fit the cluster profile well although $c_{\rm NFW} = 10.5$ is reasonable for an average cluster with this mass and redshift. The SIS-profile also does not fit the cluster profile well because it is steeper on small scales compared to the NFW-profile.

The truncated NFW (NFW&PS) models the tangential shear profile with $r_{200} = 839^{+191}_{-186}$ kpc, $c_{200} = 2.5^{+1.6}_{-1.8}$ and $M_{200} = 1.18^{+0.81}_{-0.79} \times 10^{14} M_{\odot}$ better than our other models although the NFW-parameters do not differ much from NFW&PS. The low c_{200} values we obtained with both our NFW-models and the disturbed shear profile suggest that this object is still in the process of forming. This is also supported by the high fraction of spiral galaxies and low X-ray luminosity which indicates a shallow gravitational potential and less rich intra-cluster gas (Sect. 4.1.2).

Our NFW&PS (Table A.2) is not consistent with the literature (Fig. 6.10, Table 6.4). We cannot say whether our results agree with Smail et al. (1997), because their mass is from the mass-luminosity scaling relation without quoting a value for an overdensity radius. The mass inferred by Girardi & Mezzetti (2001) from DYN is three times larger than ours which may be a result of the forming process of this cluster because some galaxies associated to the cluster may not be in dynamical equilibrium which can cause high velocity dispersions.

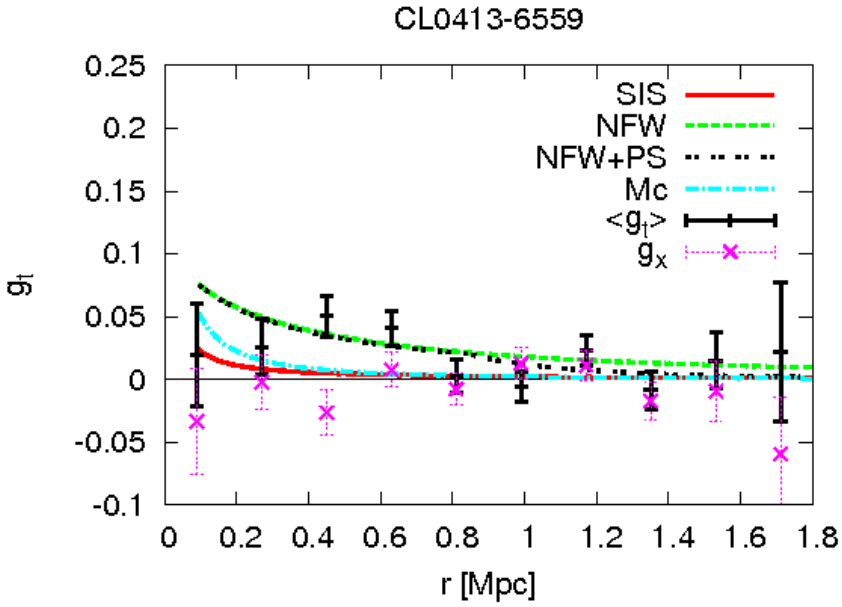

Figure 6.12: Tangential shear profile for CL0413−6559 centred on the S/N peak. We fitted the two parameter models NFW and the truncated NFW (NFW&PS) and the one parameter models SIS and the *Mc*-model to the tangential shear of all sources. Note the flatness of the shear profile and that disturbances appear pronounced, which is because CL0413−6559 is a low mass cluster.

6.3.3 MS0451.6−0305

The tangential shear profiles are plotted in Fig. 6.13 and the masses and model parameters are in Table A.3 in the appendix, where the second lower and upper errors of M_{200} and c_{200} are from Table 6.2. The shear profile of $\mathrm{MS0451}_{\mathrm{zphoto}}$ is smoother than that of $\mathrm{MS0451}_{\mathrm{ACS}}$ due to the photometric redshifts. Given r_{200} well within the field-of-view, we observed a significant difference between NFW and NFW&PS. From their χ^2_{dof}, NFW&PS with $r_{200} = 2432^{+152}_{-154}$ kpc, $c_{200} = 2.9^{+0.4+1.6}_{-0.4-1.6}$ and $M_{200} = 30.08^{+5.64+0.43}_{-5.71-0.43} \times 10^{14} M_{\odot}$ for $\mathrm{MS0451}_{\mathrm{ACS}}$ is the better fit. A truncation of the NFW-profile seems reasonable if the data cover a large area around the cluster. More observations are required to further test this. Our SIS-model with $\sigma_v = 1220^{+37}_{-43}\mathrm{km\,s^{-1}}$ provides a lower mass than the best-fit model at r_{200}. With $c_{\mathrm{NFW}} = 4.6$, the *Mc*-model agrees with the NFW-model fit.

The masses for $\mathrm{MS0451}_{\mathrm{ACS}}$ and $\mathrm{MS0451}_{\mathrm{zphoto}}$ show a spread among the different mass models, but are consistent with each other after normalising to $r_{200} = 2432$ kpc except for the SIS-model. The masses are also consistent with *Chandra*-observations by Donahue et al. (2003) and Bonamente et al. (2008) (Fig. 6.10, Tables 6.3 and 6.4). We found higher masses for $\mathrm{MS0451}_{\mathrm{zphoto}}$ than for $\mathrm{MS0451}_{\mathrm{ACS}}$, yet both are consistent with each other.

χ^2_{dof} is higher for $\mathrm{MS0451}_{\mathrm{zphoto}}$ than for $\mathrm{MS0451}_{\mathrm{ACS}}$ due to the inclusion of individual source redshifts. Yet, the results for both data sets are consistent although the masses for $\mathrm{MS0451}_{\mathrm{zphoto}}$ are higher and the concentrations are lower compared to $\mathrm{MS0451}_{\mathrm{ACS}}$. The errors on our results do not decrease for $\mathrm{MS0451}_{\mathrm{zphoto}}$ for two-parameter models, but for the one-parameter models, which may be because of the interdependence between r_{200} and c_{200}. To quantify this effect further, more photometric redshifts would be required.

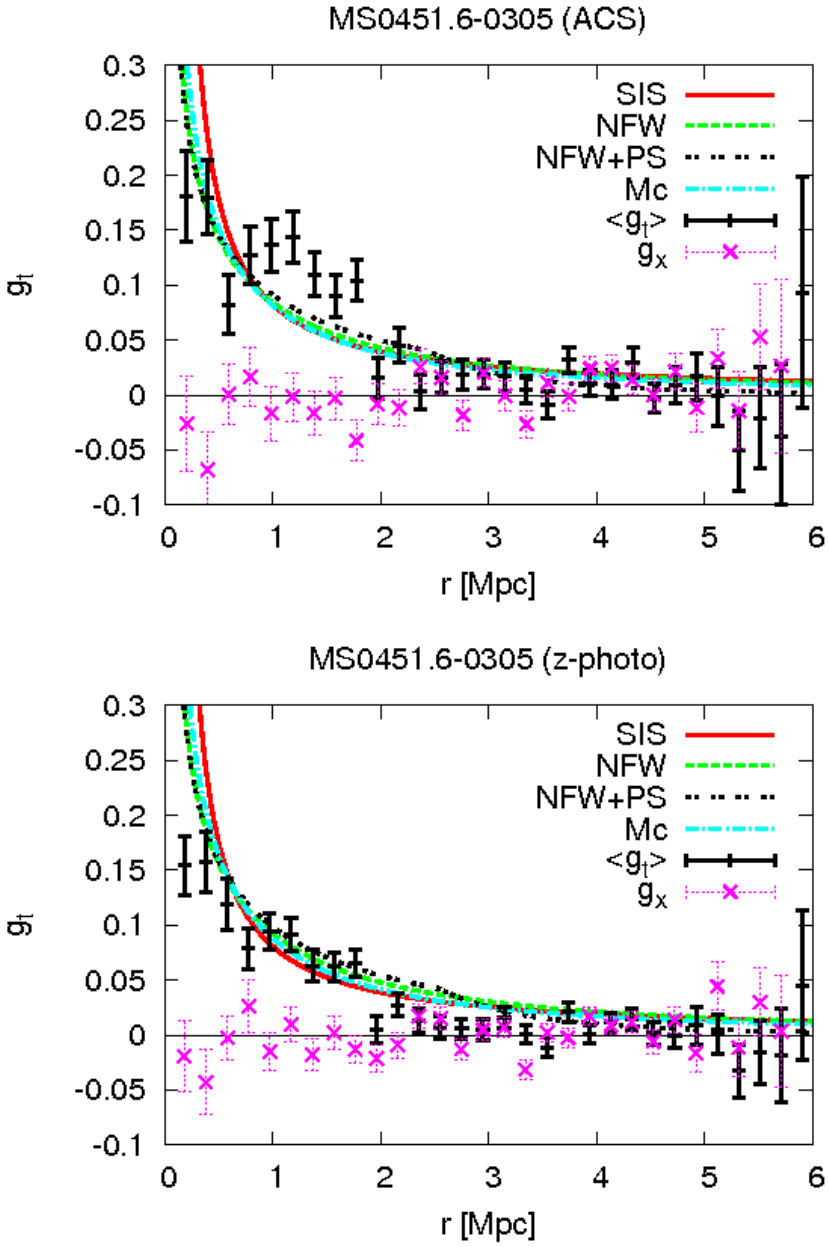

Figure 6.13: Tangential shear profile for $MS0451_{ACS}$ (*upper*) and $MS0451_{zphoto}$ (*lower*) centred on the S/N peak. We fitted the two parameter models NFW and the truncated NFW (NFW&PS) and the one parameter models SIS and the *Mc*-model to the tangential shear of all sources. The crosses with the thin, dotted error bars display the cross component $g_\times$. Due to the high number density of sources, the error bars are small. We cut out the innermost 17″. Note that for $MS0451_{zphoto}$ the first data point of $g_\times$ has a high negative value, wherefore it is not plotted which is because both plots have the same axes limits for reasons of comparison.

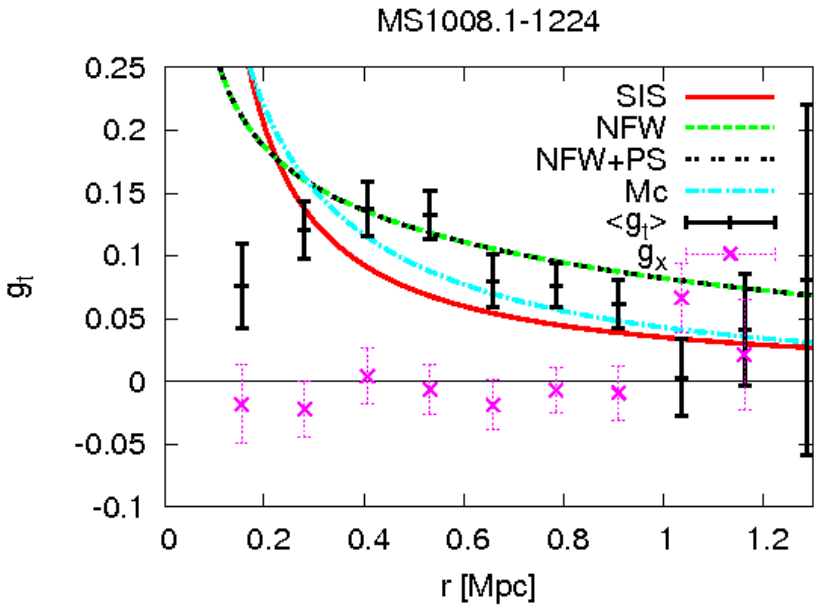

Figure 6.14: Tangential shear profile for MS1008.1−1224 centred on the S/N peak. We fitted the two parameter models NFW and the truncated NFW (NFW&PS) and the one parameter models SIS and the *Mc*-model to the tangential shear of all sources. We cut out the innermost 21″. The shear profile does not approach zero in the outskirts of the field-of-view, because r_{200} is 1 Mpc beyond the field-of-view.

6.3.4 MS1008.1−1224

The tangential shear profile is plotted in Fig. 6.14 and the masses and model parameters are in Table A.4 in the appendix. Since r_{200} lies beyond the field-of-view, NFW and NFW&PS yield the same results. For the same reason, the tangential shear does not drop to zero at the edge of the data field. The NFW-fit to the tangential shear is the best fit model with $r_{200} = 2415^{+546}_{-478}$ kpc, $c_{200} = 2.2^{+0.8}_{-0.8}$ and $M_{200} = 22.48^{+15.25}_{-13.35} \times 10^{14} M_{\odot}$. The errors on r_{200} are large because it is 1 Mpc beyond the field-of-view.

As MS1008.1−1224 is a merger, the tangential shear profile is disturbed and the concentration is low. The *Mc*-model provides a too high concentration ($c_{\rm NFW} = 6.8$) and fits the shear profile worse than the two-parameter NFW-models. Our SIS-model underpredicts the cluster mass with $\sigma_v = 850^{+35}_{-38} \mathrm{km\,s^{-1}}$ and $M_{\rm SIS} = 8.81^{+0.67}_{-0.73} \times 10^{14} M_{\odot}$, because the profile is too steep towards the centre for such a merging cluster. The best fit model agrees with Athreya et al. (2002) who fitted an SIS-lens to the cluster and to dynamical estimates (Girardi & Mezzetti 2001, Fig. 6.10 *lower right*, Table 6.4).

6.3.5 MS2137.3−2353

The tangential shear profile is plotted in Fig. 6.15 and the masses and model parameters are in Table A.5 in the appendix. All four models trace the tangential shear profile. The shape of the tangential shear profile suggests that this cluster is relaxed. The results for all mass models are consistent (Fig. 6.10 *lower left*, Tables 6.3 and 6.4).

Since r_{200} is close to the border of the field-of-view, NFW and NFW&PS provide similar results, with high concentrations. The *Mc*-model fits the shear profile slightly better towards the centre giving $c_{\rm NFW} = 7.5$, $r_{200} = 1123^{+60}_{-63}$ kpc and $M_{200} = 2.55^{+0.81}_{-1.78} \times 10^{14} M_{\odot}$ and agrees with

Gavazzi (2005) and Donnarumma et al. (2009) but not with Allen et al. (2001) (Fig. 6.10 *lower right*, Table 6.3, Table 6.4).

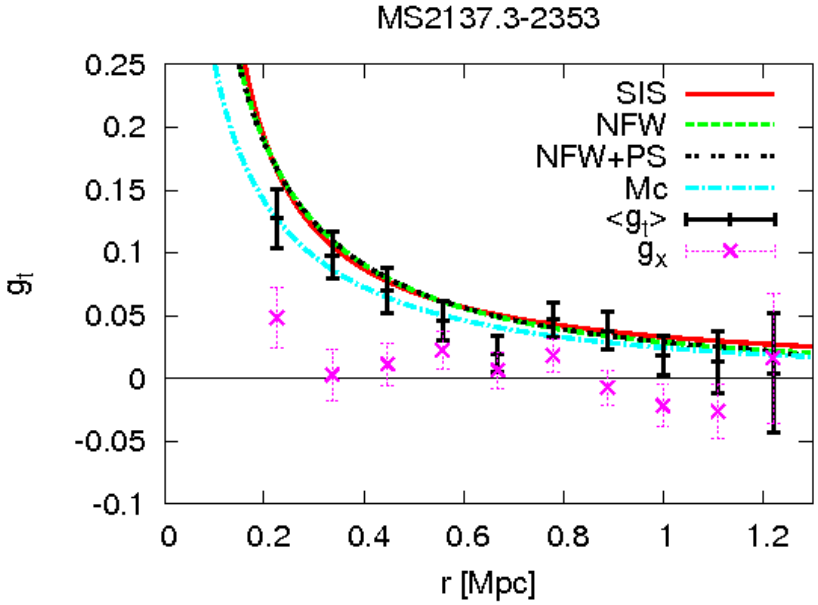

Figure 6.15: Tangential shear profile for MS2137.3−2353 centred on the S/N peak. We fitted the two parameter models NFW and the truncated NFW (NFW&PS) and the one parameter models SIS and the *Mc*-model to the tangential shear of all sources. We cut out the innermost 37″. Not the textbook-like behaviour of the tangential shear since this cluster is spherically relaxed.

Chapter 7

X-ray analysis

This chapter describes the methods and results of the X-ray analysis for those three clusters which are based on *XMM-Newton* data and for one which is based on *Chandra* data.

In Sect. 7.1, I will describe the data preparation such as point source detection, determination of the flux-weighted X-ray centroid and background subtraction. In Sect. 7.2, I will discuss the data analysis on how the surface brightness and temperature profiles were derived. From these profiles, the mass profiles will be calculated. The masses will be compared to previous studies at r_{500} and r_{2500}. Global properties such as temperature, metallicity and luminosity will be presented and discussed in Sect. 7.3.

7.1 Data preparation

7.1.1 Point source detection

While the ICM emission is predominantly composed of thermal bremsstrahlung, the X-ray emission from point sources, such as from AGN in the central cluster galaxies, is non-thermal. Point sources are hard to identify when their emission is superposed with the X-ray emission peak of the clusters. Especially for cool-core clusters, peaks due to cooling cores and central point sources such as AGN are difficult to distinguish (e.g. Zhang et al. 2006). Since they contaminate the spectra, point sources have to be removed from the data.

We used the `SAS` command "edetect_chain" to detect point sources following Zhang et al. (2006). This command generates a list of bright point sources in the field-of-view and carries out the point source detection simultaneously for all three detectors in the energy bands 0.3–0.5 keV, 0.5–2 keV, 2–4.5 keV, 4.5–7.5 keV and 7.5–12 keV. Thereby it corrects for the out-of-time events for pn. We used cut-off radii of 25″ for most point sources and 40″ for the bright point sources which is comparable to the *XMM-Newton* Point Spread Function cut-off radius of $\sim$ 45″. These radii were chosen such that they enclose $\sim$ 90% flux of the point sources. In total, we detected 65 point sources in the field of CL0015.9−1609, 81 for MS0451.6−0305 and 27 for MS2137.3−2353. The point sources were subtracted from the events lists before we proceeded the analysis further.

The point source subtraction for MS1008.1−1224 was done by Helen Eckmiller with the `Ciao`[1]-tool "wavdetect" which searches for "Mexican hat"-shaped wavelets following Hudson et al. (2006). This tool detects point sources and defines ellipses around them. The major and minor axes of those ellipses are 3 times the standard deviation of the Gaussian of the wavelet. The point source list was manually checked for bad detections and too small cut-off areas. Thus, 59

[1] http://cxc.harvard.edu/ciao4.2/threads/index.html

point sources were detected and removed from the event lists. The holes in the images were filled with the averaged emission from a surrounding area that is 2 times larger than the ellipses.

7.1.2 Determination of the X-ray centroid

For relaxed clusters the peak of the X-ray emission can be used as approximation of the cluster centre. The determination of the X-ray centre becomes more complicated for clusters which are disturbed by e.g. merging or AGN heating.

We used the method of Zhang et al. (2010) to determine the flux-weighted centroid iteratively from the flat-fielded X-ray images in the 0.7–2 keV band. This energy range is chosen because the cluster emission in this band is almost independent of the gas temperature. The algorithm is initialised by centering an aperture of radius 1′ on the X-ray emission peak. Within this aperture the initial flux-weighted centre is determined. Then, the flux-weighted centre is iteratively re-derived in an aperture which is 1′ larger than the previous one and which is centred on the previously determined flux-weighted centre. We continued this procedure until the coordinates of the flux-weighted centre do not vary anymore which usually takes less than 10 iterations (Zhang et al. 2010)[2]. Thereby, the flux-weighted X-ray centroid was defined as the coordinates of the final flux-weighted centre. As error for the position of the flux-weighted X-ray centroid the position angle error of *XMM-Newton* which is 6″ was used. For the *Chandra*-cluster, the PSF which is negligible with 0.″5 was used as uncertainty.

The flux-weighted X-ray centroids and the X-ray emission peaks are listed in Table 7.1. We compared both positions to the X-ray centres of Lewis et al. (1999) and Allen et al. (2008) in the last column of Table 7.1. Except for the relaxed cluster MS2137.3−2353, our flux-weighted X-ray centroids are not consistent with the X-ray centres of these studies because they used the X-ray emission peak as centre. Comparing our X-ray emission peak with Lewis et al. (1999) and Allen et al. (2008), we found consistency for CL0015.9+1609, MS0451.6−0305 and MS2137.3−2353. For MS1008.1−1224, we observed an offset which might be due that the X-ray emission is slightly asymmetric (Lewis et al. 1999).

Figure 7.1 shows the X-ray and weak lensing signal-to-noise contours and the respective centres. The projected distances between the S/N-peak (Table 6.1) and the flux-weighted X-ray centroid are denoted as $\Delta_{\mathrm{fw-wl}}$ and the projected distances between the S/N-peak and the X-ray emission peak are denoted as $\Delta_{\mathrm{em-wl}}$. The S/N-peak and the flux-weighted X-ray centroid agree for the relaxed cluster MS2137.3−2353, but the other clusters have offsets that are larger than the uncertainty σ_{pos} from bootstrapping (Sect. 6.1.4) plus the instrumental uncertainties. This can be due to that CL0015.9+1609 and MS1008.1−1224 are mergers. For MS0451.6−0305, the X-ray emission is slightly elliptical in the centre while the weak lensing signal-to-noise contours are not which might explain the offset for this cluster. The X-ray emission peak and the S/N-peak show better agreement, i.e. $\Delta_{\mathrm{em-wl}} < \sigma_{\mathrm{pos}}$. For MS1008.1−1224, the offset $\Delta_{\mathrm{em-wl}} = 17.''1$ smaller than $\Delta_{\mathrm{fw-wl}} = 20.''4$ but still larger than $\sigma_{\mathrm{pos}} + 0.''5$.

7.1.3 Background subtraction

While for low-redshift clusters the cosmic X-ray background (CXB, Sect. 3.1.6) has to be estimated from external fields, we can use the cluster outskirts for our clusters to statistically estimate the local CXB. We used an annulus of $1.2r_{200} - 1.5r_{200}$ whereby r_{200} is from the best weak lensing fits (Sect. 6.3). This annulus was chosen because it is not contaminated by the cluster emission and not too close to the borders of the field-of-view, where instrument effects can bias our measurements.

[2]For high-redshift clusters, the algorithm converges even faster.

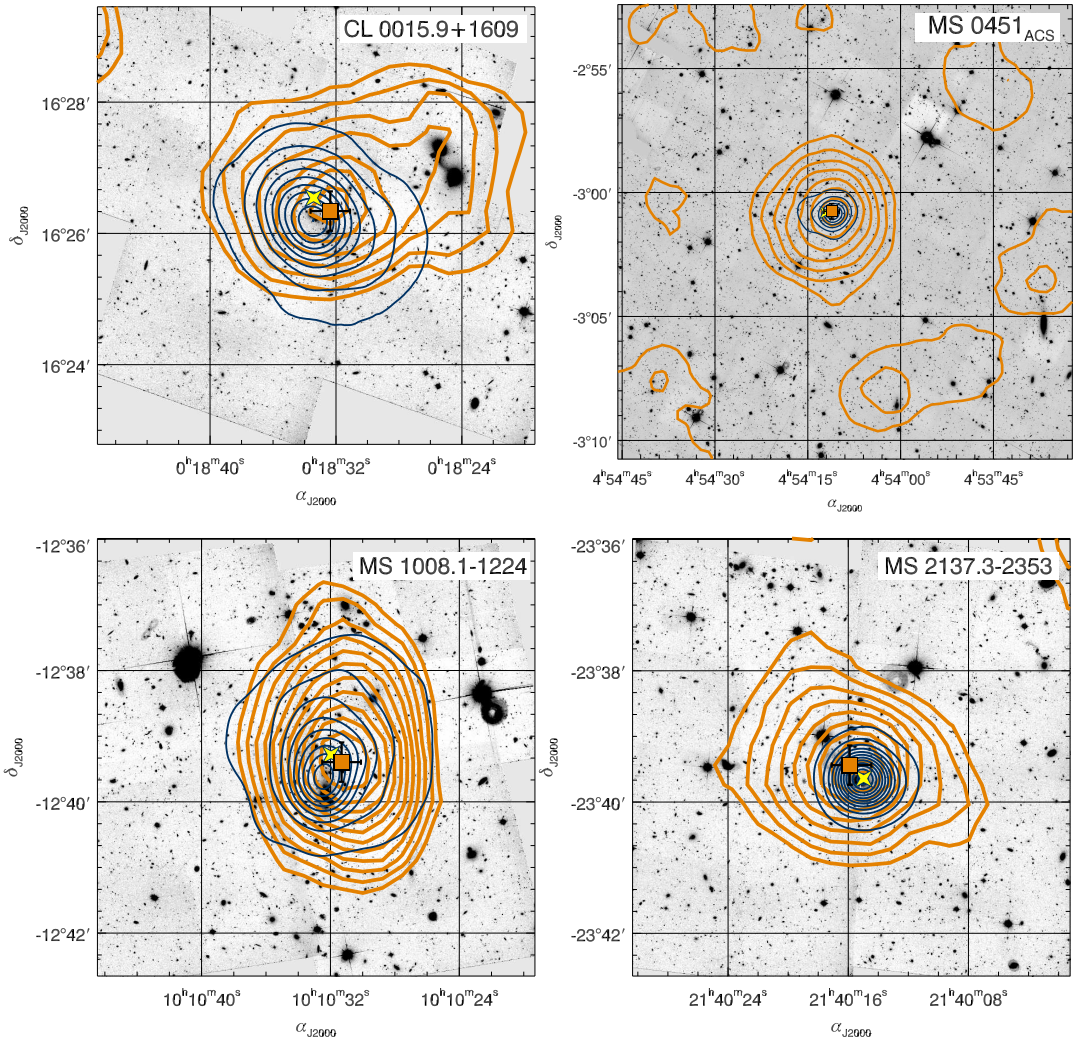

Figure 7.1: X-ray (blue) and weak lensing signal-to-noise ratio contours (orange). The orange box denotes the weak lensing centre and the yellow star is the flux-weighted X-ray centroid. Except for MS2137.3−2353, the flux-weighted X-ray centroid is not in the centre of the contours because they show the X-ray emission which has its maximum at the X-ray emission peak.

Table 7.1: Comparison of different cluster centres. RA_X^{fw} and Dec_X^{fw} are the coordinates of the flux-weighted X-ray centroid and RA_X^{em} Dec_X^{em} are the coordinates of the X-ray emission peak. Both coordinates are given in world coordinates. Δ_{fw-wl} and Δ_{em-wl} are the offsets between the flux-weighted X-ray centroid / X-ray emission peak and the S/N-peak from weak lensing, σ_{pos} is the uncertainty of the S/N-peak from bootstrapping (Sect. 6.1.4). The last column lists the offsets to the X-ray centres of Lewis et al. (1999) (2) and Allen et al. (2008) (4), whereby the first value is the offset using the flux-weighted X-ray centroid and the second one is from using the X-ray emission peak.

Cluster	RA_X^{fw}	Dec_X^{fw}	RA_X^{em}	Dec_X^{em}	Δ_{fw-wl}	Δ_{em-wl}	σ_{pos}	other
CL0015.9+1609	00:18:33.4	16:26:32	00:18:33.7	16:26:09	22.″2	10.″0	10.″5	20.″1, 6.″9 (2)
MS0451.6−0305	04:54:12.1	−03:00:49	04:54:11.5	−03:00:56	15.″2	5.″6	8.″3	10.″5, 10.″3 (2)
MS1008.1−1224	10:10:31.9	−12:39:17	10:10:32.4	−12:39:53	20.″4	17.″1	9.″2	15.″0, 21.″4 (2)
MS2137.3−2353	21:40:14.9	−23:39:39	21:40:14.9	−23:39:39	4.″2	5.″3	9.″2	1.″7, 1.″7 (4)

The background areas were scaled to the areas of the annuli which were used to measure the surface brightness and temperature distributions. For pn, we corrected for the out-of time events (OOT) by a fraction of 2.32% (Sect. 4.4.2). The particle background was removed from the data as a step of the reduction (Sect. 4.4.2).

7.2 Results

7.2.1 Spectral analysis

The temperature profiles of galaxy clusters are useful tools to study the thermodynamical history of clusters. For temperature measurements with $\sim$ 15% uncertainty, we determined suitable annuli centred on the flux-weighted X-ray centroid for the spectral fitting following the method of Zhang et al. (2008). We used the $2-7$ keV band to obtain at least 500 counts per annulus in MOS2[3] after background subtraction, which gives $\sim$ 2000 counts per annulus in total (Sect. 4.4.1). The $2-7$ keV energy range is sensitive to temperature measurements of massive clusters with $T_{\rm X} \gtrsim 3$ keV (Zhang et al. 2007). To avoid that the bins were affected by the instrument PSF, the bins had to be at least $0\farcs5$ each. We obtained 4 temperature bins for CL0015.9+1609 and 3 for MS0451.6−0305 and MS2137.3−2353, respectively, because these clusters are less extended in X-rays. For MS1008.1−1224, spectra for the following annuli were created by Helen Eckmiller following Eckmiller et al. (2011): $0-0\farcs5$, $0\farcs5-1\farcm0$ and $1\farcm0-1\farcm5$. There annuli were chosen such that we can compare the temperature profile of this cluster with the *XMM-Newton* clusters.

We regrouped the data with the "grppha"-command such that each channel consists of at least 100 counts. This provides good photon statistics in each channel. The spectral fitting was performed with the publicly available `HEASOFT` software package `XSPEC 12.6.0` (henceforth denoted as `XSPEC`). We used the $0.7-10$ keV band for the spectral fitting because this guarantees that the hot clusters ($T_{\rm X} \sim 9-11$ keV) have significant counts at higher energies. We accounted for the background by giving `XSPEC` the respective background files and for the detector response with the files generated with the tasks "rmfgen" and "arfgen". The spectra were fitted with "wabs+mekal" and are given in the appendix for the *XMM-Newton* clusters (Figs. B.1-B.3). The former is a one-parameter model that models the absorption from neutral gas via the Galactic hydrogen column number density $n_{\rm H}$ which we fixed to the values from the Leiden/Argentine/Bonn Galactic HI-Survey (LAB-Survey, Kalberla et al. 2005). The "mekal" model describes the emission spectrum of hot, diffuse gas based on Mewe et al. (1985, 1986) and Kaastra (1992) with Fe-L line emission (Liedahl et al. 1995) and line emission from other elements as observed for the ICM of galaxy clusters[4]. The "mekal" model has six parameters: (1) plasma temperature, (2) hydrogen density of the ICM, (3) metal abundance in solar units (Anders & Grevesse 1989), (4) cluster redshift, (5) a switch parameter to decide whether the model spectrum for each temperature will be fitted with "mekal" or determined from a pre-calculated table and (6) the normalisation which depends on the electron and hydrogen number densities of the ICM and the angular diameter distance of the cluster. For each temperature bin, we determined temperature, metallicity and normalisation of the "mekal"-model.

The spectra were fitted simultaneously for all three detectors. For each annulus, temperatures and metallicities of the different detectors are consistent. The MOS data provide slightly higher temperatures than pn because it is more sensitive at low energies. Thus, pn measurements are affected by the soft band.

[3] We did not use MOS1 because this detector has broken CCD-chip.

[4] The mekal model includes line emission from He, C, N, O, Ne, Na, Mg, Al, Si, S, Ar, Ca, Fe and Ni merged into one parameter.

To parametrise the temperature profiles which are plotted in Fig. 7.2, we chose the model of Zhang et al. (2006), a combination of a King model, a Gaussian and a constant ("Gaus+King+cons")

$$T(r) = T_1 \left[1 + \left(\frac{r}{r_C}\right)^2\right]^{-3\beta'+\frac{1}{2}} + T_2 \exp\left[\frac{-\left(r - r_{gc}\right)^2}{2\sigma^2}\right] + T_3\,. \tag{7.1}$$

Here, r_C and β' are core radius and slope of the King-profile, respectively, and r_{gc} is the centre of the Gaussian with width σ. T_{1-3} are the normalisations of each model. Equation (7.1) is not a physical model but follows the empirical shape of the universal temperature profiles of galaxy clusters well due to its flexibility (Zhang et al. 2007, 2008). The temperature profiles were approximated by Eq. (7.1) such that all data points in Fig. 7.2 are reasonably crossed. We list the model parameters in Table 7.2. The temperature uncertainties (dashed curves in Fig. 7.2) were approximated by $(A + rB) \cdot T(r)$ following Zhang et al. (2006).

The third bin of the temperature profile of CL0015.9+1609 is affected by a hot region along the southeast to northwest direction which was also reported by Solovyeva et al. (2007). The cluster emission is elongated along this direction. We did not exclude the hotter region in this annulus because we are interested in the total temperature distribution.

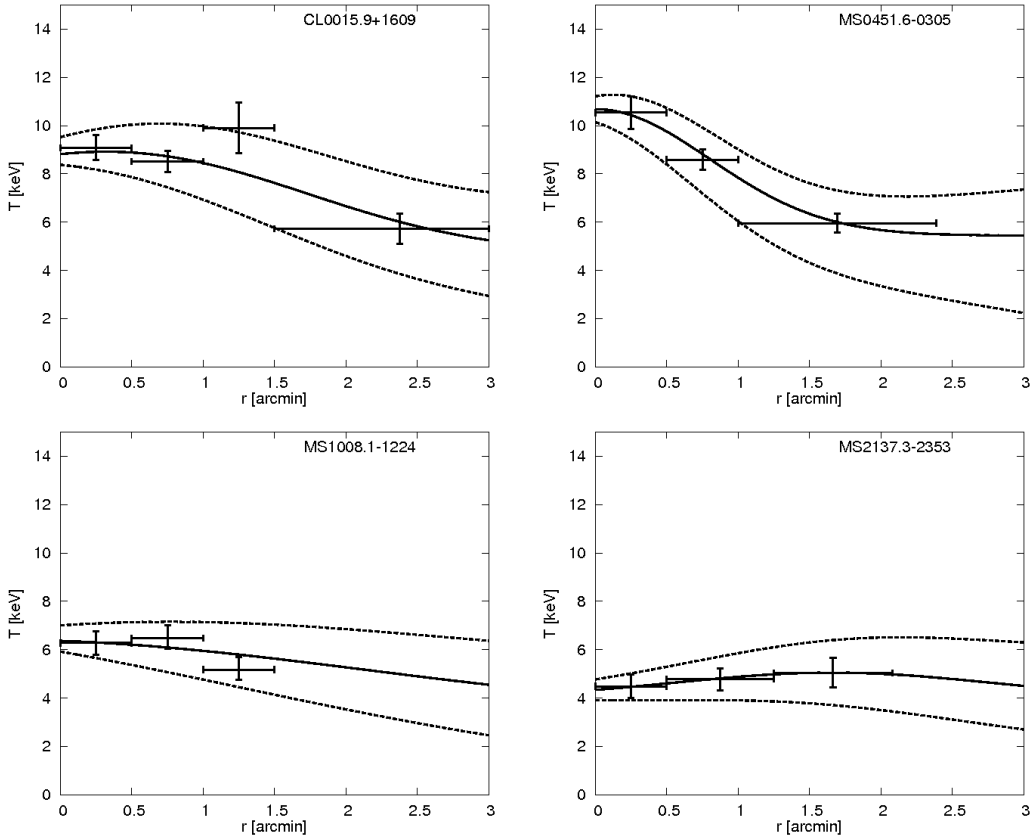

Figure 7.2: Temperature profiles: The horizontal bars denote the bin size and the vertical errors are the 1σ-errors from the spectral fitting with XSPEC. The dashed curves are the 1σ uncertainties on $T(r)$ which we approximated with $(A + rB) \cdot T(r)$.

Figure 7.3 shows the metallicity profiles. Except for MS0451.6−0305, they are similar. Metals are most abundant in the cluster centre because of feedback from AGN and supernovae in the central galaxies. Thus, the iron abundance drops from $0.3Z_\odot < Z < 0.4Z_\odot$ in the central bin to $0.2Z_\odot < Z < 0.3Z_\odot$ in the cluster outskirts. For MS0451.6−0305, the metallicity is low in the centre ($Z \sim 0.2Z_\odot$), increases to $\sim 0.35Z_\odot$ and shows a slightly decreasing trend towards the outskirts which may be due to that the this cluster is not in hydrostatic equilibrium which is also indicated by the high temperature in that annulus (Fig. 7.2) and by Donahue et al. (2003). But the low metallicity in the centre of MS0451.6−0305 may also come from instrumental artifacts due to high signal-to-noise. For CL0015.9+1609 and MS2137.3−2353, the photon statistics do not allow for metallicity measurements in the outer bins because the spectra become biased with noise from the background which artificially amplifies the iron peak. For those bins, the metallicity is fixed to $0.3Z_\odot$ in the spectral fit.

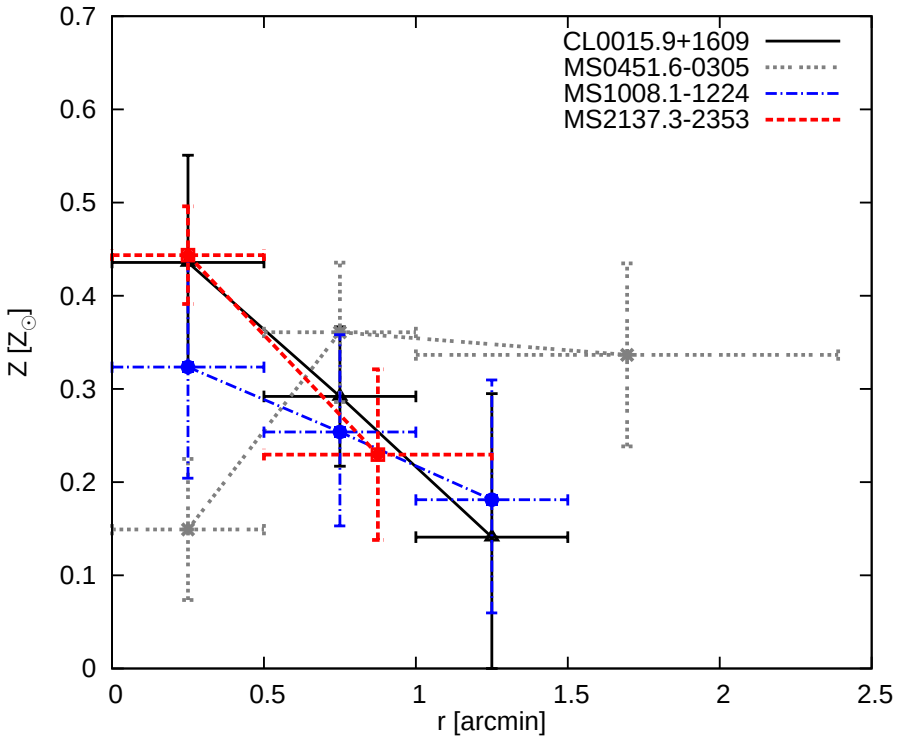

Figure 7.3: Metallicity profiles: The horizontal bars denote the bin size and the vertical errors are the 1σ-errors from the spectral fitting with XSPEC.

7.2.2 Surface brightness profiles

Since the X-ray emission is almost independent of temperature in the $0.7 - 2\,\mathrm{keV}$ energy range, this range is ideal to determine the electron number density distribution of galaxy clusters. We chose the surface brightness bins such that the signal-to-noise ratio in MOS2 for each bin is 3σ higher than the background,

$$\mathrm{S/N_{SB}} = \begin{cases} \dfrac{N_\mathrm{bin} - N_\mathrm{back} \cdot A}{\sqrt{N_\mathrm{bin}}} & \sqrt{N_\mathrm{bin}} > N_\mathrm{back} \cdot A \sqrt{1 + 0.1^2} \\ \dfrac{N_\mathrm{bin} - N_\mathrm{back} \cdot A}{N_\mathrm{back} \cdot A \sqrt{1 + 0.1^2}} & \sqrt{N_\mathrm{bin}} < N_\mathrm{back} \cdot A \sqrt{1 + 0.1^2}\,. \end{cases} \tag{7.2}$$

Here, $N_{\rm bin}$ is the number of photons per annulus, $N_{\rm back}$ is the number of photons in the background and A is the normalisation of the background area with respect to the area of the annulus. The noise is either given by the statistical error of photons per annulus, $\sqrt{N_{\rm bin}}$, or by the number of background photons normalised to the area of the annulus, $N_{\rm back} \cdot A\sqrt{1+0.1^2}$, depending on which provides the higher noise. The factor $\sqrt{1+0.1^2}$, thereby accounts for the particle-induced background which varies by $\lesssim 10\%$ compared to the target observations for most clusters (e.g. Zhang et al. 2007). This provides us with a conservative estimate of background fluctuations 10%.

We applied the annuli obtained with this method to MOS1 and pn. For each detector, the flux in each bin was measured and the surface brightness $S_{\rm X}$ was calculated and fitted with Eq. (3.9) to obtain S_0, $r_{\rm c}$ and β. Then, we normalised the surface brightness of MOS1 and MOS2 to pn by multiplying $S_0^{\rm pn}/S_0^{\rm MOS1,2}$ and fitted Eq. (3.9) for all three detectors simultaneously. Thereby, the parameters $r_{\rm c}$ and β change only marginally compared to fitting Eq. (3.9) individually for each detector. Since 3σ gave too narrow bins with high noise for our clusters, the data was re-binned by merging 5 adjacent bins for CL0015.9+1609, 4 bins for MS0451.6−0304 and 3 bins for MS2137.3−2353. The surface brightness profiles are plotted in Fig. 7.4 and β and $r_{\rm c}$ are given in Table 7.2. For MS1008.1−1224, $r_{\rm c}$ and β were obtained from fitting Eq. (3.9) to the flux measured in the ACIS-I detector which was determined by Helen Eckmiller using the *Chandra*-analysis software `Ciao` following Hudson et al. (2006).

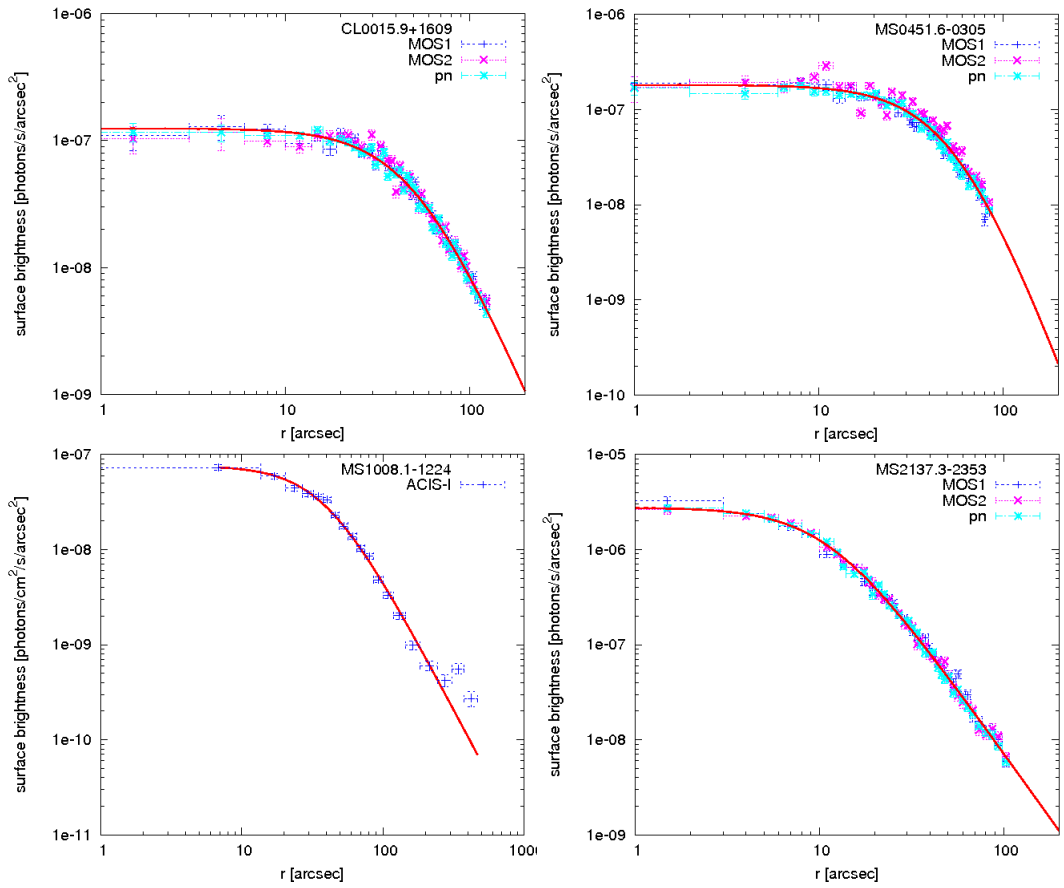

Figure 7.4: Surface brightness profiles after rescaling the MOS fluxes to the normalisation of the surface brightness in pn, $S_0^{\rm pn}$. The horizontal bars denote the bin size and the vertical errors are the 1σ-errors of the surface brightness density.

Table 7.2: Parameters for calculating the hydrostatic masses. The parameters of the temperature profile (Eq. 7.1) do not have errors because we have more degrees of freedom than data points. In the last two rows the parameters for the surface brightness profile (Eq. 3.9) are listed.

	CL0015.9+1609	MS0451.6−0305	MS1008.1−1224	MS2137.3−2353
T_1 [keV]	3.69	0	0	0
r_K [kpc]	1966	–	–	–
β'	2.31	–	–	–
T_2 [keV]	1.00	5.24	3.17	1.05
r_{gc} [kpc]	375	0	−119	271
σ [kpc]	375	303	680	415
T_3 [keV]	4.52	5.44	3.24	4.00
β	0.73 ± 0.12	1.04 ± 0.19	0.94 ± 0.05	0.62 ± 0.02
r_c [kpc]	318 ± 35	361 ± 33	170 ± 15	52 ± 3

7.2.3 Mass profiles

The mass profiles were calculated out to 3 Mpc in steps of 1 kpc with Eq. (3.14) using the parameters in Table 7.2. Figure 7.5 shows the mass profiles for the four clusters whereby the data points show the X-ray hydrostatic masses and their errors at the radii for which the temperature profiles were plotted (Fig. 7.2). The horizontal bars denote the size of the temperature bins and the vertical errors are the 1σ-errors on $M_X(< r)$ from Monte-Carlo simulation in which we generated mass profiles from simulated surface brightness and temperature profiles using

$$\begin{aligned} T_{\rm rand}(r, x_1) &= T(r) + \Delta T \cdot x_1 \\ S_{\rm X,rand}(r, x_2) &= S_X(r) + \Delta S_X \cdot x_2 \,. \end{aligned} \tag{7.3}$$

Here, $x_{1,2}$ are a functions that create Gaussian random values in the interval $[-1, 1]$ and r is the projected radius. The 1σ-errors which were measured for each temperature and surface brightness bin in Sects. 7.2.1 and 7.2.2, are denoted as ΔT and ΔS_X, respectively. Hence, the simulated surface brightness and temperature profiles vary within the errors of the measured surface brightness and temperature profiles. We simulated 100 temperature and surface brightness profiles for each cluster and fitted them with Eqs. (7.1) and (3.9), respectively. The corresponding mass profiles were calculated with Eq. (3.14). The standard deviation of the randomised mass profiles at radius r are the errors on the true mass profile at r.

Table 7.3 lists X-ray hydrostatic masses at $r_{500,X}$ and $r_{2500,X}$ calculated from the hydrostatic equation (Eq. 3.14) and our best fit weak lensing masses (Sect. 6.3) at $r_{500,X}$. We also list X-ray hydrostatic and best fit weak lensing masses at $r_{500,wl}$ derived from the mass profiles of the best fit weak lensing mass models, which are NFW for CL0015.9+1609 and MS1008.1−1224, NFW&PS for MS0451.6−0305 and the *Mc*-model for MS2137.3−2353. For reasons of consistency, we used the best fit weak lensing mass of $MS0451_{ACS}$ because we do not have photometric redshifts for the other clusters. The X-ray hydrostatic masses M_X at $r_{500,X}$ and $r_{2500,X}$ were compared to the previous X-ray and X-ray&SZE analyses we also used for the weak lensing mass comparison (Table 6.4):

For CL0015.9+1609, we have $M_X = (2.66 \pm 0.62) \times 10^{14}\, M_\odot$ at $r_{2500}^{B08} = 507$ kpc from Bonamente et al. (2008) which is 21% lower than their $M_{2500}^{B08} = (3.37 \pm 0.4) \times 10^{14} M_\odot$. Our mass is 37% lower than that of Bonamente et al. (2008) at the same overdensity. At $r_{500}^{M10} = 1470$ kpc from Mantz et al. (2010a), we have $M_X = (5.77 \pm 0.67) \times 10^{14}\, M_\odot$ which is not consistent with their $M_{500} = (16.5 \pm 2.5) \times 10^{14}\, M_\odot$. The same holds if we compare our mass with that of Mantz et al. (2010a) at the same overdensity.

Table 7.3: X-ray hydrostatic and best fit weak lensing masses at $r_{500,X}$ from X-ray and $r_{500,wl}$ from the weak lensing mass profiles and X-ray hydrostatic masses at $r_{2500,X}$. The radii are given in kpc and arcmin, respectively.

	CL0015.9+1609	MS0451.6−0305	MS1008.1−1224	MS2137.3−2353
$r_{500,X}$ [kpc]	971	1026	1231	906
$r_{500,X}$ [′]	2.′59	2.′71	4.′40	3.′36
M_X [$10^{14} M_\odot$]	4.74 ± 0.46	5.65 ± 0.45	7.44 ± 0.56	3.01 ± 0.38
M_{wl} [$10^{14} M_\odot$]	$6.17^{+7.95}_{-6.09}$	$12.12^{+2.27}_{-2.30}$	$10.56^{+7.16}_{-6.27}$	$1.99^{+0.32}_{-0.34}$
$r_{500,wl}$ [kpc]	1152	1488	1497	758
$r_{500,wl}$ [′]	3.′07	3.′93	5.′71	2.′81
M_X [$10^{14} M_\odot$]	5.12 ± 0.51	8.56 ± 0.94	8.21 ± 0.43	2.63 ± 0.39
M_{wl} [$10^{14} M_\odot$]	$7.91^{+10.21}_{-7.81}$	$19.33^{+3.62}_{-3.67}$	$13.39^{+9.08}_{-7.95}$	$1.76^{+0.28}_{-0.30}$
$r_{2500,X}$ [kpc]	435	491	620	414
$r_{2500,X}$ [′]	1.′16	1.′30	2.′37	1.′54
$M_{2500,X}$ [$10^{14} M_\odot$]	2.13 ± 0.44	3.10 ± 0.24	4.75 ± 0.25	1.43 ± 0.09

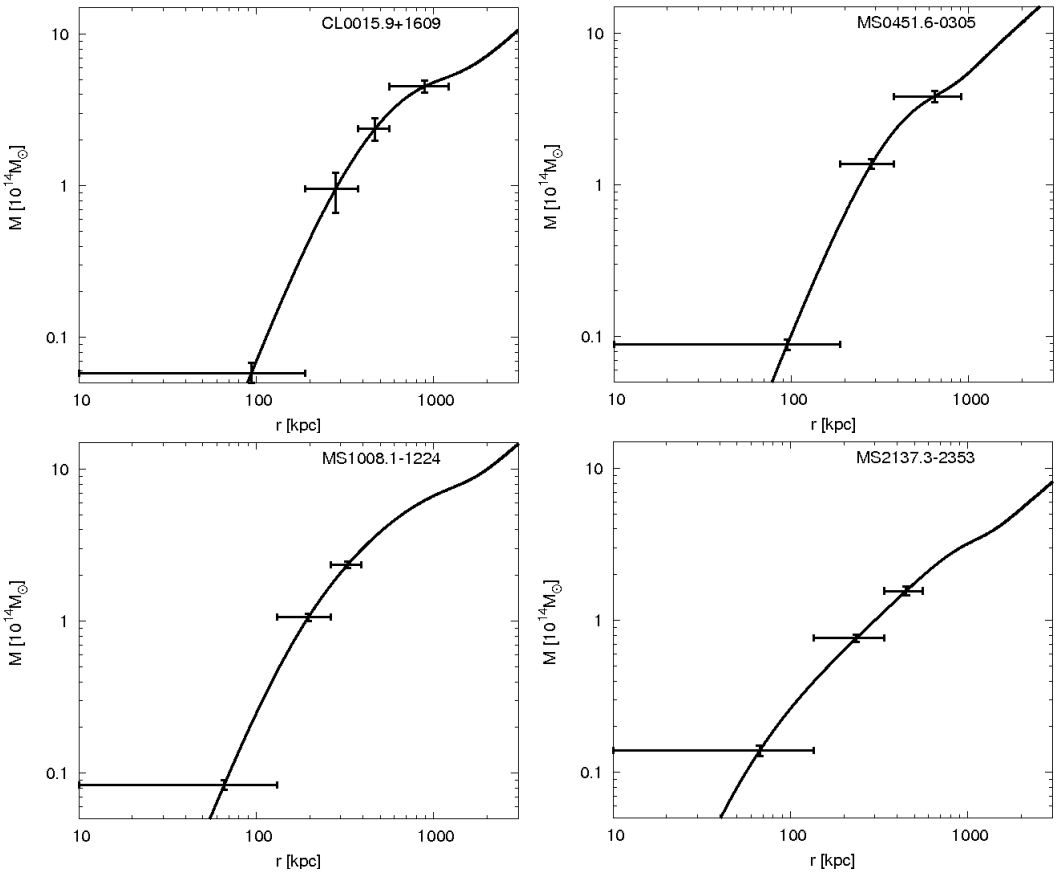

Figure 7.5: Mass profiles assuming hydrostatic equilibrium. The data points are taken from the temperature profiles (Fig. 7.2) whereby the horizontal bars denote the bin size and the vertical errors are calculated from the Monte-Carlo simulation.

For MS0451.6−0305, we obtained $M_{\rm X} = (7.48 \pm 0.60) \times 10^{14}\,M_\odot$ at $r_{500}^{\rm D03} = 1319\,$kpc from Donahue et al. (2003) which is 37% lower than their mass. Comparing both studies at $\Delta = 500$, our mass is 52% lower than that of Donahue et al. (2003). Comparing the masses at $r_{2500}^{\rm B08} = 526\,$kpc, ours is with $M_{\rm X} = (3.30 \pm 0.69) \times 10^{14}\,M_\odot \sim 13\%$ lower than that of Bonamente et al. (2008). At $\Delta = 2500$, our mass is only 6% lower. Our results for MS0451.6−0305 show better agreement with Bonamente et al. (2008) than our results for CL0015.9+1609 which may be due to that the latter is a merger. Our mass at $r_{500}^{\rm M10} = 1310\,$kpc from Mantz et al. (2010a) is with $M_{\rm X} = (7.42 \pm 0.60) \times 10^{14}\,M_\odot$ 35% lower than their mass. If we compare both masses at $\Delta = 500$, our mass is 51% lower.

For MS2137.3−2353, we obtained $M_{\rm X} = (3.31 \pm 0.61) \times 10^{14}\,M_\odot$ at $r_{500}^{\rm M10} = 1060\,$kpc from Mantz et al. (2010a) which is 30% lower than their mass. At the same overdensity, $\Delta = 500$, our mass is 36% lower.

That our masses are lower than those of Donahue et al. (2003), Bonamente et al. (2008) and Mantz et al. (2010a) may be due to: (1) Those studies used an isothermal temperature to derive the hydrostatic mass which is considered to give 20 − 25% higher masses than those using a temperature profile (e.g. Zhang et al. 2005). (2) To determine the temperature, Donahue et al. (2003) did not exclude the core region where the temperature is high (Fig. 7.2). (3) The old *Chandra*-calibration with which the observations used by Donahue et al. (2003) were performed biased the temperature to high values (e.g. Snowden et al. 2008 and references therein). (4) Mantz et al. (2010a) derived their mass from the gas mass profile by assuming a model for the gas mass fraction (Nagai et al. 2007; Allen et al. 2008).

The shapes of the mass profiles give evidence for cluster concentration (Fig. 7.5). For instance, CL0015.9+1609 is likely not in hydrostatic equilibrium and has a low concentration. The latter was also confirmed by our weak lensing analysis (Sect. 6.3.1), where we measured a concentration of $c_{200} = 1.2^{+0.9}_{-1.1}$. Furthermore, CL0015.9+1609 has a weird temperature profile (Fig. 7.2, *upper left*) which subsequently affects the mass profile even if the Gaussian in Eq. (7.1) is smoothed. Also, the mass profile of MS0451.6−0305 indicates non-hydrostatic equilibrium which was also concluded by Donahue et al. (2003). For the other two clusters, MS1008.1−1224 and MS2137.3−2352, we obtained smoother mass profiles and we conclude that those clusters are in hydrostatic equilibrium although MS1008.1−1224 is a merger.

7.3 Global properties

7.3.1 Global temperature and metallicity

We determined the global temperatures $T_{\rm X}$ and metallicities Z inside an annulus of $0.2 - 0.5 r_{500}$ centred at the X-ray centroid following Zhang et al. (2007). In this annulus, the temperature follows the universal distribution (e.g. Zhang et al. 2004; Vikhlinin et al. 2005; Pratt et al. 2007 and Sect. 3.1.3) for most clusters. At smaller radii, the scatter is larger among non-cool-core and cool-core clusters and peculiarities due to the dynamical history such as boosted temperatures in the case of merging clusters (e.g. Smith et al. 2005). For this reason, the scatter in those X-ray scaling relations that involve $T_{\rm X}$ is minimised when using the temperatures in the $0.2 - 0.5 r_{500}$ annulus. Furthermore, the difference between the normalisations of scaling relations for cool-core and non-cool-core clusters is $\lesssim 10\%$ if this annulus is used to determine the global temperature (Zhang et al. 2007).

Using XSPEC, we fitted "wabs+mekal" to the global spectra to obtain temperature and metallicity Z with both $n_{\rm H}$ fixed and as free parameter. The results are given in Table 7.4 where the global temperatures and metallicities using $0.2 - 0.5 r_{500,{\rm wl}}$ are listed as well. All global spectra

are shown in the appendix (Figs. B.4-B.11). For MS1008.1−1224, the global spectra were created by Helen Eckmiller following Eckmiller et al. (2011).

We found that global temperatures and metallicities are consistent whether we fixed $n_{\rm H}$ to the LAB-survey or determine its value by fitting. Since the errors on $T_{\rm X}$ are smaller for fixed $n_{\rm H}$, we used them for the further analysis because this will provide us with tighter scaling relations. Furthermore, the global temperatures based on $r_{500,\rm wl}$ are lower than those based on $r_{500,\rm X}$ because $r_{500\,\rm wl} > r_{500,\rm X}$ such that regions of lower temperatures are included.

We compared our global temperatures $T_{\rm X}$ within $0.2 - 0.5r_{500,\rm X}$ and fixed $n_{\rm H}$ to those in previous studies (Table 7.6) but those results can only serve as consistency check because they are obtained with different instruments and within different annuli ranges. Figure 7.6 shows the ratios between our temperature and the literature values. Except for MS1008.1−1224, our temperatures are consistent with Balestra et al. (2007). Furthermore, our temperatures are also consistent with those of Lewis et al. (1999) and Ebeling et al. (2010).

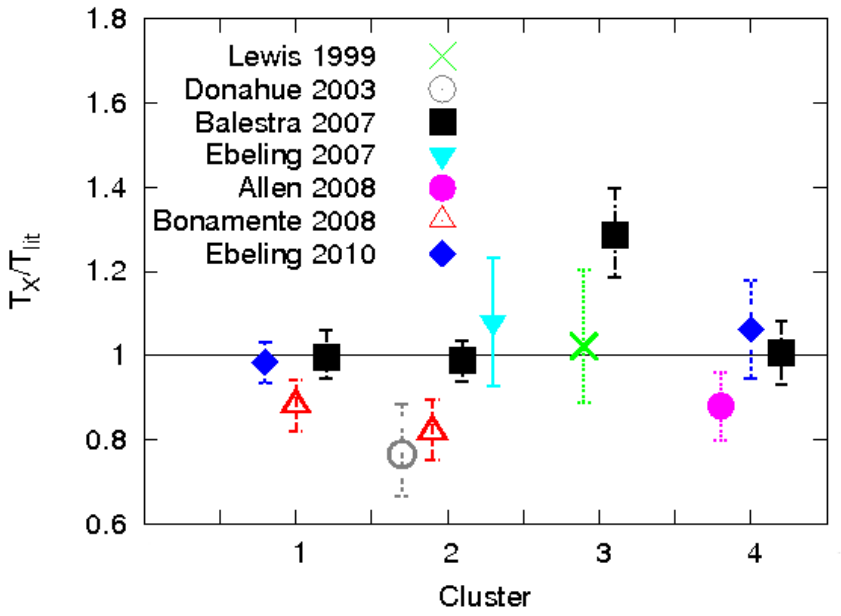

Figure 7.6: Comparison of global temperatures within $0.2 - 0.5r_{500,\rm X}$ and fixed $n_{\rm H}$ with the literature. The clusters are labelled: (1) CL0015.9+1609, (2) MS0451.6−0305, (3) MS1008.1−1224, (4) MS2137.3−2353.

Table 7.4: Global temperatures $T_{\rm X}$ and metallicities Z within $0.2 - 0.5r_{500,\rm X}$ and $0.2 - 0.5r_{500,\rm wl}$ for both fitted and fixed hydrogen column number density $n_{\rm H}$. The results for the fitted $n_{\rm H}$ are denoted with the subscript $n_{\rm H,free}$.

	CL0015.9+1609	MS0451.6−0305	MS1008.1−1224	MS2137.3−2353
$0.2 - 0.5r_{500,\rm X}$:				
$T_{\rm X}$ [keV]	9.25 ± 0.36	8.11 ± 0.37	7.46 ± 0.52	4.99 ± 0.36
$Z_{\rm X}$ [$Z_\odot$]	0.19 ± 0.06	0.20 ± 0.05	0.29 ± 0.10	0.19 ± 0.11
$T_{n_{\rm H,free}}$ [keV]	10.25 ± 1.05	8.89 ± 0.83	9.84 ± 2.67	5.78 ± 1.50
$Z_{n_{\rm H,free}}$ [$Z_\odot$]	0.20 ± 0.07	0.21 ± 0.07	0.35 ± 0.15	0.06 ± 0.16
$0.2 - 0.5r_{500,\rm wl}$:				
$T_{\rm X}$ [keV]	9.24 ± 0.36	6.88 ± 0.28	7.89 ± 0.79	4.82 ± 0.28
$Z_{\rm X}$ [$Z_\odot$]	0.11 ± 0.05	0.28 ± 0.07	0.41 ± 0.13	0.27 ± 0.11
$T_{n_{\rm H,free}}$ [keV]	9.74 ± 1.03	6.86 ± 0.75	10.44 ± 2.63	5.27 ± 1.05
$Z_{n_{\rm H,free}}$ [$Z_\odot$]	0.11 ± 0.05	0.28 ± 0.07	0.54 ± 0.21	0.19 ± 0.14

We summarise the studies to which we compared our results as follows: Lewis et al. (1999) obtained T_X using *ASCA*-observations from Mushotzky & Scharf (1997). Their measurement is consistent with ours although there is no explicit information of the area for which their T_X was measured. Donahue et al. (2003) measured T_X within $83'' = 523$ kpc with "wabs+mekal" using the $0.7 - 7.0$ keV energy band. The deviation to our temperature was discussed in Sect. 7.2.3. Balestra et al. (2007) measured T_X within $0.15 - 0.3r_{vir}$ with r_{vir} from Evrard et al. (1996) using a mekal model. Ebeling et al. (2007) measured T_X within r_{1000} excluding the innermost 70 kpc but they do not give the value for r_{1000}. Allen et al. (2008) measured the deprojected temperature T_X within $r_{2500} = 479$ kpc which is $\sim 0.5r_{500,X}$ and consistent with ours although they did not exclude the core region. Their overdensity was obtained from assuming that the gas density follows an NFW-profile. Bonamente et al. (2008) determined T_X within $r_{2500} = 507 \pm 19$ kpc which is $\sim 0.5r_{500,X}$. Their temperature is 14% higher than ours because we excluded the $r < 0.2r_{500}$-region. Mantz et al. (2010a) determined T_X within $0.15 - 1r_{500}$ whereby r_{500} was determined as described in Sect. 7.2.3. Ebeling et al. (2010) obtained $T_X = 4.7 \pm 0.4$ keV using the XSPEC "mekal" model within $r_{500} = 1060 \pm 40$ kpc which is ~ 2 times larger than $0.5r_{500,X}$. Yet, their result is consistent with ours.

We compared our global metallicities obtained within $0.2 - 0.5r_{500,X}$ for fixed n_H to Donahue et al. (2003) and Balestra et al. (2007). For MS0451.6−0305, Donahue et al. (2003) obtained a metallicity which is ~ 2 times larger than ours which may be due to the old *Chandra*-calibration. The global metallicities from Balestra et al. (2007) are $41 - 46\%$ higher than our metallicities for CL0015.9−1609, MS0451.6−0305 and MS2137.3−2353. Only for MS1008.1−1224 our metallicity is consistent with theirs. This may be due to that Balestra et al. (2007) used the emission-weighted metallicity which is $\sim 0.4Z_\odot$ for clusters at $0.3 < z < 0.5$.

Table 7.5: Global luminosities in the energy bands 0.5–2.0 keV, 0.01–100 keV and 0.1–2.4 keV within $0.2 - 1r_{500}$.

Cluster	$L_{0.5-2.0keV}$ [10^{44} erg s^{-1}]	L_{bol} [10^{44} erg s^{-1}]	$L_{0.1-2.4keV}$ [10^{44} erg s^{-1}]
CL0015.9+1609	5.13 ± 0.23	27.13 ± 1.45	6.90 ± 0.30
MS0451.6−0305	4.37 ± 0.44	20.36 ± 2.05	5.67 ± 0.57
MS1008.1−1224	1.37 ± 0.14	6.05 ± 1.71	1.76 ± 0.08
MS2137.3−2353	1.51 ± 0.30	4.78 ± 0.95	1.94 ± 0.39

7.3.2 Global luminosities

We used the XSPEC-command "lumin" to determine the global luminosities within $0.2 - 1r_{500,X}$ following Zhang et al. (2011a). The cool-core region was excluded because the luminosity can be strongly affected by cooling cores. With a "mekal"-model, we fixed all parameters except the normalisation, whereby we used T_X and Z and their errors for fixed n_H (Table 7.4). The corresponding spectra are presented in Figs. B.12-B.13 in the appendix. We did not use $r_{500,wl}$ because for MS1008.1−1224, this radius exceeds the *Chandra* field-of-view. The global spectra for MS1008.1−1224 were created by Helen Eckmiller following Eckmiller et al. (2011).

The global luminosities are given in Table 7.5 for the following energy bands: the soft band ($0.5 - 2.0$ keV), the bolometric band ($0.01 - 100$ keV) and the *ROSAT*-band ($0.1 - 2.4$ keV). Here, the luminosities for the *XMM-Newton* clusters are the mean of the luminosities obtained for MOS and pn and their error is the scatter of the luminosities measured in the three detectors with respect to the mean value. For MS1008.1−1224, we estimated the error on L_X from the errors on T_X and Z.

The global luminosities are not a good mass indicator for galaxy clusters. The luminosity can be boosted at different levels due to merging. Thus, CL0015.9+1609 has a high luminosity, but

the luminosity of MS1008.1−1224 is ∼ 3 times lower although both are massive mergers. This is also indicated in the literature (Sect. 4.1).

The luminosities in the *ROSAT*-band are not consistent with the literature (Table 7.6) which is due to that these luminosities were calculated at radii $r > r_{500}$, i.e. r_{200} (Ebeling et al. 2007) and $1h^{-1}$ Mpc (Donahue et al. 2003). Mantz et al. (2010a) calculated $L_{0.1-2.4\,\mathrm{keV}}$ within $r_{500} = (1060 \pm 40)$ kpc and without excluding the cool-core region. We assume that our luminosity is ∼ 6 times lower than theirs because the X-ray emission in the centre of MS2137.3−2353 is contaminated by the bright cD-galaxy in the centre (Luppino et al. 1999).

We did not compare our luminosities to the other analyses (Sect. 4.1) because they were either measured in the 0.3–3.5 or 0.3–4.5 keV band, and within different annuli. Yet, we observed a similar trend in our luminosities than those in the 0.3 – 3.5 keV band (Luppino et al. 1999).

Table 7.6: Global temperatures T_X, metallicities Z and luminosities L_X from the literature. Column 5 lists the energy bands in which the luminosities were measured. The last column lists the references, i.e. Le99 Lewis et al. 1999, Lu99 Luppino et al. 1999, D03 Donahue et al. 2003, B07 Balestra et al. 2007, E07 Ebeling et al. 2007, A08 Allen et al. 2008, B08 Bonamente et al. 2008 and M10 Mantz et al. 2010a.

Cluster	T_X [keV]	Z [$Z_\odot$]	L_X [10^{44} erg s^{-1}]	energy band [keV]	instrument	ref
CL0015.9+1609			14.6	0.3 – 3.5	*Einstein*	Lu99
	$9.3^{+0.5}_{-0.3}$	$0.33^{+0.05}_{-0.05}$			*Chandra*	B07
	9.4 ± 0.3		19.6 ± 0.3	0.1 – 2.4	*Chandra*	E07
	10.5 ± 0.6				*Chandra*	B08
			11.84 ± 0.67	bolometric	*Chandra*	M10
MS0451.6−0305			19.98	0.3 – 3.5	*Einstein*	Lu99
	$10.6^{+1.6}_{-1.3}$	0.40 ± 0.14	8.87	0.1 – 2.4	*Chandra*	D03
	$8.2^{+0.4}_{-0.3}$	0.34 ± 0.06			*Chandra*	Ba07
	7.5 ± 1.0		16.8 ± 0.6	0.1 – 2.4	*Chandra*	E07
	$9.9^{+0.8}_{-0.7}$				*Chandra*	B08
			9.50 ± 0.41	bolometric	*Chandra*	M10
MS1008.1−1224	$7.3^{+1.2}_{-0.8}$				*Chandra*	Le99
			4.49	0.3 – 3.5	*Einstein*	Lu99
	$5.8^{+0.3}_{-0.2}$	$0.30^{+0.07}_{-0.06}$			*Chandra*	B07
MS2137.3−2353			15.62	0.3 – 3.5	*Einstein*	Lu99
	4.96 ± 0.11	0.35 ± 0.03			*Chandra*	B07
	5.65 ± 0.3				*Chandra*	A08
	4.67 ± 0.43		11.1 ± 0.4	0.1 – 2.4	*Chandra*	M10

Chapter 8

Weak lensing versus X-ray mass calibrations

In this chapter, mass-observable scaling relations using X-ray hydrostatic masses $M_{\rm X}$ and weak lensing masses $M_{\rm wl}$ from the best fit models (Sect. 6.3, Table 7.3) will be studied. I will also discuss scaling relations using weak lensing masses M_{Mc} from our one-parameter NFW-model with fixed concentration (Mc-model, Sect. 6.2.1) to cross-check how the systematic uncertainty of $M_{\rm wl}$ due to different concentration parameters c_{200} affects the normalisation of the scaling relations. I will compare weak lensing and X-ray hydrostatic masses in Sect. 8.1 and discuss the mass-temperature relations with the global temperatures from Sect. 7.3.1 determined within $0.2 - 0.5 r_{500,\rm X}$ with fixed $n_{\rm H}$ ($T_{0.2-0.5r_{500}}$) in Sect. 8.2. In Sect. 8.3, I will discuss mass-luminosity relations using the luminosities determined within $0.2 - 1 r_{500,\rm X}$ from Table 7.5 and the three different mass estimates $M_{\rm X}$, $M_{\rm wl}$ and M_{Mc}. Scaling relations not involving total cluster masses will be discussed in Sects. 8.4 and 8.5, i.e. temperature-luminosity relations and the temperature-metallicity relation, respectively. In Sect. 8.6, the scaling relations from this work will be compared to simulations.

The scaling relations were fitted by a power law $Y = Y_0 X^{\gamma}$ with the Orthogonal Distance Regression method (ODR, e.g. Feigelson & Babu 1992; Akritas & Bershady 1996) using the software package `Odrpack 2.01` (Boggs et al. 1987) following Zhang et al. (2008). This method uses linear regression and accounts for the errors on both variables which can be different for each observation and each data point. The slope γ was fixed with well-established values from large samples (Zhang et al. 2006, 2008, 2010) because it is too unreliable to fit the slope with four clusters only. We used the four clusters to determine the normalisation Y_0.

To check the dependence of scaling relations on the evolution of cosmological parameters due to LSS growth, the redshift evolution correction (Eq. 1.16) following Zhang et al. (2008) was applied as follows: $M \cdot E(z)$ and $L \cdot E(z)^{-1}$. With this correction, the clusters are assumed to be self-similar.

Slopes and normalisations of the scaling relations including $M_{\rm X}$, $M_{\rm wl}$ and M_{Mc} are listed and compared to the literature in Table 8.1. Scaling relations between the observables temperature, metallicity and luminosity are presented in Table 8.2. Selected scaling relations are plotted in the figures in the subsequent sections. The scaling relations will be compared to previous analyses and to simulations as far as they assumed a ΛCDM-cosmology. For our cluster redshifts, $E(z)$ using the redshifts of our sample differs by less than 2% between our cosmology and $\Omega_{\rm m} = 0.3$ and $\Omega_{\Lambda} = 0.7$ (Markevitch et al. 1998; Ettori et al. 2004; Kotov & Vikhlinin 2005; Maughan et al. 2006; Balestra et al. 2007; Borgani et al. 2004; Vikhlinin et al. 2009a; Zhang et al. 2006, 2008, 2010; Fabjan et al. 2011) and by less than 6% assuming $\Omega_{\rm m} = 0.2$ and $\Omega_{\Lambda} = 0.8$ (Evrard et al.

1996; Ikebe et al. 2002). The scaling relations from this work will also be compared to each other with respect to $M_{\rm X}$, $M_{\rm wl}$ and M_{Mc}.

8.1 X-ray hydrostatic versus weak lensing masses

8.1.1 $M_{\rm wl}$ from the best fit model

The comparison of weak lensing and X-ray hydrostatic masses provides an important test of the systematics in both methods. The mass ratios are plotted in Fig. 8.1. To be consistent with the mass-observable scaling relations, the redshift evolution correction was also applied for the comparison of weak lensing and X-ray hydrostatic masses. We compared $M_{\rm wl}$ and $M_{\rm X}$ at $r_{500,\rm X}$ from Table 7.3. We did not compare X-ray hydrostatic and weak lensing masses at $r_{500,\rm wl}$ for the following reasons: (1) Extrapolating the X-ray mass profile to $r_{500,\rm wl}$ may cause uncertainties in mass because X-ray hydrostatic masses are only reliable out to $r_{500,\rm X}$. (2) Only one cluster, MS0451.6−0305, has r_{200} within the field-of-view of the HST-mosaic data. For MS2137.3−2353, r_{200} was fitted to the border of the field-of-view and for the two mergers CL0015.9+1609 and MS1008.1−1224, r_{200} was fitted well beyond the field-of-view. In addition, c_{200} cannot be well determined in weak lensing.

With the slope fixed at $\gamma = 1.0$, the X-ray masses are $\sim$ 18% lower than the weak lensing masses. The huge error bars on the weak lensing masses of two clusters have two reasons which were also discussed in Sect. 6.3: First, these clusters are merging clusters (CL0015.9+1609 and MS1008.1−1224) and as a consequence their tangential shear profile is disturbed. Second, these clusters have r_{200} well outside the field-of-view.

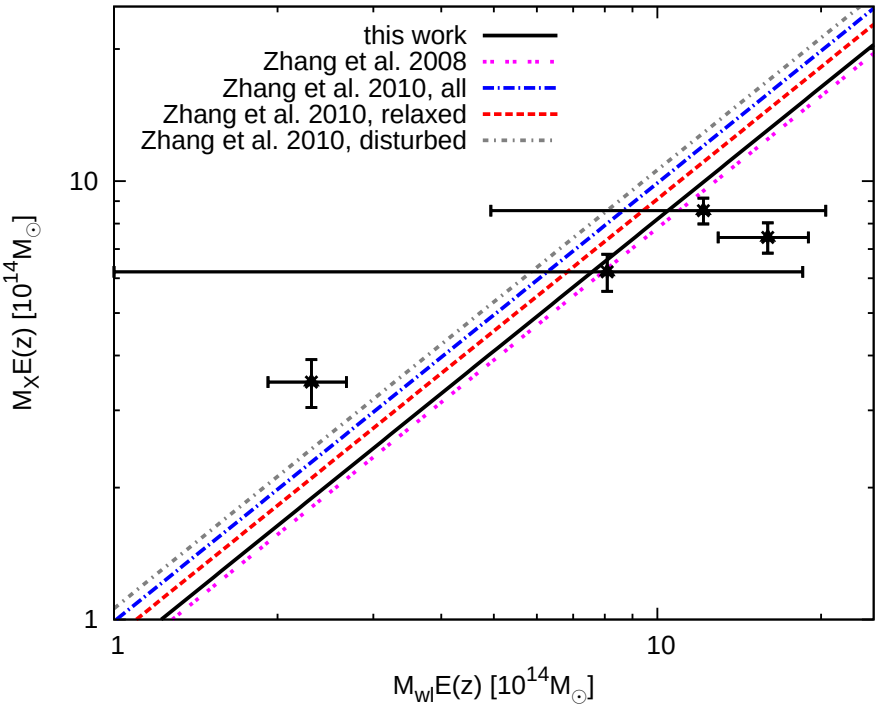

Figure 8.1: Hydrostatic masses $M_{\rm X}$ versus weak lensing masses $M_{\rm wl}$ at $r_{500,\rm X}$ for our sample and the samples from Zhang et al. (2008) and Zhang et al. (2010). To be consistent with the mass-observable scaling relations, $E(z)$ was also applied for the comparison of weak lensing and X-ray hydrostatic masses.

Table 8.1: Parameters of the X-ray scaling relations for fitting the power law $Y = Y_0 X^\gamma$ including total cluster masses M_X, M_wl and M_{Mc}. To compare our results to the literature, we transformed our scaling relations to the notation of Zhang et al. (2006, 2008, 2010). The results of our $M_\mathrm{wl} - M_\mathrm{X}$ relation are compared to the total sample of Zhang et al. (2010) and to their sub-samples consisting only of relaxed and disturbed clusters. $(\Delta_{c,z}/\Delta_{c,0})^{\pm 0.5}$ is the density contrast of a virialised halo with respect to the critical density with the analytical approximation $\Delta_{c,z}$ derived from the spherical collapse model for a flat universe (Bryan & Norman 1998). The abbreviations for the literature are: E04 for Ettori et al. (2004), Z06 for Zhang et al. (2006), B07 for Balestra et al. (2007), Z08 for Zhang et al. (2008), V09a for Vikhlinin et al. (2009a) and Z10 for Zhang et al. (2010).

X	Y	Y_0	γ	Sample
$\frac{M_\mathrm{wl}}{M_\odot} E(z)$	$\frac{M_\mathrm{X}}{M_\odot} E(z)$	0.819 ± 0.065	1.0	this work
$\frac{M_{Mc}}{M_\odot} E(z)$	$\frac{M_\mathrm{X}}{M_\odot} E(z)$	1.119 ± 0.155	1.0	this work
		0.781 ± 0.096	1.0	Z08
		0.91 ± 0.06	1.0	Z10, relaxed
		1.06 ± 0.12	1.0	Z10, disturbed
		0.990 ± 0.070	1.0	Z10, all
$\frac{T_{0.2-0.5r_{500}}}{\mathrm{keV}}$	$\frac{M_\mathrm{X}}{M_\odot} E(z)$	$10^{13.47\pm0.06}$	1.5	this work
$\frac{T_{0.2-0.5r_{500}}}{\mathrm{keV}}$	$\frac{M_\mathrm{X}}{M_\odot} E(z)$	$10^{13.48\pm0.06}$	1.59	this work
$\frac{T_\mathrm{X}}{\mathrm{keV}}$	$\frac{M_\mathrm{X}}{M_\odot} E(z)$	$10^{13.57\pm0.02}$	1.5	E04
$\frac{T_{0.1-0.5r_{500}}}{\mathrm{keV}}$	$\frac{M_\mathrm{X}}{M_\odot} (\Delta_{c,z}/\Delta_{c,0})^{0.5} E(z)$	$10^{13.80\pm0.04}$	1.5	Z06
$\frac{T_{0.2-0.5r_{500}}}{\mathrm{keV}}$	$\frac{M_\mathrm{X}}{M_\odot} E(z)$	$10^{13.55\pm0.02}$	1.499	Z08
$\frac{T_{0.2-0.5r_{500}}}{\mathrm{keV}}$	$\frac{M_\mathrm{X}}{M_\odot} E(z)$	$10^{13.42\pm0.22}$	1.654 ± 0.256	Z08, γ fitted
$\frac{T_{0.15-0.5r_{500}}}{5\,\mathrm{keV}}$	$\frac{M_\mathrm{X}}{M_\odot} E(z)$	$10^{13.39\pm0.02}$	1.5	V09a
$\frac{T_{0.2-0.5r_{500}}}{\mathrm{keV}}$	$\frac{M_\mathrm{wl}}{M_\odot} E(z)$	$10^{13.37\pm0.15}$	1.5	this work
$\frac{T_{0.2-0.5r_{500}}}{\mathrm{keV}}$	$\frac{M_\mathrm{wl}}{M_\odot} E(z)$	$10^{13.37\pm0.14}$	1.59	this work
$\frac{T_{0.2-0.5r_{500}}}{\mathrm{keV}}$	$\frac{M_{Mc}}{M_\odot} E(z)$	$10^{13.47\pm0.17}$	1.5	this work
$\frac{T_{0.2-0.5r_{500}}}{\mathrm{keV}}$	$\frac{M_{Mc}}{M_\odot} E(z)$	$10^{13.49\pm0.18}$	1.59	this work
$\frac{T_{0.2-0.5r_{500}}}{\mathrm{keV}}$	$\frac{M_\mathrm{wl}}{M_\odot} E(z)$	$10^{13.57\pm0.05}$	1.59	Z08
$\frac{T_{0.2-0.5r_{500}}}{\mathrm{keV}}$	$\frac{M_\mathrm{wl}}{M_\odot} E(z)$	$10^{13.53\pm0.04}$	1.59	Z08, $r_{500}^{Y_\mathrm{X},\mathrm{X}}$
$\frac{M_\mathrm{X}}{M_\odot} E(z)$	$\frac{L_{0.1-2.4\,\mathrm{keV}}(0.2-1r_{500})}{\mathrm{erg/s}} E(z)^{-1}$	$10^{25.11\pm0.18}$	1.3	this work
$\frac{M_\mathrm{X}}{M_\odot} (\Delta_{c,z}/\Delta_{c,0})^{0.5} E(z)$	$\frac{L_{0.1-2.4\,\mathrm{keV}}(0.1r_{500}-20')}{\mathrm{erg/s}} (\Delta_{c,z}/\Delta_{c,0})^{-0.5} E(z)^{-1}$	$10^{25.00\pm0.06}$	1.3	Z06
$\frac{M_\mathrm{X}}{M_\odot} E(z)$	$\frac{L_\mathrm{bol}(0.2-1r_{500})}{\mathrm{erg/s}} E(z)^{-1}$	$10^{25.88\pm0.13}$	1.3	this work
$\frac{M_\mathrm{X}}{M_\odot} E(z)$	$\frac{L_\mathrm{bol}(0.2-1r_{500})}{\mathrm{erg/s}} E(z)^{-1}$	$10^{18.23\pm0.16}$	1.814	this work
$\frac{M_\mathrm{X}}{M_\odot} E(z)$	$\frac{L_\mathrm{bol}(r_{500})}{\mathrm{erg/s}} E(z)^{-1}$	$10^{25.38\pm0.02}$	1.33	E04
$\frac{M_\mathrm{X}}{M_\odot} E(z)$	$\frac{L_\mathrm{bol}(r_{500})}{\mathrm{erg/s}} E(z)^{-1}$	$10^{17.05\pm0.63}$	1.88 ± 0.42	E04, γ fitted
$\frac{M_\mathrm{X}}{10^{14} M_\odot} (\Delta_{c,z}/\Delta_{c,0})^{0.5} E(z)$	$\frac{L_\mathrm{bol}(0.1r_{500}-20')}{\mathrm{erg/s}} (\Delta_{c,z}/\Delta_{c,0})^{-0.5} E(z)^{-1}$	$10^{25.35\pm0.06}$	1.3	Z06
$\frac{M_\mathrm{X}}{M_\odot} E(z)$	$\frac{L_\mathrm{bol}(0.2-2.5r_{500})}{\mathrm{erg/s}} E(z)^{-1}$	$10^{18.03\pm0.05}$	1.814	Z08
$\frac{M_\mathrm{X}}{M_\odot} E(z)$	$\frac{L_\mathrm{bol}(0.2-2.5r_{500})}{\mathrm{erg/s}} E(z)^{-1}$	$10^{10.46\pm10.39}$	2.325 ± 0.701	Z08, γ fitted
$\frac{M_\mathrm{X}}{10^{14} M_\odot} E(z)$	$\frac{L_{0.5-2.0\,\mathrm{keV}}(0.2-1r_{500})}{10^{44}\,\mathrm{erg/s}} E(z)^{-1}$	$10^{25.09\pm0.17}$	1.3	this work
$\frac{M_\mathrm{wl}}{M_\odot} E(z)$	$\frac{L_{0.1-2.4\,\mathrm{keV}}(0.2-1r_{500})}{\mathrm{erg/s}} E(z)^{-1}$	$10^{25.14\pm0.21}$	1.3	this work
$\frac{M_{Mc}}{M_\odot} E(z)$	$\frac{L_{0.1-2.4\,\mathrm{keV}}(0.2-1r_{500})}{\mathrm{erg/s}} E(z)^{-1}$	$10^{25.24\pm0.23}$	1.3	this work
$\frac{M_\mathrm{wl}}{M_\odot} E(z)$	$\frac{L_\mathrm{bol}(0.2-1r_{500})}{\mathrm{erg/s}} E(z)^{-1}$	$10^{25.63\pm0.16}$	1.3	this work
$\frac{M_\mathrm{wl}}{M_\odot} E(z)$	$\frac{L_\mathrm{bol}(0.2-1r_{500})}{\mathrm{erg/s}} E(z)^{-1}$	$10^{21.61\pm0.22}$	1.572	this work
$\frac{M_\mathrm{wl}}{M_\odot} E(z)$	$\frac{L_\mathrm{bol}(0.2-1r_{500})}{\mathrm{erg/s}} E(z)^{-1}$	$10^{18.04\pm0.28}$	1.814	this work
$\frac{M_{Mc}}{M_\odot} E(z)$	$\frac{L_\mathrm{bol}(0.2-1r_{500})}{\mathrm{erg/s}} E(z)^{-1}$	$10^{25.81\pm0.25}$	1.3	this work
$\frac{M_{Mc}}{M_\odot} E(z)$	$\frac{L_\mathrm{bol}(0.2-1r_{500})}{\mathrm{erg/s}} E(z)^{-1}$	$10^{21.77\pm0.29}$	1.572	this work
$\frac{M_{Mc}}{M_\odot} E(z)$	$\frac{L_\mathrm{bol}(0.2-1r_{500})}{\mathrm{erg/s}} E(z)^{-1}$	$10^{18.18\pm0.32}$	1.814	this work
$\frac{M_\mathrm{wl}}{M_\odot} E(z)$	$\frac{L_\mathrm{bol}(0.2-2.5r_{500})}{\mathrm{erg/s}} E(z)^{-1}$	$10^{21.59\pm0.05}$	1.572	Z08, $r_{500}^{Y_\mathrm{X},\mathrm{X}}$
$\frac{M_\mathrm{wl}}{M_\odot} E(z)$	$\frac{L_{0.5-2.0\,\mathrm{keV}}(0.2-1r_{500})}{\mathrm{erg/s}} E(z)^{-1}$	$10^{25.03\pm0.21}$	1.3	this work
$\frac{M_{Mc}}{M_\odot} E(z)$	$\frac{L_{0.5-2.0\,\mathrm{keV}}(0.2-1r_{500})}{\mathrm{erg/s}} E(z)^{-1}$	$10^{25.13\pm0.23}$	1.3	this work

We compared our results to Zhang et al. (2008) and Zhang et al. (2010). Zhang et al. (2008) obtained their $M_{\rm wl} - M_{\rm X}$ relation from 19 galaxy clusters of the LoCuSS-sample. This sample consists of more than 100 low-redshift clusters ($0.14 < z < 0.3$) selected from the *ROSAT* All Sky Survey with $L_{0.1-2.4\,\rm keV} \gtrsim 2 \times 10^{44}\,\rm erg\,s^{-1}$. The X-ray masses were obtained from *XMM-Newton* data and the weak lensing masses were derived from CFHT-data by Bardeau et al. (2005, 2007). For $\gamma = 1$, Zhang et al. (2008) found that the weak lensing masses are systematically higher by $28 \pm 14\%$ than the X-ray masses. They concluded that the ratio of both mass estimates is biased by the huge errors on $M_{\rm wl}$ for some clusters because the mass errors for each cluster are weighted individually. Our normalisation is 5% higher than, but consistent with theirs.

Zhang et al. (2010) calibrated the $M_{\rm wl} - M_{\rm X}$ relation for 12 LoCuSS clusters observed with *XMM-Newton* and SUBARU. For a more detailed mass comparison, the sample was divided into sub-samples with seven disturbed and five undisturbed clusters. Zhang et al. (2010) assumed that the X-ray masses for their disturbed sub-sample are 6% higher than their weak lensing masses because of adiabatic compression and shock-heating that may overestimate X-ray hydrostatic masses. Our normalisation is 10% lower, but consistent with the normalisation of their relaxed sub-sample. It is not consistent with the normalisation of their disturbed sub-sample and their total sample which are 23% and 17% higher than ours.

8.1.2 $M_{\rm wl}$ from Mc

The huge errors on the weak lensing masses of the merging clusters may bias the derived weak lensing to X-ray mass ratio because our fitting method accounts for the errors on both mass estimates individually for each cluster. This bias can be checked with either simulations or using weak lensing masses with smaller errors. The mass estimates M_{Mc} from the one-parameter NFW-model with fixed concentration, for instance, provide a good cross-check because for a fixed concentration the weak lensing mass-profile is more accurate and the errors on weak lensing masses are significantly smaller (Tables A.1-A.5). However, our weak lensing masses from the *Mc*-model can only serve to check the bias induced by huge error bars because for disturbed clusters this model underpredicts the cluster mass and does not provide good fits to the tangential shear profile of such clusters (Sects. 6.2.1 and 6.3).

The $M_{Mc} - M_{\rm X}$ relation is plotted in Fig. 8.2. The normalisation is $\sim 37\%$ higher than that of the $M_{\rm wl} - M_{\rm X}$ relation. Our results agree best with the disturbed sub-sample of Zhang et al. (2010) which has $\sim 6\%$ lower normalisation than ours. Due to the large error of our normalisation, the $M_{Mc} - M_{\rm X}$ relation is also consistent with their total sample, but not consistent with their relaxed sub-sample and Zhang et al. (2008).

The significant difference to the $M_{\rm wl}$-$M_{\rm X}$ relation may be due to: The *Mc*-model poorly fits our mergers CL0015.9+1609 and MS1008.1−1224. Furthermore, MS0451.6−0305 is not fitted well by that mass model as well. Only for MS2137.3−2353, the *Mc*-model fits the tangential shear profile best. Thus, $M_{\rm X}$ is $\sim 12\%$ higher than M_{Mc} at $r_{500,\rm X}$. That the *Mc*-model poorly fits three of our clusters is also reflected in the error on normalisation which is ~ 2 times larger than that of the $M_{\rm wl} - M_{\rm X}$ relation.

8.2 X-ray hydrostatic and weak lensing masses versus temperature

The slope for the $M - T_{\rm X}$ relations was fixed at $\gamma = 1.5$ according to Sect. 3.2.2 which is convenient to compare to the REFLEX-DXL sample at $z \sim 0.3$ (Zhang et al. 2006). For the $M_{\rm wl} - T_{\rm X}$ and $M_{Mc} - T_{\rm X}$ relations we also fixed the slope at $\gamma = 1.59$ to compare our results with Zhang et al. (2008).

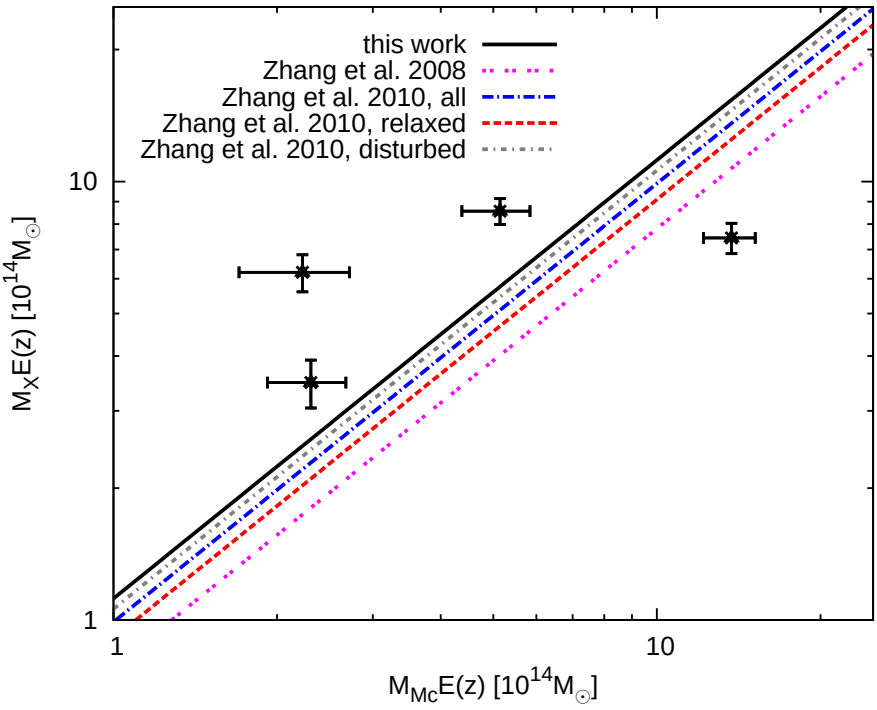

Figure 8.2: Hydrostatic masses $M_{\rm X}$ versus weak lensing masses M_{Mc} at $r_{500,\rm X}$ for our sample and the samples from Zhang et al. (2008) and Zhang et al. (2010). To be consistent with the mass-observable scaling relations, $E(z)$ was also applied for the comparison of weak lensing and X-ray hydrostatic masses.

8.2.1 $M_{\rm X}$ versus $T_{\rm X}$

We compared our results to Ettori et al. (2004), Zhang et al. (2006), Zhang et al. (2008) and Vikhlinin et al. (2009a). The $M_{\rm X} - T_{\rm X}$ relation is plotted in the upper panel of Fig. 8.3.

Ettori et al. (2004) used a sample of 28 clusters at $0.4 < z < 1.3$ with luminosities between $10^{44}\,{\rm erg/s} < L_{\rm X} < 1.2 \times 10^{46}\,{\rm erg\,s^{-1}}$. The sample was observed with *Chandra* to study the evolution of scaling relations. The emission-weighted temperatures ($3 - 11\,{\rm keV}$) were determined from spectra in the $0.6 - 8.0\,{\rm keV}$ energy band assuming a "mekal"-model. The radius within which the temperatures were determined was chosen individually for each cluster to optimise the signal-to-noise ratio in the $0.5 - 5.0\,{\rm keV}$ energy band because this energy band consists of most of the effective area of *Chandra*. The masses within r_{500} were derived from the hydrostatic equation (Eq. 3.14) assuming an isothermal temperature. For the redshift evolution correction $E(z)$ and $\Delta_{\rm c,z} = 18\pi^2 + 82(\Omega_{\rm m,z} - 1) - 39(\Omega_{\rm m,z} - 1)^2$ were applied to $M_{\rm X}$. The latter is the analytic approximation derived from the spherical collapse model (Sect. 1.3.2) for a flat universe and $\Omega_{\rm m,z}$ is the matter density at redshift z. This factor accounts for the fact that their masses and observables were obtained for an overdensity Δ_z which is 500 times the critical density at the cluster redshift z. Ettori et al. (2004) obtained $M_{\rm X}/M_\odot = 10^{13.21\pm0.03}(T_{\rm X}/{\rm keV})^{1.98\pm0.03}$ with free slope and $M_{\rm X}/M_\odot = 10^{13.57\pm0.02}(T_{\rm X}/{\rm keV})^{1.5}$ with fixed slope. The temperatures were originally normalised to 6 keV but we transformed the scaling relations to our notation in Table 8.1. Our mass-temperature relation for $\gamma = 1.5$ is 21% lower than theirs.

The REFLEX-DXL was constructed by Zhang et al. (2006). It is an unbiased, flux-limited and almost volume-complete sample consisting of 13 X-ray luminous clusters ($L_{0.1-2.4\,{\rm keV}} \gtrsim 5.9 \times 10^{44}\,{\rm erg\,s^{-1}}$) observed with *XMM-Newton*. The clusters are at $z \sim 0.3$ which is at the lower redshift-end of our sample. Zhang et al. (2006) determined the global temperatures within

$0.1 - 0.5r_{500}$ because the temperature profiles of their clusters show self-similarity in this range. Besides $E(z)$, these authors used $(\Delta_{c,z}/\Delta_{c,0})^{0.5}$ for the redshift evolution correction of M_X to compare their results with Ettori et al. (2004). We assume that our normalisation is not consistent with theirs because they excluded a smaller core region and because of $(\Delta_{c,z}/\Delta_{c,0})^{0.5}$.

Zhang et al. (2008) determined global temperatures within $0.2-0.5r_{500}$ and accounted for the redshift evolution of M_X only with $E(z)$ which we adopted. Thus, our normalisation for the fixed slope $\gamma = 1.5$ agrees better with theirs for $\gamma = 1.499$ than with the normalisation of their previous work (Zhang et al. 2006). The normalisation for our $M_X - T_X$ relation with slope fixed at $\gamma = 1.59$ is 13% higher than their normalisation of the $M_X - T_X$ relation with fitted slope $\gamma = 1.654 \pm 0.256$.

We also compared our $M_X - T_X$ relation to that of the low-redshift sub-sample of relaxed *Chandra*-clusters from Vikhlinin et al. (2009a). This sub-sample consists of 49 flux-limited clusters ($f_{0.5-2.0\,\mathrm{keV}} > 1.3 \times 10^{-11}\,\mathrm{erg\,s^{-1}\,cm^{-2}}$) from the 400 Square Degree ROSAT PSPC Galaxy Cluster Survey (Burenin et al. 2007) with a mean redshift of $z \sim 0.15$. For the $M_X - T_X$ relation, only 19 clusters from this survey were used because those are relaxed. The global temperatures were determined within $0.15 - 0.5r_{500}$ because their temperature profiles appear self-similar in that range. The temperatures were normalised to 5 keV since this is approximately the median temperature of the sample. A redshift evolution correction $E(z)$ was applied to M_X. With the slope fixed at $\gamma = 1.5$, our normalisation is 17% higher than, but consistent with theirs. Vikhlinin et al. (2009a) extrapolated the $M_X - T_X$ relation of their low-redshift sample to clusters at higher redshifts using simulations of Nagai et al. (2007). Thereby, they accounted for an increasing fraction of merging clusters towards higher redshifts. These simulations indicated a systematic offset in the normalisations of $M_X - T_X$ for relaxed and disturbed clusters because merging clusters have lower temperatures than relaxed clusters of the same mass. Vikhlinin et al. (2009a) concluded that the normalisations of $M_X - T_X$ relations differs by 7% for clusters at $z = 0$ and $z \sim 0.6$. Our normalisation is 17% higher but consistent with theirs.

8.2.2 M_{wl} from the best fit model versus T_X

To compare the $M_X - T_X$ relation to the $M_{wl} - T_X$ relation, the slope for the latter was fixed at $\gamma = 1.5$. We show the scaling relation in the middle panel of Fig. 8.3. Our normalisation of the $M_{wl} - T_X$ relation is 21% lower, but consistent with that of the $M_X - T_X$ relation. The errors on the normalisation are ~ 2 times larger compared to using M_X.

To compare our results to Zhang et al. (2008) the slope was also fixed to $\gamma = 1.59$. Zhang et al. (2008) used fixed slopes for r_{500} and for $r_{500}^{Y_X,X}$, where the superscript "Y_X, X" states that this overdensity radius was derived from the $M - Y_X$ relation because $Y_X = M_{gas}T_X$ provides a good mass proxy as found in simulations (Nagai et al. 2007). Zhang et al. (2008) used this alternative radial scale because some merging clusters in their sample consisting of 37 LoCuSS clusters in total show significant offset from the best fit scaling relations. Our normalisation is 37% higher than that of Zhang et al. (2008) for r_{500} and 31% lower than their normalisation for $r_{500}^{Y_X,X}$.

8.2.3 M_{Mc} versus T_X

The $M_{Mc} - T_X$ relation is plotted in the lower panel of Fig. 8.3. The normalisation is consistent with that of the $M_X - T_X$ relation and with that of the $M_{wl} - T_X$ relation although it is 21% higher than the latter. The errors on the normalisation are slightly larger than that of the $M_{wl} - T_X$ relation which may be because the *Mc*-model provides a poor fit to most of our clusters.

Our normalisation is consistent with those of Zhang et al. (2008) for r_{500} and $r_{500}^{Y_X,X}$ which are 17% and 9% lower than our normalisation, respectively.

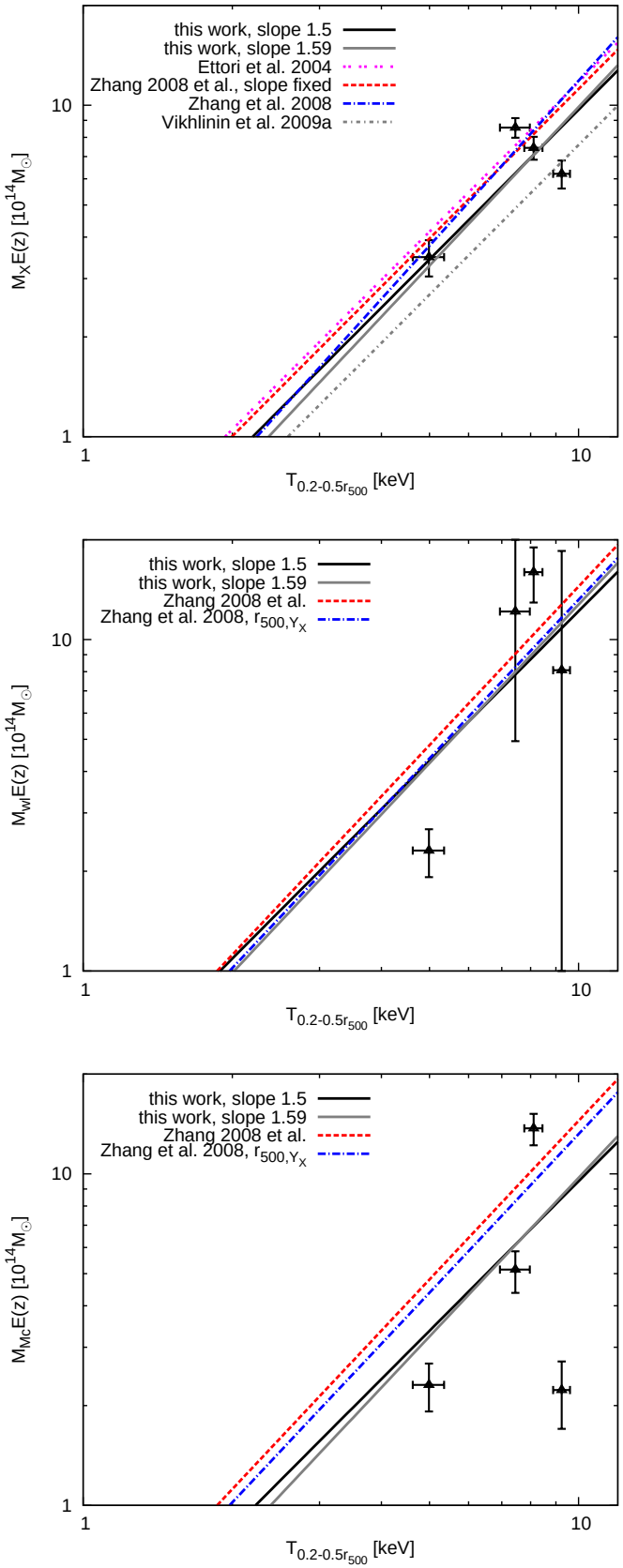

Figure 8.3: X-ray hydrostatic masses M_X (*upper*) and weak lensing masses from the best fit model M_{wl} (*middle*) and from the *Mc*-model, M_{Mc} (*lower*) versus the global temperature T_X. All three scaling relations are compared to Zhang et al. (2008) and the $M_X - T_X$ relation is also compared to Ettori et al. (2004) and Vikhlinin et al. (2009a).

8.3 X-ray hydrostatic and weak lensing masses versus luminosity

We calibrated $M_{\rm X} - L_{\rm X}$-relations for the luminosities in the soft band, $L_{0.5-2.0\,{\rm keV}}$, the *ROSAT*-band $L_{0.1-2.4\,{\rm keV}}$ and the bolometric luminosity, $L_{\rm bol}$ with X-ray hydrostatic masses, $M_{\rm X}$, weak lensing masses from the best-fit model and from the *Mc*-model, $M_{\rm wl}$ and M_{Mc}, respectively. For all relations, the slope was fixed at $\gamma = 1.3$ which is convenient to compare to Zhang et al. (2006) and close to the self-similar prediction $\gamma = 1.33$ (Sect. 3.2.2). To compare our results to Zhang et al. (2008), the slope for the $M_{\rm X} - L_{\rm bol}$ relation was also fixed at $\gamma = 1.814$ and the slopes of the $M_{\rm wl} - L_{\rm bol}$ and the $M_{Mc} - L_{\rm bol}$ relations were fixed at $\gamma = 1.572$. Zhang et al. (2008) used $\gamma = 1.814$ to check the self-consistency of their $M_{\rm X} - L_{\rm bol}$ relation ($L_{\rm bol} \propto T^{2.719}$, $M_{\rm X} \propto T_{\rm X}^{1.499} \Rightarrow L_{\rm bol} \propto M_{\rm X}^{1.814}$) and $\gamma = 1.572$ was used to compare their results to Borgani et al. (2004).

All mass-luminosity relations can have large scatter because the luminosity is not necessarily correlated with mass or dynamical state. $L_{\rm X}$ can easily be affected by merging but also by cooling cores wherefore it can be used to probe the evolution of cool cores. Thus, to calculate global luminosities, the core region is often excluded in the literature.

8.3.1 $M_{\rm X}$ versus luminosity

We compared our $M_{\rm X} - L_{0.1-2.4\,{\rm keV}}$ relation to Zhang et al. (2006). The $M_{\rm X} - L_{\rm bol}$ relation was compared to Ettori et al. (2004), Zhang et al. (2006) and Zhang et al. (2008). Our $M_{\rm X} - L_{\rm bol}$ relations for $\gamma = 1.3$ and $\gamma = 1.814$ are plotted and compared to the literature Fig. 8.4.

Ettori et al. (2004) measured the luminosities of their sample within r_{500}. For a fitted slope, they obtained $L_{\rm bol}({\rm erg^{-1}\,s}) = 10^{17.05\pm0.63}(M_{\rm X}/M_\odot)^{1.88\pm0.42}$ and for a fixed slope they obtained $L_{\rm bol}({\rm erg^{-1}\,s}) = 10^{25.38\pm0.03}(M_{\rm X}/M_\odot)^{1.33}$. The results are already rescaled to our notation. Our normalisations with $\gamma = 1.814$ and $\gamma = 1.3$ are not consistent with theirs for $\gamma = 1.88 \pm 0.42$ and $\gamma = 1.3$, respectively which may be due to that they normalised their scaling relation using Δ_z, i.e. $L_{\rm bol}E(z)^{-1} \propto \Delta_z^{7/6}[M_{\rm X}E(z)]^{4/3}$.

Zhang et al. (2006) applied $(\Delta_{{\rm c},z}/\Delta_{{\rm c},0})^{0.5}\,E(z)$ to $M_{\rm X}$ and $(\Delta_{{\rm c},z}/\Delta_{{\rm c},0})^{-0.5}\,E(z)^{-1}$ to $L_{0.1-2.4\,{\rm keV}}$ and $L_{\rm bol}$. $L_{0.1-2.4\,{\rm keV}}$ and $L_{\rm bol}$ were calculated within $r = 20'$ and to account for cool core the $r < 0.1r_{500}$-region was excluded. Our normalisation of the $M_{\rm X} - L_{0.1-2.4\,{\rm keV}}$ relation with $\gamma = 1.3$ is 22% higher than, but consistent with theirs and our normalisation of the $M_{\rm X} - L_{\rm bol}$ relation with $\gamma = 1.3$ is not consistent with theirs. We assume that this is due to: (1) Our luminosities were determined within $0.2 - 1r_{500}$ instead of $0.1r_{500} - 20'$ which gives lower luminosities. (2) Zhang et al. (2006) used $(\Delta_{{\rm c},z}/\Delta_{{\rm c},0})^{\pm0.5}$ in addition to account for evolution effects.

To calculate the bolometric luminosity, Zhang et al. (2008) used the $0.2 - 2.5r_{500}$ range to account for cool cores. Luminosities and masses were redshift corrected with $E(z)^{-1}$ and $E(z)$, respectively. With our slope fixed at $\gamma = 1.814$, our normalisation is 37% higher than, but consistent with theirs. We do not compare our normalisation for $\gamma = 1.814$ to the normalisation of their fitted slope $\gamma = 2.325 \pm 0.701$ because the slopes are too different.

8.3.2 $M_{\rm wl}$ from the best fit model versus luminosity

The normalisations of the $M_{\rm wl} - L_{\rm X}$ relations with $\gamma = 1.3$ are consistent with those of the $M_{\rm X} - L_{\rm X}$ relations, except for $L_{\rm bol}$. Figure 8.4 shows that our scaling relation with slope $\gamma = 1.814$ fits the data better than that with slope $\gamma = 1.3$ which is close to the self-similar prediction $\gamma = 1.33$. Comparing our $M_{\rm wl} - L_{\rm bol}$ relation to our $M_{\rm X} - L_{\rm bol}$ relation with $\gamma = 1.814$, the former is 35% higher than, but consistent with the latter.

Our normalisation of the $M_{\rm wl} - L_{\rm bol}$ relation is 37% higher than, but consistent with Zhang et al. (2008) for $r_{500}^{Y_{\rm X},{\rm X}}$ and $\gamma = 1.814$.

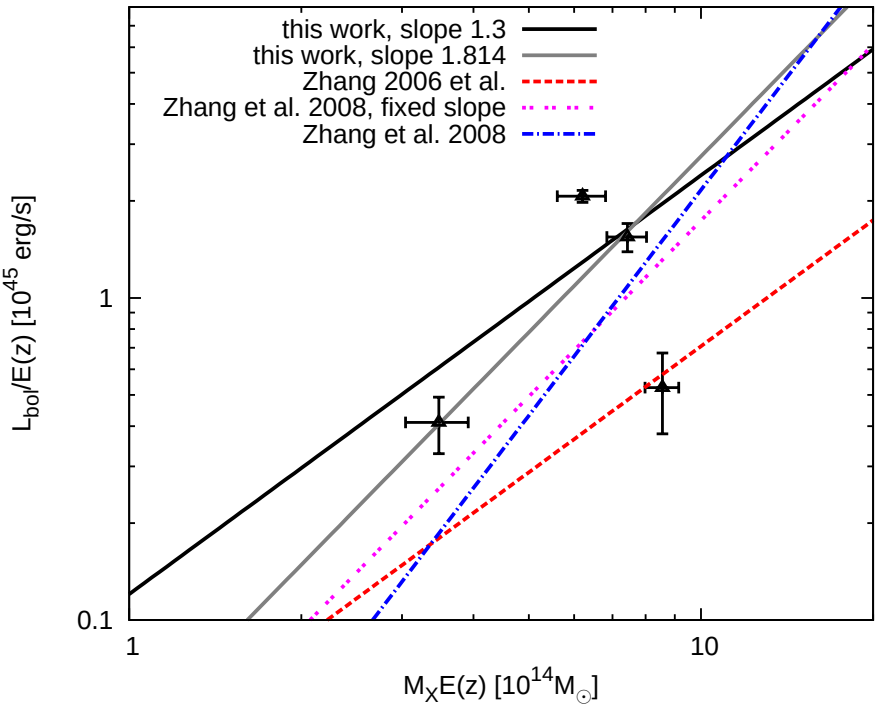

Figure 8.4: $M_{\rm X} - L_{\rm bol}$ relations for $\gamma = 1.3$ and $\gamma = 1.814$ compared to Zhang et al. (2006) and Zhang et al. (2008).

8.3.3 M_{Mc} versus luminosity

We compared our normalisations of the $M_{Mc} - L_{\rm X}$ relations to the mass-luminosity relations with $M_{\rm X}$ and $M_{\rm wl}$ to check the effect of the errors on mass. The $M_{Mc} - L_{\rm bol}$ relation is also compared to Zhang et al. (2008).

The normalisations of the $M_{Mc} - L_{\rm X}$ relations agree with those of the $M_{\rm X} - L_{\rm X}$ relations. The errors on normalisation do not change much between using $M_{\rm wl}$ and M_{Mc}, although they are slightly larger for the latter which may be due to that M_{Mc} poorly fits the tangential shear profiles three out of four clusters.

With the slope fixed at $\gamma = 1.572$, our normalisation is 5% higher than, but consistent with that of Zhang et al. (2008) for $r_{500}^{Y_{\rm X},{\rm X}}$.

8.4 Luminosity versus temperature

The luminosity-temperature relation $L_{\rm X} - T_{\rm X}$ has been extensively studied for cluster samples at low and intermediate redshifts (e.g. Markevitch et al. 1998; Arnaud & Evrard 1999; Ikebe et al. 2002; Zhang et al. 2006; Chen et al. 2007; Zhang et al. 2008).

At higher redshifts ($0.4 < z < 1.3$), this relation was investigated by e.g. Ettori et al. (2004), Kotov & Vikhlinin (2005) and Maughan et al. (2006). Kotov & Vikhlinin (2005) found an evolution in the bolometric luminosity $L_{\rm bol}$ as $\propto (1+z)^{1.8\pm0.3}$ with *XMM-Newton* data. Although this result is consistent with previous observations using *Chandra*-data (e.g. Vikhlinin et al. 2002) and former *XMM-Newton* studies (e.g. Lumb et al. 2004) it disagrees with Ettori et al. (2004).

In the literature, cool cores are often excluded (e.g. Markevitch 1998; Kotov & Vikhlinin 2005; Zhang 2001; Zhang et al. 2006, 2008) because the luminosity is sensitive to cool cores.

Thus, the scatter of the $L_X - T_X$ can be reduced by excluding cool cores which also reduces its normalisation.

The $L_{bol} - T_X$ relation is plotted and compared with the literature in Fig. 8.5. Slopes and normalisations of all $L_X - T_X$ relations are listed and compared in Table 8.2.

Table 8.2: Parameters of the X-ray scaling relations not including total cluster masses for fitting the power law $Y = Y_0 X^\gamma$. To compare our results to the literature, we transformed our scaling relations to the notation of Zhang et al. (2006, 2008, 2010). $(\Delta_{c,z}/\Delta_{c,0})^{\pm 0.5}$ is the density contrast of a virialised halo with respect to the critical density with the analytical approximation $\Delta_{c,z}$ derived from the spherical collapse model for a flat universe (Bryan & Norman 1998). The abbreviations for the literature are: M98 for Markevitch et al. (1998), AE99 for Arnaud & Evrard (1999), I02 for Ikebe et al. (2002), M06 for Maughan et al. (2006), Z06 for Zhang et al. (2006), B07 for Balestra et al. (2007), Z08 for Zhang et al. (2008), V09a for Vikhlinin et al. (2009a), Z10 for Zhang et al. (2010) and Z11 for Zhang et al. (2011a).

X	Y	Y_0	γ	Sample
$\frac{T_{0.2-0.5r_{500}}}{\mathrm{keV}}$	$\frac{L_{0.1-2.4\,\mathrm{keV}}(0.2-1r_{500})}{\mathrm{erg/s}}\,E(z)^{-1}$	$10^{42.17\pm0.08}$	2.6	this work
$\frac{T_{0.2-0.5r_{500}}}{\mathrm{keV}}$	$\frac{L_{0.1-2.4\,\mathrm{keV}}(0.2-1r_{500})}{\mathrm{erg/s}}\,E(z)^{-1}$	$10^{42.36\pm0.08}$	2.219	this work
$\frac{T_{0.6-1.0\,h^{-1}\,\mathrm{Mpc}}}{\mathrm{keV}}$	$\frac{L_{0.1-2.4\,\mathrm{keV}}(0.05-1.0\,h^{-1}\,\mathrm{Mpc})}{\mathrm{erg/s}}$	$10^{42.52\pm0.12}$	2.10 ± 0.12	M98, γ fitted
$\frac{T_X}{\mathrm{keV}}$	$\frac{L_{0.1-2.4\,\mathrm{keV}}}{\mathrm{erg/s}}$	$10^{42.14}$	2.5	I02
$\frac{T_{0.1-0.5r_{500}}}{\mathrm{keV}}$	$\frac{L_{0.1-2.4\,\mathrm{keV}}(0.1r_{500}-20')}{\mathrm{erg/s}}\,(\Delta_{c,z}/\Delta_{c,0})^{-0.5}\,E(z)^{-1}$	$10^{42.37\pm0.06}$	2.6	Z06
$\frac{T_{0.2-0.5r_{500}}}{\mathrm{keV}}$	$\frac{L_{0.1-2.4\,\mathrm{keV}}(0.2-2.5r_{500})}{\mathrm{erg/s}}\,E(z)^{-1}$	$10^{42.67\pm0.03}$	2.219	Z08
$\frac{T_{0.2-0.5r_{500}}}{\mathrm{keV}}$	$\frac{L_{0.1-2.4\,\mathrm{keV}}(0.2-2.5r_{500})}{\mathrm{erg/s}}\,E(z)^{-1}$	$10^{42.75\pm0.28}$	2.127 ± 0.323	Z08, γ fitted
$\frac{T_{0.2-0.5r_{500}}}{\mathrm{keV}}$	$\frac{L_{bol}(0.2-1r_{500})}{\mathrm{erg/s}}\,E(z)^{-1}$	$10^{42.44\pm0.05}$	2.98	this work
$\frac{T_{0.2-0.5r_{500}}}{\mathrm{keV}}$	$\frac{L_{bol}(0.2-1r_{500})}{\mathrm{erg/s}}\,E(z)^{-1}$	$10^{42.68\pm0.05}$	2.719	this work
$\frac{T_{0.6-1.0\,h^{-1}\,\mathrm{Mpc}}}{\mathrm{keV}}$	$\frac{L_{bol}(0.05-1.0\,h^{-1}\,\mathrm{Mpc})}{\mathrm{erg/s}}$	$10^{42.44\pm0.27}$	2.64 ± 0.27	M98, γ fitted
$\frac{T_X}{\mathrm{keV}}$	$\frac{L_{bol}}{\mathrm{erg/s}}$	$10^{42.82\pm0.14}$	2.88 ± 0.05	AE99, γ fitted
$\frac{T_{r_{200}}}{\mathrm{keV}}$	$\frac{L_{bol}(r_{200})}{\mathrm{erg/s}}$	$10^{42.55\pm0.12}$	2.78 ± 0.55	M06, γ fitted
$\frac{T_{0.1-0.5r_{500}}}{\mathrm{keV}}$	$\frac{L_{bol}(0.1r_{500}-20')}{\mathrm{erg/s}}\,(\Delta_{c,z}/\Delta_{c,0})^{-0.5}\,E(z)^{-1}$	$10^{42.38\pm0.06}$	2.98	Z06
$\frac{T_{0.2-0.5r_{500}}}{\mathrm{keV}}$	$\frac{L_{bol}(0.2-2.5r_{500})}{\mathrm{erg/s}}\,E(z)^{-1}$	$10^{42.65\pm0.03}$	2.719	Z08
$\frac{T_{0.2-0.5r_{500}}}{\mathrm{keV}}$	$\frac{L_{bol}(0.2-2.5r_{500})}{\mathrm{erg/s}}\,E(z)^{-1}$	$10^{42.74\pm0.27}$	2.614 ± 0.319	Z08, γ fitted
$\frac{T_{0.2-0.5r_{500}}}{\mathrm{keV}}$	$\frac{L_{0.5-2.0\,\mathrm{keV}}(0.2-1r_{500})}{\mathrm{erg/s}}\,E(z)^{-1}$	$10^{42.08\pm0.07}$	2.6	this work
$\frac{T_{0.2-0.5r_{500}}}{\mathrm{keV}}$	$\frac{Z_{0.2-0.5r_{500}}}{Z_\odot}$	$10^{-0.202\pm0.043}$	-0.324	this work
$\frac{T_{0.2-0.5r_{500}}}{\mathrm{keV}}$	$\frac{Z_{0.2-0.5r_{500}}}{Z_\odot}$	$10^{-0.323\pm0.061}$	-0.324 ± 0.098	Z11, γ fitted
$\frac{T_{0.15-0.3r_{500}}}{\mathrm{keV}}$	$\frac{Z}{Z_\odot}$	$10^{-0.056}$	-0.47	B07

8.4.1 $L_X - T_X$ relations for *ROSAT* and *ASCA*

Early $L_X - T_X$ relations were investigated with *ROSAT*- and *ASCA*-observations. Since *ASCA* had low spatial resolution ($\sim 3'$), it was used for temperature measurements in the studies described below. The luminosity, however, was determined from *ROSAT*-data.

Markevitch (1998) calibrated $L_X - T_X$ relations for $L_{0.1-2.4\,\mathrm{keV}}$ and L_{bol} for a sample of 32 Abell clusters selected from the *ROSAT* All Sky Survey (RASS) Abell cluster list (Ebeling et al. 1996) plus three non-Abell clusters. The sample is located at $0.04 < z < 0.09$ and has fluxes of $f_{0.1-2.4\,\mathrm{keV}} > 2 \times 10^{11}\,\mathrm{erg\,s^{-1}\,cm^{-2}}$. The flux was measured within $1\,h^{-1}$ Mpc whereby the innermost $50\,h^{-1}$ kpc were excluded to account for cooling flows which reduces the scatter in the $L_X - T_X$ relations. For this reason, flux and luminosity were multiplied by a factor of 1.06 to account for the flux inside that region. The emission-weighted cooling-flow excluding *ASCA*-temperatures were determined in apertures of $(0.6 - 1)\,h^{-1}$ Mpc depending on the observational details because the cluster emission is dominated by bright central regions. After transforming the luminosities to our notation, Markevitch (1998) obtained $L_{0.1-2.4\,\mathrm{keV}}(\mathrm{erg^{-1}\,s}) = 10^{42.52\pm0.12}(T_X/\mathrm{keV})^{2.10\pm0.24}$

and $L_{\rm bol}(\mathrm{erg^{-1}\,s}) = 10^{42.44\pm0.26}(T_{\rm X}/\mathrm{keV})^{2.64\pm0.27}$. Our normalisation of the $L_{\rm bol} - T_{\rm X}$ relation with $\gamma = 2.719$ is 42% higher, but consistent with theirs and our normalisation for the $L_{0.1-2.4\,\mathrm{keV}} - T_{\rm X}$ relation for $\gamma = 2.219$ is 34% lower, but also consistent with theirs.

Arnaud & Evrard (1999) calibrated a $L_{\rm bol} - T_{\rm X}$ relation for 24 clusters selected for statistically accurate temperature measurements with weak cooling flows ($\dot{M} \lesssim 100\,M_\odot\,\mathrm{yr^{-1}}$) and temperatures above $\gtrsim$ 2 keV. The clusters are at $0.01 < z < 0.37$. Temperature and luminosity of 18 of the clusters were measured with the *Ginga*-satellite. The temperatures for the other clusters were obtained with *ACSA*, *Einstein* and *EXOSAT* and the luminosities arise from *ROSAT*. Arnaud & Evrard (1999) found that the bolometric luminosities measured with *Ginga* and *ROSAT* agree well. The scaling relation between both observables is tight with $L_{\rm bol}(\mathrm{erg^{-1}\,s}) = 10^{42.82\pm0.14} \cdot (T_{\rm X}/\mathrm{keV})^{2.88\pm0.15}$ whereby we have transformed their scaling relation to our notation. Our normalisation using $\gamma = 2.98$ is not consistent with theirs and our normalisation using $\gamma = 2.719$ is 28% lower than, but consistent with theirs.

Ikebe et al. (2002) calibrated the $L_{0.1-2.4\,\mathrm{keV}} - T_{\rm X}$ relation for a flux-limited sample ($f \gtrsim 2.0 \times 10^{-11}\,\mathrm{erg\,s^{-1}\,cm^{-2}}$) of 88 low-redshift clusters ($z \lesssim 0.2$) using *ASCA*- and *ROSAT*- observations covering a temperature range of 1.4 – 11 keV. Luminosities were determined with *ROSAT* PSPC observations (Reiprich & Böhringer 2002). The temperatures were determined using a two-temperature model which assumes an isothermal plasma in the cluster region with a cooler isothermal gas component in the central region. For a flat universe with $\Omega_{\rm m} = 0.2$ and $\Omega_\Lambda = 0.8$, Ikebe et al. (2002) obtained $L_{0.1-2.4\,\mathrm{keV}}(\mathrm{erg^{-1}\,s}) = 10^{42.14}(T_{\rm X}/\mathrm{keV})^{2.5}$ after correcting the relation with respect to less luminous clusters. Our normalisation for this relation with the slope fixed at $\gamma = 2.6$ is not consistent with theirs. Since $E(z)$ differs by less than 6% between their cosmology and our ΛCDM-model, we assume that this disagreement is due to the different temperature models.

Chen et al. (2007) investigated the $L_{0.1-2.4\,\mathrm{keV}} - T_{\rm X}$ relation for the flux-limited HIFLUGCS sample ($f_{0.1-2.4\,\mathrm{keV}} > 2\times10^{11}\,\mathrm{erg\,s^{-1}\,cm^{-2}}$) consisting of 106 clusters $z < 0.1$ observed with *ASCA* and *ROSAT*. The luminosities in the *ROSAT*-band were derived from Ikebe et al. (2002). For the temperature, Chen et al. (2007) used two definitions: (1) the emission weighted temperature $T_{\rm m}$ from a single temperature fit to the global spectrum (Markevitch et al. 1998; Reiprich 2001); (2) the hotter bulk component $T_{\rm h}$ of a two temperature model (Ikebe et al. 2002). $T_{\rm m}$ was only used without cooling flow correction because for some clusters $T_{\rm m}$ was measured including the cooling flow region. The slopes for the $L_{0.1-2.4\,\mathrm{keV}} - T_{\rm X}$ relation with $T_{\rm m}$ and $T_{\rm h}$ are with 2.23 ± 0.15 and 2.73 ± 0.13 higher than the self-similar prediction 1.5 which is, however, consistent with Reiprich & Böhringer (2002). Chen et al. (2007) assumed that the slope of the $L_{0.1-2.4\,\mathrm{keV}} - T_{\rm m}$ relation is smaller than that of the $L_{0.1-2.4\,\mathrm{keV}} - T_{\rm h}$ relation because $T_{\rm m}$ has an offset towards low temperatures and because fewer low-luminosity clusters were included in the $L_{0.1-2.4\,\mathrm{keV}} - T_{\rm m}$ relation. We did not compare our results with their study because they assumed an Einstein-de Sitter cosmology which is too different from our cosmology. Comparing both cosmologies for our high-redshift clusters, the $E(z)$ differs by $\sim 32\%$.

8.4.2 $L_{\rm X} - T_{\rm X}$ relations for *XMM-Newton* and *Chandra*

Temperature-luminosity relations based on high-resolution instruments were performed with data from *XMM-Newton* and *Chandra*. Those studies also include the higher redshift range $0.3 < z < 1.3$.

Ettori et al. (2004) obtained $L_{\rm bol}(\mathrm{erg^{-1}\,s}) = 10^{41.90\pm0.11}(T_{\rm X}/\mathrm{keV})^{3.72\pm0.47}$ for a free slope and $L_{\rm bol}(\mathrm{erg^{-1}\,s}) = 10^{43.44\pm0.02}(T_{\rm X}/\mathrm{keV})^{2.00}$ for a fixed slope using the linear regression algorithm BCES (Akritas & Bershady 1996). Both scaling relations are already transformed to our notation. We did not compare their results with ours because the slopes are too different from our sample.

Lumb et al. (2004) calibrated the $L_{\rm bol} - T_{\rm X}$ relation for a sample of eight clusters selected from the SHARC and 160 Square Degree (160SD) *ROSAT* surveys at $0.45 < z < 0.62$ (Romer et al. 2000; Burke et al. 2003) with *XMM-Newton*. The temperatures were obtained within a radius that varies between 90″ and 145″ among the clusters using a "mekal"-model plus a model for interstellar absorption. Following Markevitch et al. (1998), cool cores were excised by excluding the innermost $50h_{50}^{-1}$ kpc. Bolometric luminosities were obtained with `XSPEC` within the virial radius $r_{\rm vir}$ using the $T_{\rm X} - r_{\rm vir}$ relation from Evrard et al. (1996). The best fit "mekal"-model was used to determine the bolometric luminosity which is here defined as the luminosity in the $0 - 20\,{\rm keV}$ band. After rescaling to our notation, Lumb et al. (2004) obtained $L_{\rm bol}({\rm erg}^{-1}\,{\rm s}) = 10^{43.10\pm0.03^{+0.89}_{-0.74}}(T_{\rm X}/{\rm keV})^{2.7\pm0.4}$ assuming an Einstein-de Sitter cosmology with $h = 0.5$ and using the bisector method for linear regression (Akritas & Bershady 1996). Lumb et al. (2004) compared their scaling relation to that of Markevitch et al. (1998) and found an evolutionary effect such that clusters having the same temperature were more luminous in the past. We did not compare our results to their study because their cosmology is too different from ours.

Kotov & Vikhlinin (2005) investigated the $L_{\rm bol} - T_{\rm X}$ relation from a sample of 10 *XMM-Newton* clusters at $0.4 < z < 0.7$ with temperatures of $2.5 - 9\,{\rm keV}$. Temperatures were fitted in the $0.5 - 10\,{\rm keV}$ energy band within $70\,{\rm kpc} < r < r_{500}$ using a "mekal"-model and renormalised by +8% to account for the cross-calibration of *Chandra* and *XMM-Newton*. Luminosities were calculated within $70 - 1400\,{\rm kpc}$ using the emission weighted temperature $T_{\rm X,ew}$. The innermost 70 kpc were excluded to reduce the scatter from cool cores. To calibrate the $L_{\rm bol} - T_{\rm X}$ relation, the best fit temperature from the spectral fitting was used for clusters with irregular morphology and $T_{\rm X,ew}$ was used for the others. Kotov & Vikhlinin (2005) found $L_{\rm bol}({\rm erg}^{-1}\,{\rm s}) \propto (1+z)^{1.8\pm0.3}(T_{\rm X,ew}/{\rm keV})^{2.64}$ using the bisector method of Akritas & Bershady (1996) modified such that it accounts for measurement errors and intrinsic scatter. Compared to the low-redshift sample of Markevitch et al. (1998), Kotov & Vikhlinin (2005) found an evolution with redshift.

Maughan et al. (2006) used 11 high-redshift clusters ($0.6 < z < 1.0$) from the Wide Angle *ROSAT* Pointed Survey (WARPS, e.g Scharf et al. 1997; Perlman et al. 2002) to investigate the evolution of scaling relations with redshift. The clusters were observed with *XMM-Newton* and *Chandra*. Originally, the sample was flux limited ($f_{0.5-2.0\,{\rm keV}} > 6.4\times10^{-13}\,{\rm erg\,s^{-1}\,cm^2}$). but two *XMM-Newton* clusters were excised because of high background. The spectra which were used to determine the temperature were drawn from within a radius $r_{\rm d}$, inside which cluster emission could be detected at least at the 3σ-level, and fitted to a "mekal"-model in the $0.4 - 7.0\,{\rm keV}$ band. To calibrate the scaling relations, the bolometric luminosities measured within $r_{\rm d}$ were rescaled to r_{200} and redshift weighted with $L_{\rm bol}E(z)^{-1}(\Delta_{{\rm c},z}/\Delta_{{\rm c},0})^{-0.5}$. In our notation, Maughan et al. (2006) obtained $L_{\rm bol}({\rm erg}^{-1}\,{\rm s}) = 10^{42.55\pm0.12}(T_{\rm X}/{\rm keV})^{2.78\pm0.55}$. Thus, our normalisation for $\gamma = 2.98$ is 22% lower, but consistent with theirs. Our normalisation for $\gamma = 2.719$ is 26% higher than, but consistent with theirs. Maughan et al. (2006) found the evolution in the scaling relation is consistent with self-similar predictions.

Zhang et al. (2006) calibrated $L_{0.1-2.4\,{\rm keV}} - T_{\rm X}$ and $L_{\rm bol} - T_{\rm X}$ relations for the REFLEX-DXL sample (see Sects. 8.2.1 and 8.3.1 for sample characteristics and details of their analysis). Using a fixed slope, they obtained $L_{0.1-2.4\,{\rm keV}}({\rm erg}^{-1}\,{\rm s}) = 10^{42.37\pm0.06}(T_{\rm X}/{\rm keV})^{2.6}$ and $L_{\rm bol}({\rm erg}^{-1}\,{\rm s}) = 10^{42.38\pm0.06}(T_{\rm X}/{\rm keV})^{2.98}$. Our normalisation for the $L_{0.1-2.4\,{\rm keV}} - T_{\rm X}$ relation is not consistent with theirs and our normalisation for the $L_{\rm bol} - T_{\rm X}$ relation is 13% higher, but consistent with theirs using the same slopes. Zhang et al. (2006) reduced the scatter in the $L_{\rm X} - T_{\rm X}$ relations by 10% excluding cool cores. Their $L_{\rm bol} - T_{\rm X}$ relation also agrees with Markevitch et al. (1998), Arnaud & Evrard (1999), Reiprich & Böhringer (2002) and Kotov & Vikhlinin (2005) after applying their alternative redshift evolution $(1+z)^{1.8}$, i.e. $L_{\rm bol}({\rm erg}^{-1}\,{\rm s}) \propto (1+z)^{1.8}(T_{\rm X}/{\rm keV})^{2.98}$.

Zhang et al. (2008) calibrated $L_{0.1-2.4\,{\rm keV}} - T_{\rm X}$ and $L_{\rm bol} - T_{\rm X}$ relations for the LoCuSS-sample (see Sects. 8.2.1 and 8.3.1 for sample characteristics and details of their analysis). The fixed slope

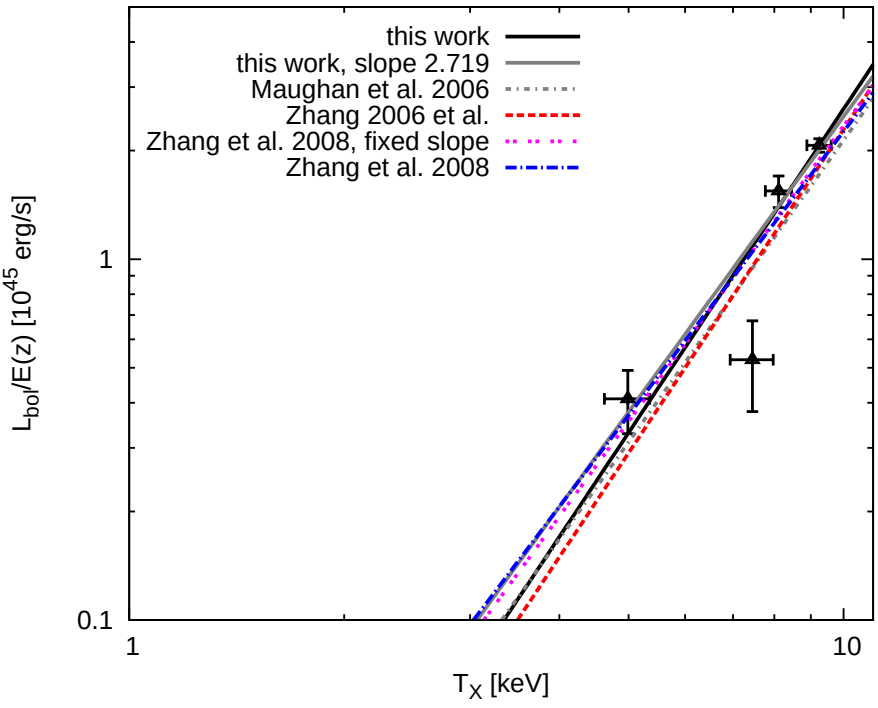

Figure 8.5: $L_{\rm bol}$ versus global temperatures $T_{\rm X}$. Our luminosities and temperatures are determined within $0.2 - 1r_{500}$ and $0.2 - 0.5r_{500}$, respectively. The results from this work are compared to Maughan et al. (2006), Zhang et al. (2006) and Zhang et al. (2008).

of their $L_{\rm bol} - T_{\rm X}$ relation is with 2.614 ± 0.319 higher than the self-similar prediction $L_{\rm X} \propto T_{\rm X}^2$ (Sect. 3.2.2). Their normalisation agrees with Markevitch et al. (1998), Arnaud & Evrard (1999) and Chen et al. (2007). The normalisation of the $L_{0.1-2.4\,{\rm keV}} - T_{\rm X}$ relation further agrees with Ikebe et al. (2002). Zhang et al. (2008) found that the evolution in their scaling relation is consistent with LSS growth predictions and that the difference between the normalisation of the $L_{\rm X} - T_{\rm X}$ relations using *ROSAT/ASCA* and *XMM-Newton/Chandra* is marginal. With our slope fixed at $\gamma = 2.219$, our normalisation of the $L_{0.1-2.4\,{\rm keV}} - T_{\rm X}$ relation is not consistent with theirs for $\gamma = 2.219$ and $\gamma = 2.127 \pm 0.323$. Our normalisation of the $L_{\rm bol} - T_{\rm X}$ relation for $\gamma = 2.719$ is 7% higher than, but consistent with theirs for the same slope and 13% lower than, but also consistent with their normalisation for $\gamma = 2.614 \pm 0.319$.

8.5 Temperature versus metallicity

The $T_{\rm X} - Z$ relation checks if line emission boosts the X-ray luminosity of flux-limited samples because low-mass systems with high metallicity might be included in such samples since their luminosity is boosted due to the high metallicity. Our slope was fixed to $\gamma = 0.324$ which is convenient to compare to Zhang et al. (2011a) who fitted this value. We compared our results to Balestra et al. (2007) and Zhang et al. (2011a) in the lower part of Table 8.2 and in Fig. 8.6.

Balestra et al. (2007) used a sample of 56 *Chandra*-clusters at $0.3 < z < 1.3$ with temperatures in the $3 - 15\,{\rm keV}$ range. Their emission-weighted metallicities and temperatures were determined within $0.15 - 0.3r_{\rm vir}$ with $r_{\rm vir}$ from Evrard et al. (1996) assuming a "mekal"-model. Balestra et al. (2007) found that the metallicity decreases towards higher redshifts with $\propto (1+z)^{-1.25}$ and that low-temperature clusters have higher metallicities than hot clusters at all redshifts. Our $T_{\rm X} - Z$

relation is not consistent with this study which may be due to that Balestra et al. (2007) used the emission weighted metallicities.

Zhang et al. (2011a) calibrated the $T_X - Z$ relation for 62 HIFLUGCS-clusters observed with *XMM-Newton*. They found that for their flux-limited HIFLUGCS-sample, low-mass clusters are included because their high metallicity increases the luminosity by line emission. Subsequently, this affects the scaling relations at the low-mass end with respect to the mass dependence of the slope. We found a similar trend although the massive cluster MS1008.1−1224 disturbs the relation because of its high metallicity. Our normalisation is 24% lower than, but consistent with Zhang et al. (2011a) who obtained $Y_0 = 10^{-0.323\pm0.061}$ using the bisector method (Akritas & Bershady 1996).

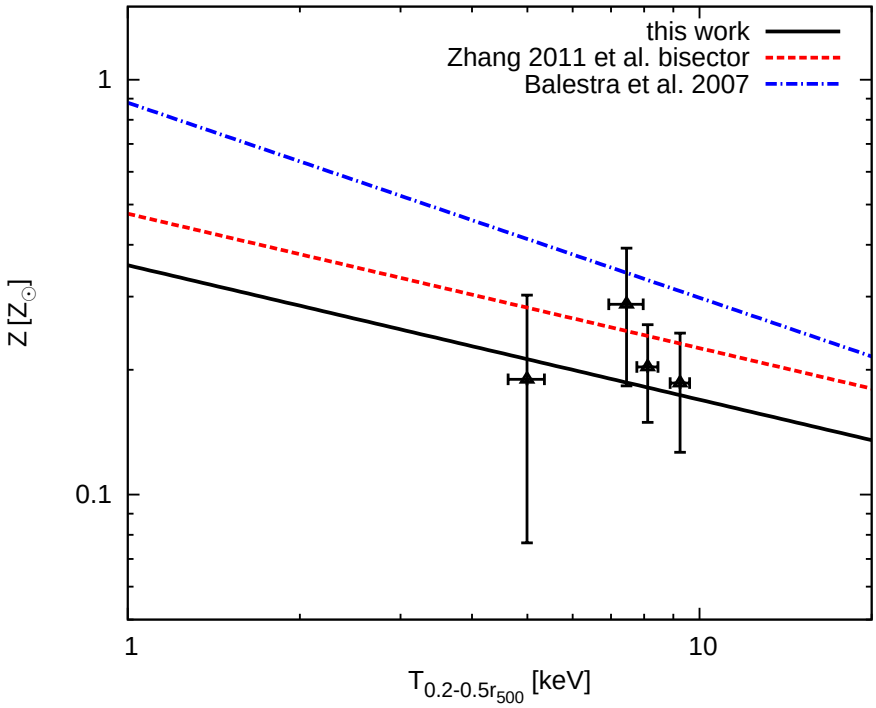

Figure 8.6: Global temperatures T_X versus metallicities Z in solar units for our sample and the samples of Balestra et al. (2007) and Zhang et al. (2011a).

8.6 Comparison with simulations

Hydrodynamic simulations have been used to investigate X-ray hydrostatic mass estimates and their results can be compared to observations to calibrate the cluster mass measurements.

Early simulations were performed by Evrard et al. (1996) who simulated the formation of galaxy clusters in different cosmologies, i.e. the Einstein-de Sitter model with $\sigma_8 = 0.59$, an open universe with $\sigma_8 = 1.0$, $\Omega_m = 0.2$ and $\Omega_\Lambda = 0$ and a flat, low-density universe with $\sigma_8 = 1.0$, $\Omega_m = 0.2$ and $\Omega_\Lambda = 0.8$. Evrard et al. (1996) found that hydrostatic masses assuming an isothermal β-model are very accurate when they are obtained for overdensities between $500\rho_{cr}$ and $2500\rho_{cr}$. Their $M_X - T_X$ relation with mass and temperature within r_{500} for the Einstein-de Sitter model reads in our notation: $M_X/M_\odot = 10^{13.85}(T_X/\mathrm{keV})^{1.5}$. Thereby, the temperature within r_{500} was obtained from fitting a power law to $T_X \propto M(< r_{500})/r_{500} \propto r_{500}^2$, i.e.

$r_{500}(T_{\rm X}) = (2.48 \pm 0.17)(T_{\rm X}/10\,{\rm keV})^{0.5}$ Mpc. The masses therein were obtained from the hydrostatic equation assuming a β-model for the electron number density and an isothermal temperature. Our normalisation is not consistent with their simulation which may be due to the different cosmologies.

Borgani et al. (2004) performed a large hydrodynamical simulation to simulate a cube of $192h^{-1}$ Mpc with 480^3 dark matter and gas particles having masses of $6.6{\times}10^9 M_\odot$ and $9.9{\times}10^8 M_\odot$, respectively. The underlying cosmology is a ΛCDM-cosmology with $\sigma_8 = 0.8$, $\Omega_{\rm m} = 0.3$, $\Omega_\Lambda = 0.7$ and $\Omega_{\rm b} = 0.04$. The simulation is initialised at a redshift of $z = 46$, whereby energy and entropy were conserved. Luminosities and emission weighted temperatures within $0.5 - 10\,{\rm keV}$ were calculated within the virial radius $r_{\rm vir}$. Borgani et al. (2004) obtained a mass-temperature relation which reads in our notation as $M_{\rm X}/M_\odot = 10^{13.40\pm0.01}(T_{\rm X}/{\rm keV})^{1.59\pm0.05}$. Thus, our normalisation is 20% higher than theirs for the same slope. Their luminosity-temperature relation reads in our notation as: $L_{\rm bol}({\rm erg^{-1}\,s}) = 10^{43.00\pm0.10}(T_{\rm X}/{\rm keV})^{2.5\pm0.1}$. We did not compare the $L_{\rm bol} - T_{\rm X}$ relation to ours because the slopes are too different.

Fabjan et al. (2011) performed high-resolution hydrodynamical simulations to study the scaling relations between mass, temperature, gas mass and the $Y_{\rm X}$-parameter, $Y_{\rm X} = M_{\rm gas}T_{\rm X}$. In their simulations, 140 clusters with $M > 5 \times 10^{13}h^{-1}M_\odot$ were generated with (1) non-radiative physics and (2) cooling, star formation, chemical enrichment and feedback from supernovae. A ΛCDM-model consistent with the results from *WMAP*-7 data was assumed with $\Omega_{\rm m} = \Omega_{\rm dm} + \Omega_{\rm b} = 0.24 + 0.04$, whereby $\Omega_{\rm dm}$ is dark matter density parameter, $h = 0.72$, $\sigma_8 = 0.8$ and $n_{\rm s} = 0.96$ for the primordial spectral index (Komatsu et al. 2011). The simulations did not account for observational effects that affect temperature measurements from X-ray spectra and X-ray surface brightness profiles. Fabjan et al. (2011) investigated the scaling relations for both non-radiative clusters and clusters with radiative cooling, star formation etc at redshifts of $z = 0$, 0.25, 0.50, 0.80, 1.0. For the clusters with non-radiative physics, the scaling relations are close to self-similarity, i.e. $\gamma = 1.5$. Including radiative cooling physics leads to higher ICM temperatures for less massive clusters and subsequently steeper temperature profiles. For the mass-temperature relation, Fabjan et al. (2011) obtained at $z = 0$: $M_{\rm X}/M_\odot = 10^{13.67\pm0.02}(T_{\rm X}/{\rm keV})^{1.64\pm0.02}$ and $M_{\rm X}/M_\odot = 10^{13.69\pm0.01}(T_{\rm X}/{\rm keV})^{1.5}$ assuming radiative physics for best fitting parameters and fixing the slope at the self-similar prediction $\gamma = 1.5$, respectively. Our normalisation is 29% lower than that of their relation with $\gamma = 1.5$ and not consistent. For non-radiative physics, Fabjan et al. (2011) obtained $M_{\rm X}/M_\odot = 10^{13.80\pm0.02}(T_{\rm X}/{\rm keV})^{1.53\pm0.02}$ for a fitted slope and $M_{\rm X}/M_\odot = 10^{13.81}(T_{\rm X}/{\rm keV})^{1.5}$ when the slope is fixed to $\gamma = 1.5$, respectively. Their temperature is the mass-weighted temperature determined within r_{500}, which may account for why our normalisations are not consistent with theirs. Fabjan et al. (2011) found that ICM physics affect the $M_{\rm X} - Y_{\rm X}$ relation less than the other scaling relations and that the slope and redshift evolution of $M_{\rm X} - Y_{\rm X}$ relation are close to the self-similar prediction $\gamma = 0.6$. The $M_{\rm X} - T_{\rm X}$ relation has the largest scatter among all the scaling relations in their simulation. This scatter increases with redshift from $5 - 6\%$ at low redshifts to $\sim 8\%$ at $z = 1$. This indicates a positive evolution of the $M_{\rm X} - T_{\rm X}$ relation toward higher redshift because the temperature is sensitive to ICM substructures which are more abundant at higher redshifts as mergers become more frequent.

Chapter 9

Summary & Discussion

In this thesis, a detailed mass-calibration study of a sample of five galaxy clusters at intermediate to high redshifts ($0.3 \lesssim z \lesssim 0.55$) was performed using weak gravitational lensing and X-rays.

For the weak lensing analysis, we used deep mosaics observed with ACS@HST which enabled us to precisely measure the shapes of the source galaxies and to determine their effective mean distance ratios $\langle D_{\rm ds}/D_{\rm s}\rangle$ with magnitude-redshift relations and redshift probability distributions (Schrabback et al. 2007, 2010). We used the $\hat{M}_{\rm ap}$–statistics (e.g. Schneider 1996; Schirmer et al. 2007) to quantify the weak lensing properties of our sample. We used the position where the weak lensing signal-to-noise ratio S/N reaches a maximum, $(\mathrm{S/N})_{\rm max}$, as alternative definition for and demonstrated that it is consistent with other definitions for the cluster centre such as the BCG position as well as X-ray centres (Lewis et al. 1999; Allen et al. 2008) and optical centres (Gioia & Luppino 1994; Smail et al. 1997) from previous studies. We found that $(\mathrm{S/N})_{\rm max}$ is correlated with the total cluster mass after accounting for cluster redshift and number density of the background galaxies. Amplitude and position of $(\mathrm{S/N})_{\rm max}$ were confirmed in simulations and we thus conclude that the S/N-peak can be associated with the cluster centre besides the BCG and the X-ray centre. Using weak lensing mass reconstructions (Seitz & Schneider 2001), we constructed the projected mass distribution κ which we compared to the S/N-contours. Both κ- and S/N-contours allowed to find evidence for e.g. relaxation state and projected 2d-morphology, but also for merger processes.

We calculated the tangential shear profiles using the S/N-peak, the BCG position and optical and X-ray centres. The influence of centering on other cluster centres is within the mass uncertainty. We fitted the mass profiles SIS, NFW, a truncated NFW-profile (NFW&PS) and a one-parameter NFW-model assuming a fixed concentration (*Mc*-model) to the tangential shear profiles. We found that the tangential shear profiles can be used to characterise the cluster properties such as relaxation state and projected 2d-morphology, but also merger processes. Comparing the NFW-profile to the truncated NFW-profile one can check whether the NFW-profile can be applied at $r > r_{200}$ and the *Mc*-model can probe the influence of the choice of the concentration. Since r_{200} is well inside the field-of-view for CL0413−6559 and MS0451.6−0305, we could compare NFW and NFW&PS for these clusters. For MS0451.6−0305, we found a larger difference between the two models because the field-of-view is larger than that of CL0413−6559. For both clusters, NFW&PS fitted better than the NFW-model. We found that the *Mc*-model produces reasonable results for clusters with regular morphology, such as MS2137.3−2353, while it completely fails for mergers (e.g. CL0015.9+1609 and MS1008.1−1224). Furthermore, we observed that merging clusters are poorly fitted by an SIS-model and that NFW and NFW&PS better fit the tangential shear profiles. Our weak lensing masses are consistent with mass estimates from previous studies using X-rays, the Sunyaev-Zeldovich effect, dynamical estimates, strong lensing or combinations of these approaches. Those mass estimates, however, are not uniformly obtained

for all clusters. For the clusters CL0015.9+1609 and MS1008.1−1224, r_{200} is well outside and for MS2137.3−2353 at the border of the field-of-view wherefore the errors on mass are large for these clusters. Thus, large field-coverages that ensure r_{200} within the field-of-view, are required to obtain accurate weak lensing masses.

As an example study for MS0451.6−0305, we used archival multi-colour data from the ground-based facilities MegaPrime@CFHT and Suprime-Cam@SUBARU to study the effect of individual source redshifts in a weak lensing analysis. The photometric redshifts were estimated with a scatter of $\sigma_z = 0.035$ and an outlier fraction of less than 2% which was determined by calibrating the photometric redshifts against 1561 spectroscopic redshifts from DEIMOS@Keck-II (Moran et al. 2007). We cross-checked the accuracy of the estimated photometric redshifts using simulations. Since the ground-based data are shallower than the HST-data, only 5% of photometric redshifts could be assigned to the background galaxies. We included these in our weak lensing analysis as individual source redshifts according to Seitz & Schneider (1997) and Bartelmann & Schneider (2001) and calibrated the other sources against them. The errors of the model parameters are only marginally smaller if photometric redshifts are included because the lower number density due to removing unlensed foreground galaxies compensate their effect. We confirmed this counteracting influence of including photometric redshifts and having a smaller number density in simulations. To improve weak lensing analyses with photometric redshifts, deep multi-colour observations that provide enough sheared sources to which the photometric redshifts can be assigned, are required.

The X-ray analysis was performed to obtain independent cluster masses which are uniformly inferred. We used high-quality *XMM-Newton* and *Chandra* data to calculate X-ray hydrostatic masses $M_{\rm X}$ for all clusters except for CL0413−6559, where only a short *ROSAT* PSPC observation was available. We quantified X-ray properties, such as X-ray centre, temperature $T_{\rm X}$ and luminosity $L_{\rm X}$, as well as the distributions of temperature and gas density following the methods of Zhang et al. (2005, 2006, 2007, 2008). The X-ray hydrostatic masses were used to calibrate the weak lensing masses. Our X-ray emission peak is more consistent with the S/N-peak and the X-rays centres of Lewis et al. (1999) and Allen et al. (2008) than the flux-weighted X-ray centroid because the latter defines the X-ray centre with respect to the total cluster emission instead of determining only the position where the X-ray emission attains a maximum. Thus, for merging clusters the X-ray centres determined with both methods differ strongly. We constructed temperature and surface brightness profiles and used them to calculate the X-ray hydrostatic masses within r_{500}. The global temperatures $T_{\rm X}$ and metallicities Z were determined within $0.2-0.5r_{500}$, and the global luminosities in the soft band ($L_{0.5-2.0\,\rm keV}$), the bolometric band ($L_{\rm bol}$) and the *ROSAT* band ($L_{0.1-2.4\,\rm keV}$) were determined within $0.2-1r_{500}$, whereby radii at $r < 0.2r_{500}$ were excluded to account for cool cores. We compared $M_{\rm X}$ and $T_{\rm X}$ to previous analyses. We found that our X-ray hydrostatic masses are not consistent with those studies because their masses were calculated using isothermal temperature which gives $\sim 20-25$% higher masses (Zhang et al. 2005). Our global temperatures are widely consistent with previous studies.

We constructed scaling relations using weak lensing and X-ray hydrostatic masses, $M_{\rm wl}$ and $M_{\rm X}$, as well as the X-ray observables $T_{\rm X}$, Z, $L_{0.5-2.0\,\rm keV}$, $L_{\rm bol}$ and $L_{0.1-2.4\,\rm keV}$. We found that our weak lensing masses are 18% higher than the X-ray hydrostatic masses which is consistent with e.g. Zhang et al. (2008) and Zhang et al. (2010) and expected for samples with non-relaxed clusters. To check whether the huge errors on $M_{\rm wl}$ of the merging clusters CL0015.9+1609 and MS1008.1−1224 influence the normalisation of our scaling relations, we used the masses from the *Mc*-model, M_{Mc}. We found that the error of the normalisation is ~ 2 times larger because the *Mc*-model poorly fits the disturbed clusters. Thus, investigating scaling relations involving M_{Mc} is not meaningful. We found that the normalisation for our $L_{\rm X}-M$ relations cannot be well determined, especially for small samples, because the luminosity is not a good mass proxy. Our scaling

relations were compared to previous studies and to simulations. We found that our normalisations are widely consistent with those as far as cosmology, method and slope are comparable to ours. We found no evidence for an evolution with redshift for our scaling relations. Either there is no evolution or the uncertainty of the normalisation is too high to detect it. In the latter case, a larger sample would be required and for scaling relations including weak lensing masses we would also need deep observations with larger field-of-views.

Appendix A

Weak lensing cluster masses

Table A.1: Cluster masses for CL0015.9+1609 using the S/N-peak as cluster centre as well as the BCG and the optical centre of Gioia & Luppino (1994), Opt (1), and the X-ray centre of Lewis et al. (1999), X-ray (1). The results for NFW and NFW&PS are identical because r_{200} is outside the field-of-view.

	S/N-Peak	Opt (1)	X-ray (1)	BCG
NFW:				
r_{200} [kpc]	1993^{+857}_{-656}	1941^{+859}_{-629}	2032^{+802}_{-670}	2234^{+834}_{-740}
c_{200}	$1.2^{+0.9}_{-1.1}$	$1.2^{+0.9}_{-1.1}$	$1.1^{+1.0}_{-1.0}$	$0.8^{+0.9}_{-0.7}$
M_{200} [$10^{14} M_\odot$]	$16.39^{+21.14}_{-16.18}$	$15.14^{+20.10}_{-14.72}$	$17.37^{+20.57}_{-17.18}$	$23.08^{+25.85}_{-22.94}$
$\chi^2_{\rm dof}$	0.929021	0.929399	0.930108	0.929052
NFW&PS:				
r_{200} [kpc]	1993^{+857}_{-656}	1941^{+859}_{-629}	2032^{+802}_{-670}	2234^{+834}_{-740}
c_{200}	$1.2^{+0.9}_{-1.1}$	$1.2^{+0.9}_{-1.1}$	$1.1^{+1.0}_{-1.0}$	$0.8^{+0.9}_{-0.7}$
M_{200} [$10^{14} M_\odot$]	$16.39^{+21.14}_{-16.18}$	$15.14^{+20.10}_{-14.72}$	$17.37^{+20.57}_{-17.18}$	$23.08^{+25.85}_{-22.94}$
$\chi^2_{\rm dof}$	0.929021	0.929399	0.930108	0.929052
Mc				
$c_{\rm NFW}$	$6.8^{+0.3}_{-0.2}$	$6.8^{+2.2}_{-2.1}$	$6.8^{+0.3}_{-0.2}$	$6.8^{+2.0}_{-2.0}$
r_{200} [kpc]	927^{+68}_{-73}	912^{+70}_{-77}	918^{+69}_{-74}	905^{+83}_{-99}
M_{200} [$10^{14} M_\odot$]	$1.65^{+0.36}_{-0.39}$	$1.57^{+0.36}_{-0.40}$	$1.60^{+0.26}_{-0.39}$	$1.53^{+0.36}_{-0.39}$
$\chi^2_{\rm dof}$	0.933824	0.934841	0.935240	0.935190
SIS:				
σ_v [km s^{-1}]	762^{+50}_{-55}	745^{+53}_{-60}	747^{+50}_{-57}	747^{+50}_{-57}
$M_{\rm SIS}$ [$10^{14} M_\odot$]	$5.38^{+0.71}_{-0.78}$	$5.01^{+0.71}_{-0.81}$	$5.27^{+0.71}_{-0.80}$	$5.66^{+0.80}_{-0.92}$
$\chi^2_{\rm dof}$	0.933857	0.935164	0.935632	0.932000

Table A.2: Cluster masses for CL0413−6559 using the S/N-peak as cluster centre as well as the BCG and the optical centre of Smail et al. (1997), Opt (2).

	S/N-Peak	Opt (2)	BCG
NFW			
r_{200} [kpc]	863^{+173}_{-230}	852^{+169}_{-254}	872^{+186}_{-257}
c_{200}	$2.4^{+1.8}_{-1.7}$	$2.0^{+2.0}_{-1.6}$	$1.9^{+2.1}_{-1.8}$
M_{200} [$10^{14} M_\odot$]	$1.29^{+0.77+0.38}_{-1.03-0.38}$	$1.24^{+0.74+0.36}_{-1.11-0.36}$	$1.33^{+0.85+0.39}_{-1.17-0.39}$
$\chi^2_{\rm dof}$	0.970599	0.975272	0.973202
NFW&PS			
r_{200} [kpc]	839^{+191}_{-186}	838^{+145}_{-208}	871^{+170}_{-196}
c_{200}	$2.5^{+1.6}_{-1.8}$	$2.1^{+1.9}_{-1.4}$	$1.9^{+1.6}_{-1.3}$
M_{200} [$10^{14} M_\odot$]	$1.18^{+0.81+0.35}_{-0.79-0.35}$	$1.18^{+0.61+0.35}_{-0.88-0.35}$	$1.32^{+0.77+0.39}_{-0.89-0.39}$
$\chi^2_{\rm dof}$	0.970492	0.975036	0.973029
Mc			
$c_{\rm NFW}$	$10.5^{+1.8}_{-0.8}$	$8.8^{+1.0}_{-0.6}$	$9.4^{+1.4}_{-0.7}$
r_{200} [kpc]	370^{+67}_{-112}	538^{+91}_{-112}	475^{+92}_{-123}
M_{200} [$10^{14} M_\odot$]	$0.10^{+0.06}_{-0.09}$	$0.31^{+0.16}_{-0.19}$	$0.21^{+0.12}_{-0.17}$
$\chi^2_{\rm dof}$	0.973134	0.976450	0.975117
SIS			
σ_v [km s^{-1}]	202^{+47}_{-83}	425^{+72}_{-90}	341^{+63}_{-87}
$M_{\rm SIS}$ [$10^{14} M_\odot$]	$0.16^{+0.08}_{-0.13}$	$0.72^{+0.24}_{-0.30}$	$0.47^{+0.17}_{-0.24}$
$\chi^2_{\rm dof}$	0.973304	0.976124	0.974863

Table A.3: Cluster masses for $MS0451_{ACS}$ (*upper table*) and $MS0451_{zphoto}$ (*lower table*) using the S/N-peak as cluster centre as well as the BCG and the optical centre of Gioia & Luppino (1994), Opt (1), and the X-ray centre of Lewis et al. (1999), X-ray (1). The second upper and lower errors on the masses are the large-scale structure errors calculated with Eq. (6.2.3). Note that $\chi^2_{\rm dof}$ does not vary significantly among the models because of the larger number of free parameters for this cluster.

	S/N-Peak	Opt (1)	X-ray (1)	BCG
NFW				
r_{200} [kpc]	2239^{+141}_{-156}	2260^{+115}_{-136}	2253^{+110}_{-138}	2240^{+128}_{-136}
c_{200}	$3.5^{+0.5+1.6}_{-0.5-1.6}$	$2.9^{+0.5+1.6}_{-0.4-1.6}$	$3.2^{+0.5+1.6}_{-0.4-1.6}$	$3.3^{+0.3+1.6}_{-0.5-1.6}$
M_{200} [$10^{14} M_\odot$]	$23.47^{+4.43+0.43}_{-4.91-0.43}$	$24.14^{+3.68+0.43}_{-4.36-0.43}$	$23.92^{+3.50+0.43}_{-4.39-0.43}$	$23.50^{+4.03+0.43}_{-4.28-0.43}$
$\chi^2_{\rm dof}$	0.948834	0.948496	0.949237	0.949525
NFW&PS				
r_{200} [kpc]	2432^{+152}_{-154}	2468^{+123}_{-139}	2443^{+118}_{-140}	2440^{+116}_{-133}
c_{200}	$2.9^{+0.4+1.6}_{-0.4-1.6}$	$2.4^{+0.4+1.6}_{-0.4-1.6}$	$2.7^{+0.4+1.6}_{-0.4-1.6}$	$2.7^{+0.4+1.6}_{-0.3-1.6}$
M_{200} [$10^{14} M_\odot$]	$30.08^{+5.64+0.43}_{-5.71-0.43}$	$31.44^{+4.70+0.43}_{-5.31-0.43}$	$30.49^{+4.42+0.43}_{-5.24-0.43}$	$30.38^{+4.33+0.43}_{-4.97-0.43}$
$\chi^2_{\rm dof}$	0.948593	0.948244	0.949000	0.949285
Mc				
$c_{\rm NFW}$	$4.6^{+0.1}_{-0.1}$	$4.7^{+0.1}_{-0.1}$	$4.7^{+0.1}_{-0.1}$	$4.7^{+0.1}_{-0.1}$
r_{200} [kpc]	2098^{+74}_{-78}	2014^{+75}_{-79}	2056^{+73}_{-77}	2051^{+71}_{-76}
M_{200} [$10^{14} M_\odot$]	$19.31^{+2.04+0.34}_{-2.15-0.34}$	$17.08^{+1.99+0.34}_{-2.01-0.34}$	$18.17^{+1.94+0.34}_{-2.04-0.34}$	$18.04^{+1.87+0.34}_{-2.01-0.34}$
$\chi^2_{\rm dof}$	0.948911	0.948755	0.929389	0.949681
SIS				
σ_v [km s^{-1}]	1220^{+37}_{-43}	1140^{+39}_{-46}	1171^{+38}_{-43}	1157^{+37}_{-43}
$M_{\rm SIS}$ [$10^{14} M_\odot$]	$15.47^{+0.94+0.34}_{-1.09-0.34}$	$13.65^{+0.93+0.34}_{-1.10-0.34}$	$14.36^{+0.93+0.34}_{-1.05-0.34}$	$13.94^{+0.89+0.34}_{-1.04-0.34}$
$\chi^2_{\rm dof}$	0.949701	0.949684	0.950362	0.950702

	S/N-Peak	Opt (1)	X-ray (1)	BCG
NFW				
r_{200} [kpc]	2362^{+132}_{-155}	2379^{+133}_{-156}	2359^{+127}_{-142}	2353^{+129}_{-130}
c_{200}	$3.4^{+0.4+1.6}_{-0.4-1.6}$	$3.0^{+0.4+1.6}_{-0.4-1.6}$	$3.2^{+0.4+1.6}_{-0.4-1.6}$	$3.2^{+0.3+1.6}_{-0.4-1.6}$
M_{200} [$10^{14} M_\odot$]	$27.56^{+4.62+0.43}_{-5.43-0.43}$	$28.16^{+4.72+0.43}_{-5.54-0.43}$	$27.45^{+4.43+0.43}_{-4.96-0.43}$	$27.24^{+4.48+0.43}_{-4.52-0.43}$
$\chi^2_{\rm dof}$	0.988139	0.988415	0.988953	0.988971
NFW&PS				
r_{200} [kpc]	2538^{+128}_{-151}	2584^{+115}_{-169}	2522^{+125}_{-113}	2540^{+104}_{-129}
c_{200}	$2.9^{+0.4+1.6}_{-0.3-1.6}$	$2.5^{+0.4+1.6}_{-0.3-1.6}$	$2.8^{+0.3+1.6}_{-0.4-1.6}$	$2.7^{+0.3+1.6}_{-0.3-1.6}$
M_{200} [$10^{14} M_\odot$]	$34.19^{+5.17+0.43}_{-6.10-0.43}$	$36.08^{+4.82+0.43}_{-7.08-0.43}$	$33.54^{+4.99+0.43}_{-4.51-0.43}$	$34.27^{+4.21+0.43}_{-5.22-0.43}$
$\chi^2_{\rm dof}$	0.987933	0.988210	0.989055	0.988780
Mc				
$c_{\rm NFW}$	$4.6^{+0.1}_{-0.1}$	$4.6^{+0.1}_{-0.1}$	$4.6^{+0.1}_{-0.1}$	$4.6^{+0.1}_{-0.1}$
r_{200} [kpc]	2177^{+66}_{-70}	2123^{+66}_{-72}	2132^{+64}_{-68}	2125^{+63}_{-68}
M_{200} [$10^{14} M_\odot$]	$21.57^{+1.96+0.34}_{-2.08-0.34}$	$20.01^{+1.87+0.34}_{-2.03-0.34}$	$20.27^{+1.22+0.34}_{-1.29-0.34}$	$20.07^{+1.78+0.34}_{-1.93-0.34}$
$\chi^2_{\rm dof}$	0.988263	0.988596	0.989055	0.989080
SIS				
σ_v [km s^{-1}]	1210^{+33}_{-37}	1159^{+33}_{-40}	1157^{+33}_{-38}	1144^{+32}_{-38}
$M_{\rm SIS}$ [$10^{14} M_\odot$]	$14.38^{+0.78+0.34}_{-0.88-0.34}$	$16.14^{+0.92+0.34}_{-1.11-0.34}$	$14.68^{+0.84+0.34}_{-0.94-0.34}$	$14.32^{+0.80+0.34}_{-0.95-0.34}$
$\chi^2_{\rm dof}$	0.989593	0.990016	0.990646	0.990742

Table A.4: Cluster masses for MS1008.1−1224 using the S/N-peak as cluster centre as well as the BCG and the optical centre of Gioia & Luppino (1994), Opt (1), and the X-ray centre of Lewis et al. (1999), X-ray (1). The results for NFW and NFW&PS are identical because r_{200} is outside the field-of-view.

	S/N-Peak	Opt (1)	X-ray (1)	BCG
NFW:				
r_{200} [kpc]	2415^{+546}_{-478}	2431^{+690}_{-481}	2406^{+757}_{-542}	2422^{+755}_{-514}
c_{200}	$2.2^{+0.8}_{-0.8}$	$2.1^{+0.7}_{-1.0}$	$1.9^{+0.7}_{-0.9}$	$1.9^{+0.7}_{-0.9}$
M_{200} [$10^{14} M_\odot$]	$22.48^{+15.25}_{-13.35}$	$22.93^{+19.52}_{-13.61}$	$22.23^{+20.98}_{-15.02}$	$22.68^{+21.21}_{-15.20}$
$\chi^2_{\rm dof}$	0.922594	0.924114	0.928339	0.927994
NFW&PS:				
r_{200} [kpc]	2415^{+546}_{-478}	2431^{+690}_{-481}	2406^{+757}_{-542}	2422^{+755}_{-514}
c_{200}	$2.2^{+0.8}_{-0.8}$	$2.1^{+0.7}_{-1.0}$	$1.9^{+0.7}_{-0.9}$	$1.9^{+0.7}_{-0.9}$
M_{200} [$10^{14} M_\odot$]	$22.48^{+15.25}_{-13.35}$	$22.93^{+19.52}_{-13.61}$	$22.23^{+20.98}_{-15.02}$	$22.68^{+21.21}_{-15.20}$
$\chi^2_{\rm dof}$	0.922594	0.924114	0.928339	0.927994
Mc				
$c_{\rm NFW}$	$6.8^{+0.2}_{-0.1}$	$6.8^{+0.2}_{-0.1}$	$7.0^{+0.2}_{-0.2}$	$7.0^{+0.2}_{-0.2}$
r_{200} [kpc]	1465^{+66}_{-71}	1451^{+68}_{-73}	1369^{+73}_{-77}	1548^{+74}_{-80}
M_{200} [$10^{14} M_\odot$]	$5.02^{+0.68}_{-0.73}$	$4.88^{+0.69}_{-0.74}$	$4.10^{+0.66}_{-0.69}$	$4.14^{+0.64}_{-0.70}$
$\chi^2_{\rm dof}$	0.931006	0.935466	0.935684	0.935684
SIS:				
σ_v [km s^{-1}]	850^{+35}_{-38}	846^{+37}_{-39}	798^{+39}_{-42}	798^{+39}_{-43}
$M_{\rm SIS}$ [$10^{14} M_\odot$]	$8.81^{+0.67}_{-0.73}$	$8.09^{+0.71}_{-0.75}$	$7.12^{+0.70}_{-0.75}$	$7.17^{+0.70}_{-0.77}$
$\chi^2_{\rm dof}$	0.935058	0.936179	0.939657	0.940300

Table A.5: Cluster masses for MS2137−2353 using the S/N-peak as cluster centre as well as the BCG and the optical centre of Gioia & Luppino (1994), Opt (1), and the X-ray centre of Allen et al. (2008), X-ray (2). The results for NFW and NFW&PS are almost identical because r_{200} is close to the border of the field-of-view.

	S/N-Peak	Opt (1)	X-ray (2)	BCG
NFW:				
r_{200} [kpc]	1194^{+117}_{-257}	1186^{+112}_{-264}	1185^{+107}_{-183}	1204^{+119}_{-252}
c_{200}	$9.5^{+9.9}_{-4.4}$	$9.8^{+10.9}_{-4.7}$	$9.8^{+7.5}_{-4.2}$	$8.7^{+7.7}_{-4.1}$
M_{200} [$10^{14} M_\odot$]	$2.75^{+0.81}_{-1.78}$	$2.70^{+0.76}_{-1.86}$	$2.69^{+0.73}_{-1.25}$	$2.82^{+0.85}_{-1.77}$
$\chi^2_{\rm dof}$	0.961206	0.949545	0.919767	0.948735
NFW&PS:				
r_{200} [kpc]	1199^{+116}_{-262}	1191^{+110}_{-258}	1194^{+102}_{-195}	1207^{+120}_{-233}
c_{200}	$9.3^{+9.8}_{-4.2}$	$9.6^{+10.9}_{-4.7}$	$9.5^{+7.7}_{-4.0}$	$8.6^{+7.7}_{-3.9}$
M_{200} [$10^{14} M_\odot$]	$2.79^{+0.81}_{-1.83}$	$2.73^{+0.76}_{-1.77}$	$2.75^{+0.70}_{-1.35}$	$2.84^{+0.85}_{-1.65}$
$\chi^2_{\rm dof}$	0.961214	0.949539	0.919767	0.948727
Mc				
$c_{\rm NFW}$	$7.5^{+0.2}_{-0.2}$	$7.6^{+0.2}_{-0.2}$	$7.6^{+0.2}_{-0.2}$	$7.6^{+0.2}_{-0.2}$
r_{200} [kpc]	1123^{+60}_{-63}	1251^{+64}_{-68}	1120^{+56}_{-58}	1113^{+62}_{-65}
M_{200} [$10^{14} M_\odot$]	$2.29^{+0.37}_{-0.39}$	$2.27^{+0.37}_{-0.40}$	$2.27^{+0.34}_{-0.35}$	$2.23^{+0.37}_{-0.39}$
$\chi^2_{\rm dof}$	0.960896	0.949250	0.921743	0.948404
SIS:				
σ_v [km s^{-1}]	820^{+38}_{-41}	818^{+40}_{-42}	818^{+37}_{-38}	812^{+40}_{-43}
$M_{\rm SIS}$ [$10^{14} M_\odot$]	$3.73^{+0.35}_{-0.37}$	$3.69^{+0.36}_{-0.38}$	$3.69^{+0.33}_{-0.34}$	$3.69^{+0.36}_{-0.39}$
$\chi^2_{\rm dof}$	0.960831	0.949248	0.921325	0.948480

Appendix B

X-ray spectra

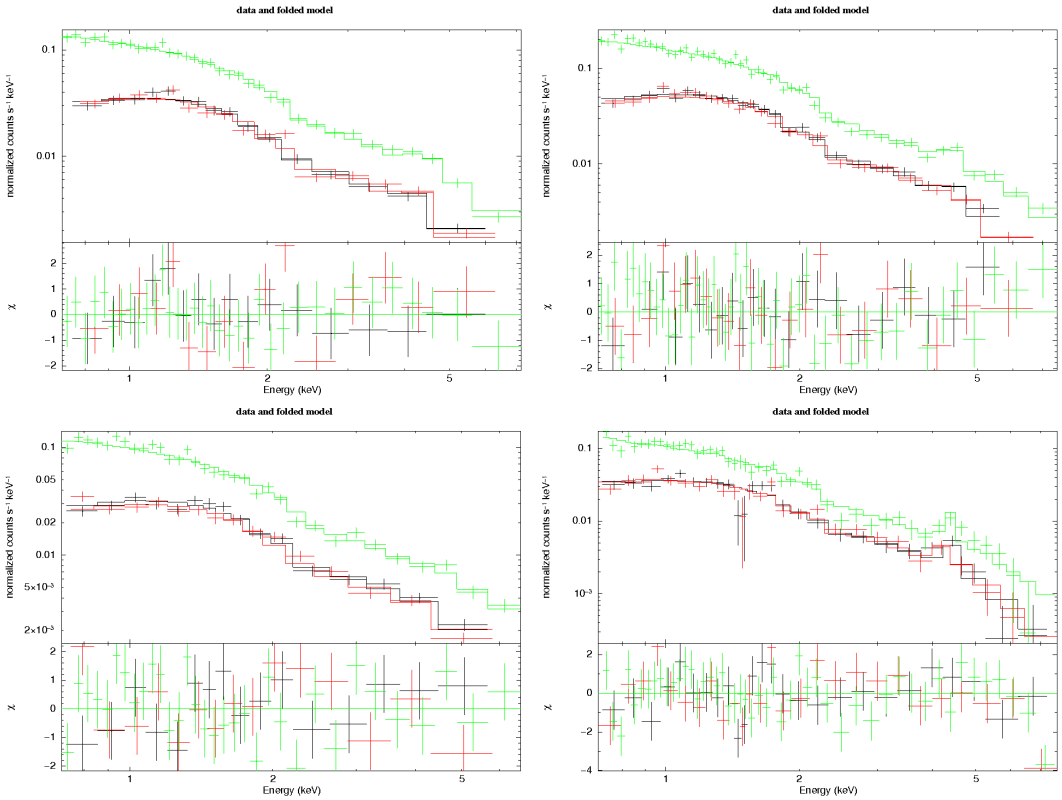

Figure B.1: Spectra of the bins of the temperature profile for CL0015.9+1609, i.e. bin 1 0 – 0.5′ (*upper left*), bin 2 0.5 – 1′ (*upper right*), bin 3 1 – 1.5′ (*lower left*) and bin 4 1.5 – 3.25′ (*lower right*).

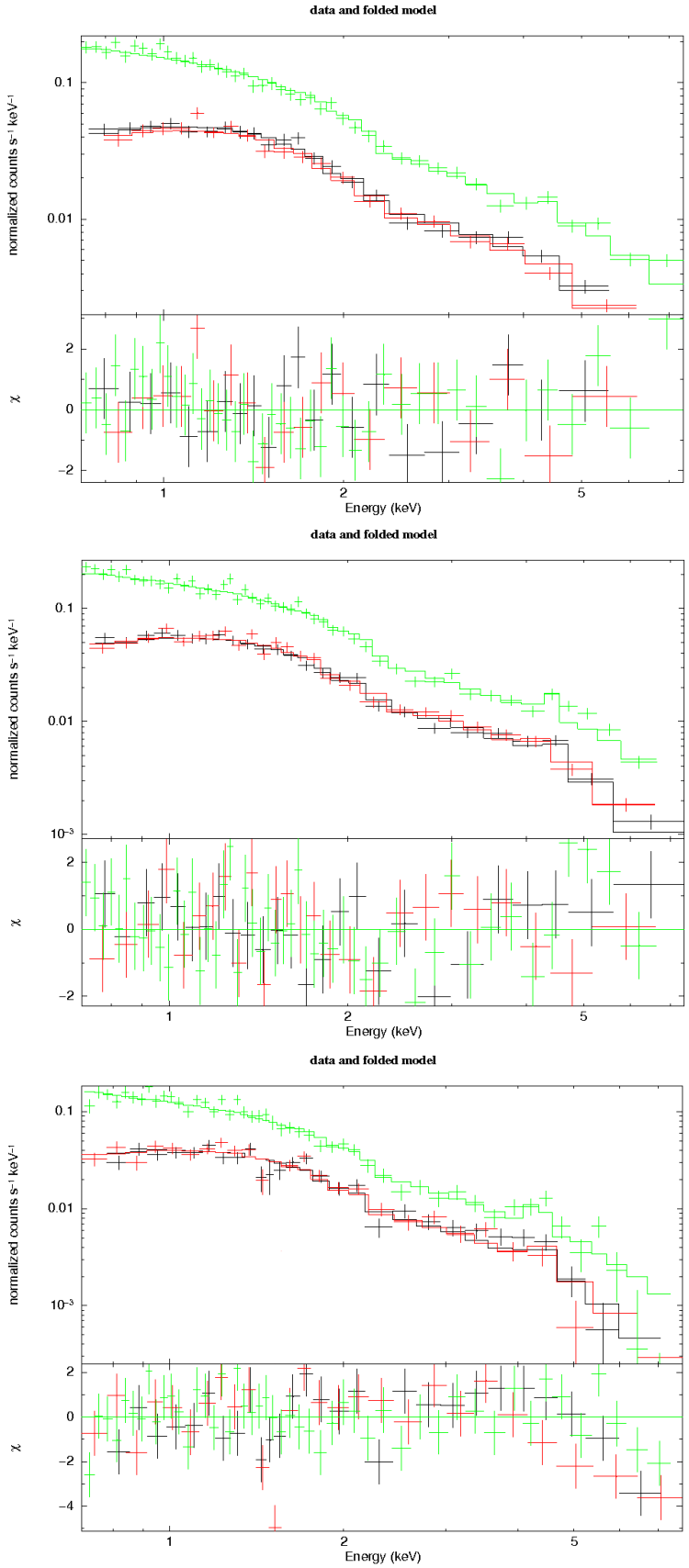

Figure B.2: Spectra of the bins of the temperature profile for MS0451.6−0305, i.e. bin 1 0 – 0.5′ (*upper*), bin 2 0.5 – 1′ (*middle*) and bin 3 1 – 2.4′ (*lower*).

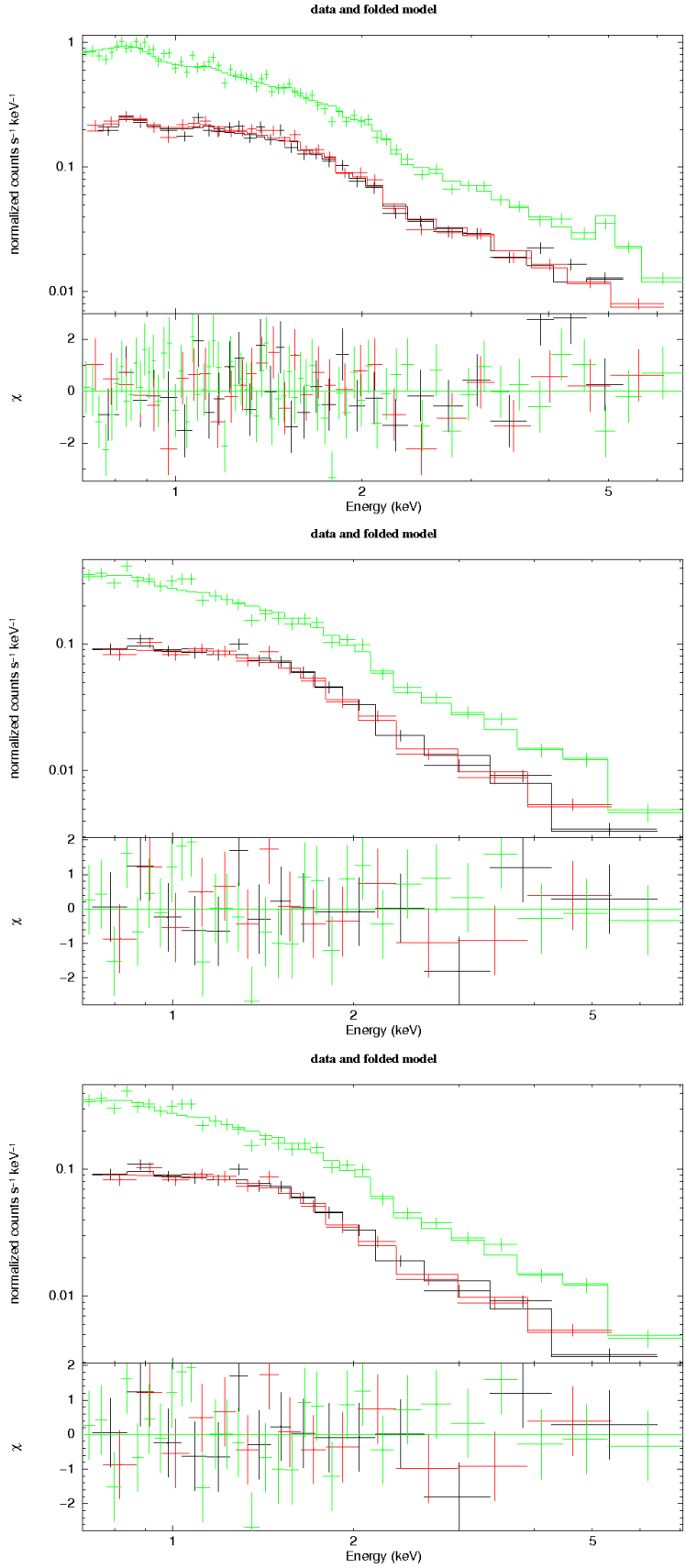

Figure B.3: Spectra of the bins of the temperature profile for MS2137.3−2353, i.e. bin 1 0 – 0.5′ (*upper*), bin 2 0.5 – 1′ (*middle*) and bin 3 1 – 2.1′ (*lower*).

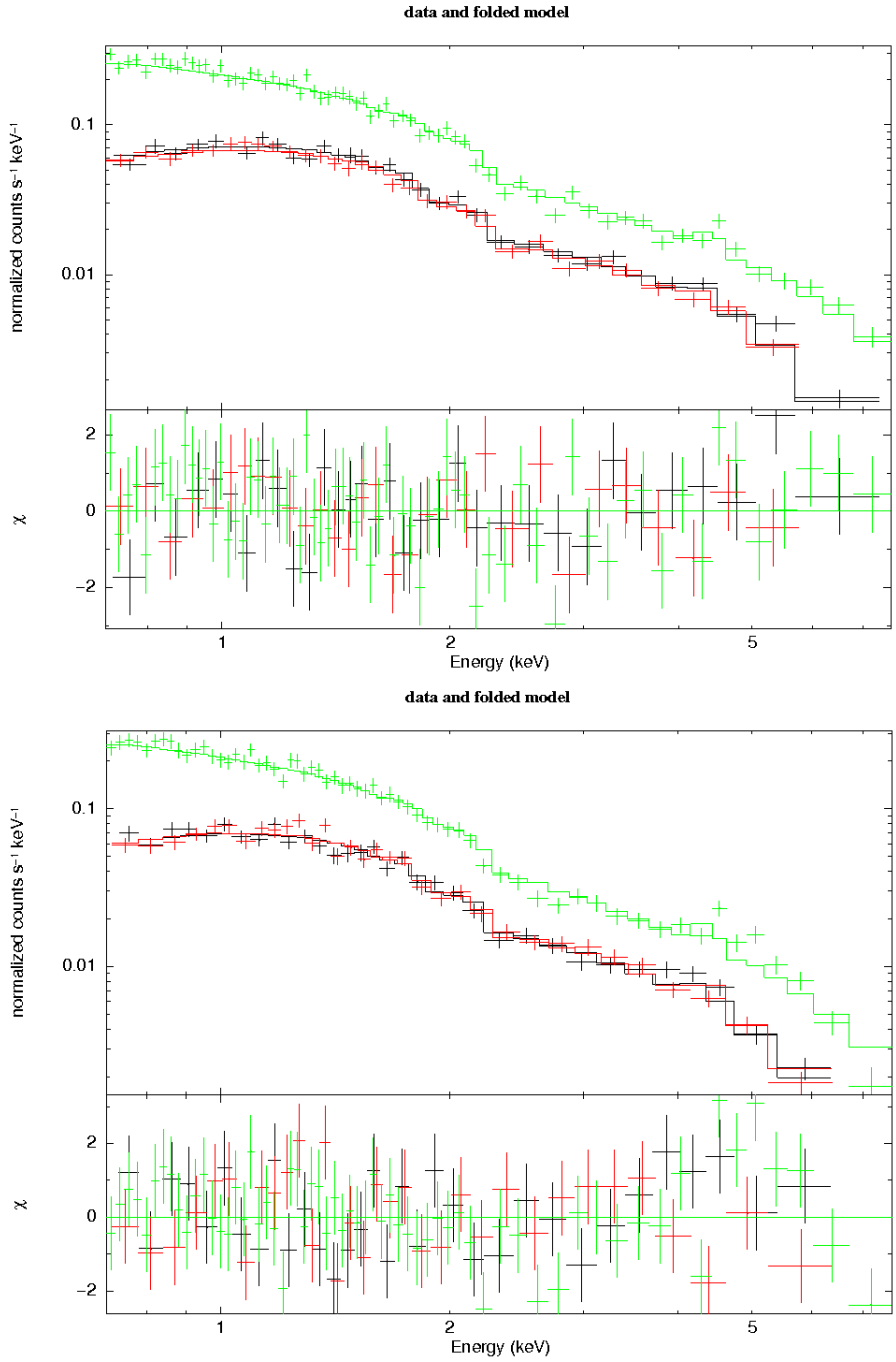

Figure B.4: Global spectra from which global temperatures and metallicities were determined for fixed $n_{\rm H}$ for CL0015.9+1609 (*upper*) and MS0451.6−0305 (*lower*) using an annulus of $0.2 - 0.5 r_{500,\rm X}$.

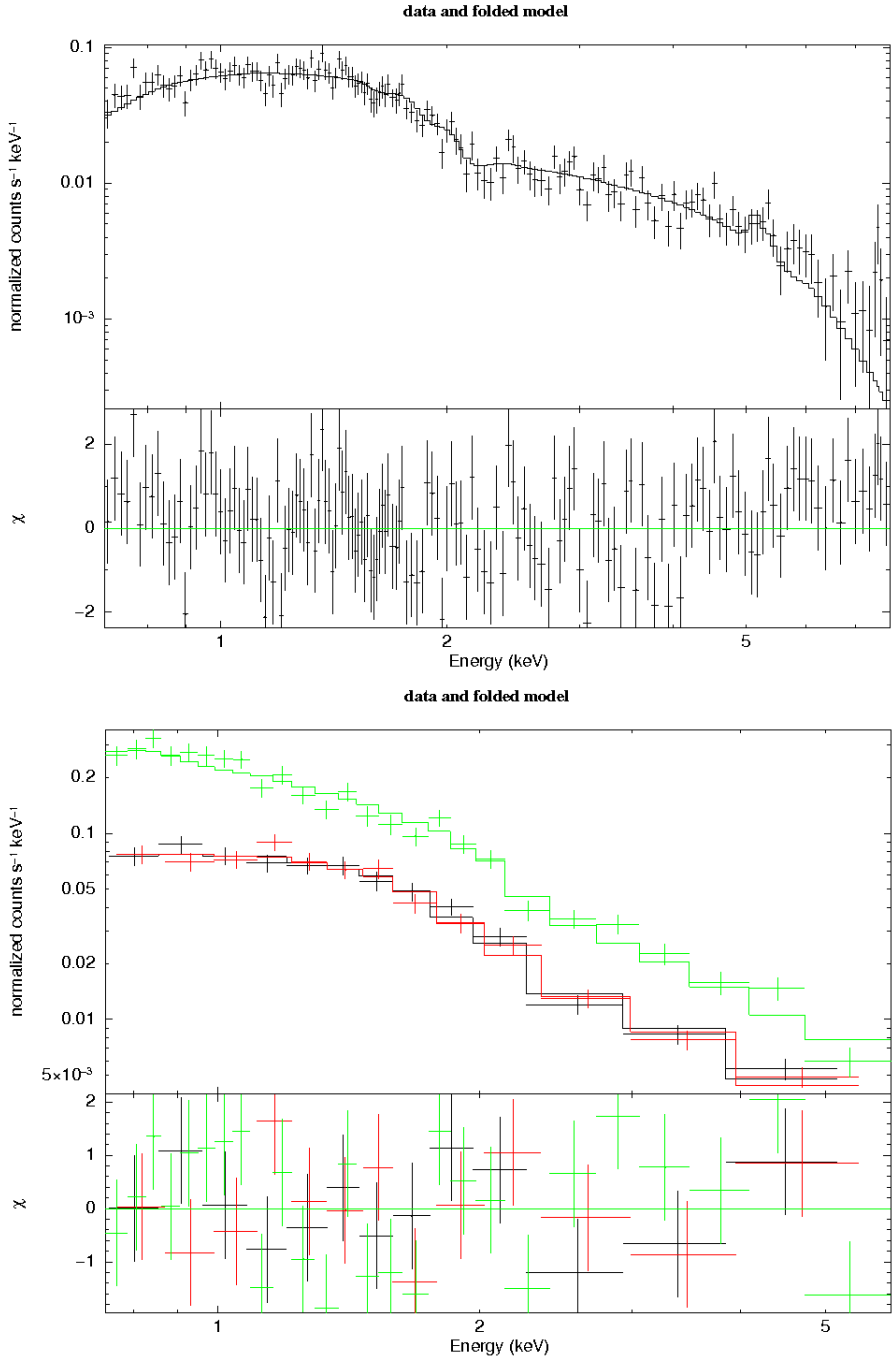

Figure B.5: Global spectra from which global temperatures and metallicities were determined for fixed $n_{\rm H}$ for MS1008.1−1224 (*upper*) and MS2137.3−2353 (*lower*) using an annulus of $0.2 - 0.5r_{500,\rm X}$.

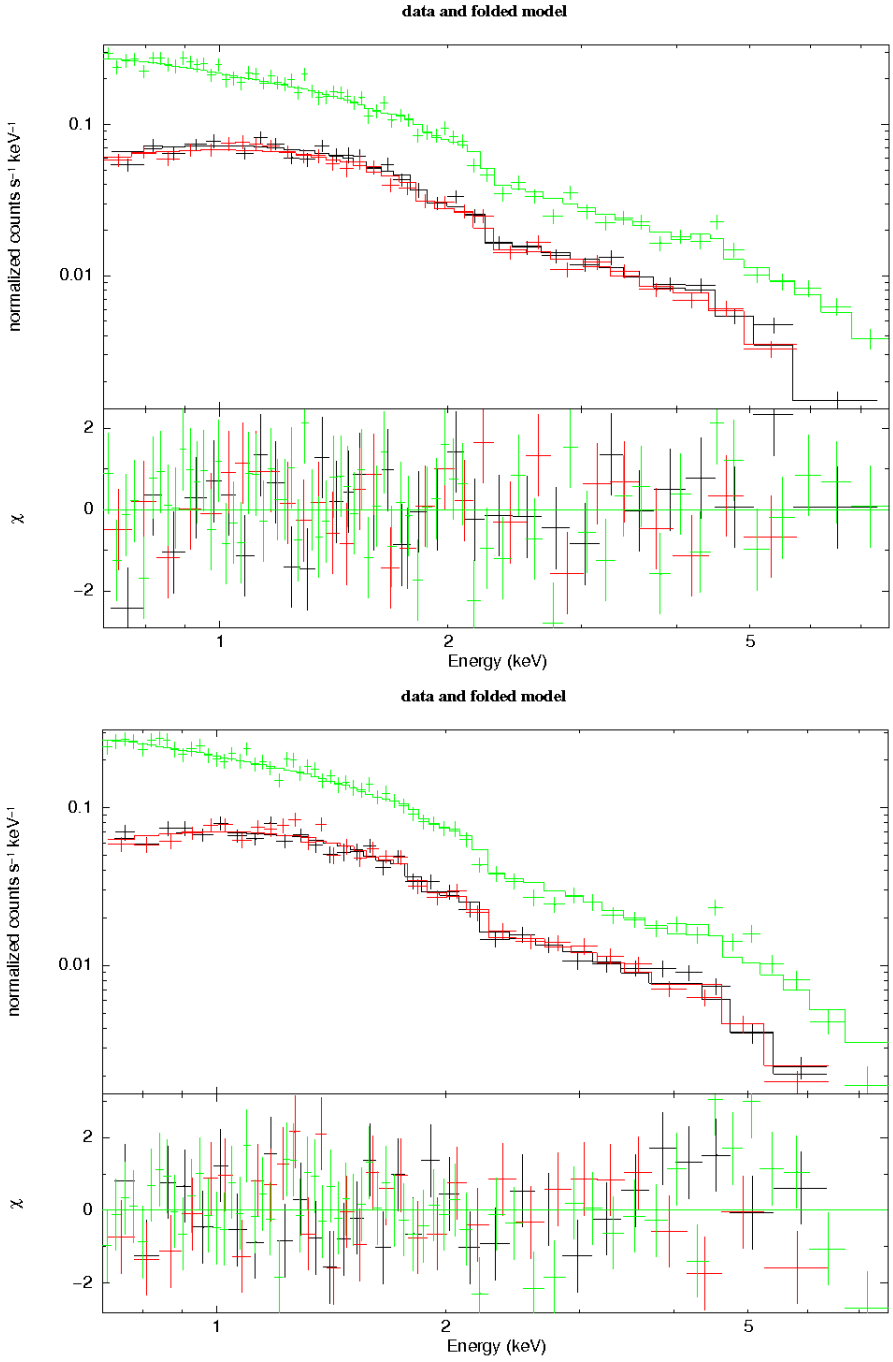

Figure B.6: Global spectra from which global temperatures and metallicities were determined by fitting n_{H} for CL0015.9+1609 (*upper*) and MS0451.6−0305 (*lower*) using an annulus of $0.2 - 0.5 r_{500,\mathrm{X}}$.

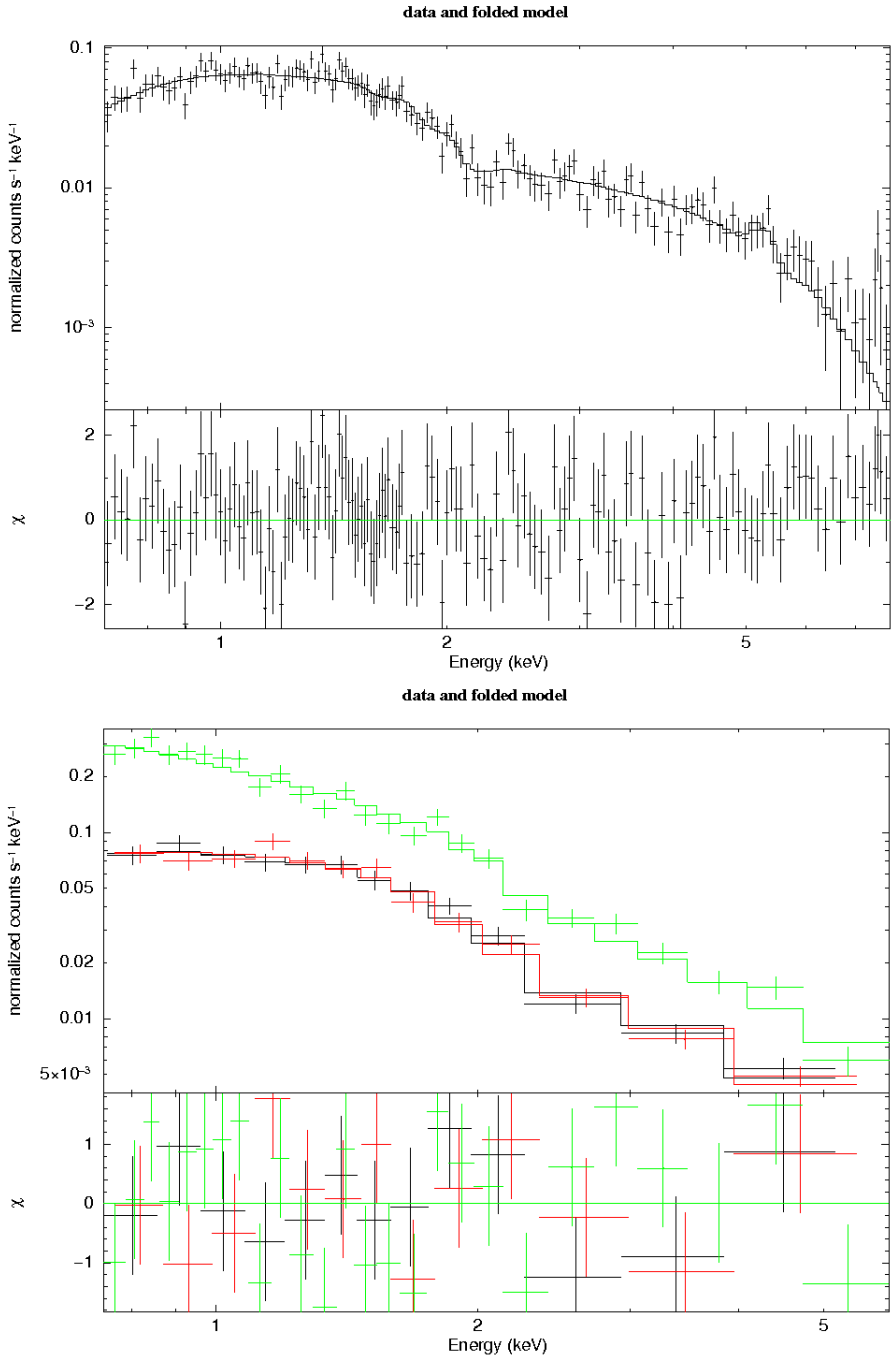

Figure B.7: Global spectra from which global temperatures and metallicities were determined by fitting $n_{\rm H}$ for MS1008.1−1224 (*upper*) and MS2137.3−2353 (*lower*) using an annulus of $0.2 - 0.5r_{500,\rm X}$.

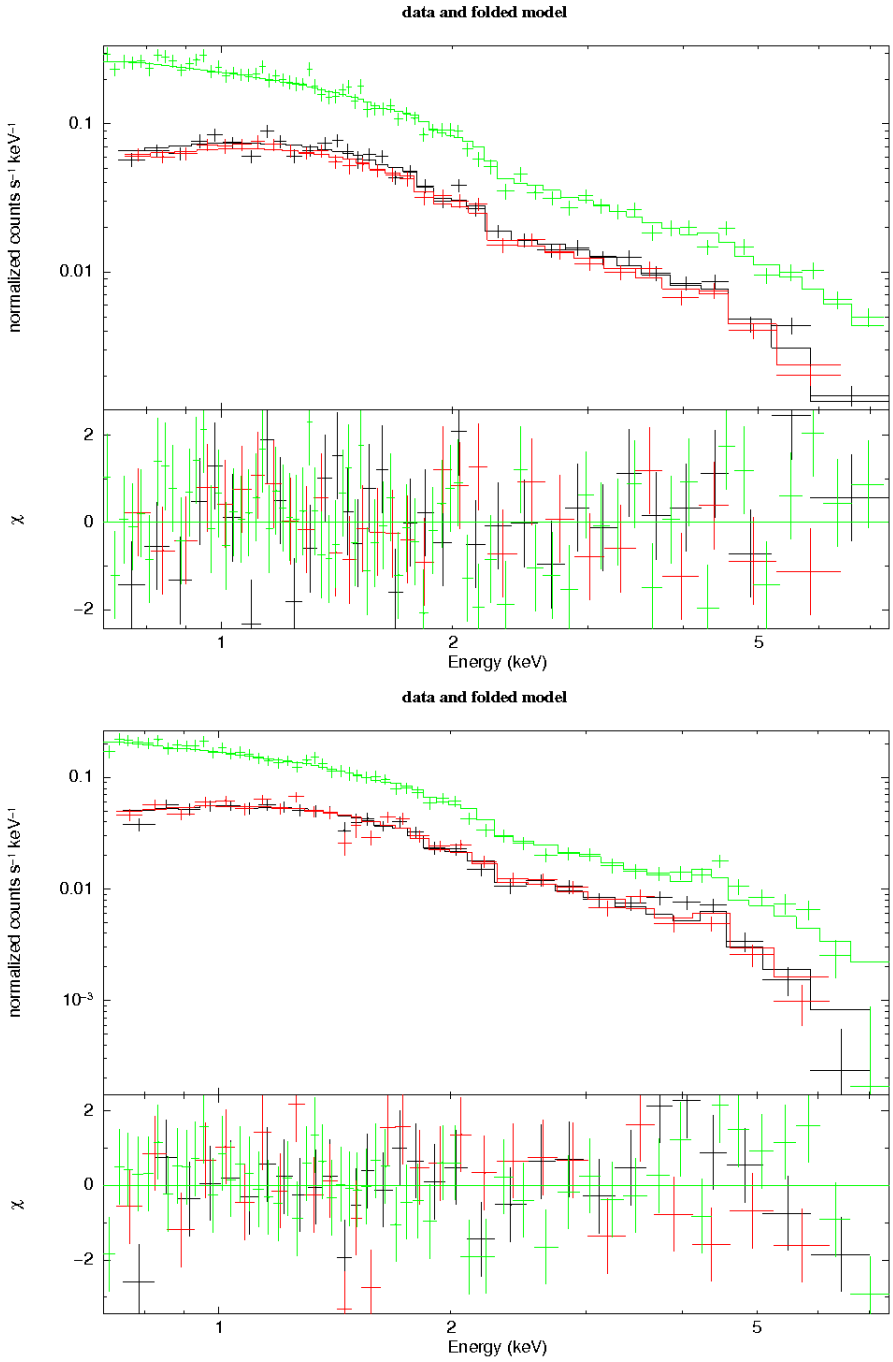

Figure B.8: Global spectra from which global temperatures and metallicities were determined for fixed n_{H} for CL0015.9+1609 (*upper*) and MS0451.6−0305 (*lower*) using an annulus of $0.2 - 0.5 r_{500,\mathrm{wl}}$.

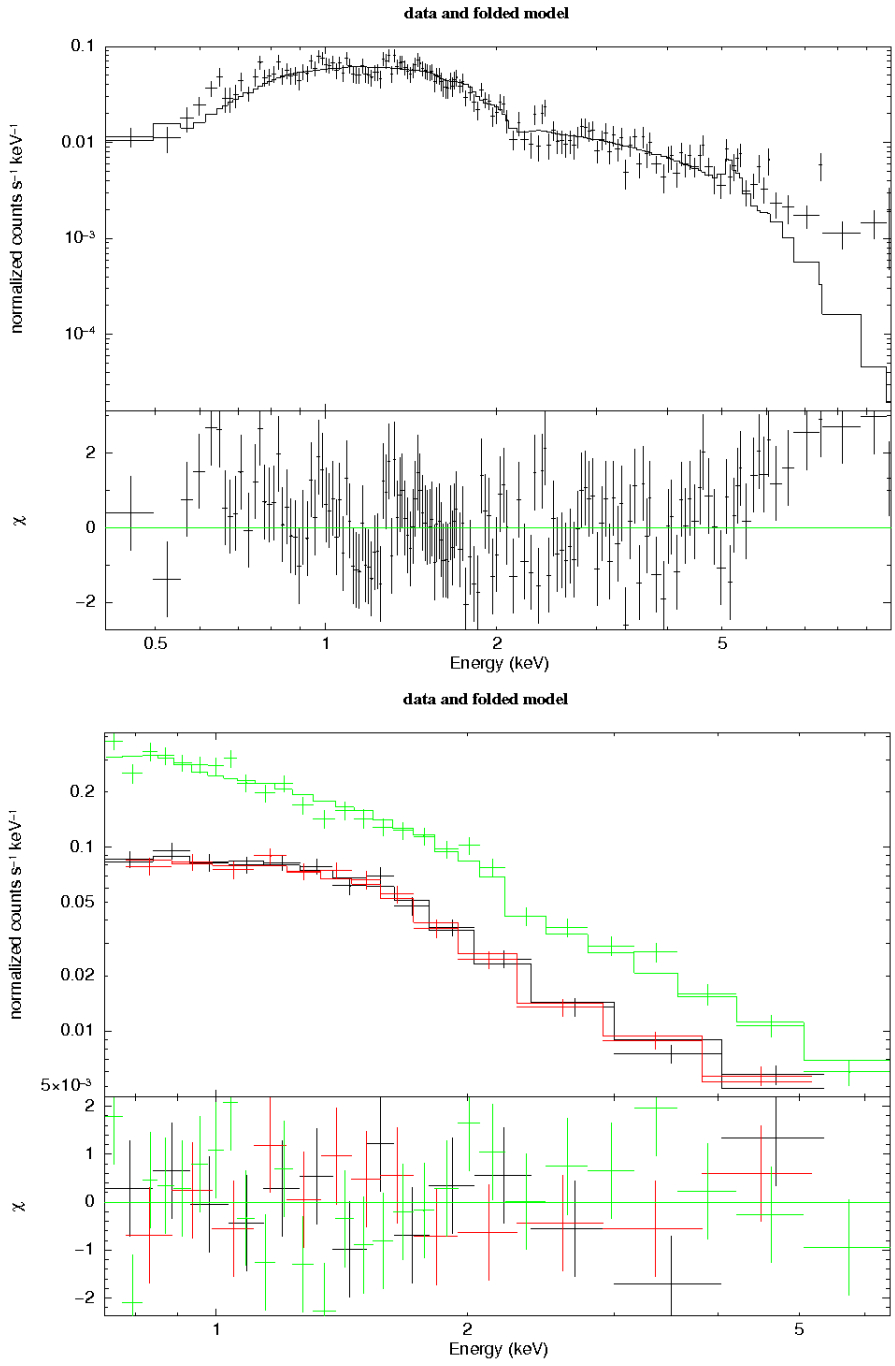

Figure B.9: Global spectra from which global temperatures and metallicities were determined for fixed $n_{\rm H}$ for MS1008.1−1224 (*upper*) and MS2137.3−2353 (*lower*) using an annulus of $0.2 - 0.5r_{500,\rm wl}$.

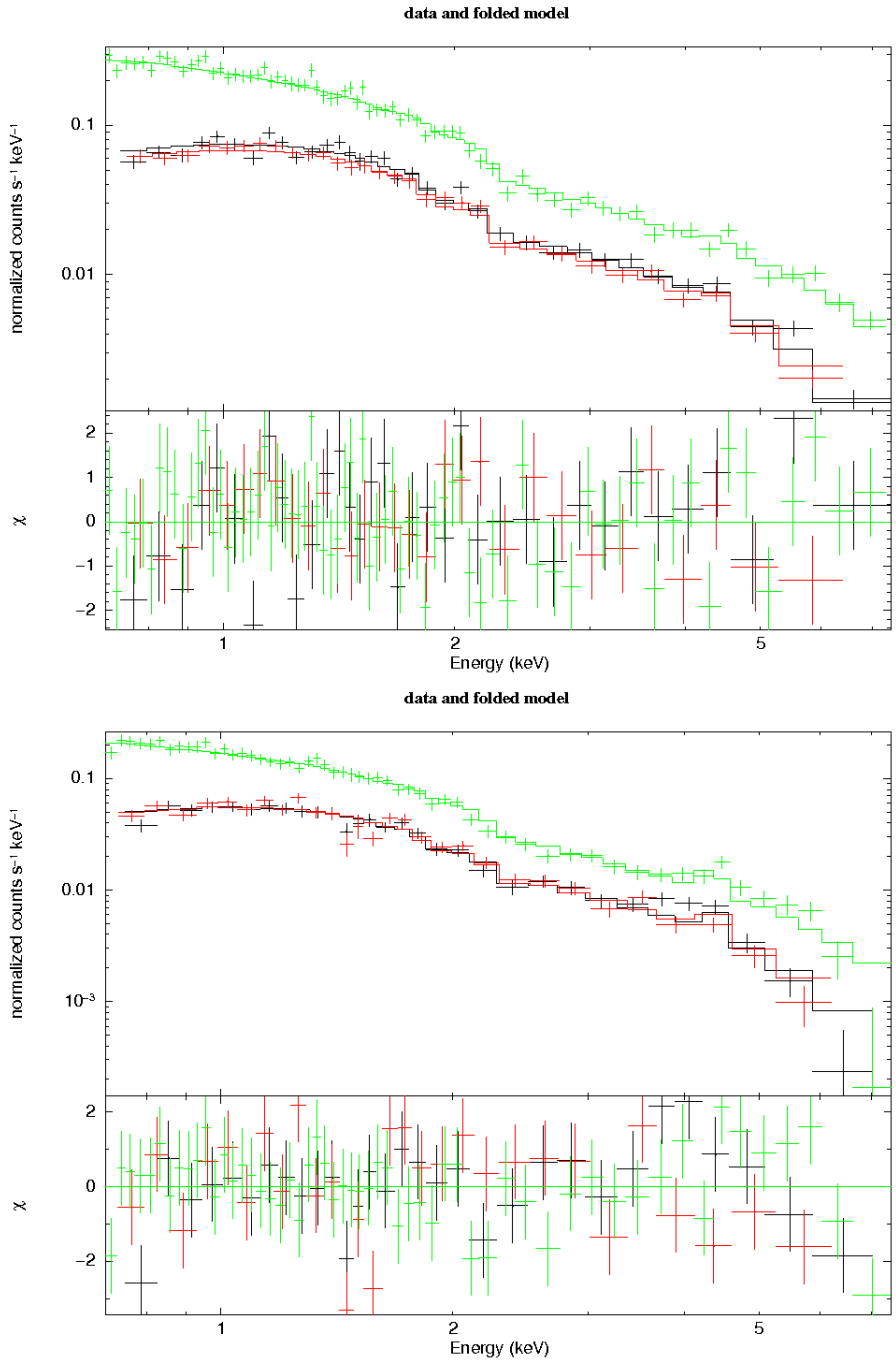

Figure B.10: Global spectra from which global temperatures and metallicities were determined by fitting n_{H} for CL0015.9+1609 (*upper*) and MS0451.6−0305 (*lower*) using an annulus of $0.2 - 0.5 r_{500,\mathrm{wl}}$.

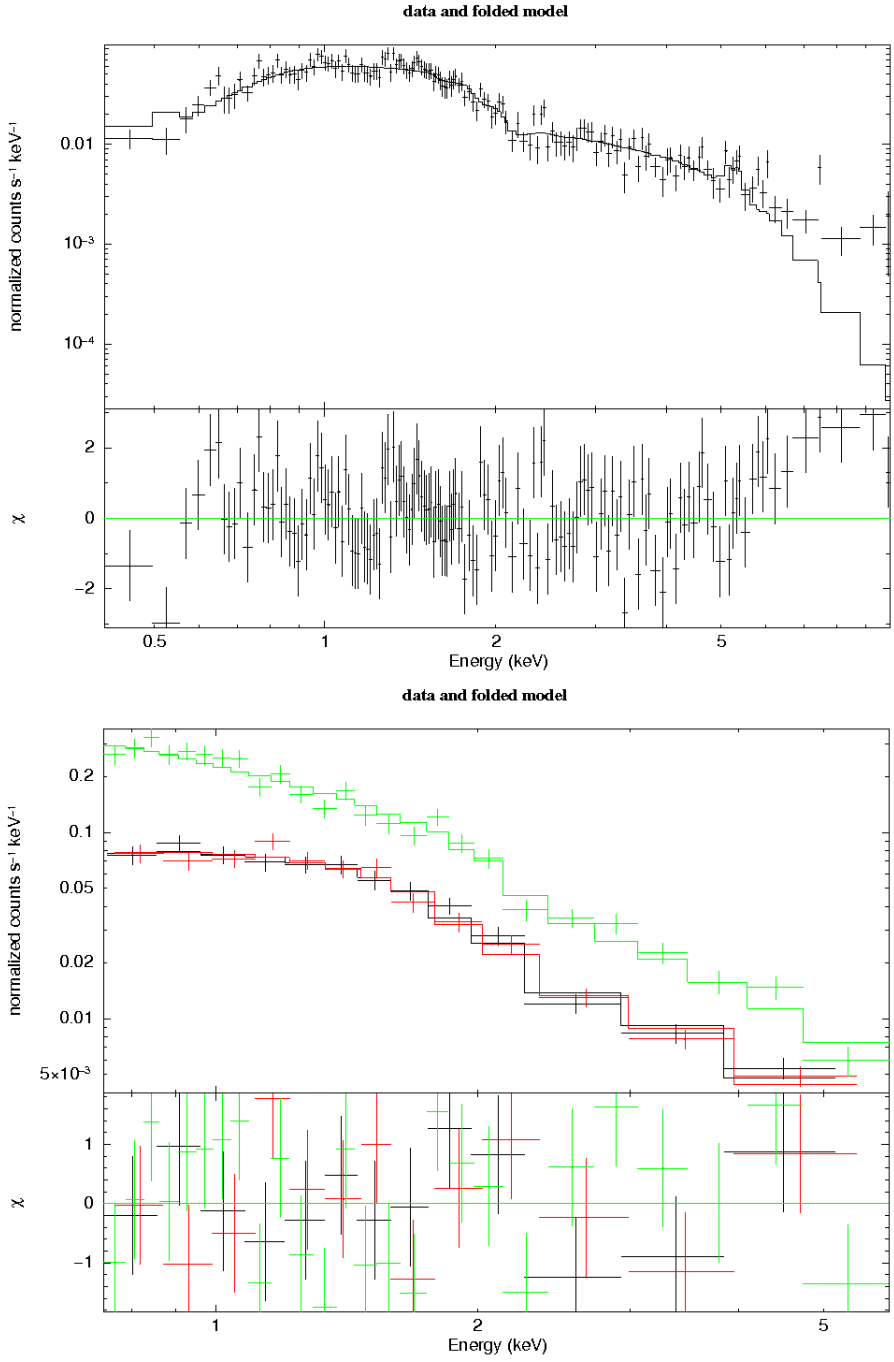

Figure B.11: Global spectra from which global temperatures and metallicities were determined by fitting $n_{\rm H}$ for MS1008.1−1224 (*upper*) and MS2137.3−2353 (*lower*) using an annulus of $0.2 - 0.5r_{500,\rm wl}$.

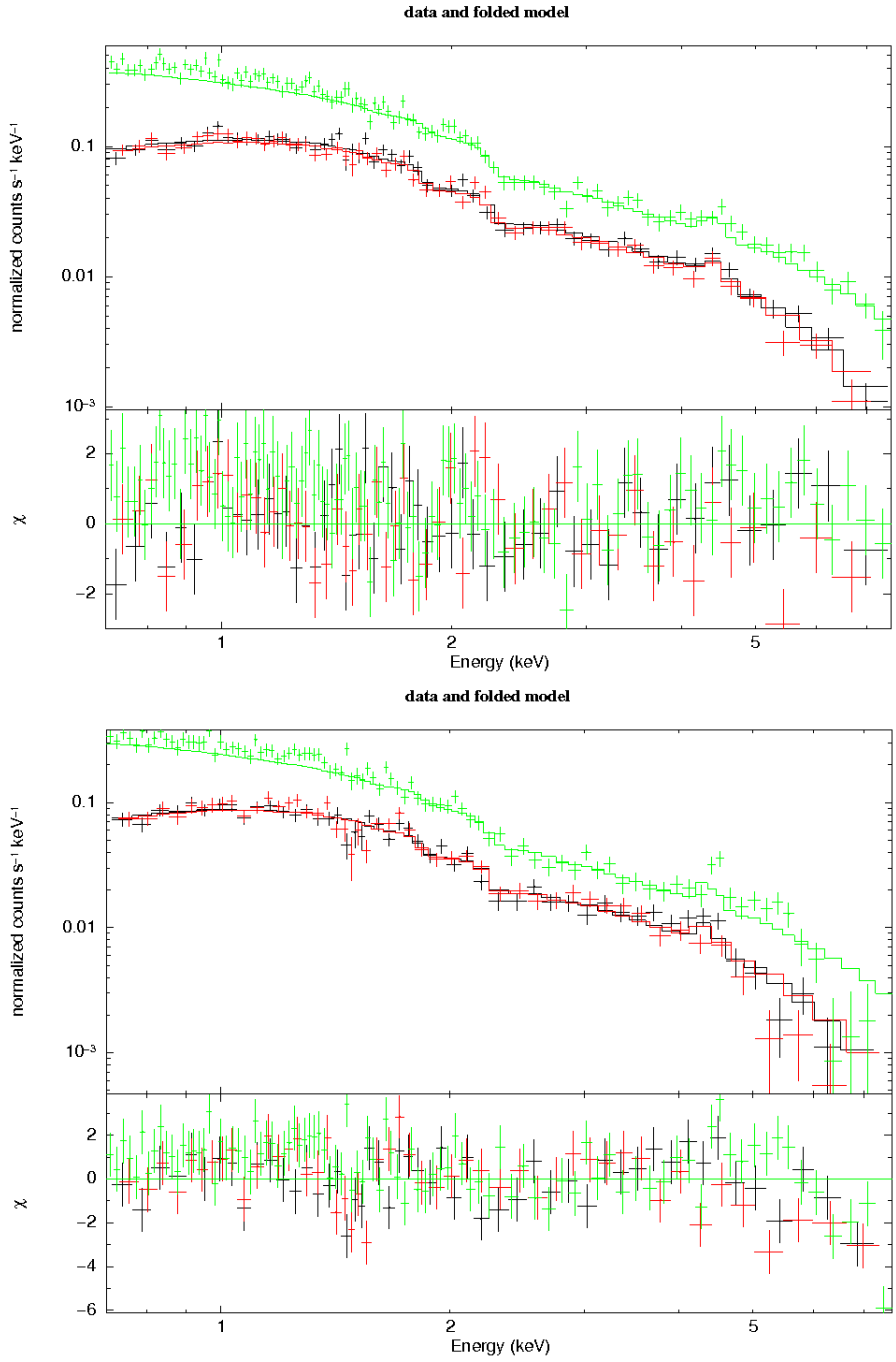

Figure B.12: Global spectra from which global luminosities were determined for CL0015.9+1609 (*upper*) and MS0451.6−0305 (*lower*) using an annulus of $0.2 - 1r_{500,\mathrm{X}}$ and the global temperatures and metallicities for fixed n_{H}.

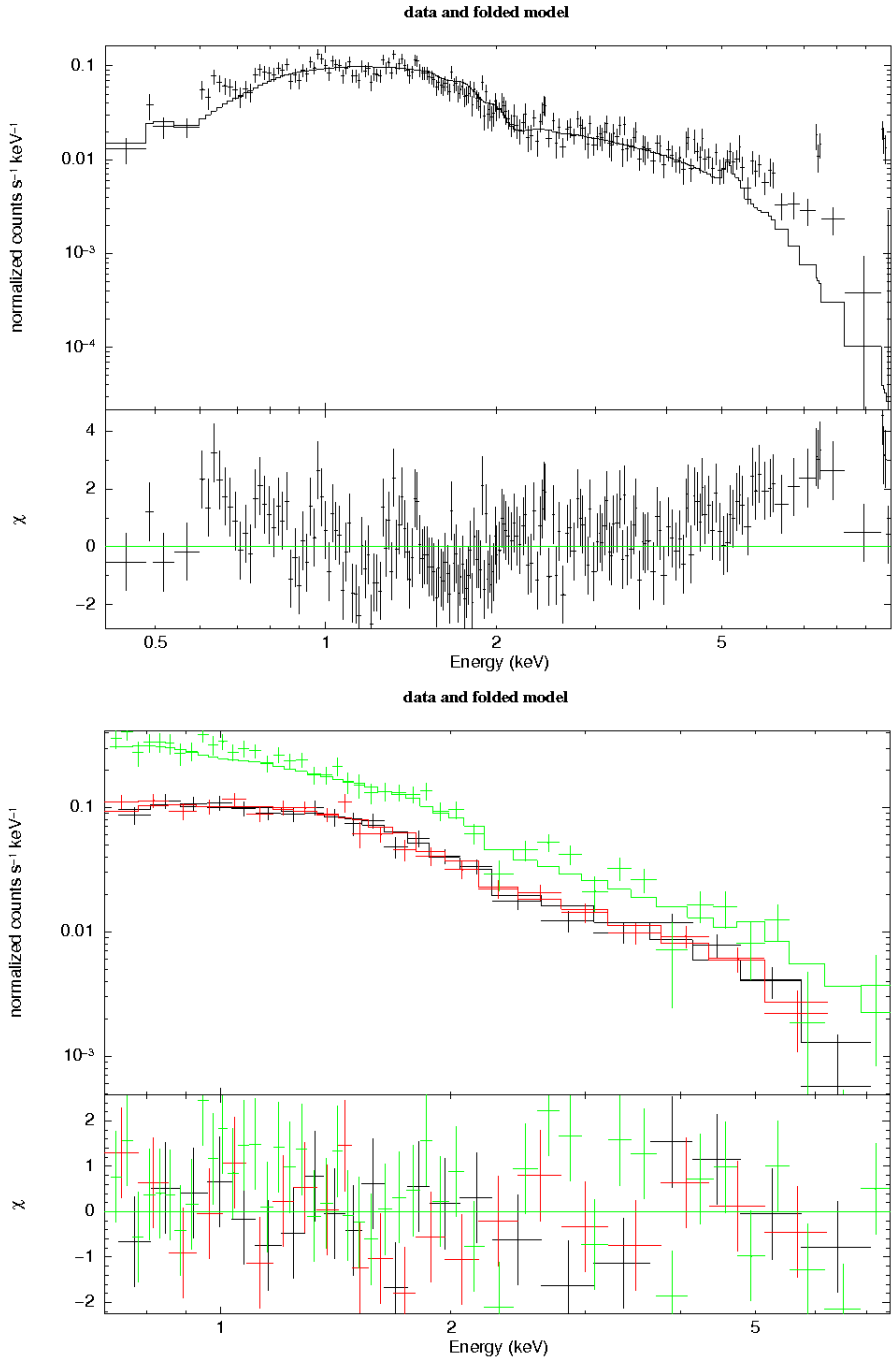

Figure B.13: Global spectra from which global luminosities were determined for MS1008.1−1224 (*upper*) and MS2137.3−2353 (*lower*) using an annulus of $0.2 - 1r_{500,\mathrm{X}}$ and the global temperatures and metallicities for fixed n_{H}.

Bibliography

Abell, G. O., Corwin, Jr. H. G., & Olowin, R. P. 1989, ApJS, 70, 1

Akritas, M. G. & Bershady, M. A. 1996, ApJ, 470, 706

Allen, S. W., Rapetti, D. A., Schmidt, R. W., et al. 2008, MNRAS, 383, 879

Allen, S. W., Schmidt, R. W., & Fabian, A. C. 2001, MNRAS, 328, L37

Allen, S. W., Schmidt, R. W., Fabian, A. C., & Ebeling, H. 2003, MNRAS, 342, 287

Alpher, R. A., Bethe, H., & Gamow, G. 1948, Physical Review, 73, 803

Anders, E. & Grevesse, N. 1989, Geochim. Cosmochim. Acta, 53, 197

Arnaud, M. & Evrard, A. E. 1999, MNRAS, 305, 631

Arnaud, M., Pointecouteau, E., & Pratt, G. W. 2005, A&A, 441, 893

Arnaud, M., Pointecouteau, E., & Pratt, G. W. 2007, A&A, 474, L37

Athreya, R. M., Mellier, Y., van Waerbeke, L., et al. 2002, A&A, 384, 743

Bahcall, N. A. & Fan, X. 1998, ApJ, 504, 1

Bahcall, N. A., McKay, T. A., Annis, J., et al. 2003, ApJS, 148, 243

Balestra, I., Tozzi, P., Ettori, S., et al. 2007, A&A, 462, 429

Balogh, M. L., Babul, A., Voit, G. M., et al. 2006, MNRAS, 366, 624

Bardeau, S., Kneib, J.-P., Czoske, O., et al. 2005, A&A, 434, 433

Bardeau, S., Soucail, G., Kneib, J.-P., et al. 2007, A&A, 470, 449

Bartelmann, M. & Schneider, P. 2001, Phys. Rep., 340, 291

Bekenstein, J. D. 2004, Phys. Rev. D, 70, 083509

Benítez, N. 2000, ApJ, 536, 571

Bennett, C. L., Halpern, M., Hinshaw, G., et al. 2003, ApJS, 148, 1

Bertin, E. & Arnouts, S. 1996, A&AS, 117, 393

Bertschinger, E. 1998, ARA&A, 36, 599

Binney, J. & Tremaine, S. 2008, Galactic Dynamics: Second Edition, ed. Binney, J. & Tremaine, S. (Princeton University Press)

Birkinshaw, M. 1999, Phys. Rep., 310, 97

Boggess, N. W., Mather, J. C., Weiss, R., et al. 1992, ApJ, 397, 420

Boggs, P. T., Byrd, R. H., & Schnabel, R. B. 1987, A stable and efficient algorithm for nonlinear orthogonal distance regression, Vol. 8 (SIAM J. Sci. Stat. Comput.), 1052–1078

Böhringer, H., Nulsen, P. E. J., Braun, R., & Fabian, A. C. 1995, MNRAS, 274, L67

Böhringer, H., Schuecker, P., Guzzo, L., et al. 2004, A&A, 425, 367

Böhringer, H., Voges, W., Fabian, A. C., Edge, A. C., & Neumann, D. M. 1993, MNRAS, 264, L25

Böhringer, H., Voges, W., Huchra, J. P., et al. 2000, ApJS, 129, 435

Bonamente, M., Joy, M., LaRoque, S. J., et al. 2008, ApJ, 675, 106

Borgani, S. & Guzzo, L. 2001, Nature, 409, 39

Borgani, S., Murante, G., Springel, V., et al. 2004, MNRAS, 348, 1078

Borgani, S., Rosati, P., Tozzi, P., & Norman, C. 1999, ApJ, 517, 40

Bower, R. G., Lucey, J. R., & Ellis, R. S. 1992, MNRAS, 254, 601

Bradač, M., Allen, S. W., Treu, T., et al. 2008a, ApJ, 687, 959

Bradač, M., Schrabback, T., Erben, T., et al. 2008b, ApJ, 681, 187

Brainerd, T. G., Blandford, R. D., & Smail, I. 1996, ApJ, 466, 623

Brodwin, M., Ruel, J., Ade, P. A. R., et al. 2010, ApJ, 721, 90

Bryan, G. L. & Norman, M. L. 1998, ApJ, 495, 80

Bullock, J. S., Kolatt, T. S., Sigad, Y., et al. 2001, MNRAS, 321, 559

Burenin, R. A., Vikhlinin, A., Hornstrup, A., et al. 2007, ApJS, 172, 561

Burke, D. J., Collins, C. A., Sharples, R. M., Romer, A. K., & Nichol, R. C. 2003, MNRAS, 341, 1093

Burkey, J. M., Keel, W. C., Windhorst, R. A., & Franklin, B. E. 1994, ApJ, 429, L13

Burns, J. O., Hallman, E. J., Gantner, B., Motl, P. M., & Norman, M. L. 2008, ApJ, 675, 1125

Carlstrom, J. E., Holder, G. P., & Reese, E. D. 2002, ARA&A, 40, 643

Cavaliere, A. & Fusco-Femiano, R. 1976, A&A, 49, 137

Chen, Y., Reiprich, T. H., Böhringer, H., Ikebe, Y., & Zhang, Y.-Y. 2007, A&A, 466, 805

Clowe, D., Bradač, M., Gonzalez, A. H., et al. 2006a, ApJ, 648, L109

Clowe, D., Luppino, G. A., Kaiser, N., & Gioia, I. M. 2000, ApJ, 539, 540

Clowe, D., Randall, S. W., & Markevitch, M. 2007, Nuclear Physics B Proceedings Supplements, 173, 28

Clowe, D., Schneider, P., Aragón-Salamanca, A., et al. 2006b, A&A, 451, 395

Comerford, J. M. & Natarajan, P. 2007, MNRAS, 379, 190

Dahle, H., Pedersen, K., Lilje, P. B., Maddox, S. J., & Kaiser, N. 2003, ApJ, 591, 662

de Blok, W. J. G. & McGaugh, S. S. 1997, MNRAS, 290, 533

De Luca, A. & Molendi, S. 2004, A&A, 419, 837

De Lucia, G., Weinmann, S., Poggianti, B., Aragon-Salamanca, A., & Zaritsky, D. 2011, ArXiv e-prints, http://arxiv.org/abs/1111.6590

Dodelson, S. 2003, Moden Cosmology (Elsevier), 180 ff

Donahue, M., Gaskin, J. A., Patel, S. K., et al. 2003, ApJ, 598, 190

Donnarumma, A., Ettori, S., Meneghetti, M., et al. 2011, A&A, 528, A73

Donnarumma, A., Ettori, S., Meneghetti, M., & Moscardini, L. 2009, MNRAS, 398, 438

Dressler, A. 1980, ApJS, 42, 565

Dunkley, J., Komatsu, E., Nolta, M. R., et al. 2009, ApJS, 180, 306

Ebeling, H., Barrett, E., Donovan, D., et al. 2007, ApJ, 661, L33

Ebeling, H., Edge, A. C., Mantz, A., et al. 2010, MNRAS, 407, 83

Ebeling, H., Voges, W., Böhringer, H., et al. 1996, MNRAS, 281, 799

Eckmiller, H. J., Hudson, D. S., & Reiprich, T. H. 2011, A&A, 535, A105

Eisenstein, D. J., Zehavi, I., Hogg, D. W., et al. 2005, ApJ, 633, 560

Eke, V. R., Cole, S., & Frenk, C. S. 1996, MNRAS, 282, 263

Ellis, R. S., Smail, I., Dressler, A., et al. 1997, ApJ, 483, 582

Erben, T., Hildebrandt, H., Lerchster, M., et al. 2009, A&A, 493, 1197

Erben, T., Schirmer, M., Dietrich, J. P., et al. 2005, Astronomische Nachrichten, 326, 432

Erben, T., Van Waerbeke, L., Bertin, E., Mellier, Y., & Schneider, P. 2001, A&A, 366, 717

Etherington, I. M. H. 1933, Philosophical Magazine, 15, 761

Ettori, S., Tozzi, P., Borgani, S., & Rosati, P. 2004, A&A, 417, 13

Evrard, A. E., Metzler, C. A., & Navarro, J. F. 1996, ApJ, 469, 494

Fabian, A. C. 1993, in Astronomical Society of the Pacific Conference Series, Vol. 51, Observational Cosmology, ed. G. L. Chincarini, A. Iovino, T. Maccacaro, & D. Maccagni, 380

Fabian, A. C., Sanders, J. S., Ettori, S., et al. 2000, MNRAS, 318, L65

Fabjan, D., Borgani, S., Rasia, E., et al. 2011, MNRAS, 416, 801

Fabjan, D., Borgani, S., Tornatore, L., et al. 2010, MNRAS, 401, 1670

Fakhouri, O. & Ma, C.-P. 2008, MNRAS, 386, 577

Feigelson, E. D. & Babu, G. J. 1992, ApJ, 397, 55

Feretti, L., Fusco-Femiano, R., Giovannini, G., & Govoni, F. 2001, A&A, 373, 106

Feretti, L. & Giovannini, G. 2008, in Lecture Notes in Physics, Berlin Springer Verlag, Vol. 740, A Pan-Chromatic View of Clusters of Galaxies and the Large-Scale Structure, ed. M. Plionis, O. López-Cruz, & D. Hughes, 143

Foley, R. J., Andersson, K., Bazin, G., et al. 2011, ApJ, 731, 86

Forman, W. & Jones, C. 1991, in Clusters and Superclusters of Galaxies, ed. M. M. Colless, A. Babul, A. C. Edge, R. M. Johnstone, & S. Raychaudhury , 113

Fort, B., Le Fevre, O., Hammer, F., & Cailloux, M. 1992, ApJ, 399, L125

Freedman, W. L., Madore, B. F., Gibson, B. K., et al. 2001, ApJ, 553, 47

Friedmann, A. 1922, Zeitschrift fur Physik, 10, 377

Friedmann, A. 1924, Zeitschrift fur Physik, 21, 326

Fumagalli, M., O'Meara, J. M., & Prochaska, J. X. 2011, Science, 334, 1245

Gavazzi, R. 2005, A&A, 443, 793

Gavazzi, R., Fort, B., Mellier, Y., Pelló, R., & Dantel-Fort, M. 2003, A&A, 403, 11

Gavazzi, R. & Soucail, G. 2007, A&A, 462, 459

George, M. R., Fabian, A. C., Sanders, J. S., Young, A. J., & Russell, H. R. 2009, MNRAS, 395, 657

Giacconi, R., Gursky, H., Paolini, F. R., & Rossi, B. B. 1962, Physical Review Letters, 9, 439

Gioia, I. M., Luppino, G., Annis, J., Hammer, F., & Le Fèvre, O. 1996, in IAU Symposium, Vol. 168, Examining the Big Bang and Diffuse Background Radiations, ed. M. C. Kafatos & Y. Kondo, 549

Gioia, I. M. & Luppino, G. A. 1994, ApJS, 94, 583

Giovannini, G. & Feretti, L. 2000, New A, 5, 335

Giovannini, G., Tordi, M., & Feretti, L. 1999, New A, 4, 141

Girardi, M. & Mezzetti, M. 2001, ApJ, 548, 79

Gladders, M. D. & Yee, H. K. C. 2000, AJ, 120, 2148

Gladders, M. D. & Yee, H. K. C. 2005, ApJS, 157, 1

Gladders, M. D., Yee, H. K. C., Majumdar, S., et al. 2007, ApJ, 655, 128

Gonzalez, A. H., Zaritsky, D., & Zabludoff, A. I. 2007, ApJ, 666, 147

Goto, T., Sekiguchi, M., Nichol, R. C., et al. 2002, AJ, 123, 1807

Gott, III, J. R., Jurić, M., Schlegel, D., et al. 2005, ApJ, 624, 463

Grazian, A., Fontana, A., de Santis, C., et al. 2006, A&A, 449, 951

Gull, S. F. & Northover, K. J. E. 1976, Nature, 263, 572

Guth, A. H. 1981, Phys. Rev. D, 23, 347

Haines, C. P., Smith, G. P., Egami, E., et al. 2009, ApJ, 704, 126

Halverson, N. W., Lanting, T., Ade, P. A. R., et al. 2009, ApJ, 701, 42

Hammer, F., Gioia, I. M., Shaya, E. J., et al. 1997, ApJ, 491, 477

Hartlap, J., Schrabback, T., Simon, P., & Schneider, P. 2009, A&A, 504, 689

Hennawi, J. F., Dalal, N., Bode, P., & Ostriker, J. P. 2007, ApJ, 654, 714

Henry, A. L., Siana, B., Malkan, M. A., et al. 2009, ApJ, 697, 1128

Heymans, C., Van Waerbeke, L., Bacon, D., et al. 2006, MNRAS, 368, 1323

Hickox, R. C. & Markevitch, M. 2007, ApJ, 661, L117

Hilbert, S., Hartlap, J., White, S. D. M., & Schneider, P. 2009, A&A, 499, 31

Hildebrandt, H., Erben, T., Kuijken, K., et al. 2012, MNRAS, 2386

Hildebrandt, H., Pielorz, J., Erben, T., et al. 2009, A&A, 498, 725

Hoekstra, H. 2003, MNRAS, 339, 1155

Hoekstra, H. 2007, MNRAS, 379, 317

Hoekstra, H., Franx, M., Kuijken, K., & Squires, G. 1998, ApJ, 504, 636

Hoekstra, H., Hartlap, J., Hilbert, S., & van Uitert, E. 2011, MNRAS, 412, 2095

Holhjem, K., Schirmer, M., & Dahle, H. 2009, A&A, 504, 1

Hubble, E. 1929, Proceedings of the National Academy of Science, 15, 168

Hudson, D. S., Reiprich, T. H., Clarke, T. E., & Sarazin, C. L. 2006, A&A, 453, 433

Huterer, D. & Turner, M. S. 2001, Phys. Rev. D, 64, 123527

Ikebe, Y., Reiprich, T. H., Böhringer, H., Tanaka, Y., & Kitayama, T. 2002, A&A, 383, 773

Ilbert, O., Capak, P., Salvato, M., et al. 2009, ApJ, 690, 1236

Israel, H., Erben, T., Reiprich, T. H., et al. 2010, A&A, 520, A58

Israel, H., Erben, T., Reiprich, T. H., et al. 2011, ArXiv e-prints, http://arxiv.org/abs/1112.4444

Izotov, Y. I., Thuan, T. X., & Stasińska, G. 2007, ApJ, 662, 15

Jäger, K., Ziegler, B. L., Böhm, A., et al. 2004, A&A, 422, 907

Jenkins, A., Frenk, C. S., White, S. D. M., et al. 2001, MNRAS, 321, 372

Kaastra, J. S. 1992, An X-Ray Spectral Code for Optically Thin Plasmas (Internal SRON-Leiden Report, updated version 2.0)

Kaiser, N. 1986, MNRAS, 222, 323

Kaiser, N. 1995, ApJ, 439, L1

Kaiser, N. & Squires, G. 1993, ApJ, 404, 441

Kalberla, P. M. W., Burton, W. B., Hartmann, D., et al. 2005, A&A, 440, 775

Kawaharada, M., Okabe, N., Umetsu, K., et al. 2010, ApJ, 714, 423

Kim, A., Goobar, A., & Perlmutter, S. 1996, PASP, 108, 190

King, I. 1962, AJ, 67, 471

Koekemoer, A. M., Fruchter, A. S., Hook, R. N., & Hack, W. 2002, in The 2002 HST Calibration Workshop : Hubble after the Installation of the ACS and the NICMOS Cooling System, ed. S. Arribas, A. Koekemoer, & B. Whitmore, 337

Koester, B. P., McKay, T. A., Annis, J., et al. 2007, ApJ, 660, 239

Komatsu, E., Smith, K. M., Dunkley, J., et al. 2011, ApJS, 192, 18

Kotov, O. & Vikhlinin, A. 2005, ApJ, 633, 781

Kowalski, M., Rubin, D., Aldering, G., et al. 2008, ApJ, 686, 749

Kravtsov, A. V., Vikhlinin, A., & Nagai, D. 2006, ApJ, 650, 128

Krick, J. E. & Bernstein, R. A. 2007, AJ, 134, 466

Kuntz, K. D. & Snowden, S. L. 2001, ApJ, 554, 684

Lallement, R. 2004, A&A, 418, 143

LaRoque, S. J., Bonamente, M., Carlstrom, J. E., et al. 2006, ApJ, 652, 917

Larson, D., Dunkley, J., Hinshaw, G., et al. 2011, ApJS, 192, 16

Le Fevre, O., Hammer, F., Angonin, M. C., Gioia, I. M., & Luppino, G. A. 1994, ApJ, 422, L5

Leccardi, A. & Molendi, S. 2008, A&A, 486, 359

Lemaître, G. 1927, Annales de la Societe Scietifique de Bruxelles, 47, 49

Lemaître, G. 1933, Annales de la Societe Scietifique de Bruxelles, 53, 51

Lewis, A. D., Ellingson, E., Morris, S. L., & Carlberg, R. G. 1999, ApJ, 517, 587

Liedahl, D. A., Osterheld, A. L., & Goldstein, W. H. 1995, ApJ, 438, L115

Lin, L., Koo, D. C., Willmer, C. N. A., et al. 2004, ApJ, 617, L9

Lumb, D. H., Bartlett, J. G., Romer, A. K., et al. 2004, A&A, 420, 853

Luppino, G. A., Gioia, I. M., Hammer, F., Le Fèvre, O., & Annis, J. A. 1999, A&AS, 136, 117

Luppino, G. A. & Kaiser, N. 1997, ApJ, 475, 20

Magnier, E. A. & Cuillandre, J.-C. 2004, PASP, 116, 449

Mahdavi, A., Hoekstra, H., Babul, A., & Henry, J. P. 2008, MNRAS, 384, 1567

Mantz, A., Allen, S., Rapetti, D., Ebeling, H., & Drlica-Wagner, A. 2009, in Chandra's First Decade of Discovery, ed. S. Wolk, A. Fruscione, & D. Swartz

Mantz, A., Allen, S. W., Ebeling, H., & Rapetti, D. 2008, MNRAS, 387, 1179

Mantz, A., Allen, S. W., Ebeling, H., Rapetti, D., & Drlica-Wagner, A. 2010a, MNRAS, 406, 1773

Mantz, A., Allen, S. W., Rapetti, D., & Ebeling, H. 2010b, MNRAS, 406, 1759

Markevitch, M. 1998, ApJ, 504, 27

Markevitch, M., Forman, W. R., Sarazin, C. L., & Vikhlinin, A. 1998, ApJ, 503, 77

Massey, R., Heymans, C., Bergé, J., et al. 2007, MNRAS, 376, 13

Maturi, M., Schirmer, M., Meneghetti, M., Bartelmann, M., & Moscardini, L. 2007, A&A, 462, 473

Maughan, B. J., Jones, L. R., Ebeling, H., & Scharf, C. 2006, MNRAS, 365, 509

Maughan, B. J., Jones, L. R., Pierre, M., et al. 2008, MNRAS, 387, 998

Mayen, C. & Soucail, G. 2000, A&A, 361, 415

Mellier, Y. 1999, ARA&A, 37, 127

Menanteau, F., González, J., Juin, J.-B., et al. 2010, ApJ, 723, 1523

Mendes de Oliveira, C. L. & Carrasco, E. R. 2007, ApJ, 670, L93

Merten, J., Cacciato, M., Meneghetti, M., Mignone, C., & Bartelmann, M. 2009, A&A, 500, 681

Mewe, R., Gronenschild, E. H. B. M., & van den Oord, G. H. J. 1985, A&AS, 62, 197

Mewe, R., Lemen, J. R., & van den Oord, G. H. J. 1986, A&AS, 65, 511

Milkeraitis, M., van Waerbeke, L., Heymans, C., et al. 2010, MNRAS, 406, 673

Miller, C. J., Nichol, R. C., Reichart, D., et al. 2005, AJ, 130, 968

Mitchell, R. J., Culhane, J. L., Davison, P. J. N., & Ives, J. C. 1976, MNRAS, 175, 29P

Mobasher, B., Capak, P., Scoville, N. Z., et al. 2007, ApJS, 172, 117

Moran, S. M., Ellis, R. S., Treu, T., et al. 2007, ApJ, 671, 1503

Mushotzky, R. F. & Scharf, C. A. 1997, ApJ, 482, L13

Mushotzky, R. F., Serlemitsos, P. J., Boldt, E. A., Holt, S. S., & Smith, B. W. 1978, ApJ, 225, 21

Nagai, D., Vikhlinin, A., & Kravtsov, A. V. 2007, ApJ, 655, 98

Navarro, J. F., Frenk, C. S., & White, S. D. M. 1996, ApJ, 462, 563

Navarro, J. F., Frenk, C. S., & White, S. D. M. 1997, ApJ, 490, 493

Neumann, D. M. & Arnaud, M. 2001, A&A, 373, L33

Neumann, D. M. & Böhringer, H. 1997, MNRAS, 289, 123

Noterdaeme, P., Petitjean, P., Srianand, R., Ledoux, C., & López, S. 2011, A&A, 526, L7

Oguri, M. & Hamana, T. 2011, MNRAS, 414, 1851

Oguri, M., Takada, M., Okabe, N., & Smith, G. P. 2010, MNRAS, 405, 2215

Okabe, N. & Umetsu, K. 2008, PASJ, 60, 345

Okabe, N., Zhang, Y.-Y., Finoguenov, A., et al. 2010, ApJ, 721, 875

Oke, J. B. & Sandage, A. 1968, ApJ, 154, 21

Parker, L. C., Hoekstra, H., Hudson, M. J., van Waerbeke, L., & Mellier, Y. 2007, ApJ, 669, 21

Peacock, J. 1999, Cosmological Physics (Cambridge University Press)

Peacock, J. A., Cole, S., Norberg, P., et al. 2001, Nature, 410, 169

Penzias, A. A. & Wilson, R. W. 1965, ApJ, 142, 419

Percival, W. J., Cole, S., Eisenstein, D. J., et al. 2007, MNRAS, 381, 1053

Perlman, E. S., Horner, D. J., Jones, L. R., et al. 2002, ApJS, 140, 265

Perlmutter, S., Turner, M. S., & White, M. 1999, Physical Review Letters, 83, 670

Pierpaoli, E., Scott, D., & White, M. 2001, MNRAS, 325, 77

Pillepich, A., Porciani, C., & Hahn, O. 2010, MNRAS, 402, 191

Pinzke, A. & Pfrommer, C. 2010, MNRAS, 409, 449

Planck Collaboration, Aghanim, N., Arnaud, M., et al. 2011, A&A, 536, A26

Pospelov, M. & Pradler, J. 2010, Annual Review of Nuclear and Particle Science, 60, 539

Postman, M., Lubin, L. M., Gunn, J. E., et al. 1996, AJ, 111, 615

Pratt, G. W. & Arnaud, M. 2005, A&A, 429, 791

Pratt, G. W., Böhringer, H., Croston, J. H., et al. 2007, A&A, 461, 71

Pratt, G. W., Böhringer, H., & Finoguenov, A. 2005, A&A, 433, 777

Pratt, G. W., Croston, J. H., Arnaud, M., & Böhringer, H. 2009, A&A, 498, 361

Press, W. H. & Schechter, P. 1974, ApJ, 187, 425

Qin, B. & Wu, X.-P. 2001, Physical Review Letters, 87, 061301

Rasia, E., Meneghetti, M., Martino, R., et al. 2012, ArXiv e-prints, http://arxiv.org/abs/1201.1569

Reiprich, T. H. 2001, PhD thesis, Max-Planck-Institut für extraterrestrische Physik, P.O. Box 1312, Garching bei München, Germany

Reiprich, T. H. 2011, X-ray Astronomy, ed. T. H. Reiprich, Lecture Notes in X-ray Astronomy

Reiprich, T. H. & Böhringer, H. 2002, ApJ, 567, 716

Reiprich, T. H., Hudson, D. S., Zhang, Y.-Y., et al. 2009, A&A, 501, 899

Richard, J., Smith, G. P., Kneib, J.-P., et al. 2010, MNRAS, 404, 325

Ricker, P. M. & Sarazin, C. L. 2001, ApJ, 561, 621

Riess, A. G., Strolger, L.-G., Tonry, J., et al. 2004, ApJ, 607, 665

Robertson, H. P. 1935, ApJ, 82, 284

Robertson, I. P. & Cravens, T. E. 2003, Geophys. Res. Lett., 30, 080000

Romer, A. K., Nichol, R. C., Holden, B. P., et al. 2000, ApJS, 126, 209

Rood, H. J. & Sastry, G. N. 1971, PASP, 83, 313

Rosati, P., Borgani, S., & Norman, C. 2002, ARA&A, 40, 539

Rosati, P., Tozzi, P., Gobat, R., et al. 2009, A&A, 508, 583

Rybicki, G. B. & Lightman, A. P. 1979, Radiative processes in astrophysics, ed. Rybicki, G. B. & Lightman, A. P.

Sarazin, C. L. 1988, X-Ray Emission from Clusters of Galaxies, Journal of the British Astronomical Association, 98, 212

Sarazin, C. L. & Bahcall, J. N. 1977, ApJS, 34, 451

Sato, K. 1981, MNRAS, 195, 467

Scharf, C. A., Jones, L. R., Ebeling, H., et al. 1997, ApJ, 477, 79

Schindler, S. 1996, A&A, 305, 756

Schindler, S. 2004, Interaction of galaxies with the intra-cluster medium and ICM metal enrichment, ed. R. Dettmar, U. Klein, & P. Salucci

Schirmer, M., Erben, T., Hetterscheidt, M., & Schneider, P. 2007, A&A, 462, 875

Schirmer, M., Suyu, S., Schrabback, T., et al. 2010, A&A, 514, A60

Schneider, P. 1996, MNRAS, 283, 837

Schneider, P. 2006a, Introduction to Gravitational Lensing and Cosmology, Saas-Fee Advanced Courses, ed. Schneider, P., Kochanek, C. S., & Wambsganss, J., Springer-Verlag Berlin Heidelberg, 1 ff

Schneider, P. 2006b, Weak Gravitational Lensing, Saas-Fee Advanced Courses, ed. Schneider, P., Kochanek, C. S., & Wambsganss, J., Springer-Verlag Berlin Heidelberg, 269

Schneider, P., Ehlers, J., & Falco, E. E. 1992, Gravitational Lenses, ed. Springer-Verlag Berlin Heidelberg

Schneider, P., King, L., & Erben, T. 2000, A&A, 353, 41

Schrabback, T., Erben, T., Simon, P., et al. 2007, A&A, 468, 823

Schrabback, T., Hartlap, J., Joachimi, B., et al. 2010, A&A, 516, A63

Schuecker, P., Böhringer, H., Collins, C. A., & Guzzo, L. 2003a, A&A, 398, 867

Schuecker, P., Böhringer, H., Reiprich, T. H., & Feretti, L. 2001, A&A, 378, 408

Schuecker, P., Caldwell, R. R., Böhringer, H., et al. 2003b, A&A, 402, 53

Seitz, C. & Schneider, P. 1997, A&A, 318, 687

Seitz, S. & Schneider, P. 2001, A&A, 374, 740

Sheth, R. K. & Tormen, G. 1999, MNRAS, 308, 119

Simionescu, A., Allen, S. W., Mantz, A., et al. 2011, Science, 331, 1576

Skrutskie, M. F., Cutri, R. M., Stiening, R., et al. 2006, AJ, 131, 1163

Smail, I., Ellis, R. S., Dressler, A., et al. 1997, ApJ, 479, 70

Smith, G. P., Haines, C. P., Pereira, M. J., et al. 2010, A&A, 518, L18

Smith, G. P., Kneib, J.-P., Smail, I., et al. 2005, MNRAS, 359, 417

Snowden, S. L., Mushotzky, R. F., Kuntz, K. D., & Davis, D. S. 2008, A&A, 478, 615

Solovyeva, L., Anokhin, S., Sauvageot, J. L., Teyssier, R., & Neumann, D. 2007, A&A, 476, 63

Sonnenfeld, A., Bertin, G., & Lombardi, M. 2011, A&A, 532, A37

Springel, V., White, M., & Hernquist, L. 2001, ApJ, 549, 681

Stanek, R., Rasia, E., Evrard, A. E., Pearce, F., & Gazzola, L. 2010, ApJ, 715, 1508

Steigman, G. 2006, International Journal of Modern Physics E, 15, 1

Stocke, J. T., Morris, S. L., Gioia, I. M., et al. 1991, ApJS, 76, 813

Stockton, A. 1980, ApJ, 242, L141

Story, K., Aird, K. A., Andersson, K., et al. 2011, ApJ, 735, L36

Strüder, L., Briel, U., Dennerl, K., et al. 2001, A&A, 365, L18

Sunyaev, R. A. & Zeldovich, Y. B. 1970, Comments on Astrophysics and Space Physics, 2, 66

Suyu, S. H., Marshall, P. J., Auger, M. W., et al. 2010, ApJ, 711, 201

Takada, M. & Jain, B. 2003a, MNRAS, 340, 580

Takada, M. & Jain, B. 2003b, MNRAS, 344, 857

Tanaka, I., Yamada, T., Turner, E. L., & Suto, Y. 2001, ApJ, 547, 521

Tanaka, M., Kodama, T., Arimoto, N., et al. 2005, MNRAS, 362, 268

Tegmark, M., Blanton, M. R., Strauss, M. A., et al. 2004, ApJ, 606, 702

Tegmark, M., Eisenstein, D. J., Strauss, M. A., et al. 2006, Phys. Rev. D, 74, 123507

Thuan, T. X. 2008, in IAU Symposium, Vol. 255, IAU Symposium, ed. L. K. Hunt, S. Madden, & R. Schneider, 348–360

Tinker, J., Kravtsov, A. V., Klypin, A., et al. 2008, ApJ, 688, 709

Turner, M. J. L., Abbey, A., Arnaud, M., et al. 2001, A&A, 365, L27

Tyson, J. A., Wenk, R. A., & Valdes, F. 1990, ApJ, 349, L1

van Uitert, E., Hoekstra, H., Velander, M., et al. 2011, A&A, 534, A14

Vikhlinin, A., Burenin, R. A., Ebeling, H., et al. 2009a, ApJ, 692, 1033

Vikhlinin, A., Kravtsov, A., Forman, W., et al. 2006, ApJ, 640, 691

Vikhlinin, A., Kravtsov, A. V., Burenin, R. A., et al. 2009b, ApJ, 692, 1060

Vikhlinin, A., Markevitch, M., Murray, S. S., et al. 2005, ApJ, 628, 655

Vikhlinin, A., van Speybroeck, L., Markevitch, M., Forman, W. R., & Grego, L. 2002, ApJ, 578, L107

Voit, G. M. 2005, Reviews of Modern Physics, 77, 207

Walker, A. G. 1937, Proceedings of the London Mathematical Society, 2-42, 90

Walsh, D. 1989, in Lecture Notes in Physics, Berlin Springer Verlag, Vol. 330, Gravitational Lenses, ed. J. M. Moran, J. N. Hewitt, & K.-Y. Lo, 11

Warren, M. S., Abazajian, K., Holz, D. E., & Teodoro, L. 2006, ApJ, 646, 881

Whitmore, B. C., Gilmore, D. M., & Jones, C. 1993, ApJ, 407, 489

Willson, M. A. G. 1970, MNRAS, 151, 1

Worrall, D. M. & Birkinshaw, M. 2003, MNRAS, 340, 1261

Wright, C. O. & Brainerd, T. G. 2000, ApJ, 534, 34

Wu, X.-P., Chiueh, T., Fang, L.-Z., & Xue, Y.-J. 1998, MNRAS, 301, 861

Young, P., Gunn, J. E., Oke, J. B., Westphal, J. A., & Kristian, J. 1980, ApJ, 241, 507

Zhang, Y., Finoguenov, A., Böhringer, H., et al. 2008, A&A, 482, 451

Zhang, Y.-Y. 2001, Chinese J. Astron. Astrophys., 1, 29

Zhang, Y.-Y., Andernach, H., Caretta, C. A., et al. 2011a, A&A, 526, A105

Zhang, Y.-Y., Böhringer, H., Finoguenov, A., et al. 2006, A&A, 456, 55

Zhang, Y.-Y., Böhringer, H., Mellier, Y., Soucail, G., & Forman, W. 2005, A&A, 429, 85

Zhang, Y.-Y., Finoguenov, A., Böhringer, H., et al. 2004, A&A, 413, 49

Zhang, Y.-Y., Finoguenov, A., Böhringer, H., et al. 2007, A&A, 467, 437

Zhang, Y.-Y., Laganá, T. F., Pierini, D., et al. 2011b, A&A, 535, A78

Zhang, Y.-Y., Okabe, N., Finoguenov, A., et al. 2010, ApJ, 711, 1033

Zhang, Y.-Y., Reiprich, T. H., Finoguenov, A., Hudson, D. S., & Sarazin, C. L. 2009, ApJ, 699, 1178

Zhang, Y.-Y. & Wu, X.-P. 2003, ApJ, 583, 529

Zhao, H. S. 2000, ApJ, 530, 299

Zibetti, S., White, S. D. M., Schneider, D. P., & Brinkmann, J. 2005, MNRAS, 358, 949

Ziegler, B. L., Böhm, A., Jäger, K., Heidt, J., & Möllenhoff, C. 2003, ApJ, 598, L87

Zwicky, F. 1933, Helvetica Physica Acta, 6, 110

Acknowledgements

First of all, I would like to thank Prof. Dr. Peter Schneider and Dr. Thomas Erben for giving me the possibility to write my PhD thesis at the Argelander Institut für Astronomie and for supervising the weak lensing part of my project. I also appreciate the supervision of Dr. Yu-Ying Zhang for the X-ray analysis of my cluster sample and her counsel.

Especially I want to thank Prof. Dr. Thomas Reiprich for co-refereeing this thesis, as well as PD. Dr. Bernard Metsch and Prof. Dr. Andreas Hense for agreeing to be members of my thesis committee.

I like to thank Tim Schrabback, Thomas Erben, Mischa Schirmer and Hendrik Hildebrandt for providing the optical data without which this thesis would not have been possible. These data are from the NASA/ESA Hubble Space Telescope which is operated by the Association of Universities for Research in Astronomy, Inc.; the Subaru Telescope, which is operated by the National Astronomical Observatory of Japan; from MegaPrime/MegaCam, a joint project of CFHT and CEA/DAPNIA, at the Canada-France-Hawaii Telescope (CFHT) which is operated by the National Research Council (NRC) of Canada, the Institut National des Sciences de l'Univers of the Centre National de la Recherche Scientifique (CNRS) of France, and the University of Hawaii; and the W.M. Keck Observatory, which is operated as a scientific partnership among the California Institute of Technology, the University of California and the National Aeronautics and Space Administration. The X-ray data of this work are archival data from *XMM-Newton*, an ESA science mission with instruments and contributions directly funded by ESA member states and the USA (NASA); and from the Chandra Data Archive and the Chandra Source Catalog. Here, I also want to thank Helen Eckmiller for the reduction of the *Chandra* data and for providing the spectra and Yu-Ying Zhang for carrying out the point source subtraction and the determination of the flux-weighted X-ray centroid of the *XMM-Newton* clusters as well as for providing the fits of the scaling relations with the `ODR`-package. Thanks also to Holger Israel for making the contour maps.

The weak lensing analysis of this thesis was recently submitted to the journal Astronomy& Astrophysics. I very much appreciate the contributions of my co-authors Thomas Erben, Tim Schrabback, Mischa Schirmer, Hendrik Hildebrandt, Peter Schneider, Bodo Ziegler and Holger Israel in terms of constructive comments and discussions. I also want to thank Stefan Hilbert for discussing how to estimate the LSS-error for MS0451.6−0305.

Many thanks also to all those people who proof-read this thesis, i.e. Sandra Burkutean, Helen Eckmiller, Thomas Erben and Yu-Ying Zhang as well as Peter Schneider and Thomas Reiprich for correcting the final draft version. Special thanks go to Robert Izzard for his lecture on scientific writing and to Yu-Ying Zhang who put much effort in improving my scientific writing skills.

I also like to thank the AIfA staff, especially the secretaries Christina Stein-Schmitz, Kathy Schrüfer and Ellen Vasters for helping me with bureaucratic matters in terms of business trips and contracts, but also with their advice. Thanks also to the computer group, in particular to Andreas Bödewig, Oliver-Marc Cordes, Ole Marggraf and Reinhold Schaaf for solving various computer problems.

Many thanks also to Thomas Reiprich for giving me the opportunity to observe at La Silla, Chile which provided me with practical experience on observational astronomy.

I acknowledge financial support by the BMBF/DLR through research grant 50 OR 0601 and from the Deutsche Forschungsgemeinschaft under project ER 327/3-1. For two years of my PhD thesis, I was a member of the International Max Planck Research School (IMPRS) for Astronomy and Astrophysics at the Universities of Bonn and Cologne which gave me the possibility to met PhD students from other research fields and to attend exciting lectures and trainings. Here, I particularly want to thank Emmanouil Angelakis and Simone Pott for organising those events.

Last but not least want to thank those people from the AIfA, I consider as friends and which accompanied me during the past three years, i.e. Verena Darmstädter, Helen Eckmiller, Kerstin Enders-Brehm, Holger Israel, Matthias Klein, Daniela Kübler, Ismael Tereno, Bharadwaj Vijaysarathy and Yu-Ying Zhang. Thank you for making my time at the AIfA most enjoyable. I would also like to thank all those others I forgot due to my usual distraction.

Finally, and with all my heart I want to thank Martin Scherer, my sun-and-stars, for his love, his patience and his encouragement.